Direct Detection of Electrons with the pnCCD for Applications in Transmission Electron Microscopy

Henning Ryll

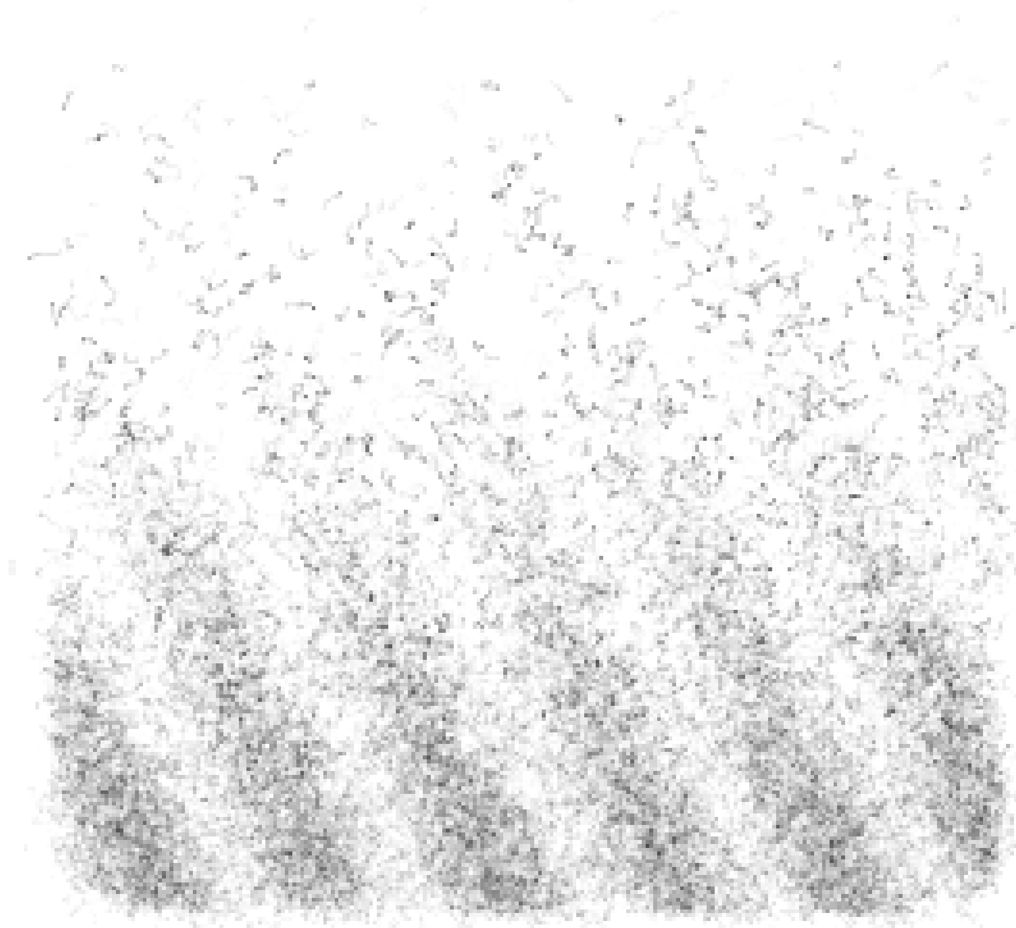

Direct Detection of Electrons with the pnCCD for Applications in Transmission Electron Microscopy

DISSERTATION
zur Erlangung des Grades eines Doktors
der Naturwissenschaften

vorgelegt von
Dipl.-Phys. Henning Ryll

eingereicht bei der Naturwissenschaftlich-Technischen Fakultät
der Universität Siegen
Siegen 2017

Tag der mündlichen Prüfung: 18.12.2017

Erstgutachter: Prof. Dr. Lothar Strüder
Zweitgutachter: Prof. Dr. Dr. h.c. Ullrich Pietsch

Gedruckt auf alterungsbeständigem holz- und säurefreiem Papier.

Dedicated to my grandfather Hansjürgen Rietzke

for his encouragement of fun creative thinking.

Abstract

In this dissertation, the signal response of the pnCCD under electron illumination was studied comprehensively. The pnCCD is a spatially resolving, fast, energy dispersive, charge-coupled-device (CCD) semiconductor detector that has great potential for applications in transmission electron microscopes (TEMs) as deduced from previous measurements with (X-ray) photons. However, there had not been an elaborate analysis of the pnCCD under electron illumination. The present work closes this gap with a detailed physical explanation and modelling of the signal response of the pnCCD to electrons established on a systematic investigation with experiments, simulations and analysis. A series of conducted, application-oriented experiments showed that the pnCCD improves analysis and methods in electron microscopy.

As part of this work, a camera with the pnCCD was developed and mounted at TEMs at numerous research institutes. In a diversity of experiments, single TEM electrons were imaged in the energy range of 20 keV to 300 keV. From this data, energy spectra of single electrons were determined. With the analysis of these spectra in combination with simulations, the scattering of the TEM electrons inside the detector could be explained as well as the readout signals. A relevant influence on the measured signal is exerted by the backscattered electrons that do not deposit their full energy in the detector, but rather scatter out of it. On the basis of the developed analysis, the precise number of incoming TEM electrons can now be determined.

The relationships between the readout signals, the pnCCD's parameters and the parameters of the TEM (mainly the energy of the TEM electrons) were determined and explained. Furthermore, the spatial resolution was investigated. The spatial resolution could be increased with several models allowing images created with single TEM electrons to offer pixel sizes smaller than the given physical sizes. For TEM electron energies of ≤ 80 keV, images with 5×5 sub-pixel resolution showed increased contrast and resolved finer details than images without sub-pixel resolution.

With the help of five selected applications (holography, tomography, measurement of magnetic domains, measurement of lattice strain, ptychography), it is shown that the pnCCD is an excellent imager for electrons in TEM because the pnCCD improves existing experimental methods significantly or even enables methods that previously could only be used on a proof of concept basis due to technical limitations

of other detectors. Primarily, this includes methods that presuppose the fast acquisition of signals spatially distributed in two dimensions. In particular, applications in the scanning mode (STEM), in which a focused electron beam is scanned over a sample quickly and a two dimensional image is recorded for each probe position, are enabled by the fast readout of the pnCCD.

To highlight one STEM method, the ptychographic method allows the reconstruction of the amplitude *and* phase of the electron wave that has passed the sample. Based on the modification of the phase by the sample, conclusions can be drawn about the sample that are not accessible with other methods. As an example, a complex sample was investigated consisting of carbon nanotubes and biological active components. Using the pnCCD and ptychography, it could be clearly shown that the synthesis of this sample was only partially successful. This was the first time that such results could be verified experimentally.

This dissertation lays the comprehensive foundation for the ongoing and future use of the pnCCD for the detection and imaging of electrons, in particular in electron microscopy. In addition, the analysis and findings of this work will provide a valuable basis for the development and characterization of further future electron detectors.

Zusammenfassung

In dieser Dissertation wurde die Signalantwort des pnCCDs unter Bestrahlung mit Elektronen umfassend untersucht. Der pnCCD ist ein ortsauflösender, schneller und energiedispersiver »charged coupled device« (CCD)-Halbleiterdetektor, welchem abgeleitet von vorausgegangenen Messungen mit (Röntgen-) Photonen auch ein enormes Potenzial für Anwendungen in Transmissionselektronenmikroskopen (TEM) zugesprochen wurde. Es hatte jedoch bisher keine ausführliche Analyse des pnCCDs unter Beleuchtung mit Elektronen gegeben. Die vorliegende Arbeit füllt diese Lücke mit einer detaillierten physikalischen Beschreibung und Modellierung der Signalantwort des pnCCDs auf Elektronen, aufbauend auf einer systematischen Untersuchung durch Experimente, Simulationen und Analysen. In einer Reihe von anwendungsorientierten Experimenten wurde gezeigt, dass mit dem pnCCD Analysen und Methoden in der Elektronenmikroskopie grundlegend verbessert werden.

Im Rahmen dieser Arbeit wurde eine Kamera mit dem pnCCD als bildgebenden Sensor entwickelt und an TEMs mehrerer Forschungsinstitute installiert. In verschiedenen Experimenten wurden unter anderem einzelne Elektronen im Bereich von 20 keV bis 300 keV abgebildet. Anhand dieser Aufnahmen konnten Energiespektren von einzelnen TEM Elektronen gewonnen werden. Durch die Analyse der Spektren konnten in Kombination mit Simulationen die Streuvorgänge in dem pnCCD untersucht und die ausgelesenen Signale erklärt werden. Einen signifikanten Einfluss haben hierbei TEM Elektronen, die nicht ihre gesamte Energie im Detektor deponieren, sondern wieder aus dem sensitiven Detektorvolumen heraus streuen. Die in diesem Zusammenhang entwickelten Analysen ermöglichen nun die präzise Anzahl der eintreffenden TEM Elektronen zu bestimmen.

Die Abhängigkeiten zwischen den ausgelesenen Signalen, den pnCCD Parametern und den TEM Parametern (hauptsächlich die Energie der TEM Elektronen) wurden bestimmt und beschrieben. Weiterhin wurde das räumliche Auflösungsvermögen untersucht welches für die Abbildung von Einzelelektronen mit mehreren Modellen signifikant gesteigert werden konnte, so dass die Pixelgrößen in resultierenden Bildern kleiner sind als die gegebene physikalische Pixelgröße. Besonders für Elektronenenergien von $\leq$ 80 keV konnten Bilder mit einer 5×5 sub-pixel Auflösung erzeugt werden, die einen erhöhten Kontrast und kleinere Details zeigen als Bilder ohne sub-pixel Auflösung.

Anhand von fünf ausgewählten Anwendungen (Holographie, Tomographie, Abbildung von magnetischen Domänen, Messung von Kristallgitterverspannungen, Ptychographie) wurde gezeigt, dass der pnCCD verschiedenste experimentelle Methoden in der Transmissionselektronenmikroskopie entscheidend verbessert und dass Methoden, die ehemals im »proof-of-concept« Stadium waren, nun mit dem pnCCD praktisch anwendbar sind. Dazu zählen Methoden, die eine schnelle Aufzeichnung von räumlich in zwei Dimensionen verteilten Signalen zwingend voraussetzen. Insbesondere Anwendungen im »scanning« Modus (STEM), in dem eine Probe mit einem fokussierten Elektronenstrahl in zwei Dimensionen abgerastert und für jede Probenposition ein zweidimensionales Bild aufgenommen wird, werden durch die schnelle Auslese des pnCCDs ermöglicht.

Hervorzuheben ist ein ptychographisches Verfahren, mit dem die Elektronenwellenfunktion, die die Probe passierte, in Amplitude *und* Phase bestimmt wird. Daraus lässt sich die Phasenveränderung der Wellenfunktion durch die Probe bestimmen, welche Rückschlüsse auf die Probe zulassen, die mit herkömmlichen Methoden nicht zugänglich sind. In einem konkreten Fall wurde eine komplexe Probe bestehend aus Kohlenstoffnanoröhrchen und biologisch aktiven Komponenten untersucht. Mit dem pnCCD und der ptychographischen Methode konnte erstmals eindeutig festgestellt werden, dass die Synthese der Probe selbst nur zum Teil erfolgreich war.

Diese Dissertation bildet die Basis für die zukünftige Verwendung des pnCCDs zur Detektion und Abbildung von Elektronen insbesondere für die Elektronenmikroskopie. Darüber hinaus können aufbauend auf den Erkenntnissen und Ergebnissen dieser Arbeit zukünftige Detektorsysteme für Elektronen charakterisiert und optimiert werden.

Contents

1 Introduction 17

2 Transmission Electron Microscopy 21

2.1 Wavelengths of Electrons in TEM 22
2.2 The Transmission Electron Microscope Instrument 23
2.3 Detectors for the Transmission Electron Microscope 26
2.4 Direct Electron Detectors 29

3 Interaction of Electrons With Matter 31

3.1 Inelastic Scattering of Electrons 31
3.2 Electron-hole Pair Generation 33
3.3 Energy Loss of Electrons in Matter 34
3.4 Path Length of Electron Tracks 35
3.5 Atomic Relaxation 37
3.6 Statistical Variation in the Generation of Signal Electrons 38
3.7 Elastic Scattering 38
3.8 Scattering Angles 39
3.9 Scattering of Electrons in the Sample 40
3.10 Scattering of Electron Waves 44

4 The pnCCD 45

4.1 The pnCCD Principle 45
4.2 Charge Spreading in the pnCCD 46
4.3 The Readout of the pnCCD 47
4.4 Charge Handling Capacity 49
4.5 Operation Modes of the pnCCD 49
4.6 The pnCCD TEM Camera System 51

5 *Data Analysis Methods* 53
5.1 *Units of Energy in the Data Analysis* 53
5.2 *Raw Data Analysis* 54
5.3 *Intensity Imaging Mode* 57
5.4 *Event Imaging Mode* 58

6 *Simulation of Signal Generation by Electrons* 63
6.1 *Simulation Process* 63
6.2 *Simulation of Electron Tracks Results* 65
6.3 *Simulation of the Detection Efficiency* 70
6.4 *Statistical Considerations on the Number of Detectable Electrons* 74

7 *Signal Response to Electron Illumination* 79
7.1 *Energy Spectrum of the pnCCD under Electron Illumination* 80
7.2 *Pile-Up Events* 88
7.3 *Probability Distributions on Number of Pixels per Event* 97
7.4 *The Calibration Factor* 100
7.5 *The Conversion Factor* 100
7.6 *The Detective Quantum Efficiency* 101
7.7 *Energy Resolution of the pnCCD under Electron Illumination* 102
7.8 *Summary on the Signal Response* 103

8 *Spatial Resolution in Single Electron Imaging* 105
8.1 *Quantification of Spatial Resolution* 105
8.2 *Spatial Resolution in Intensity Imaging Mode* 107
8.3 *Point of Entry Models* 108
8.4 *Discussion of Models* 115

9 *Application of the pnCCD in Transmission Electron Microscopy* 123
9.1 *Demonstration of the Wave-Particle Duality of Electrons* 124
9.2 *Electron Tomography with the pnCCD* 128
9.3 *4D-STEM Imaging* 132
9.4 *Imaging Magnetic Domains* 134
9.5 *Lattice-Strain Measurement* 137
9.6 *Ptychography with the pnCCD* 141
9.7 *Summary of Applications* 145

10 Conclusions 147

10.1 Future Devices 148

A Appendix 151

A.1 Modulation Transfer Function 151

A.2 Detective Quantum Efficiency 153

A.3 Intensity Distribution of Interference Pattern 154

A.4 Calculation of Stopping Power 155

A.5 Stopping Power and Electron Path Length 156

A.6 The Landau Distribution Function 157

A.7 Detection Efficiency Data 158

A.8 Gauss Correction Code 159

A.9 Gauss Correction Comparison 160

A.10 Data Reference 161

Bibliography 163

Acronyms

ADC analog to digital converter 27
ADF annular dark field 27, 43
AES Auger electron spectroscopy 40, 42

BF bright field 26, 27, 43
BSE back scattered electron 42

CBED convergent beam electron diffraction 137
cdf cumulative distribution function 69, 108
CHC charge handling capacity 49, 50, 148
CL cathodoluminescence 40, 41
CNT carbon nanotube 144
CoG Center of Gravity 58, 105, 109, 111, 160
CSDA continuous slowing down approximation 35

DE detection efficiency 70, 71, 158
DEPFET depleted p-channel field-effect transistor 148
DF dark field 26, 43
DP diffraction pattern 44
DPC differential phase contrast 27
DQE detective quantum efficiency 80, 101

EDX energy dispersive X-ray spectroscopy 27, 40, 41
EELS electron energy loss spectroscopy 27, 40, 42, 43, 177
EFTEM energy filtered transmission electron microscopy 27, 43, 177
EIM event imaging mode 53, 58
EM electron microscope / microscopy 18, 19, 21
ESF edge spread function 106
ET Electron Tomography 128
ETRM electron track reconstruction model 37
EW entrance window 65, 70, 82

FWHM full width at half maximum 102

HAADF high angle annular dark field 26

IIM intensity imaging mode 53, 57, 74, 105

LSF line spread function 106
LTFPA long track furthest pixel away 105

MID measurement identifier 161
MTF modulation transfer function 105, 151

pdf probability density function 108
PID processing identifier 86, 87, 161
PoE Point of Entry 33, 36, 37, 50, 60, 99, 105, 109, 147
PSF point spread function 106

SDD silicon drift detector 27
SE secondary electron 42
SEA single electron analysis 58, 59, 70, 80, 81, 83, 127

SEM scanning electron microscope / microscopy 21

SNR signal to noise ratio 28, 101

STEM scanning transmission electron microscope / microscopy 24

TEM transmission electron microscope / microscopy 7, 17

XRF X-ray fluorescence analysis 43

ZLP zero loss peak 42

1 Introduction

Richard P. Feynman once hoped that we would be able to identify samples not by their precipitates but by looking at their atoms.[1] With the development of the transmission electron microscope (TEM), this has become a reality. Today, not only does electron microscopy tell us what kind of material we are looking at, but also what their properties are. More importantly, we can figure out on what the properties of the material depend on, for instance the atomic arrangement, the crystal structure, the position of proteins and many more. This quest to gain an even deeper understanding about samples drives the development of the electron microscope instrument and of experimental methods. As part of a TEM, spatially resolving electron detectors have also been improved over time. Properties of a digital detector that can be improved include readout rates, signal response and spatial resolution.

[1] Feynman, 1959.

Previous experimental data and theoretical considerations suggested that the pnCCD provides these improvements. In this dissertation, the pnCCD is used as a direct electron detector to record images with electrons. On the one hand, information about the investigated samples is gained in improved ways. On the other hand, the pnCCD's properties are characterized under electron illumination. A detailed description of the signal response to electrons had been missing which is now provided with this thesis.

There are many investigations on the pnCCD under X-ray illumination. The pnCCD was originally developed as one of the three European photon counting cameras (EPIC) on board of the X-ray Multi Mirror (XMM-Newton) observatory to image space in the X-ray spectral regime.[2] Since its launch in 1999, the XMM-Newton has delivered images that provide a wealth of information about our universe.[3] The mission is still flying successfully and new discoveries are still made.[4] A follow-up mission including seven pnCCDs is planned to be launched in 2017 called the extended ROentgen Survey with an Imaging Telescope Array (eROSITA).[5] On the ground, the pnCCD has also been used in X-ray applications at synchrotrons,[6] at the X-ray free electron laser facility LCLS (linac coherent light source)[7] and in table top experiments. A compact table top X-ray color camera has also been developed.[8] In addition, in an optical light application, the pnCCD is used in the adaptive optics system of the large binocular telescope (LBT).[9]

[2] Strüder et al., 1997; Strüder et al., 2001.

[3] Strüder et al., 2003; Brusa et al., 2010.

[4] Nicastro et al., 2016; Irwin et al., 2016.

[5] Meidinger et al., 2010.

[6] Send et al., 2016.

[7] Strüder et al., 2010; Ferguson et al., 2015; Schot et al., 2015.

[8] Ordavo et al., 2011.

[9] Xivry and Rabien, 2012.

During the work for this thesis, it was shown, that the pnCCD is a suitable detector for electrons. In combination with TEM, the pnCCD provides answers to actual scientific questions which will be further motivated by two explicit examples.

Moore's Law states that the number of integrated circuits per area doubles approximately every two years as achieved by shrinking the size of the contained transistors. Today, commercially available structure sizes are 14 nm[10] to 10 nm.[11] Developments are ongoing to make the 7 nm process commercially viable.[12] With such small structure sizes, further physical limitations arise. New materials and processes can alleviate these problems by increasing the conductivity with an increased charge carrier mobility. One of the parameters influencing the electron mobility is strain in the crystal lattice.[13] Potential material combinations are SiGe[14] or InGaAs.[15] The lattice strain can be engineered through various techniques[16] which must then be characterized. Principle methods to measure the lattice strain with nanometer precision had been developed with slow cameras, however the low throughput impedes practical use.[17] During this thesis, it is shown that these methods become actually feasible with a fast imager like the pnCCD.[18]The measurement of lattice strain is shown in the application section 9.5.

[10] *AMD 14 nm* 2016.

[11] *Samsung 10 nm* 2016.

[12] *IBM 7 nm* 2015.

[13] Smith, 1954; Welser, Hoyt, and Gibbons, 1992.

[14] S. E. Thompson et al., 2004.

[15] Bennett et al., 2014.

[16] Bedell, Khakifirooz, and Sadana, 2014.

[17] Müller et al., 2012a.

[18] Müller, . . . , Ryll, . . . , et al., 2012b.

The second example relates to medical science. To cure certain diseases, medicine is administered. The medicine's effectiveness can be increased if the medicine is not dispensed in the whole body but can be directly transported to the site of the problem, for example to certain types of cells or to an organ. A new way of drug delivery employs carbon nanotubes containing the active ingredient which are only released at specific cells. The characterization of such systems is difficult, due to the inclusion of weakly interacting materials that result in images with very low contrast. The emerging field in electron microscopy (EM) of ptychography provides a method to image weakly interacting materials.[19] The ptychographic method depends on a fast spatially resolving detector. Experiments conducted during this thesis showed that the pnCCD fulfills this requirement and that ptychography in a TEM is enabled with the pnCCD. The weakly scattering materials of the drug delivery nanotube could be imaged with the pnCCD.[20]In combination with a single element detector imaging strongly scattering material, it was shown clearly, that the synthesis of the intended nanotube system was only partially successful. Based on theses findings, the fabrication of the nanotube system can be improved. The application of the pnCCD in ptychography is shown in the application section 9.6.

[19] Rodenburg, McCallum, and Nellist, 1993; Pennycook et al., 2015.

[20] Yang, . . . , Ryll, . . . , et al., 2016.

To understand and optimize the images that are recorded in these applications, the signal response of the pnCCD to electron illumination has been investigated in this thesis. For this, first the TEM instrument is explained (chapter 2) providing an understanding where the sam-

ple and pnCCD are located in the microscope and how images are formed. The electrons of the TEM impinge on the detector and scatter inside of the detector material. The theory of electron scattering (chapter 3) builds the basis for many explanations throughout this thesis. When the TEM electron scatter in the pnCCD, signals are recorded that are influenced by the peculiar properties of the pnCCD (chapter 4). The raw recorded signals are corrected during post-processing. If single electrons are imaged, images with sub-pixel resolution can be created (chapter 5). A qualitative description of the scattering of electrons can be achieved by simulating the signal generation by electrons coming from the TEM (chapter 6). Throughout this thesis, simulations are used to explain relationships between recorded signals, properties of the pnCCD and the electrons. These relationships are examined especially with the help of energy spectra when single electrons are imaged (chapter 7). The characteristics and origins of the recorded signals can be explained based on the analyzed data. The spatial resolution for various electron energies is determined. With the learned knowledge, the spatial resolution can be enhanced when imaging single electrons (chapter 8). Various models are explained and evaluated. The understanding gained in the previous chapters is applied, when the pnCCD is employed in a TEM, to improve and enable methods in EM (chapter 9). The success of the applications shows that the pnCCD is a valuable tool for electron microscopy.

2 *Transmission Electron Microscopy*

The first TEMs were iron cast and supported on wooden tables. Levers had to be turned manually to adjust microscope parameters (see figure 2.1). Presently, TEMs are fully digitally controlled, can be accessed remotely and some models are hidden away in a box, resembling more a monolith than a complex microscope. The principal components however have not changed over the years.

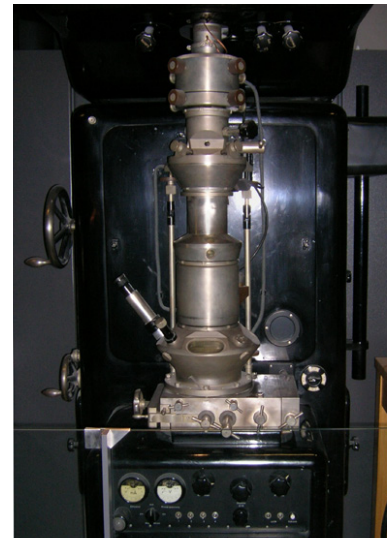

Figure 2.1: Replica of early electron microscope from 1933. Image taken from Brew, 2017.

In this chapter, the components of a TEM are described as well as the working principles. Starting in the *first section*, the calculation of the electron wavelength is done, since the short wavelength is one of the reasons for the success of EM. In the *second section*, the instrument and its components are described as well as the two operation modes (imaging in TEM and scanning in STEM). The ray paths of the two main image types, real space images and diffraction patterns, are shown. In the *third section*, the different detector types are introduced that are used in the TEM. In the *fourth section*, directly detecting and spatially resolving imagers are described.

To convey information in an efficient way, in this thesis, three main types of electrons are distinguished based on their location and origin: The *TEM electrons*, the *primary electrons* and the *signal electrons* (see figure 2.2). TEM electrons originate from the electron gun and scatter in the sample. The TEM electrons are the electrons in the microscope before impinging on the detector. A TEM electron inside the detector is called a primary electron, which can have a different energy than the TEM electron as it loses energy in the detector. The primary electron interacts with the material of the detector generating signal electrons.

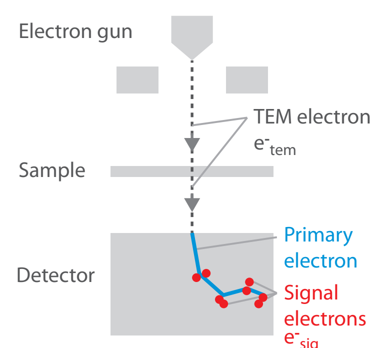

Figure 2.2: The three types of electrons.

There are some references to scanning electron microscopes (SEMs) throughout the text. A SEM is a type of electron microscope which is similar to a TEM but operated at lower energies ($< 1\,\text{keV}$ to $60\,\text{keV}$) and mainly detects the back scattered electrons and X-ray photons. Therefore there are no post sample optics resulting in a much more compact microscope. Most concepts can be applied to SEMs as well, however the focus in this work is on TEMs and the pnCCD is only applied in a TEM for the time being.

2.1 *Wavelengths of Electrons in TEM*

In general, the smallest dimensions of a sample that can be resolved are similar to the wavelength of the light being used (Abbe criterion[1]). In 1924, Louis de Broglie postulated in his PhD thesis[2] that electrons could also be described as waves with a corresponding wavelength λ:

[1] Abbe, 1873.

[2] Broglie, 1924.

$$\lambda = \frac{h}{p} \tag{2.1}$$

with p the momentum and h the Planck constant.[3] For electrons, the wavelength is in the range of picometers compared to nanometers for optical light. Theoretically, microscopy using electrons should resolve much smaller features than light microscopy, which Ernst Ruska and Max Knoll proved to be correct already in 1933.[4] The wave nature of the electron was confirmed experimentally in diffraction experiments by Davisson and Germer in 1927.[5]

[3] Interestingly, until 1931, Ruska and Knoll did not know of this theory when they built their first microscope (Ruska, 1986).

[4] Ruska, 1934.

[5] Davisson and Germer, 1927.

In an electron microscope, electrons are accelerated through a potential U resulting in a velocity v:

$$v = \sqrt{\frac{2eU}{m_0}} = \frac{p}{m_0} \tag{2.2}$$

with the elementary charge e and the electron's rest mass m_0. The uncorrected electron wavelength becomes:

$$\lambda = \frac{h}{\sqrt{2m_0eU}} \tag{2.3}$$

Since the electrons in a TEM are accelerated to considerate fractions of the speed of light c, relativistic corrections have to be applied.

$$\lambda = \frac{h}{\sqrt{2m_0eU + \left(\frac{eU}{c}\right)^2}} \tag{2.4}$$

$$v = c\sqrt{1 - \left(\frac{m_0c^2}{eU + m_0c^2}\right)^2} \tag{2.5}$$

$$\beta = \frac{v}{c} \tag{2.6}$$

$$\gamma = \frac{1}{\sqrt{1-\beta^2}} \tag{2.7}$$

For an acceleration voltage of 300 keV, the electron wavelength is 1.9 pm. That is two orders smaller than the wavelength in typical X-ray diffraction experiments (e.g. $\lambda = 154\,\mathrm{pm}$ for Cu Kα with $E = 8\,\mathrm{keV}$). A comparison of the typical accelerating voltages that are used in electron microscopy and the corresponding electron wavelengths are compiled in table 2.1.

Type	Energy	Wavelength λ		v/c
		Non-Relativistic	Relativistic	
	keV	pm	pm	
e^-	5	17.35	17.30	0.14
e^-	10	12.27	12.21	0.20
e^-	20	8.67	8.59	0.27
e^-	40	6.13	6.02	0.37
e^-	60	5.01	4.87	0.45
e^-	80	4.34	4.18	0.50
e^-	100	3.88	3.70	0.55
e^-	120	3.54	3.35	0.59
e^-	200	2.74	2.51	0.70
e^-	300	2.24	1.97	0.78
e^-	1000	1.23	0.87	0.94
Mn $K\alpha_1$ γ	5.898		210.19	1.00
Cu $K\alpha_1$ γ	8.047		154.06	1.00
Mo $K\alpha_1$ γ	17.479		70.93	1.00
W $K\alpha_1$ γ	59.318		20.90	1.00

Table 2.1: Overview of electron energies that are used in electron microscopy and their corresponding de Broglie wavelengths of the electrons. For comparison, selected X-ray energies and wavelengths are included.

2.2 *The Transmission Electron Microscope Instrument*

The transmission electron microscope consists of several main components. Starting from the top, there is: The electron gun delivering the electron beam, the pre-sample electron optics, the sample stage, the post-sample electron optics and finally one or more electron detectors (see figure 2.3).

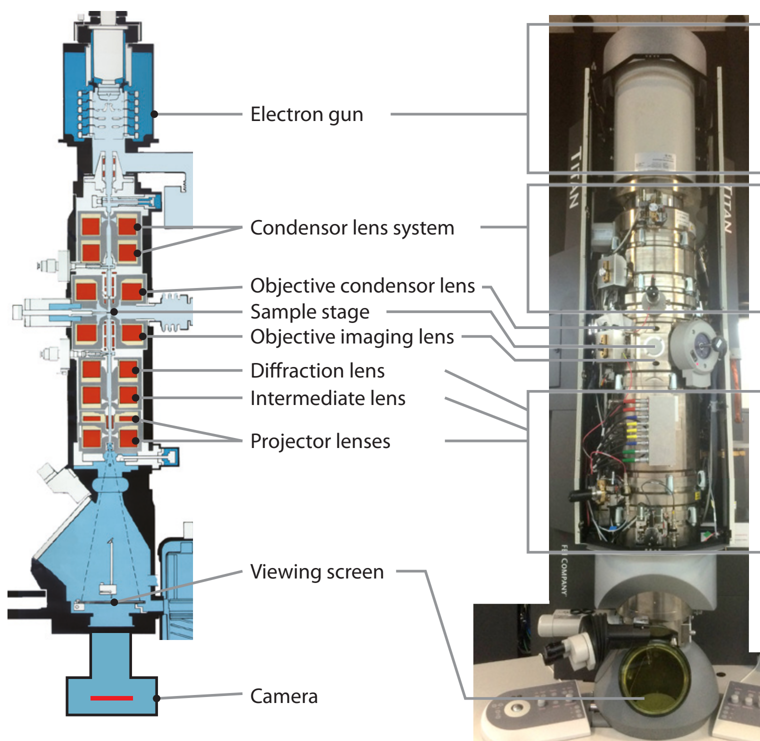

Figure 2.3: Schematic side view cut illustration of a TEM and a front view image of a TEM. Left image adapted from TU Dresden, 2017.

The *electron gun* assembly generates the free electrons that are then accelerated to an energy set by the accelerating potential.[6] The *condenser lens system* consists of several magnetic lenses and apertures that project the electron beam on the sample. The samples must be

[6] An overview on electron guns can be found for example in Reimer and Kohl, 2008, p. 78.

thin enough that electrons can pass through, typically in the range of 10 nm to 200 nm. The sample is held with a *sample stage*. The sample stage can fulfill more tasks than just holding the sample, for example there are sample holders that tilt the sample in one or two axes, that heat or cool the sample, that put the sample under mechanical stress or that provide electric contacts. There are so called environmental sample holders, that maintain various pressures and atmospheres providing dedicated environmental conditions to the sample.

After the sample, the *objective lens* enlarges the electron beam exiting the sample. The objective lens is the most important lens, since it creates the first and largest magnification. Below the objective lens, there is a system of a *diffraction lens* and an *intermediate lens* that select whether an image or a diffraction pattern is imaged. The *projector lenses* further magnify and project the image downstream either on the viewing screen or onto electron detectors (see section 2.3 for details). The *viewing screen* is a phosphor screen that can be tilted into the electron beam, providing a direct live image for the operator through a radiation shielding glass window. A single or even multiple cameras are situated below the viewing screen. For recording of images, the viewing screen is tilted upwards and the electron beam is projected on a *camera*.[7] Typically, the cameras can be moved mechanically into and out of the optical axes.

[7] At first analog film and photographic plates were used.

There are two modes of operation in a TEM which differ in the illumination on the sample and the recording of the signals. In the mode called TEM imaging, the sample is illuminated with a parallel beam homogeneously over a field of interest and one image (real space image or diffraction pattern) is recorded (figure 2.4a). In the other mode called scanning transmission electron microscopy (STEM), the electron beam is focused on the sample, forming an electron probe (figure 2.4b). The position of the electron probe is then scanned over the sample and for each probe position a measurement is recorded with the electron detectors. From the recorded data points and the known position of the electron probe, an image of the sample is reconstructed in a post-processing step. The electron beam is shifted off and on the optical axis with pairs of scan coils that are situated

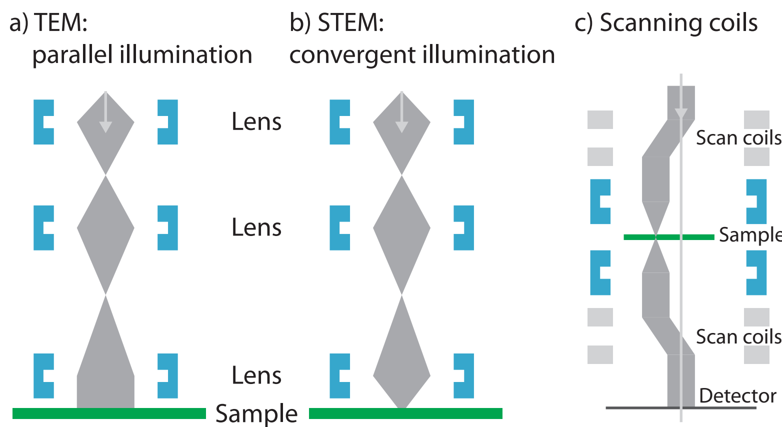

Figure 2.4: Operation modes of a TEM. a) In TEM mode, the sample is illuminated in parallel. b) In STEM mode, the electron beam forms a convergent probe on the sample. The probe position is scanned over the sample during measurements. c) Scan coils above and below the sample can shift the electron beam off and on the optical axis.

above and below the sample (figure 2.4c).

Two principle types of images are produced in a TEM: A real space image or a diffraction pattern. The type of image is selected

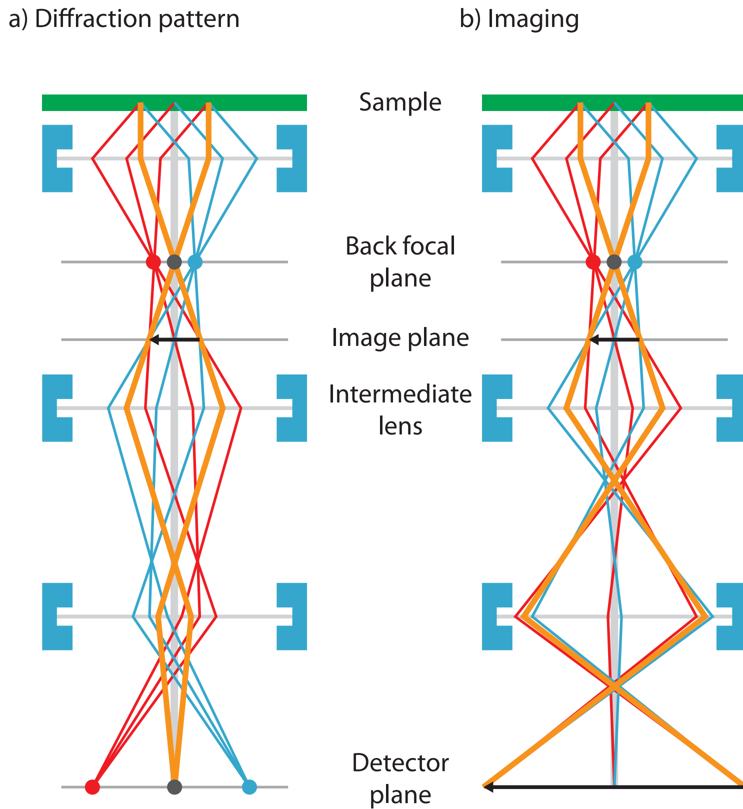

Figure 2.5: Ray path diagram in a TEM after the sample. Either the back focal plane (BFP) or the image plane is projected on the detector by changing the magnetic field of the intermediate lens. a) The diffraction pattern is imaged. All rays leaving the sample under the same angle (red or blue) intersect at the BFP and at the detector plane as indicated by the dots. b) A magnified image is projected. All rays leaving the sample from one point intersect again at the image plane and at the detector plane. Magnification and distances are not to scale. The lens setup shown is simplified compared to a real TEM. Image adapted from Williams and Carter, 2009, p. 153

by projecting either the back focal plane or the image plane of the objective lens on the detector. For both types of images, an illustration of the the ray paths of the electron is given in figure 2.5a and b. In the imaging mode under homogeneous illumination (non-scanning), the diffraction pattern consists of diffraction spots. In the scanning mode, with a converging electron beam on the sample, the diffraction spots widen to diffraction discs.[8,9]

[8] Williams and Carter, 2009, p. 337.

[9] See the application section 9.5 for more details.

Further details on the microscope components are given here, while electron detectors are explained in the next section 2.3. Due to the strong interaction of electrons with matter, the inner volume of the microscope is in various levels of vacuum conditions, ranging from ultra-high vacuum conditions ($<10^{-9}$ mbar) at the electron gun to lower vacuum conditions at the sample stage or in the imaging chamber (10^{-5} mbar).

The electron lenses are magnetic lenses. The basic types of lenses consist of wound coils of conductors inside a pole piece (see figure 2.6). When current flows through the conducting coils, a magnetic field is generated that extends into the volume of the electron beam through a gap in the pole piece. The electrons are deflected due to the magnetic field. The magnetic field is weaker in the center of the optical axes and stronger at the edge. The electron beam is thus

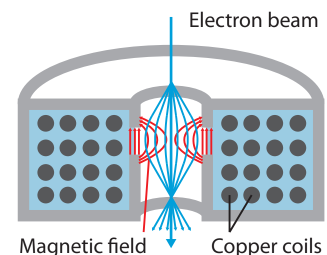

Figure 2.6: Schematic cut view of a basic magnetic lens.

deflected more strongly further away from the optical axes than at the center. In this, a magnetic lens behaves similar to an optical convex lens. By adjusting the current through the coils, the strength of the lens can be changed.

As optical lenses, electron lenses show aberrations of the different types: Chromatic and spherical aberrations, astigmatism and higher order aberrations. Today's best optical lenses are almost free of aberrations through a high degree of corrections. On the contrary, electron lenses have not reached the equivalent level of performance. A big improvement in electron optics has been reached by introducing complex corrector systems with multipole lens elements.[10]

[10] Haider et al., 1998; H. H. Rose, 2009.

2.3 *Detectors for the Transmission Electron Microscope*

One of the strengths of a TEM is that a multitude of signals are created when the TEM electrons interact with a sample. The interaction processes and the resulting signals are described in section 3.9, the detectors that record the signals are described in this section. In general, there are detectors for electrons and photons (mainly X-ray photons).

In TEM imaging with a parallel illumination (non-scanning), an imaging detector is used to record the real space image or the diffraction pattern. The direct transmitted beam beam can be used to form an image, which is called bright field (BF) imaging. Alternatively, a scattered (diffracted) beam can be used to form an image, which is called dark field (DF) imaging.

In STEM, multiple detectors can be used simultaneously to record several signals during the same measurement. Electrons that leave the sample in forward direction can be scattered into various angles, as shown in figure 2.7 (see also section 3.8). The scattering into

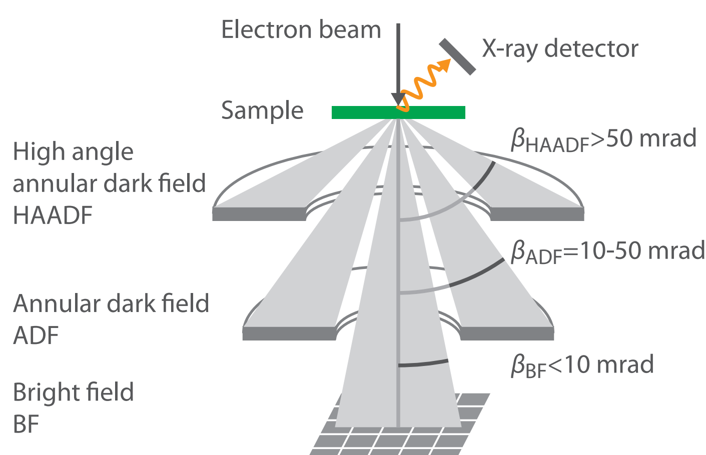

Figure 2.7: The most used detectors in STEM and electron scattering angles in transmission direction. Typical collection angles β are given for the various detectors. Angles are exaggerated in the illustration.

different angles encodes information about the sample that can be recorded with electron detectors that cover specific angles. Electrons that are scattered into high angles ($\beta > 50\,\mathrm{mrad}$) can be detected with the high angle annular dark field (HAADF) detector, electrons that

are scattered into low angles ($\beta \approx 10$ mrad–50 mrad) can be detected with the annular dark field (ADF) detector and the electrons that are collected in a very low angle ($\beta < 10$ mrad) can be detected with a bright field (BF) detector.

The ADF and HAADF detectors are ring shaped to let the central beam pass (either the DF and the BF or just the BF). A typical ADF detector consists of a scintillator that converts the incoming electrons into optical photons. The photons are then guided onto a photomultiplier tube generating a current. The readout of the current is digitized with an analog to digital converter (ADC).

The TEM electrons in the bright field (BF) are either detected with a dedicated BF detector without spatial resolution or with a spatially resolving detector. In the latter case, an image or a diffraction pattern is recorded.

The ADF and BF detector can also be segmented (two examples are given in figure 2.8). The segmentation provides spatial information about the recorded signal. Such detectors are used for example in differential phase contrast (DPC) imaging in which the movement of a disc can be reconstructed with a 4 segmented ring detector. More details are given in the application section 9.3.

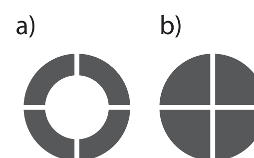

Figure 2.8: Segmented ADF and BF detector.

The TEM electrons also induce emission of (characteristic) X-ray photons from the sample. The X-ray photons are detected with energy dispersive X-ray spectroscopy (EDX) detectors that are situated closely above the sample to increase the collection angle. At first, X-rays were detected with SiLi-detectors that need to be operated at low temperatures with cooling provided by liquid nitrogen for good energy resolutions.[11] Today, mostly silicon drift detectors (SDDs) are used for the detection of X-Rays. SDDs can be operated at much higher temperatures with cooling provided by only thermoelectric coolers and still achieve good energy resolutions.[12] Advanced SDD detector systems consist of multiple SDD cells to increase the active area and the collection angle.

[11] FWHM=135 eV @ 5.9 keV

[12] FWHM=129 eV @ 5.9 keV

More measurement methods using various detectors are only briefly mentioned here:

- Energy filters that allow imaging of electrons that lost a specific amount of energy through the interaction with the sample (energy filtered TEM (EFTEM)).[13] Alternatively, a spectrum of the energy of the transmitted electrons can be recorded (electron energy loss spectroscopy (EELS)). There are energy filters that are below the camera chamber (post-column)[14] and there are energy filters that are between the sample and the camera chamber (in-column).[15]

[13] See also section 3.9.4.

[14] A. Gubbens et al., 2010.

[15] Mukai et al., 2015.

- Electron detectors that image electron backscatter diffraction patterns (EBSD). The detector is situated close to the sample and detects electrons via a scintillator coupled to a spatially resolving camera. This method is mostly used in SEMs.

- Detectors for optical photons, created through cathodoluminescence (see section 3.9.2).

- In SEMs, there are electron detectors situated above the sample detecting backscattered electrons (BSE) and secondary electrons (SE).

All detectors can be categorized into three groups, depending on how many spatial elements are available for recording one measurement:

- One element detectors: Detectors that provide one signal per readout. No spatial information is recorded other than that the electron (or photon) hit the detector. As examples, the ring shaped ADF and HAADF detector shown in figure 2.7 provide one current value per readout, even though the area over that the TEM electrons are collected is two dimensional. An energy dispersive X-ray detector with one cell records an energy spectrum (counts depending on X-ray photon energy) over all incoming photons during one readout, but without spatial information.
- Multi-element detectors: Detectors with multiple segments provide a certain degree of spatial information about the scattered electrons. For example, there are ADF and BF detectors with 4-16 readout areas that are spatially separated. X-ray detectors with multiple cells usually only increase the collection efficiency and provide only limited spatial information since the emission of characteristic X-rays is isotropic in all directions.
- Two dimensional resolving detectors: Detectors that provide one image per readout containing the full information about the spatial distribution of the scattered electrons. The pnCCD and other types of CCDs and CMOS imagers are examples of this category.

Each of the detector group, detector type and specific model has properties that make the detector more suited for a specific application. The most important properties are:

- Readout speed
- Signal to noise ratio (SNR), influenced by:
  - conversion efficiency (how large is the readout signal per incoming TEM electron)
  - Noise at all stages of the readout chain
- Degree of spatial information about the distribution of scattered electrons (one-element, multiple-element or imaging detector)
- Spatial resolution in the case of an imaging detector

Detectors for TEMs and SEMs should also be radiation hard. The properties of a detector should not change over a reasonable amount of electrons that hit the detector. The radiation hardness is the reason

why most detectors in TEM use a scintillator which is radiation hard compared to standard diodes, CCDs or CMOS imagers.

The first spatially resolving image recording mediums in TEM were analog film and imaging plates. Nowadays, mostly digital detectors are used due to their ease of use, higher throughput, possibility for automation and direct feedback to the user. The image quality is also improved for most applications.

The first digital cameras used in TEM detected the TEM electrons indirectly via a scintillator.[16] These detectors were not radiation hard and could not be directly exposed to the TEM electrons. The scintillator converted the TEM electrons into optical light. The optical photons are guided either with a lens system or with optical fibers onto a detector. During each conversion process and at each physical interface, there are photon losses and scattering of the photons. Both result in a loss of signal and a loss of spatial resolution.

[16] Spence and Zuo, 1988; O. Krivanek and Mooney, 1993; Ruijter, 1995.

Using a radiation hard detector that can directly detect electrons offers some advantages that are explained in the next section.

2.4 *Direct Electron Detectors*

With a direct detector, the TEM electrons impinge directly on the detector generating signal electrons directly in the detector (see section 3.2). Thus, in principle, the advantage of direct detection is a greater signal per TEM electron and better spatial resolution.[17]

[17] Faruqi and Henderson, 2007; McMullan et al., 2009.

Apart from the pnCCD, investigations on direct imagers are done by other research groups and companies. There are the generations of the Falcon detectors (1-3) by FEI Company Inc. (now owned by Thermo Fisher Scientific Inc.),[18] the K2 detector by Gatan Inc.,[19] the MediPix detectors (1-3) developed by a collaboration hosted by CERN,[20] the DDD detector by Direct Electron LP[21] and the EMPAD detector.[22] Properties of the detectors are compiled in table 2.2. These direct detectors including the pnCCD have in common that they offer low noise and a high signal per TEM electron.

[18] Kuijper et al., 2015.

[19] Krieger et al., 2011.

[20] *Medipix Collaboration* 2017; McMullan et al., 2009; Krajnak et al., 2016.

[21] Milazzo et al., 2011.

[22] Tate et al., 2016.

Detector	Pixel size	Pixel count	Frame rate	Reference
	µm	pix	fps	
Falcon 3	14	4096 × 4096	40	Kuijper et al., 2015
DDD (DE-16)	6.5	4096 × 4096	60	*DDD DE-16 Datasheet* 2017
K2 (Summit)	5	3838 × 3710	400	McMullan et al., 2014
Medipix 3	55	256 × 256	500	Ballabriga et al., 2011; Krajnak et al., 2016
EMPAD	150	128 × 128	1100	Tate et al., 2016
pnCCD	48	264 × 264	1150	(See also table 4.1)

Table 2.2: Specifications of several direct detectors.

The first three detectors (Falcon, DDD and K2) offer a high pixel count which translates into a large field of view on the sample. A large field of view is beneficial for cryo-electron microscopy in which a large number of biological structures like proteins are imaged. An increasing number of proteins have been reconstructed in 3D

at high resolutions (2 Å to 5 Å) in the last couple of years thanks to these detectors.[23] These three detectors also offer sub-pixel resolutions (named counting mode and super-resolution mode by the companies).

[23] Kuijper et al., 2015; McMullan, Faruqi, and Henderson, 2016; Nogales, 2016.

Compared to these three detectors, the EMPAD and the Medipix detector offer higher frame rates and are more suited for STEM applications.

The pnCCD offers high readout frame rates which can be further increased by binning and windowing methods (see table 4.1). In combination with its radiation hardness and good signal per TEM electron, the pnCCD is best suited for STEM applications. This potential has been investigated during this thesis as is shown in the application chapter 9.[24]

[24] See sections 9.3, 9.4, 9.5 and 9.6

3 Interaction of Electrons With Matter

When an energetic electron enters a material, the electron scatters through elastic and inelastic interactions with the nucleus and electrons of the material. In case of inelastic scattering, the primary electron loses part of its energy at each scattering point. The scattering track of the electron depends on the initial energy of the primary electron[1] and the type of material it scatters in. In the next sections, the characteristics of the scattering and their consequences are described.

[1] See note 2 and figure 2.2 for description of electron types.

Throughout this text, silicon is used as the material since it is the detector material of the pnCCD. Of course, the concepts and formalisms are applicable to other materials as well.

First, the electron is treated as a particle. The particle view is used to describe the interaction of electrons with the detector. These results can already explain many characteristics of the recorded pnCCD signals that are caused by incoming electrons.

Then, in section 3.9, the electron is treated with both particle and wave characteristics to describe the interaction of electrons with the sample in a TEM. Both characteristics help understanding the different sources of signals originating from the sample and thus the way information is obtained about the sample.

As will be shown in detail in chapter 4, the quantity that is measured in the pnCCD is the amount of charge that is collected in the pixel structure, i.e. the signal electrons. The readout signal for the pixels of the pnCCD is proportional to this charge. The number of signal electrons that are generated depends on the energy that is deposited in the material. Therefore, the process of energy deposition in the material and the underlying physical processes and the characteristics and dependencies of the energy deposition of electrons in material is explained in the next section.

3.1 Inelastic Scattering of Electrons

First, the electron is treated as a particle. The main scattering process of electrons in matter for energies below 1 MeV is inelastic scattering on atomic orbital electrons leading to ionization and excitation of atoms. The fast incoming electron ejects a bound electron of the atom. The energy of the ejected electron depends on the energy loss of the primary electron ΔE_{prim} and the binding energy of the ejected

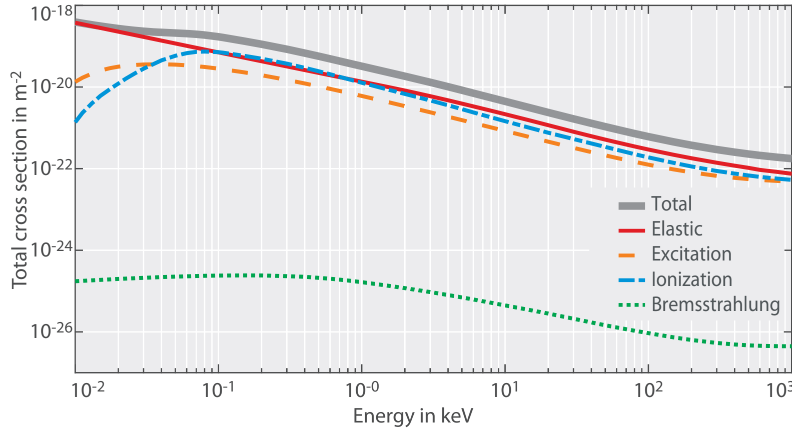

Figure 3.1: Total cross sections for the scattering processes in silicon. Excitation and ionization scattering are summed into collisional effects. The inelastic scattering due to Bremsstrahlung can be neglected for the energy range of TEMs shown in this plot. Data from the EEDL library, Perkins, Cullen, and S. Seltzer, 1991.

electron E_{bind}:

$$E_{\text{ejected}} = \Delta E_{\text{prim}} - E_{\text{bind}}. \tag{3.1}$$

The magnitude of the scattering can be described by the energy loss of the electron per unit path length $\mathrm{d}E/\mathrm{d}x$. This figure is also termed *stopping power* S, which is a characteristic property of a material.

$$S = -\frac{\mathrm{d}E}{\mathrm{d}x} \tag{3.2}$$

Since the stopping power S_{rad} due to radiation effects (Bremsstrahlung) below 500 keV is two orders of magnitude smaller than the stopping power due to collision effects (ionization S_{ion} and excitation S_{exc}), only the collision effects are treated here.[2]

With each inelastic scattering process, the primary electron loses part of its energy. This energy is used to knock out other electrons. In most cases, the kinetic energy of the ejected electrons is small compared to the primary electron. The ejected electrons can undergo further scattering processes also losing part of their energy by ionizing further atoms. Finally, the energy of the electrons is too low to ionize further electrons. Additionally, the electron can excite vibrations of the crystal lattice, generating phonons. The probability for an electron-phonon interaction is greater than for ionization at energies below 10 eV.[3] Excitation of the free electron gas inside the silicon is also possible, resulting in the generation of plasmons.

In summary, the primary electron enters the material and scatters in it continuously losing part of its energy. This energy is partially transferred to the free electrons that scatter themselves in the material, ionizing further atoms. This cascade will continue until the energies of the electrons are below 10 eV, when the electrons generate mainly phonons. The last part of the process is called *thermalization*. In the further text, the expression is used, that the energy that is lost by the primary electron at each scattering point, is deposited at that scattering point or in close proximity.

A simplified scattering track is shown in figure 3.2. A primary electron enters a silicon bulk. After a distance $s1$, the primary electron

[2] $S_{\text{rad}} = 1.374 \times 10^{-2}$ MeVcm²/g compared to $S_{\text{ion}} = 1.64$ MeVcm²/g at 500 keV.

[3] Lechner, 1998.

scatters, changes its trajectory and loses part of its energy. In most cases, the lost energy is deposited locally. After the distance $s2$, the primary electron scatters again. This process continues until the energy of the primary electron is too low to further ionize atoms and the primary electron comes to rest. The generalized quantities

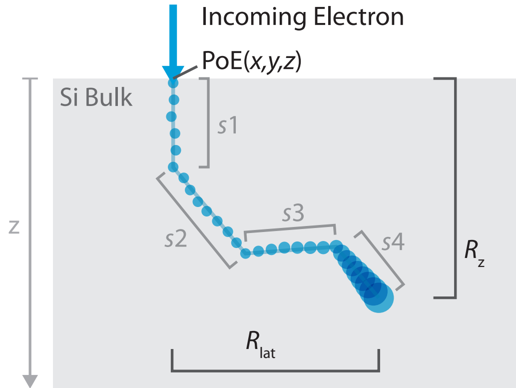

Figure 3.2: Schematic of a primary electron that enters a solid and randomly scatters inside it. At each interaction point, the primary electron loses part of its energy that is deposited locally in the solid, illustrated by the discs. See the text for the explanation of the symbols.

describing the scattering track are the point of entry (PoE), the lateral range R_{lat}, the range in depth R_z, the position of each interaction and the amount of energy deposited at each scattering point (illustrated by differently sized discs).

These quantities have a direct impact on the signal that is recorded with silicon detectors including the pnCCD. The theoretical description follows in the next sections.

This is a simplified model. Actually, the primary electron loses energy along the whole path, not just at specific points. The path can be described to consist of segments in which no significant change in the trajectory (and connected large energy loss) occurs. The energy that is lost by the primary electron during each path segment is the quantity $\mathrm{d}E/\mathrm{d}x$.

3.2 *Electron-hole Pair Generation*

Energy that is deposited in the silicon bulk is used to generate electron-hole pairs. Throughout this thesis, these electrons are called signal electrons. As will be explained in section 4.2 and 4.3, the number of signal electrons determines the amplitude of the readout signal of the pnCCD.

The mean energy w that is needed to create one electron-hole pair in silicon is 3.66 eV at room temperature (20 °C).[4] The temperature dependence is given by:[5]

$$w = w(293\,\mathrm{K}) \cdot (1 + 0.0001 \cdot \Delta T) \tag{3.3}$$

For the typical operation temperature of the pnCCD of -20 °C, $w = 3.67$ eV. This energy is higher than the band gap energy of 1.12 eV for silicon because in the electron-hole pair generation process also phonons and plasmons are created.

[4] Scholze et al., 2000.

[5] Fraser et al., 1994.

The mean total number of generated electron-hole pairs per primary electron and thus mean total number of signal electrons N_{sig} is directly related to the energy E_{dep} that is deposited by the primary electron:

$$N_{\text{sig}} = \frac{E_{\text{dep}}}{w} = \frac{E_{\text{dep}}}{3.67\,\text{eV}} \tag{3.4}$$

$$E_{\text{dep}} \leq E_{\text{tem}} \tag{3.5}$$

The inequality in the last equation 3.5 arises since not all of the energy E_{tem} of the primary electron is always deposited in the silicon bulk. The primary electron can also scatter out of the silicon bulk, before depositing all of its energy in the detector. This is further described in the section 6.2 in which the electron tracks are simulated and in section 7.1 in which the experimental energy depositions are discussed. Because of the direct proportionality between generated signal electrons and deposited energy, the characteristic of energy deposition is described in the next sections.

3.3 *Energy Loss of Electrons in Matter*

The energy loss of an electron per unit path length due to 'collisional' scattering depending on its energy E_{kin} is approximated by the formula developed by Bethe:[6]

[6] Bethe, 1930; Bethe, 1932.

$$-\frac{\mathrm{d}E}{\mathrm{d}x} = \frac{e^4}{4\pi\epsilon_0^2 m_e c^2} \frac{N_A \rho Z}{A} \frac{1}{\beta^2} \ln\left(1.166 \frac{E_{\text{kin}}}{I}\right) \tag{3.6}$$

with $\beta = v/c$ from equation 2.6. The constants are: e the elementary charge, N_A the Avogadro constant, ϵ_0 the vacuum permitivity, m_e the electron rest mass, c the speed of light. The material properties are: ρ the density, Z the atomic number, A the atomic weight.[7] The parameter I describes the mean excitation energy and can be found in tabulated databases (for example from NIST[8]). For silicon, $I = 174\,\text{eV}$.

[7] See appendix A.4 for the derivation of the used units.

[8] M. Berger et al., 2005.

It is known, that this approximation fails at lower electron energies below 1 keV underestimating the true energy loss. The logarithm becomes negative for an energy below $E_{\text{kin}} = I/1.166$. There are a few models that try to correct this discrepancy that use either fitted parameters[9] or are of analytical form.[10] A semi-empirical model developed by Joy[11] adjusts the mean excitation energy so that it is energy dependent:

[9] Nguyen-Truong, 2013.

[10] Shinotsuka et al., 2012; Nguyen-Truong, 2015.

[11] Joy and Luo, 1989.

$$I' = \frac{I}{1 + k\frac{I}{E}} \tag{3.7}$$

The parameter k is element (or material) dependent, with $k = 0.822$ for electrons in silicon.[12] Substituting I in the Bethe equation 3.6 with I' from equation 3.7 results in:

[12] Ibid.

$$-\frac{\mathrm{d}E}{\mathrm{d}x} = \frac{e^4 N_A \rho Z}{4\pi\epsilon_0^2 A m_e c^2 \beta^2} \ln\left(1.166 \frac{E_{\text{kin}} + kI}{I}\right) \tag{3.8}$$

The energy loss for electrons in silicon is plotted in figure 3.3 for the Bethe formula ($k = 0$), the modification by Joy ($k = 0.822$) and experimental data.[13] A good agreement is seen between the modified model and the experimental data.

[13] Luo, Zhang, and Joy, 1991.

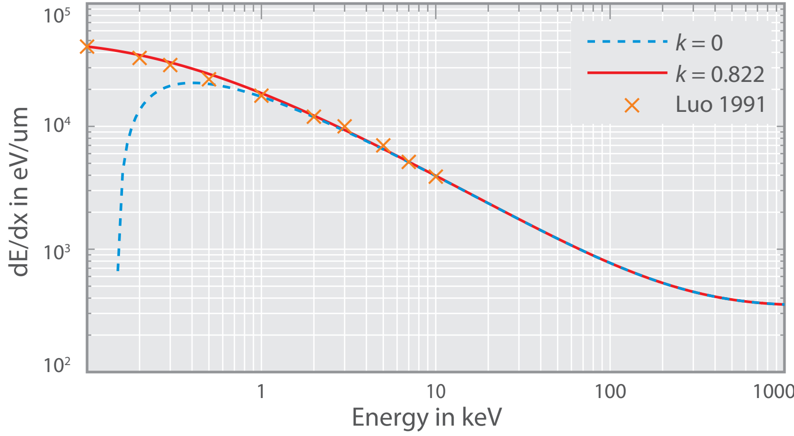

Figure 3.3: Energy loss per unit path length dE/dx for electrons in silicon. Crosses denote experimental data from Luo, Zhang, and Joy, 1991

The precise knowledge of the stopping power at low energies is important, if the corresponding length dimensions (<100 nm) or the precise energy of ejected electrons is of interest. This is the case for back scattered electrons in TEM and SEM applications. For the length scales of interest in the detector view, the model described by equation 3.8 is sufficient. For the simulation of electron scattering that is described in section 6.1, a model developed by Berger-Seltzer[14] including all effects is used.

[14] M. J. Berger and S. M. Seltzer, 1964.

It is important to note, that the energy loss described by the Bethe formalism gives a *mean* energy loss. The scattering interaction is a random process and thus the energy that is lost by primary electrons in single interactions fluctuates. So the energy loss per unit path length will also fluctuate for each primary electron.

The distribution of the energy loss of many electrons in a certain thickness of an absorber is generally described with Landau distributions. Landau first developed the formalism,[15] followed by further studies.[16]

[15] Landau, 1944.

[16] Blunck and Leisegang, 1950; Vavilov, 1957; Bichsel, 1988.

3.4 *Path Length of Electron Tracks*

In the continuous slowing down approximation (CSDA), it is assumed that the primary electron loses its energy continuously along its scattering path with exactly the mean value of the energy loss described by equation 3.8. Then, the path length s of electrons can be calculated by integrating the reciprocal of the energy loss with respect to the electron's energy:

$$s(E_{\text{kin}}) = \int_0^{E_{\text{kin}}} \frac{\mathrm{d}x}{\mathrm{d}E}\,\mathrm{d}E \tag{3.9}$$

$$= s(E_{\text{min}}) + \int_{E_{\text{min}}}^{E_{\text{kin}}} \frac{\mathrm{d}x}{\mathrm{d}E}\,\mathrm{d}E \tag{3.10}$$

As a practical approximation, the lower integration limit E_{min} is set at 200 eV, so that for silicon $s(E_{min}) < 2\,nm \approx 0$ and the inaccuracies at lower energies can be avoided.

The path length of electrons in silicon depending on their energy is plotted in figure 3.5 and tabulated in 3.1.

E_{kin}	keV	10	20	40	60	80	120	200	300	400
$s(E_{kin})$	µm	1.5	5	16	33	53	105	239	446	679

Table 3.1: Path length of electrons in silicon for $k = 0.822$.

Again, it must be noted that the path length for an individual electron can differ from the mean path length given by equation 3.9 since the energy loss at each scattering fluctuates.

Additionally, the path length given by equation 3.9 describes the total length along the track. The ranges in depth (R_z) and the lateral range (R_{lat}) from the PoE are shorter, since the scattering track is not a straight line, but a track in the bulk in three dimensions with random trajectory changes at each scattering point (see figure 3.4).

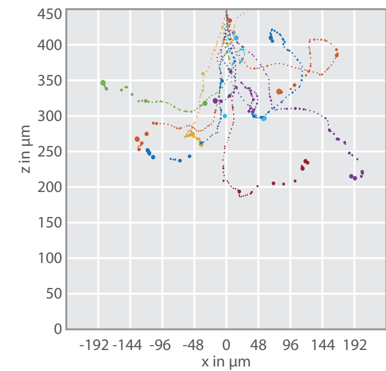

Figure 3.4: Simulated electron tracks with an energy of 300 keV.

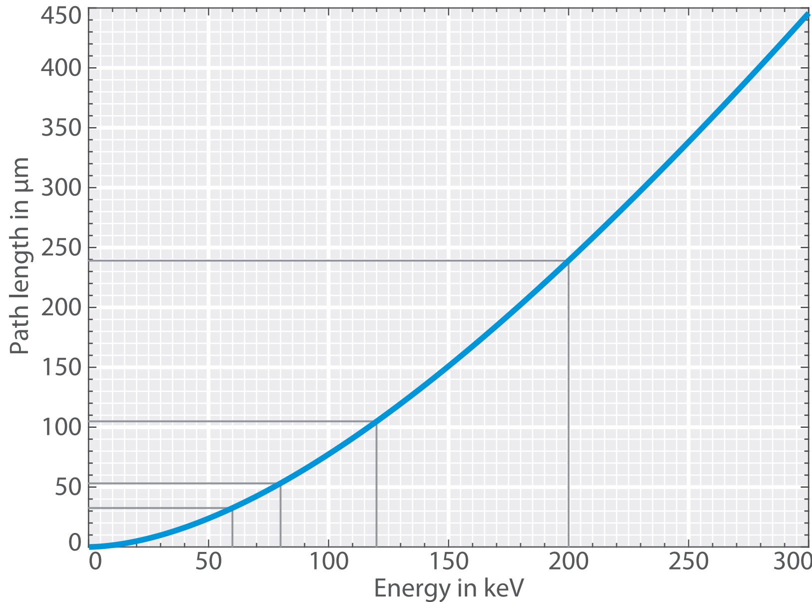

Figure 3.5: Path length of electrons in silicon for $k = 0.822$. For energies of 60 keV, 80 keV, 120 keV and 200 keV marker lines have been added.

A few important conclusions can be drawn from the calculation of path lengths. The path length of an electron increases with its energy from a few micrometers at 20 keV to a few hundred of micrometers at 300 keV. Therefore, the combination of electron energy and pixel size plays a crucial role in the signal generation of a spatially resolving electron detector. In the case of the considered pnCCD with pixel dimensions of 48 µm, the primary electron will cover distances of less than one pixel or up to several pixels depending on the energy. This corresponds to energy depositions and signal electron generation distributions that are very localized in terms of pixel size for low energies. For higher energies, the energy depositions are distributed over distances of multiple pixels.

Another relevant conclusion can be drawn from the graphs of the path length and the energy loss (figures 3.5 and 3.3). The primary

electron loses most of its energy towards the end of its track. Approximately 25 % of the initial energy is deposited in the last 10 % of the path length. A 300 keV electron looses 75 keV at the last 48 µm of its 450 µm long path.

In figure 3.6, a part of an image recorded with the pnCCD is shown, that displays a signal track caused by a TEM electron with an energy of 300 keV which is presumably fairly parallel to the detector surface. Without going into detail, a higher intensity is seen at one end of the track, probably corresponding to the end the electron path with the aforementioned high energy deposition at a localized area.

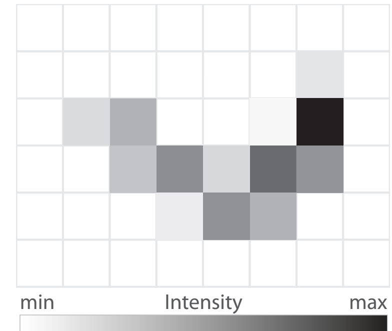

Figure 3.6: Example of a track of an electron with an energy of 300 keV measured with the pnCCD.

The knowledge about this characteristic energy loss and energy deposition can be used to determine the PoE of the primary electron. Several electron track reconstruction models are investigated in section 8.3. Since the scattering of individual primary electrons are random events, simulations that simulate single electron tracks in solids aid the understanding of the signal response of the pnCCD. These simulations are described in chapter 6.

3.5 *Atomic Relaxation*

After the ionization of an atom, the atom is in an excited state. The atom will relax into a lower energy state through a cascade of processes. There are two processes possible, shown in figure 3.7: One is the emission of a characteristic photon, the other the emission of another electron, which is called *Auger* electron.

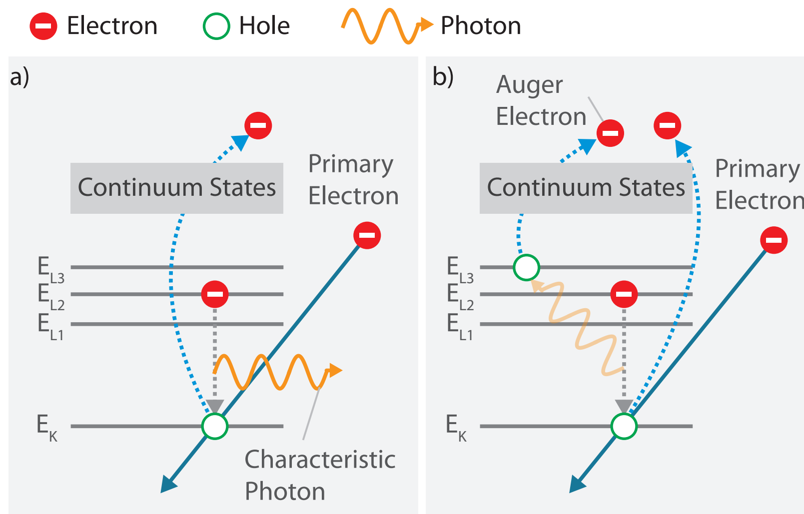

Figure 3.7: Schematics of possible atomic relaxation processes when a primary electron ejects a bound electron (in this example from the K shell) and leaves a vacancy. a) The vacancy is filled by an electron of a higher shell (in this case from the L shell), emitting a photon (shown here as a wave) with an energy that is characteristic for the involved energy levels. b) A non-radiative process could also occur, in which the vacancy is filled by an electron from a higher energy level. The excess energy is transferred to another electron that is ejected.

One such process is the generation of characteristic X-rays[17] with element specific energies (see figure 3.7a). When an electron of a shell is ejected, an electron of a higher shell fills the vacancy. In this process, the excess energy is transferred to generate a photon with an energy E_{ph} that is specific of the transition from the two involved shells and their binding energies ($E_{\mathrm{bind},0}$, $E_{\mathrm{bind},1}$).

$$E_{\mathrm{ph}} = E_{\mathrm{bind},0} - E_{\mathrm{bind},1} \tag{3.11}$$

[17] "It is customary *not* to refer to electron-induced X-ray emission as fluorescence", Williams and Carter, 2009, p. 55

Depending on the element and the involved atomic shell, the photon energy is in the range of a few hundreds of eV up to to a few keV for light elements and tens of keV for heavy elements (for a full table, see for example[18]).

A non-radiative process is also possible. The excess energy is transferred to eject another electron of the same or higher shell (higher energy level) (see figure 3.7b). The second ejected electron is called Auger electron. The energy of the Auger electron depends on the energy levels of the electron that fills the vacancy ($E_{\text{bind},0}$, $E_{\text{bind},1}$) and the binding energy $E_{\text{bind},2}$ of the shell from which the Auger electron is ejected.

$$E_{\text{Auger}} = E_{\text{bind},0} - E_{\text{bind},1} - E_{\text{bind},2} \tag{3.12}$$

The energy of the ejected Auger electrons is in the range of a few eV up to 3 keV (for a full table, see for example[19]).

Since the binding energies of the electrons of the various shells are element specific, the energies of the emitted Auger electrons and characteristic photons have energies that correspond to the element. If the Auger electrons and photons are detected in an energy dispersive detector, they can be used to identify the elements in the sample. This is done for example in XRF measurements and explained in section 3.9.

[18] A. C. Thompson, Kirz, and Attwood, 2009.

[19] Ibid., p. 1-31.

3.6 Statistical Variation in the Generation of Signal Electrons

For many TEM electrons with the same energy, the number of generated number of electron-hole pairs fluctuates. There is the possibility that interactions of the TEM electron with the detector material generate phonons and plasmons, and not only electron-hole pairs. Thus the effective energy that is used to generate signal electrons fluctuates. This variation in the number of generated signal electrons is described with the Fano factor F (after Ugo Fano[20]):[21]

$$F = \frac{\sigma^2(N_{\text{sig}})}{\langle N_{\text{sig}} \rangle} \tag{3.13}$$

$$\sigma_{\text{Fano}} = \sqrt{F \cdot \frac{E_{\text{tem}}}{w}} \tag{3.14}$$

with $\langle N_{\text{sig}} \rangle$ the mean number of generated signal electrons and σ^2 the variance. At a temperature of $-20\,°\text{C}$, $F = 0.115$ for silicon.[22]

The Fano factor influences the resolution of an energy measurement of the primary electron that can be reached in theory.[23]

[20] Fano, 1947.

[21] Alig, Bloom, and Struck, 1980; Lechner, 1998.

[22] Alig, Bloom, and Struck, 1980; Lechner and Strüder, 1995.

[23] See also section 7.7

3.7 Elastic Scattering

In elastic scattering, the sum kinetic energy and the sum momentum of the interacting particles, the primary electron and nucleus, are conserved while the trajectory of the electron changes. Elastic scattering of the primary electron is mostly in the forward direction (see next

section 3.8). In general the energy transfer from the kinetic energy of the primary electron to the kinetic energy of the nucleus is very low. Depending on the scattering angle and energy of the primary electron, the transferred energy is below 1 meV for $\theta < 0.5°$ and an electron energy of 100 keV in silicon.[24]

[24] Reimer and Kohl, 2008, p. 145.

3.8 Scattering Angles

Inelastic and elastic scattering occurs mostly in small angles in the forward direction. The differential cross sections $d\sigma/d\Omega$ for scattering into the angle θ can be approximated by:[25]

[25] Ibid., pp. 151, 162.

$$\frac{d\sigma_{el}(\theta)}{d\Omega} = 4a_0^2\gamma^2 Z^{2/3}\left(\frac{1}{1+(\theta/\theta_0)^2}\right)^2 \tag{3.15}$$

$$\frac{d\sigma_{il}(\theta)}{d\Omega} = \frac{\lambda^4\gamma^2}{4\pi^4 a_0^2} Z\left(1-\frac{1}{\left[1+(\theta^2+\theta_E^2)/\theta_0^2\right]^2}\right)\left(\frac{1}{(\theta^2+\theta_E^2)^2}\right) \tag{3.16}$$

$$\theta_0 = \frac{\lambda}{2\pi a_0 Z^{-1/3}} \tag{3.17}$$

$$\theta_E = I\frac{1}{2\gamma\beta^2 m_e c^2} \tag{3.18}$$

With I from section 3.3, β, γ and λ as defined in section 2.1 and a_0 is the Bohr radius. The angle θ_0 is called the characteristic angle for which equation 3.15 is 1/4 of the value for $\theta = 0$.

The dependency of the cross sections on the scattering angle is plotted in figure 3.8 for various electron energies and silicon as the material. Generally, inelastic scattering occurs much more into smaller

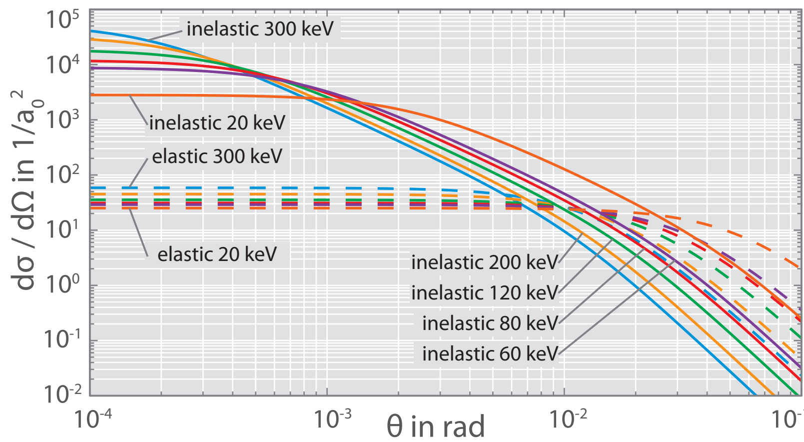

Figure 3.8: Differential cross sections for elastic and inelastic scattering in silicon for electrons with energies from 20 keV to 300 keV depending on the scattering angle θ. Calculated with equations 3.15 and 3.16.

angles than elastic scattering. Also, scattering into small angles is more probable for higher electron energies than for lower electron energies. Nevertheless, there is a non-vanishing probability for large angle scattering.

The dependence of path length and scattering angle on the energy of the primary electron is the reason why higher energy electrons penetrate much deeper into the detector than lower energy electrons.

The high energy electrons scatter more forward in the beginning and deeper into the solid.

3.9 *Scattering of Electrons in the Sample*

The various interactions of electrons with matter described in the previous sections lead to a multitude of signal types that can be used to study samples. The different interactions lead to different signals. Depending on the sample and the sample's properties, a signal providing the information of interest should be chosen. In this section, the signals due to inelastic scattering are described. In the following section 3.10, signals due to elastic scattering are explained within an electron-wave description. An overview of the achievable spatial resolutions for the different signals is shown in table 3.2.

Detected type	Technique	Resolution	
		nm	nm
Electron	Electron microscopy (TEM, STEM)	0.1	0.05 (Barthel, Houben, and Tillmann, 2015)
	Electron diffraction (SAED, CBED)	10 to 1000	0.20 (Müller et al., 2012a)
	EELS	<1	
	Auger electron spectroscopy (AES)	≈2	
Photon	EDX	2 to 10*	
	Cathodoluminescence (CL)	2 to 200	
*in practice, 200 nm to 1000 nm is reached			

Table 3.2: Achievable spatial resolution for various TEM techniques. Values are compiled from Egerton, 2011 (second last column) and more recent publications (last column).

The (inelastic) signals originating in the sample can be divided into forward and backward signals that emerge from the bottom side of the sample and the top side, respectively, with the top side of the sample facing the electron beam. In figure 3.9, the various detectable signals are shown. First, the backward directed signals are explained and then the forward directed signals, including the ones that are detected with the pnCCD.

3.9.1 *Characteristic Photons*

As explained in section 3.5, X-ray photons are created in the sample that can leave the sample. The energy spectrum of the X-ray photons contains a broad background due to Bremsstrahlung photons and sharp peaks at specific energies. The energy of the photons that contribute to the peaks is characteristic of the energy levels of the atom from which the photon originates and can thus be used to identify the elements in the sample. In general this method is commonly referred to as X-ray microanalysis including energy dispersive X-ray spectroscopy (EDX). Under homogenous illumination, the concentration of the identified elements can be determined quantitatively for the illuminated area. In the scanning mode of the TEM (STEM) or

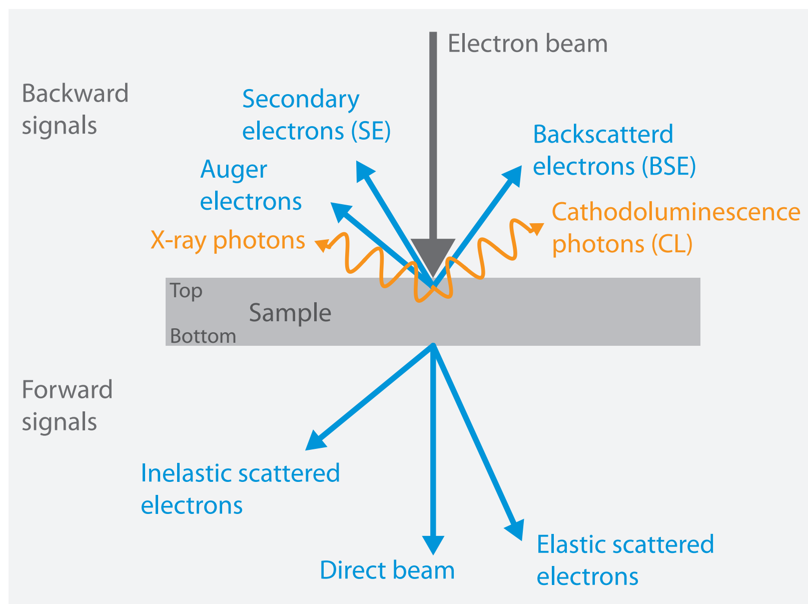

Figure 3.9: Signals that can be detected in a TEM/SEM microscope. The sample must be thin enough so that electrons can pass through it to generate forward signals. In standard SEMs, only the backward signals are detected. The Auger electrons, (characteristic) X-ray photons and the CL light photons carry element specific information and can be used for spectroscopy. In forward direction, inelastic scattered electrons carry element specific information. The electron signals in backward direction provide only surface information, while X-rays can also escape from the sample bulk.

in a SEM, the electron beam is moved to different sample positions and a X-ray spectrum is recorded for each sample position. A further analysis of the spectroscopic data then reveals the position of identified elements and their concentration in the sample (see figure 3.10 for example images). The resolution for EDX in STEM is around 2 nm to 10 nm.

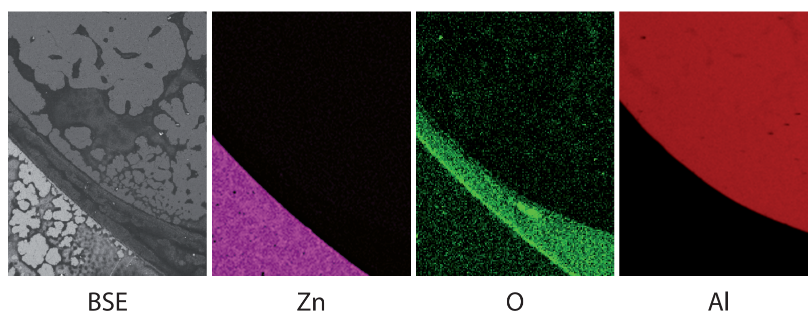

Figure 3.10: Comparison of images created from back scattered electrons and detection of X-ray photons with a SEM and a low magnification. The elemental maps of Zn, Al and O are created with the X-ray spectrum. The electron image shows better topological contrast but without elemental information.

3.9.2 *Cathodoluminescence*

Another method involving photons, although within a wavelength range of visible to ultra-violet light, is the detection of photons generated through cathodoluminescence (CL) in materials with a band gap. In this process, the TEM electron excites an atom, lifting an electron from the valence band to the conduction band. Later, an electron from the conduction band can recombine with the previously created vacancy, creating a photon in the process (see figure 3.11).

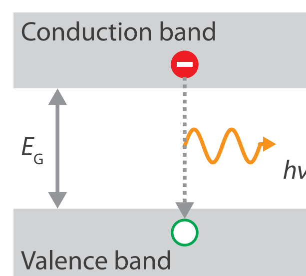

Figure 3.11: Schematic of cathodoluminescence (CL). A vacant hole in the valence band was created by a TEM electron. The hole is filled by an electron from the conduction band. The energy difference between the two energy levels is given off as a photon with a characteristic wavelength in the visible spectrum.

The energy and the corresponding wavelength depend on the energy of the involved energy levels of the material at the probe position, yielding a characteristic signal (typically $\approx E_G$). This technique is employed in SEM microscopes with special CL detectors. In a TEM with the restricted space around the pole piece, the emitted light must

be collected with special sample holders. These holders integrate optical fibers or mirrors that transfer the photons to a light photon detector out side the TEM.[26]

[26] Petroff, Logan, and Savage, 1980; Yamamoto, Spence, and Fathy, 1984.

3.9.3 Backward Scattered Electrons

There is an electron signal on the backward side. These electrons are called either back scattered electrons (BSEs), secondary electrons (SEs) or Auger electrons depending on their origin. By definition, secondary electrons are electrons that originate from within the sample through ionization processes and that have an energy below ≈50 eV. Since the energy of the SEs is very low, these types of electrons escape the sample only from a thin surface volume. The SE signal provides a topological image of the surface. The SEs exhibit a continuous energy spectrum and do not provide element specific information.

The back scattered electrons are TEM electrons that are elastically back scattered at the surface. As such, the BSEs deliver surface information. The energy of the BSE is equal to the TEM electron.[27] The back scatter coefficient η_{bs} describing the probability of the occurrence of back scattered electrons depends on the density of the material. With special detector setups, the low energy SEs can be distinguished from the higher energy BSEs.

[27] Remember the negligible energy transfer <1 meV for elastic scattering described in section 3.7.

Auger electrons have an energy that is characteristic of the element and state of the atom it originates from (see section 3.5). The detected Auger electrons will therefore contain elemental information about the sample. In addition to dedicated AES instruments, Auger electrons can also be detected in SEMs or TEMs. Since the energy of Auger electrons is low (< 3 keV), AES is also a surface technique.

3.9.4 Energy Loss Electrons

In forward direction, electrons can be detected that have lost some of their energy through inelastic scattering in the sample. With appropriate energy filters for electrons consisting of magnetic prisms, the spectrum of the energy loss can be recorded (see figure 3.12).[28] In this electron energy loss spectroscopy (EELS), a very high energy resolution below 500 meV can be reached.[29] With such high energy resolution, even different oxidation states can be differentiated in a map with atomic resolution (see for example[30]). Plasmon and phonon losses and the losses due to so called edge absorption can be detected with EELS. The probability for a specific energy loss sharply increases when the energy loss corresponds to shell transition energies of a material. Therefore, by comparing the recorded spectrum with known absorption edges, the elements in a sample can be identified and even their binding state. In general, the probability that a TEM electron looses only a small amount of energy is greater than a high energy loss. This can be seen in the decreasing amplitude of the energy spectrum with increasing energy loss. Most TEM electrons pass the sample without any inelastic scattering. Therefore, the zero loss peak (ZLP) has the highest intensity. Energy loss due to the generation of

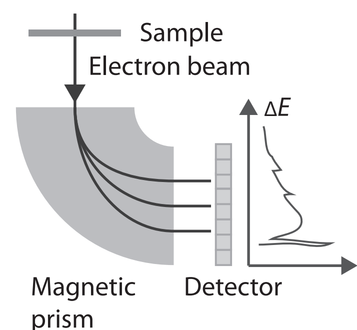

Figure 3.12: Schematic of electron energy loss spectroscopy (EELS) in STEM. The electron beam after the sample is dispersed in a magnetic prism. The electrons hit the detector on a location depending on the energy loss of the electrons.

[28] H. Rose and Plies, 1974; Bihr et al., 1991; O. L. Krivanek, A. J. Gubbens, and Dellby, 1991.

[29] Williams and Carter, 2009; Koch et al., 2006, p. 684.

[30] Tan et al., 2011.

plasmons is the most probable process, with low energy losses in the range of a few eV to a few hundred eV, the so called low energy loss region.

In STEM mode, an energy spectrum is recorded per probe position (see figure 3.13).

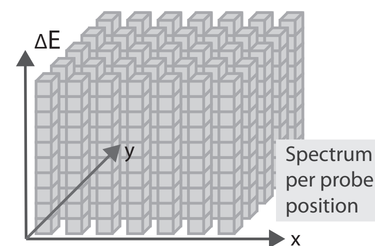

Figure 3.13: Schematic of EELS in STEM. One energy loss spectrum is recorded at each probe position (x, y).

In TEM mode, an energy filtered image can be recorded that contains only intensities due to electrons that have lost a certain amount of energy. This technique is called EFTEM. If multiple images are recorded with different energy losses, a three dimensional data cube $(x, y, \Delta E)$ is recorded just like in STEM (see figure 3.14). This type of data is comparable to the type obtained with the pnCCD color X-ray camera[31] in X-ray fluorescence analysis (XRF), although of course at different spatial resolutions and measurement goals. The energy resolution for the detection of X-rays is good enough to differentiate characteristic photons and create elemental maps from the data. The energy resolution of the pnCCD for the detection of electrons is discussed in section 7.1.

[31] Ordavo et al., 2011.

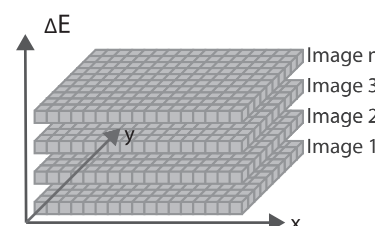

Figure 3.14: Schematic of energy filtered TEM (EFTEM). One image is recorded for each specific energy loss ΔE of the TEM electron.

3.9.5 Z Contrast

As shown in section 3.8, the cross sections for inelastic scattering are Z dependent. In a simple view, the probability that an electron is scattered in a high Z material is higher than in a low Z material. The result is a decrease in intensity of the direct transmitted beam and an increase in the intensity in the scattered directions (annular dark field (ADF)). Additionally, the probability that electrons are scattered into greater angles is increased for high Z material compared to low Z material. In a STEM image of the direct transmitted beam, a lower intensity is expected for sample volumes with a denser material than for volumes with low density material. Conversely, in a STEM image of the intensity of the scattered electrons (the dark field (DF) signal), areas will show a high intensity for high density materials. Complementary STEM images of the scattered and unscattered electrons are shown in figure 3.15. One of the methods which yield images with highest spatial resolution is the use of the HAADF signal.

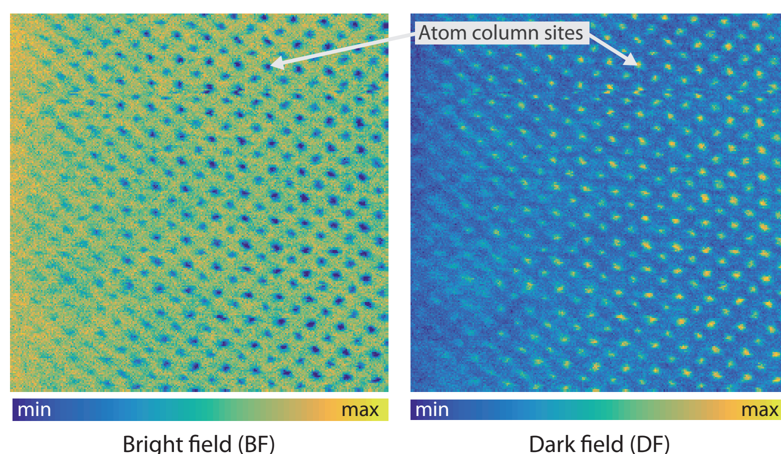

Figure 3.15: Example images of Z contrast in STEM recorded with the pnCCD and a $SrTiO_3$ sample. The scattering of electrons into greater angles is stronger near the sites of the atom columns. This results in a decreased intensity in the BF image at the atoms sites and an inverted contrast in the DF image.

This Z contrast is also called amplitude contrast. In a wave treatment of the electron scattering, the contrast that arises due to different Z results in the modulation of the amplitude of the electron wave. For some specimen, this contrast is very low. Under such conditions, the modulation of the phase of the electron wave by the specimen can provide a better contrast. The treatment of the scattering in the wave framework is described in the next section while applications that show the wave character are shown in sections 9.1.1 and 9.6.

3.10 Scattering of Electron Waves

Electrons exhibit wave properties. When two ore more electron waves superpose, constructive and destructive interference can occur.[32] In TEM, the most prominent example of this effect is the generation of diffraction patterns (DPs) after the interaction of the electron wave with a sample.

[32] See section 9.1 for an experiment in which an interference pattern is recorded with the pnCCD.

A geometric representation of constructive interference of electron waves that are scattered from crystal lattice planes is shown in figure 3.16. An incident plane wave is scattered on two lattice planes a distance d apart. The scattered plane waves interfere constructively into specific angles $\theta = \theta_B$ that fulfill Braggs' law:[33]

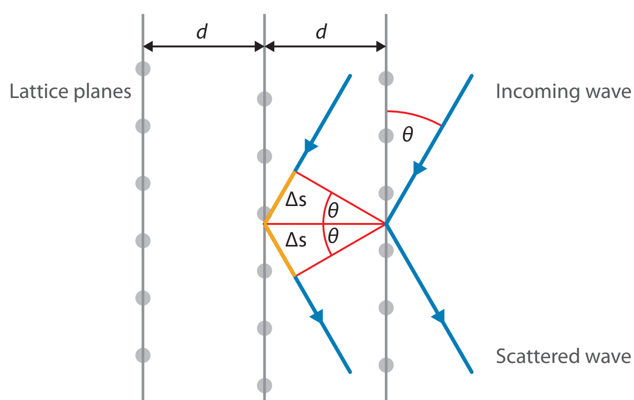

Figure 3.16: Constructive interference of electron waves under Bragg conditions.

[33] W. H. Bragg and W. L. Bragg, 1913.

$$2\Delta s = n \cdot \lambda = 2d \cdot \sin\theta_B \tag{3.19}$$

DPs are an important source of information about samples. For example, the crystal structure of a sample can be determined from analyzing the position and intensity of diffraction peaks. In figure 3.17, an example image of a DP of a barium-sulfite particle is shown that was recorded with the pnCCD. Examples of experiments in which DPs are recorded with the pnCCD are presented in section 9.5 and 9.6.

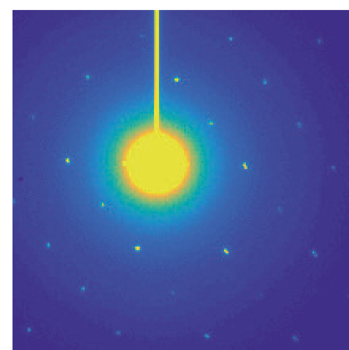

Figure 3.17: Diffraction pattern recorded with the pnCCD. The intensity is scaled to show the weak diffraction peaks and which widens the apparent direct beam at the center.

4 The pnCCD

AN OVERVIEW ON THE PNCCD that is used in this thesis is described in this chapter. There are several texts that describe the principle and structure of the pnCCD in detail.[1] In this chapter, the focus is on the principles of the pnCCD that impact the signal read out under electron illumination.

[1] Strüder et al., 2001; Lutz, 2007; Schmidt, 2017.

In the *first section* the basic principles of the pnCCD are explained. Interaction of TEM electrons in the detector bulk lead to the generation of electron hole pairs, which are separated. The signal electrons drift to the more positive front side while spreading in the bulk which is explained in the *second section*. In the *third section*, the readout process is described. The number of TEM electrons that can be stored in a single pixel is limited. This important parameter is explained in the *fourth section*. This parameter can be influenced by adjusting certain voltages of the pnCCD in four different operation modes that are described in the *fifth section*. For experiments at TEMs, a camera was built with the pnCCD. The camera system is described in the *sixth section*.

4.1 The pnCCD Principle

The pnCCD works on the principle of sidewards depletion.[2] In figure 4.1a and b, a normal pn-junction and one with sidewards depletion are compared. If a second pn-junction is created, on the backside side

[2] Gatti and Rehak, 1984.

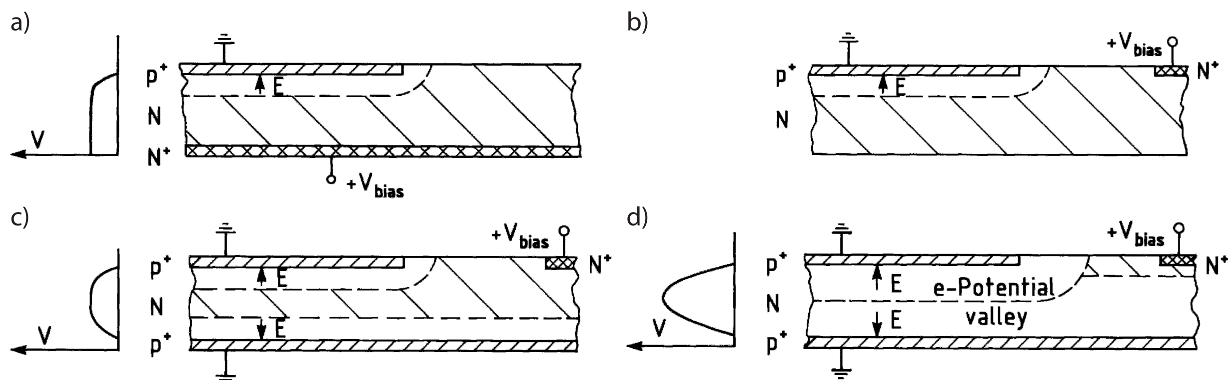

Figure 4.1: Principle of sideward and full depletion. a) A normal pn-junction is compared to b) one with sideward depletion. c) With a second pn-junction at the backside the bulk is depleted from both sides. d) With appropriate voltages, the whole bulk of the pnCCD can be depleted. Image from Lutz, 2007, p. 126

(up is the front side and down is the back side) like in figure 4.1c, the bulk material can be depleted from both sides. With an appropriately

high depletion voltage, the whole bulk material is depleted (figure 4.1d). However, the voltage to deplete the full bulk is four times higher in the case of a) and b) compared to d). Since the whole silicon bulk is depleted of mobile charge carriers, the detector is sensitive to charge carrier generation in the whole bulk. Incoming photons or TEM electrons generate electron hole pairs in the depleted bulk. Each electron hole pair is separated due to the potential gradient with the electrons drifting to the more positive front side and the holes drifting to the more negative back side where the holes are collected via the back contact (figure 4.2). The potential minimum for the electrons can

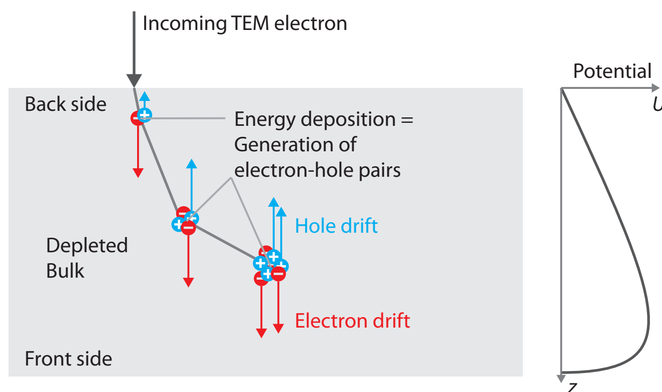

Figure 4.2: Generation of electron-hole pairs and charge separation. For simplicity, only three interaction points are shown.

be shifted towards the front side by applying a more negative bias to the back side with respect to the front side. The signal electrons are typically collected at the potential well near the front side (at $\approx 10\,\mu\text{m}$).[3]

[3] Kimmel, 2009.

4.2 *Charge Spreading in the pnCCD*

For each energy deposition at each ionization interaction point, the generated signal electrons can be assumed to be confined in a small, point like volume.[4] The signal electrons drift towards the front side due to the potential gradient. While drifting, the signal electrons spread laterally due to diffusion and electrostatic repulsion (see figure 4.3a). Eventually, the signal electrons reach their potential minimum at the front side. The three-dimensional potential inside the bulk and especially at the front side is of complex shape.[5] However, with good approximation, the lateral distribution of the signal electrons can be described with Gaussian distributions (see figure 4.3b)[6] at the charge separation depth. The charge separation depth is where the signal electrons are separated into the pixels' potential, depending on the lateral position of the signal electrons. All signal electrons inside a pixel potential well contribute to the readout signal of that pixel (see figure 4.3c). Following the path of each signal electron, a signal electron can be collected in a pixel that is not beneath the origin of that signal electron (for example the indexed dot A in figure 4.3).

[4] Kimmel et al., 2010.

[5] For detailed analysis see Kimmel, 2009; Schmidt, 2017

[6] Kimmel et al., 2010.

Recalling the track length of electrons (see section 3.4) that is on the order of a few micrometers at 20 keV, the whole energy of the

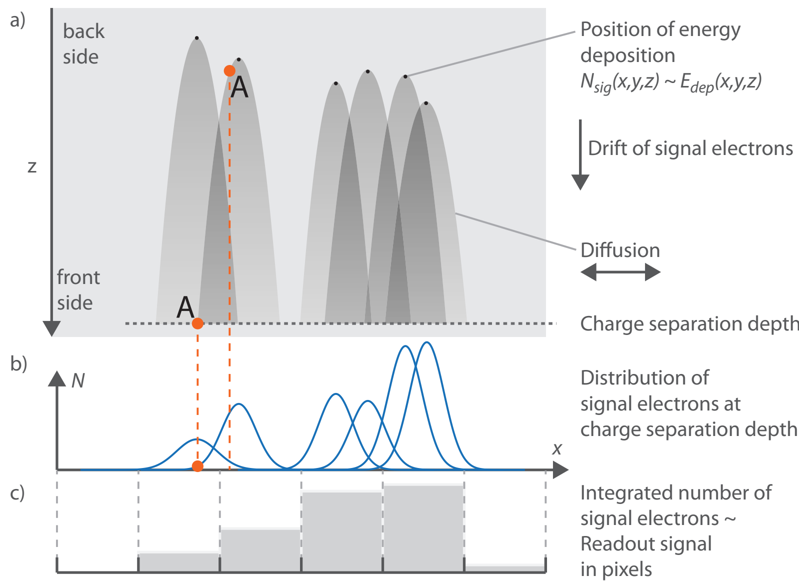

Figure 4.3: Schematic of charge spreading of signal electrons in the pnCCD. a) Signal electrons are generated at the points of energy deposition. The charge cloud drifts towards the front side while spreading laterally. b) The distributions of the number of signal electrons at the charge separation depth can be described with overlapping Gaussian functions. c) In the last step, the number of signal signal electrons are integrated over the pixel boundaries. The resulting number causes a readout signal proportional to the number of signal electrons and hence the deposited energy. Signal electrons generated over a pixel could be collected in a neighboring pixel (see Marker A).

TEM electron is deposited in a length scale smaller than the pixel size of 48 µm. Potentially, all signal electrons could be generated inside the dimension of one pixel. But the spreading of the charge cloud can lead to a distribution of the signal electrons over more than one pixel. Summarizing this important result, the signal from each single interaction point is spread out described with a Gaussian distribution and integrated in potentially multiple pixels.

4.3 *The Readout of the pnCCD*

A schematic side view cut of the pnCCD is shown in figure 4.4. The front side has structured contacts called registers (p^+implants), which allow a modulation of the potential inside the silicon bulk. Through periodic changing of the registers' voltages (ϕ_{1-6}), the stored signal electrons can be transferred along one direction, the transfer direction (perpendicular to the registers).

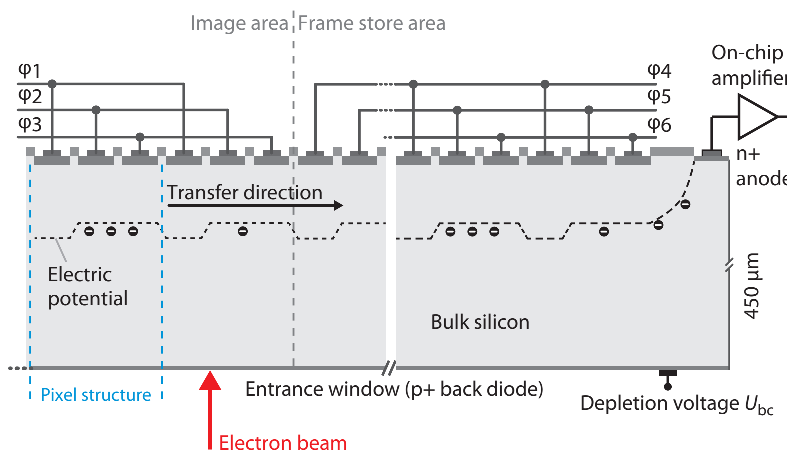

Figure 4.4: Side view of the pnCCD.

A first amplification stage for each column is integrated on the pnCCD chip. The output of each column is wire bonded to the input of a readout ASIC (application-specific integrated circuit) called CAMEX (CMOS Amplifier and MultiplEXer).[7]

[7] Herrmann et al., 2008.

The contacts for the registers are split into into two groups (ϕ_{1-3} and ϕ_{4-6}). This allows the voltages of one group to be changed independently of the other group. As a result, the pnCCD is divided into an area called the image area and the frame store area (see figure 4.5). The two areas are used to increase the readout rate. The standard

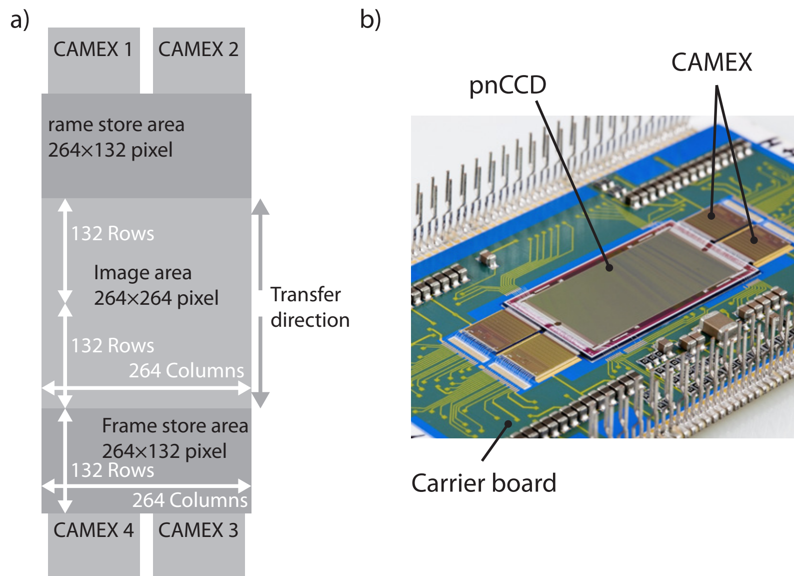

Figure 4.5: a) Readout scheme of the pnCCD. The pnCCD is divided into the central image area and the frame store areas. The image area is exposed to TEM electrons. In the first readout step, the integrated signal charges in the two halves of the image area are quickly shifted out into the frame store area. The frame store area is then read out row by row during which time, the next image is integrated in the image area. b) Image of the pnCCD mounted on a carrier board.

readout sequence starts with a fast transfer of the signal charges from the image area to the frame store area in approximately 35 µs. The signal charges are read out row by row, using the register voltages θ_4,θ_5 and θ_6 in approximately 8 µs per row. In the meantime, the register voltages of the image area (θ_1,θ_2 and θ_3) are not changed and the signal charges of the next frame are already integrated in the image area.

Additionally, the four CAMEXs provide one amplification stage for each column so that one row (one pixel of each column) is read out simultaneously. This multi-parallel readout leads to high full frame rates above 1000 fps (frames per second) which prove beneficial as shown in the application chapter 9.

The frame rate can be increased with binning and windowing methods. When binning is applied, the signal of two or more pixels is summed and read out as one value. On-chip binning is performed by shifting the signal electrons of multiple pixels on the readout anode. Therefore on-chip binning is performed only in one direction, the transfer direction. The illuminated area per readout pixel is effectively rectangular.

In windowing mode, only part of the image area is readout by only shifting rows of interest into the frame store area (see figure 4.6). In principle, any area is possible, while typically the center area is used.

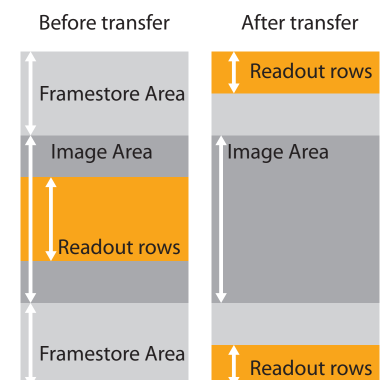

Figure 4.6: Principle of windowing.

Both methods increase the frame rate because the number of rows that need to be read out is reduced. A combination of binning and windowing is also possible. Table 4.1 provides an overview on the number of readout pixels and the frame rates. With extreme combinations of windowing and binning, a frame rate of 20 000 fps can be achieved, resulting in a final frame with 12×264 pixel.

Frame rate	Binning	Readout lines (windowing)	Effective image size
1150	1×	264	264 × 264
2000	2×	264	132 × 264
4000	4×	264	66 × 264
2000	1×	132	132 × 264
4000	2×	132	66 × 264
20 000	2×	24	12 × 264

Table 4.1: Overview of frame rates depending on windowing and binning. There is some overhead during the readout which is why the frame rate for full frame readout scales higher than linear with the number of rows.

4.4 *Charge Handling Capacity*

The number of signal electrons that can be collected in the potential of one pixel is called the charge handling capacity (CHC). This number is denoted N_{CHC}. For experiments with the pnCCD in the TEM, it is often important to know how many TEM electrons can be collected in one single pixel. The electron rate can then be adjusted accordingly. The number of TEM electrons N_{tem} with an energy E_{tem} equivalent to the CHC is:

$$N_{\text{tem}}(N_{\text{CHC}}, E_{\text{tem}}) = N_{\text{CHC}} \frac{3.67\,\text{eV}}{E_{\text{tem}}} \tag{4.1}$$

$$[N_{\text{tem}}] = \frac{\text{e}^-_{\text{tem}}}{\text{pix}} \tag{4.2}$$

The CHC depends on the resistivity of the detector material, the detector type and the parameter under which the detector is operated. For the pnCCD used in this thesis, the CHC can be adjusted with several operation modes which are explained in the following sections.

4.5 *Operation Modes of the pnCCD*

The CHC of the pnCCD can be adjusted by changing the operation voltages. The back contact voltage U_{bc} has the greatest influence on the CHC (U_{bc} ranging from $-120\,\text{V}$ to $-480\,\text{V}$). There are four operation modes, each serving a specific purpose. These modes are abbreviated HiRes (high resolution), HCHC (high CHC), AB (anti-blooming) and XPlus (*plus* for a combination of the different modes). Detailed studies regarding the CHC have been done by Schmidt, 2017. The CHCs for the operation modes are compiled in table 4.2. The operation modes are described in the next sections.

Operation Mode	N_{CHC}	$N_{tem}(E_{tem})$			
		20 keV	80 keV	200 keV	300 keV
	e^-_{sig}	e^-_{tem}	e^-_{tem}	e^-_{tem}	e^-_{tem}
HiRes	60 000	11.0	2.8	1.1	0.7
HCHC	300 000	55.1	13.8	5.5	3.7
AB	160 000	29.4	7.3	2.9	2.0
XPlus	250 000	45.9	11.5	4.6	3.1

Table 4.2: The number of TEM electrons that can be stored in one pixel per read-out assuming that all of the energy of the TEM electrons is deposited in one pixel. In the HiRes and HCHC mode, a higher number leads to blooming. In the AB mode and partially in the XPlus mode any signal elctron above N_{CHC} is drained off.

4.5.1 *High Resolution Mode - HiRes*

The HiRes mode is used for single electron imaging. At low electron rates, the TEM electrons hitting the detector are imaged spatially and temporally separated. During the post-processing, the point of entry (PoE) of the individual TEM electrons can be determined with sub-pixel resolution.[8] The spatial resolution is improved beyond the physical pixel size, hence the name of the mode. Usually in this mode, the average number of TEM electrons per pixel per frame is $\ll 1$ so that a value for N_{tem} of less than one TEM electron per pixel per frame is not a limitation.

[8] See chapter 8

The HiRes mode does not necessarily provide better noise performance compared to the other modes. The main difference is the more positive back voltage ($U_{bc} = -120$ V to -240 V) leading to longer drift times of the signal electrons and to a greater diffusion of the charge cloud.[9] The greater diffusion of the charge cloud results in the signal electrons being collected in a greater number of pixels. The signal spreading improves the determination of the correct PoE.[10] In the extreme case, there are no events with only one pixel affected. The signal is always spread over multiple number of pixels. Then the models described in section 8.3 can be used successfully to determine the PoE with sub-pixel resolution.

[9] See section 4.2

[10] See sections 7.3 and 8.3

4.5.2 *High Charge Handling Capacity Mode - HCHC*

The HCHC mode is used for measurements in which the dynamic range of the measured intensity is the most important figure of merit. The dynamic range is increased by increasing the upper limit of the number of signal electrons that can be stored in one pixel, the CHC. By lowering the back contact (-420 V to -480 V), the depth at which the signal electrons are collected is moved closer to the front side, effectively increasing the size of the potential well.[11]For the pnCCD used in this thesis, the CHC can be increased to around 300 000 signal electrons.

[11] Schmidt, . . . , Ryll, . . . , et al., 2014.

4.5.3 *Anti Blooming Mode - AB*

In measurements with very high electron rates, the deposited energy equivalent in number of signal electrons can exceed the number that can be stored in one pixel. In the HiRes and HCHC mode, any

surplus signal electrons will spill over to neighboring pixels (see figure 4.7a). This effect is usually called blooming. As a consequence, the spatial information in the image is reduced. The pnCCD can be operated with a set of voltages that allow the surplus number of signal electrons above the CHC to be drained away.[12]The signal spilling is thus prevented (see figure 4.7b), hence the mode is named anti-blomming (AB). In a basic explanation, the potential distribution

[12] Schmidt, . . . , Ryll, . . . , et al., 2016.

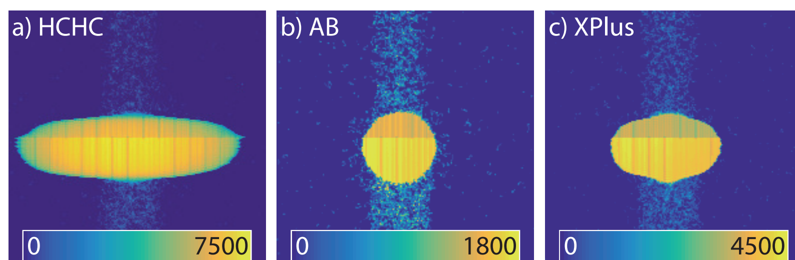

Figure 4.7: Comparison of operation modes. All images were recorded under equal illumination conditions with a homogeneous disc. a) Blooming is visible in the HCHC mode with a deformed disc. b) In the AB mode, surplus charge is drained off retaining the disc shape of the illumination. c) In the XPlus mode, some surplus charge is drained off. The maximum signal is different in each mode.

around the front side is shaped in such a way that there is a pathway for signal electrons to reach the ohmic areas at the front side. The CHC in the AB mode is lower than in the HCHC mode (see table 4.2). The signal electrons that are drained off, do not contribute to the readout signal. Therefore, above the CHC, signal amplitude is lost. The signal is linear up to the signal corresponding to the CHC.

4.5.4 *Combination Mode - XPlus*

In a hybrid mode called XPlus mode, properties of the AB and HCHC mode are combined. Excess charge is removed to a certain limit, yet the CHC is higher than in the pure AB mode.[13] Depending on the pnCCD voltages, a balance is set between the draining capabilities and an increased CHC.

[13] Ibid.

4.6 *The pnCCD TEM Camera System*

[14]The camera system (Figure 4.8) consists of the camera head (including the pnCCD), the electronic and cooling system and a computer for system control and data recording. There are multiple options for mounting the camera head to the electron microscope. Inside a mechanical housing, the camera can be directly attached to a TEM below the viewing chamber via an appropriate mechanical adapter. Alternatively, it can be attached below an existing camera with the advantage of two usable cameras. As a third option, the camera head can be easily exchanged with an already installed camera.

[14] This section is taken from Ryll et al., 2016

The schematic cross section of the camera head is shown in Figure 4.8a. The main parts are the pnCCD that is mounted on a ceramic board, the cooling mask, two thermoelectric coolers and a heat exchanger. The radiation entrance window side of the pnCCD faces upwards and is exposed to the electron beam through a square hole in the cooling mask. This mask also acts as an aperture, only exposing the imaging area of the pnCCD and preventing electrons from

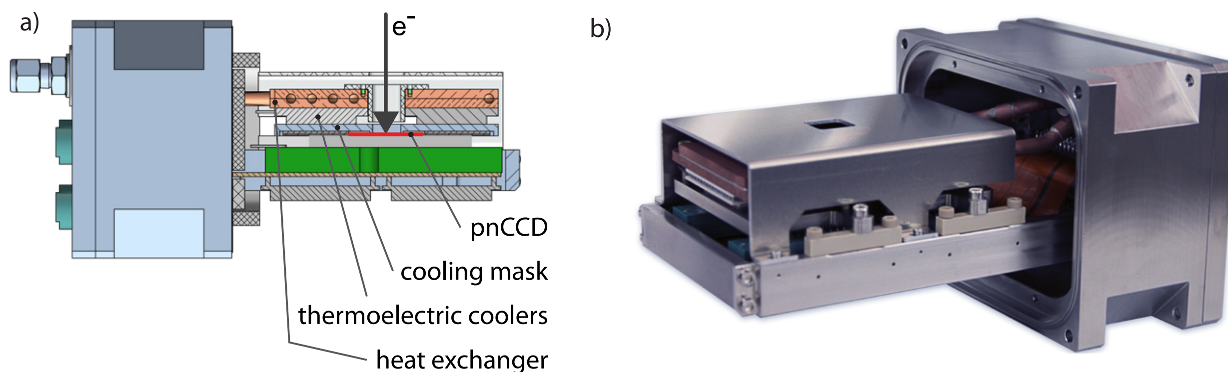

Figure 4.8: Cross section and image of the pnCCD camera system for TEM applications.

impinging on other parts of the detector.

The pnCCD is held at a stable operation temperature of −20 °C with the thermoelectric coolers (TEC), reducing the dark current. The TECs are directly coupled to the cooling mask. The heat produced by the TECs is dissipated through a water heat exchanger, running at a moderate water temperature of 10 °C, which is connectable to the TEM cooling system.

The electronic system consists of compact power supply units, a data acquisition system, a peltier controller, an uninterruptible power supply and a computer for controlling the camera system. The data are recorded and analyzed on a second computer. The data acquisition system is composed of two converter (ADC) boards, digitizing the analog signals with a resolution of 14 bit resulting in a range of 0 adu to 16 384 adu (arbitrary digital units). The digital data stream of up to 976 Mbit/s is sent to a PC for viewing and storage of the data. Four hardware input and output trigger signals can be used to synchronize the image acquisition with the microscope.

The software running the camera has two tasks. One task is to control and configure all aspects of the camera. It sets the appropriate voltages via the programmable power supplies, synchronizes the ADCs and the pnCCD electronics, monitors and records the signals from the pnCCD. The second part analyzes the data and provides live image viewing with online image corrections and processing applied. Bright field and dark field STEM images are computed and shown in real time.

5 Data Analysis Methods

The process from raw data of the pnCCD's data acquisition system to creating final images involves several steps. First, the raw data is corrected for an inhomogeneous detector response in each pixel (section 5.2). There are two modes to create final images, the intensity imaging mode (IIM) and the event imaging mode (EIM). In the IIM, the images and the intensity values in the pixel as a whole provide the data for further analysis (section 5.3). In the EIM, individual TEM electrons are imaged and information about each TEM electron is extracted from the images (section 5.4). The TEM electrons' positions can be determined with sub-pixel resolution to form images with an enhanced spatial resolution compared to the IIM. Furthermore, only the information that is gained using the EIM enables the understanding of the signal response of the pnCCD under electron illumination.

The pnCCD usually records not only a single frame but a large number of frames during one measurement (for example, a typical number of recorded frames is ≈66 000[1]). The resulting data is a stack of frames $S(i, x, y)$, in which x and y are the coordinates in the frame and i is the frame number.

[1] This number originates from a typical STEM measurement with 256×256 probe positions, see section 9.3.

The steps in analyzing the pnCCD data and forming images in the two modes are explained in the following sections. The treatment of the data to finally obtain the physically relevant information, for example intensity images and energy spectra, is shown.

5.1 Units of Energy in the Data Analysis

Three different units are used to describe energy in this thesis: electron volts (eV), number of signal electrons (e^-_{sig}) and arbitrary digital units (adu). Their use and relation are summarized below. A TEM electron that is incident on the detector has an energy that is expressed in eV. The energy it deposits in the detector is also expressed in eV. The deposited energy is converted into electron-hole pairs of which the electrons are collected in the pixels (the signal electrons). Hence, a number of signal electrons N_{sig} is equivalent to a certain amount of energy (see equation 3.4). N_{sig} determines the analog read out signal which is amplified by a gain factor G and converted into adu by the ADC. Thus, the digital readout in adu is proportional to the the number of signal electrons and also the deposited energy.

As adu are the native unit output of the ADC of the camera system, adu are used for most of the analysis and graphs. Adu can be converted in eV or e^-_{sig} using a gain dependent calibration. For some comparisons energy is expressed in fractions of the energy of the TEM electron (E/E_{tem}).

5.2 *Raw Data Analysis*

All data recorded during this thesis was streamed from the ADCs directly to a data acquisition PC and recorded on hard disk drives (hdd) in a raw file format called *.frms6. A single readout of all pixels is called a frame. Due to the split-frame readout[2], the geometry of a raw data frame is rectangular (see figure 5.1).[3] A schematic overview of the processing steps is given in figure 5.5. After recording of the raw data (a), these steps include: b) Offset correction, c) Common mode correction, d) Gain correction and e) further data analysis.

[2] See section 4.3

[3] See also figure 5.6.

In the first step (figure 5.5b), an offset correction is applied to the *raw frames* (S_{raw}) removing any constant offset of the ADC signal. So called *dark frames* (S_{dark}) were recorded at the start of each measurement without any illumination (figure 5.1). These frames were used to calculate the *offset map* (S_{offset}) for each measurement by averaging the signal for each pixel over a number of frames (typically 200 to 500 frames). The offset map is subtracted from all raw frames, resulting in *offset corrected frames* (S_{oc}) (figure 5.2):

$$S_{offset}(x,y) = \bar{S}_{dark}(i,x,y) \tag{5.1}$$

$$= \frac{1}{n}\sum_{i}^{n} S_{dark}(i,x,y) \tag{5.2}$$

$$S_{oc}(i,x,y) = S_{raw}(i,x,y) - S_{offset}(x,y) \tag{5.3}$$

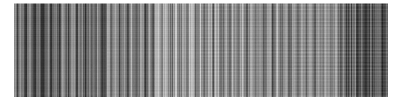

Figure 5.1: Example of a raw dark frame.

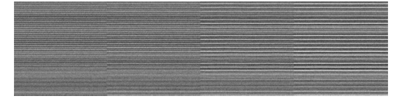

Figure 5.2: Example of an offset corrected dark frame.

A *noise map* (S_{noise}) is calculated from the offset corrected dark frames by taking the standard deviation for each pixel (figure 5.3):

$$S_{noise}(x,y) = \sigma_{S_{oc}(x,y)} \tag{5.4}$$

$$s_{noise} = \bar{S}_{noise}(x,y) \tag{5.5}$$

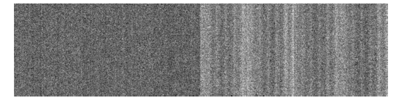

Figure 5.3: Example of a noise map.

The mean of all pixel values of the noise map gives the characteristic noise level s_{noise} for each particular combination of amplification, readout configuration (binning, windowing, readout timing), and temperature of the detector.

Figure 5.4: Example of a CM corrected dark frame.

The next (optional) correction step is the so called *common mode* correction (figure 5.5c). Common mode (CM) describes fluctuations in the supply voltages that cause an offset in the signal height of successive rows (the horizontal modulation in figure 5.2). These fluctuations affect all pixels of one row in the same manner. The CM offset of each line can be corrected with various methods (figure 5.4). All methods consider only pixels that do not contain any signal from the TEM electrons but only noise. For reach row and CAMEX output,

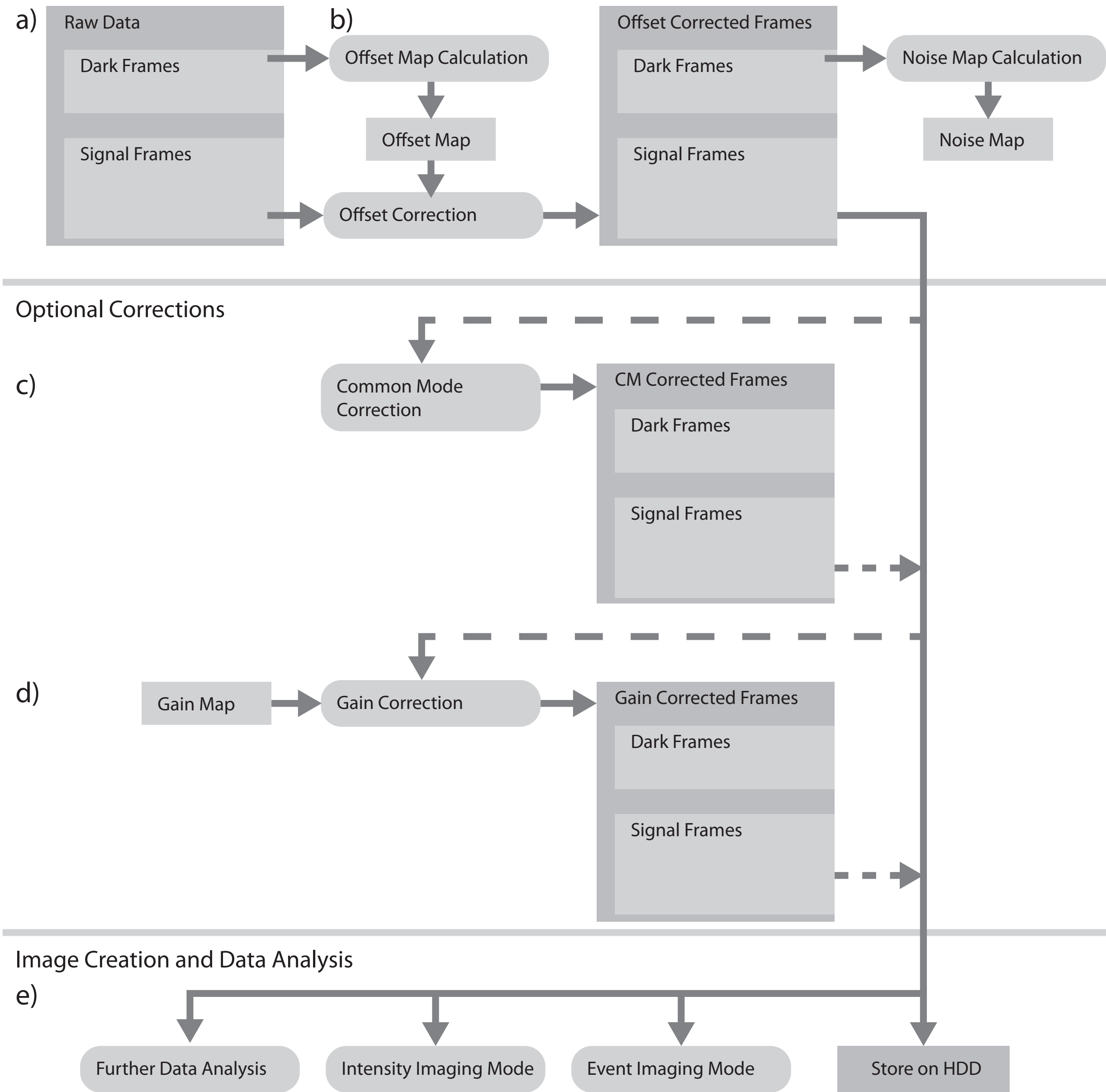

Figure 5.5: Data analysis steps for pnCCD frame data. The gain and CM corrections are optional. See text for detailed explanation.

the average of the considered pixels is calculated and then subtracted from the whole row of the CAMEX output.

If there are many pixels in a row with signal from TEM electrons, an area of the frame can be used that is masked against any illumination. In the case of the TEM camera, there is the titanium cooling mask that masks several columns at each side (6 on the left and 4 on the right). However, using only a few channels is not as effective in reducing the CM as using the whole row.

Nevertheless, there is always the possibility that primary electrons scatter into the masked columns. In this case, the CM correction for this row yields false results. TEM electrons with higher energies ($E > 200\,\text{keV}$) have a higher probability of scattering into the masked channels.

To improve the CM correction for these cases, a threshold can be used so that pixel with signals above the threshold are ignored and not used for the CM correction calculation. This might still result in an inaccurate CM correction since only (too) few pixels are left for the calculation.

The decision to apply CM correction has to be made depending on the experimental conditions and the further analysis requirements. In general, the difference between the CM corrected and non-CM corrected images are negligible. Most pixels of images recorded in the IIM contain actual signal and a CM correction is not applied. The CM correction is mostly applied when imaging single electrons in the EIM.

In a next optional step, the variation of the channels' amplification in the CAMEX can be corrected. The main contribution to the variation is due to small physical variance in the four CAMEXs. A further variation that repeats all 11 to 12 columns originates from the physical layout of the amplification stages in the CAMEX chip. The variations can be corrected with a *gain map* ($G(x,y)$) that is multiplied to each frame of the experimental data (S_{exp}) resulting in gain corrected frames (S_{gc}):

$$S_{\text{gc}}(i,x,y) = G(x,y) \circ S_{\text{exp}}(i,x,y) \tag{5.6}$$

The gain map can be calculated with the help of a gain reference measurement with homogenous illumination using the same timing and readout mode as used in the actual experimental.

Under homogenous illumination, it can be assumed that the signal is the same in every pixel. The mean value of the signal in the reference measurement $\overline{S}_{\text{ref}}(i,x,y)$ divided by the assumed mean signal $\overline{s}$ results in the gain map $G(x,y)$:

$$\overline{S}_{\text{ref}}(x,y) = \frac{1}{n}\sum_{i}^{n} S_{\text{ref}}(i,x,y) \tag{5.7}$$

$$\overline{s} = \frac{1}{n_{\text{col}}}\frac{1}{n_{\text{row}}}\sum_{x}^{n_{\text{col}}}\sum_{y}^{n_{\text{row}}} \overline{S}_{\text{ref}}(x,y) \tag{5.8}$$

$$G(x,y) = \overline{S}_{\text{ref}}(x,y)/\overline{s} \tag{5.9}$$

Alternatively, the expected signal $\bar{s}$ can be chosen such that the mean of $G(x, y)$ is one.

A second method compares the measured deposited energy of single TEM electrons with each other. The energy of the TEM electrons is fixed during one measurement. If an energy spectrum is created[4], there will be a peak in the energy spectrum that can be used as a reference point for a gain correction. If the readout is divided into quadrants or octants (two halfs per CMX), the energy spectrum of an uncorrected measurement shows the peaks at different positions. The gain map per quadrant (or octant) can then be calculated so that all the peaks in the energy spectrum coincide.

[4] See section 5.4.

The raw data stream is saved in a geometrical format that resembles the physical layout of the four readout CAMEXs. For further analysis of the images, either in the event imaging mode or in the intensity imaging mode, the frames are recomposed to match the actual image area of the pnCCD (figure 5.6). The number of rows is n_{row} and the number of columns is n_{col}. Note that the *readout* area is not always the full *image* area of the pnCCD. [5] Therefore, images can have different sizes, depending on the number of rows that are read out. In the case of binning, the pixels are effectively rectangular.

[5] See section 4.3 on readout.

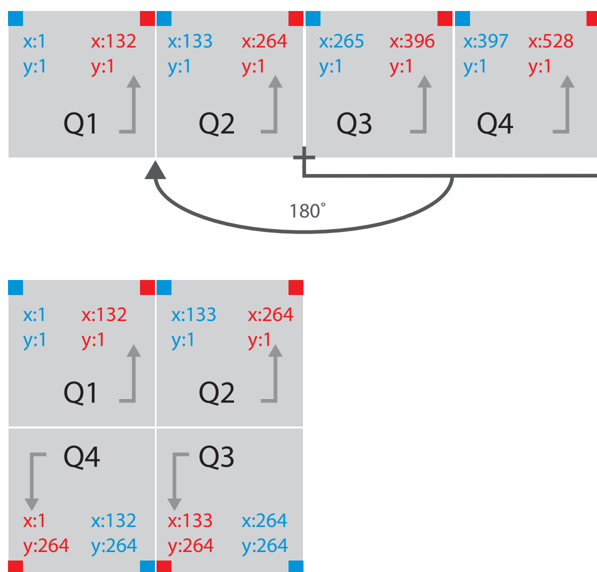

Figure 5.6: Orientation of the four quadrants of the image area before and after recomposing. Each quadrant corresponds to one readout CAMEX. Two corner pixels are highlighted for each quadrant.

5.3 *Intensity Imaging Mode*

In the intensity imaging mode (IIM), the final images are either the single corrected frames or the final images are formed by integrating multiple frames. The intensity in the images is the total intensity in the recorded frames, caused by the incoming TEM electrons. This mode is used when there are multiple TEM electrons per pixel on average. Usually, this mode is used for measurements in which a high number of TEM electrons per pixel is desirable. The IIM is used for

electron tomography and 4D-STEM imaging described in section 9.2 and 9.3.

A technique to enhance the image quality that can be applied to the stack of intensity images is post-acquisition drift correction.[6] During a measurement, the sample might drift. With a fast acquisition of multiple frames, the difference in the sample's position can be corrected.

[6] Li et al., 2013.

5.4 *Event Imaging Mode*

The event imaging mode (EIM) can be used when the electron rate is low enough that individual TEM electrons can be distinguished from each other (for example, like shown in figure 5.7). The goal is to extract information about each individual primary electron providing the data for further analysis. Energy spectra can be created for the recorded TEM electrons. Also, the spatial resolution can be increased when imaging single TEM electrons.

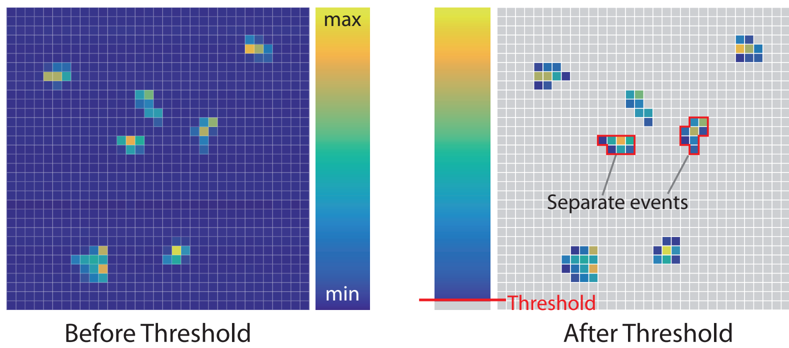

Figure 5.7: The first step in the single electron analysis (SEA). a) A crop of an image recorded with a low electron rate illumination showing clearly separated intensity distributions of TEM single electrons. b) After applying a threshold, separate events can be distinguished. All pixels that are connected belong to one event such as the two events marked with a red line. Characteristic information for each event can then be determined, like the sum intensity, number of contributing pixels and the position.

The procedure for the single electron analysis (SEA) consists of several steps. For each frame:

- Classify pixels containing only intensity from noise and pixels containing intensity due to a primary electron (see figure 5.7b)
- Assign pixels that are connected to one event
- Extract properties for each event (see figure 5.8):
  - Number of pixels with signal: n_{pix}
  - Signal in each pixel: $S(i)$
  - Sum of signal (the energy of the event): $E = \sum_{i=1}^{n_{\text{pix}}} S(i)$
  - Pixel pattern
  - Position (bounding box in units of pixel): (x_b, y_b, w, h)
  - Position of weighted centroid (Center of Gravity (CoG)): (x, y)
  - Frame number (for identification to certain frame)
- Add events to a list of events (the event list)

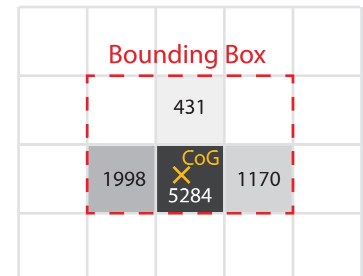

Figure 5.8: Example of an event and its properties. The signal in the pixel above threshold, the bounding box and the CoG are indicated. For this event: $n_{\text{pix}} = 4$, $E = 8883$ adu.

The result of a SEA is an event list with K entries. This list contains all the events identified during the analysis. Each event in the list contains associated information mentioned above.

Since each event has an associated energy, an energy spectrum of all events in the event list can be calculated. An example is shown in figure 5.9. The details of energy spectra are explained in chapter 7.

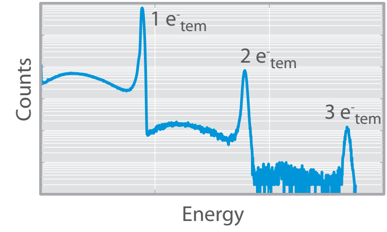

Figure 5.9: Example of an energy spectrum recorded under electron illumination.

To create an image $I(m,n)$, the number of TEM electrons is counted that have a position in each of the pixels (m,n):

$$I(m,n) = \sum_{i=1}^{K} \text{rect}\left(\frac{x(i)-m}{1}\right) \cdot \text{rect}\left(\frac{y(i)-n}{1}\right) \cdot M(E_i) \tag{5.10}$$

with $x(i)$ and $y(i)$ being the x- and y-coordinate of event i. The rectangular function (rect) (see figure 5.10) is defined here as:

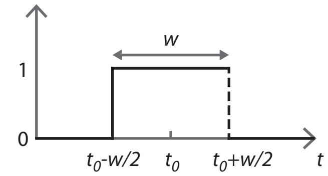

Figure 5.10: The rectangular (rect) function.

$$\text{rect}\left(\frac{t-t_0}{w}\right) = \begin{cases} 0 & \text{for } |(t-t_0)/w| > \frac{1}{2}, \\ 1 & \text{for } |(t-t_0)/w| < \frac{1}{2}, \\ 1 & \text{for } (t_0-t)/w = \frac{1}{2} \end{cases} \tag{5.11}$$

so that an event that has a position on the border of two pixels is counted in the left or upper pixel. In equation 5.10 w is set to 1 to count over the area of one pixel.[7]

The function $M(E_i)$ counts the number of TEM electrons that contribute to event i depending on the energy of the event:[8]

[7] Only square pixels are considered here, but the concept can be generalized to rectangular pixels.

[8] B stands for backscattered electron, F for a TEM electron depositing its full energy. For the detailed explanation see section 7.1.

$$M(E) = \begin{cases} 1 & \text{for } E_{\text{B1,min}} \leq E < E_{\text{F1,max}}, \\ 2 & \text{for } E_{\text{F1,max}} = E_{\text{B2,min}} \leq E < E_{\text{F2,max}}, \\ \vdots & \\ n & \text{for } E_{\text{F}n-1,\text{max}} = E_{\text{B}n,\text{min}} \leq E < E_{\text{F}n,\text{max}} \end{cases} \tag{5.12}$$

The energy limits $E_{\text{B}n,\text{min}}$ and $E_{\text{F}n,\text{max}}$ are taken from the energy spectrum.[9]The resulting image's unit is in number of TEM electrons per pixel.

[9] See figure 7.4 for a detailed example.

A basic method to determine the position of an event is to take the weighted centroid over the intensity in the pixels of that event (see figure 5.11). Due to the method of calculation, this position is not necessarily in the center of a pixel.

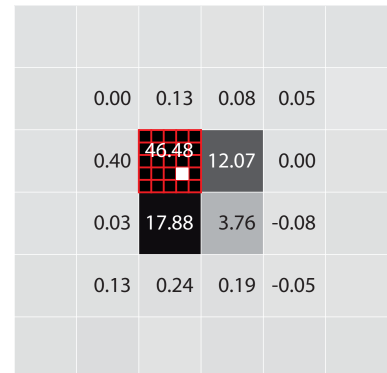

Figure 5.11: Center of gravity (CoG) for a single event ($E = 80\,\text{keV}$). The values denote the signal in the pixels in units of keV. The CoG can be used as the point of entry (PoE) with a sub-pixel resolution (the white pixel).

The size of the pixels in the image w_{pix} does not have to equal the physical pixel size w_{physical}. The physical pixel size is defined by the detector geometry. By choosing a smaller pixel size for the image than the physical pixel size ($w_{\text{pix}} < w_{\text{physical}}$), the number of pixels in the image can be greater than the number of physical pixels. Equation

5.10 is adjusted to:

$$I(m,n) = \sum_{i=1}^{K} \text{rect}\left(\frac{x(i)\cdot s - s_{\text{off}} - m}{1}\right)\cdot \text{rect}\left(\frac{y(i)\cdot s - s_{\text{off}} - n}{1}\right)\cdot M(E_i) \tag{5.13}$$

$$s = \frac{w_{\text{physical}}}{w_{\text{pix}}} \tag{5.14}$$

$$s_{\text{off}} = \left\lfloor \frac{s}{2} \right\rfloor = \max\left\{a \in \mathbb{Z} \mid a \leq \frac{s}{2}\right\} \tag{5.15}$$

Such an image has a sub-pixel resolution with a sub-pixel factor given by s in equation 5.14. The notation of equation 5.13 for $I(m,n)$ with the offset s_{off} of equation 5.15 is chosen to avoid fractional pixels when sub-pixel images are created.

As an example, the physical pixel size of the pnCCD used in this thesis has a pixel size of 48 µm. An image without sub-pixel resolution ($w_{\text{pix}} = w_{\text{physical}}$, $s = 1$) and full frame readout has 264×264 pixels. If sub-pixel resolution is applied, e.g. $s = 5$, the pixels in the image have a size of $w_{\text{pix}} = 9.6$ and there are 1320×1320 pixels in the image. Further numbers for sub-pixel resolutions are compiled in table 5.1.

s	w_{pix}	m	$m \cdot n$
	µm		pix
1	48.0	264	69 696
2	24.0	528	278 784
3	16.0	792	627 264
5	9.6	1320	1 742 400
9	5.3	2376	5 645 376
10	4.8	2640	6 969 600

Table 5.1: Size of image pixels w_{pix} depending on sub-pixel resolution s and number of pixels $m \cdot n$ in an image. An uneven sub-pixel factor is desirable, so that a PoE coordinate at the center of a physical pixel remains at the same position and is not shifted by half the length size of a sub-pixel.

A distribution of the number of pixels of each event can be calculated:

$$A(n) = \sum_{i=1}^{K} \delta\left(n - n_{\text{pix}}(i)\right) \tag{5.16}$$

$$p_{\text{pix}}(n) = \frac{A(n)}{K} \tag{5.17}$$

$$\delta(k) = \begin{cases} 1 & \text{for } k = 0, \\ 0 & \text{for } k \neq 0 \end{cases} \tag{5.18}$$

with $n_{\text{pix}}(i)$ being the number of pixels of event i.

This information about the events in total and for each event individually are used to calculate further properties of the pnCCD for the detection of electrons. One main property is the conversion factor C_{tem} that converts the measured intensity in the pixels into the number of TEM electrons that hit the detector. This property is investigated in section 7.5. The PoE of each TEM electron can also be determined with a higher spatial precision than the physical pixel size. Several models to determine the PoE are investigated in section 8.3.

The list of events can be filtered to create a subset of the event list. All events in the subset exhibit specific properties. For example, in section 7.3, in which the number of pixels per event is investigated, separate subsets of events are analyzed in which the TEM electrons deposited a certain amount of energy. By looking at only a part of the energy spectrum and only a part of a compound process, the individual processes can be understood more easily. In this case a deeper understanding is gained on how the number of pixels in an event relates to the scattering of TEM electrons in the pnCCD.

The SEA and these filtering methods are applied in the following chapters in which single electrons are simulated (chapter 6), in which the results of single electron detection are explained (chapter 7) and in which the models are explained to increase the spatial resolution (chapter 8).

6 Simulation of Signal Generation by Electrons

THE RANDOM NATURE OF THE SCATTERING of a TEM electron inside a detector prevents predicting its precise tracking. Electron tracks cannot be measured in the pnCCD, only the accumulated signal in the pixels. A solution to this problem is the simulation of individual electron tracks. The generated data can be used to understand the signals and images produced by single electrons.

Using simulations, properties were identified that influence the signals, mainly the operation voltages of the pnCCD and the TEM settings (electron energy, electron rate). Further, simulations help to determine the limit of spatial resolution in conjunction with a given detector geometry and TEM electron energy.

Visualization of electron tracks additionally provides an intuitive way to understand the signals that are recorded with a pnCCD under electron illumination. These images are included to help explain the recorded signals.

Simulations were done using the Geant4 toolkit.[1] All steps involved in the simulation are explained in section 6.1. Examples of electron tracks and basic results are presented in section 6.2. In section 6.3, the detection efficiency of the pnCCD is calculated. For many applications, the maximum number of detectable TEM electrons per pixel determines the quality of recorded data. The number of TEM electrons hitting the detector are statistically distributed in time, which is investigated in section 6.4.

[1] *Geant4* 2016.

6.1 Simulation Process

The scattering of electrons in matter is a random process. The scattering mechanisms, the interaction cross sections, and energy depositions can be described by probability distributions which allow the calculation of individual electron tracks with Monte-Carlo methods.

For this thesis, the Geant4 toolkit[2] was used to simulate the interaction of electrons with matter. The toolkit MEGAlib[3] with its tool *Cosima* provides a streamlined approach, in which the simulation can be configured via simple text parameter files. The simulation description is then translated and the calculations are carried out trough Geant4. The simulation process is shown in figure 6.1.

[2] Agostinelli et al., 2003; Allison et al., 2006; *Geant4* 2016.

[3] Zoglauer, Andritschke, and Schopper, 2006.

The Geant4 simulation in combination with Cosima results in files containing positions of energy deposits (x, y, z, E) in the detector for

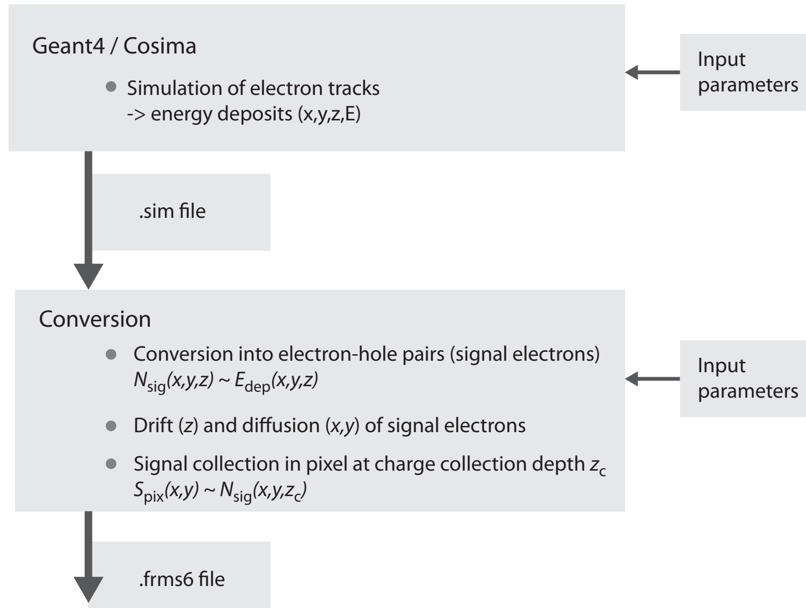

Figure 6.1: Overview of the simulation process. Electron tracks are simulated with the Geant4 and Cosima toolkit. The energy deposits (x, y, z, E) of the simulated primary electrons are stored in a .sim file. In a further step, the energy deposits are converted into standard pnCCD data files (.frms6). The conversion process considers the Fano statistic when sampling the number of generated signal electrons, drift in z-direction of the signal electrons to the front side until the charge collection depth, diffusion of the signal electrons in x and y-direction and finally binning into pixel dimensions.

each simulated primary electron. A separate conversion module[4] converts this data into standard pnCCD files. The energy depositions are converted into a number of electron-hole pairs sampled using the Fano statistics (see section 3.6).

[4] Weidenspointer, n.d., private communication.

The signal electrons created for each energy deposition are treated as point like charge clouds. In the detector, these signal electrons drift to the front side.[5] During this drift time, the charge cloud will widen due to diffusion. This process is included in the conversion module.

[5] See figure 4.3

For the simulation of low electron energies down to around 250 eV, the *Livermore* model was used, which is a low energy extension of the standard models included in Geant4. The Livermore model is integrated well into the *Cosima* framework.

Geant4 uses a so called *condensed* algorithm for the simulation of multiple scattering. Not each discrete interaction is calculated, but the net sums along a path segment, as shown in figure 6.2. This reduces the calculation effort and the simulations can be run in a practical timeframe. The accuracy of the simulation depends on the

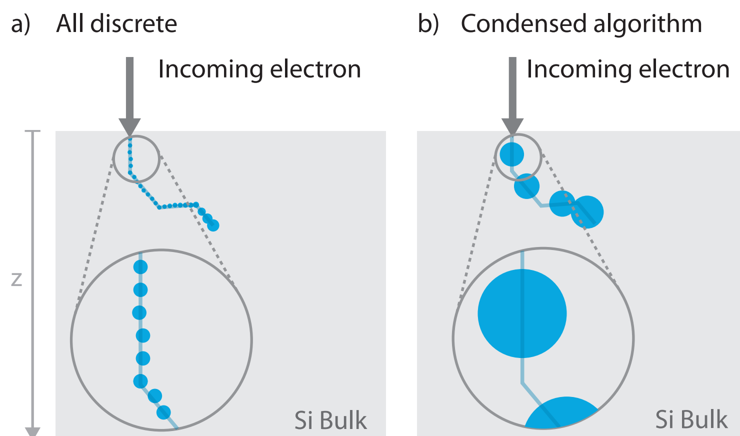

Figure 6.2: Principle of the condensed algorithm in Geant4. The real interaction path of the primary electron in (a) is translated to path segments s_i in (b) to reduce calculation time. The net sum energy deposition along the path segment is placed in the middle of the path segment. The net trajectory change is calculated at the end of each path segment. The choice of the segment path length is critical for the simulation accuracy and should be chosen to be smaller than dimensions of interest, i.e. the pixel size.

segment lengths and should be chosen to be smaller than the length dimensions of interest, in this case ≪ 48 µm, smaller than the pixel size. The simulations were set to a default range cut of 0.005 µm. For a detailed description of range cuts see the Geant4 Physics Manual.[6]

[6] *Geant4: Physics Reference Manual* 2016, p. 116.

The principle geometry that is used for the simulation is shown in figure 6.3. The simulated electrons are incident from the top under normal incidence. The base is a bulk of silicon that is 450 µm thick which is the sensitive region in which the energy deposits are recorded. On top of the silicon is an entrance window (EW) consisting of layers of silicon-dioxide (SiO_2) and silicon-nitrate (Si_3N_4). This type of EW is called optical EW (OEW), because optical light can reach the sensitive region. Another type has an additional light blocking and X-ray transparent layer of aluminum (see figure 6.3) and is called X-ray EW (XEW).[7]The pnCCD that was used for the experiments during this thesis has an OEW.

[7] For 150 nm aluminium, the transmittance for X-rays with an energy of 6 keV is 99.5 %, while for optical light (>310 nm or <3.5 eV) it is $<2 \times 10^{-8}$ %.

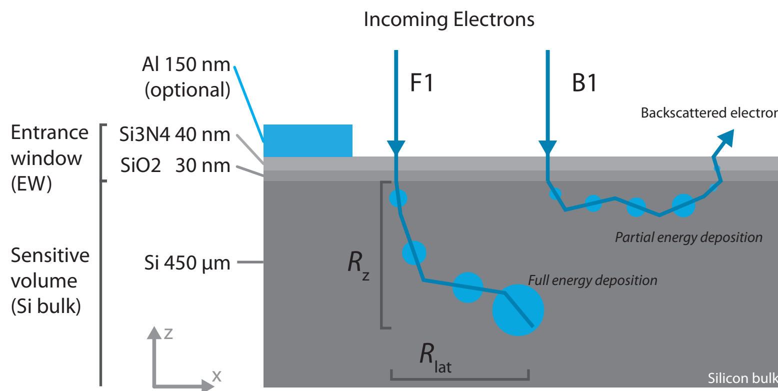

Figure 6.3: Schematic setup for Geant4 simulations. The two general cases how energy is deposited in the pnCCD. The incoming electron F1 deposits its whole energy in the detector. The incoming electron B1 deposits only part of its energy in the detector before it scatters back out of the sensitive volume. This type of electron is called a *backscattered* electron. Lengths are not to scale. Note the different unit prefixes.

The two most relevant possibilities of energy deposition in the silicon bulk are shown in figure 6.3. The most probable one (F1) is that the primary electron deposits its whole energy in the sensitive volume ($E_{dep} = E_{tem}$). The other possibility is that the primary electron scatters in such a way that it leaves the sensitive volume (B1). In this case, the deposited energy E_{ED} in the detector is less than the energy of the primary electron ($E_{ED} < E_{tem}$), which is seen in the energy spectrum (see later section 7.1).

6.2 *Simulation of Electron Tracks Results*

Single TEM electrons create a signal distribution that is unique to each TEM electron. Examples of multiple tracks for energies from 20 keV to 300 keV are shown in figure 6.4 (x-z-plane) and in figure 6.5 (x-y-plane).

Several qualitative observations can be made from the simulated tracks:

- As predicted by the Bethe-Bloch equation[8], the higher the energy of the TEM electron the longer is the *average* track. The primary electrons for 20 keV and 60 keV (figure 6.4a and b and 6.4a and b)

[8] See equation 3.6

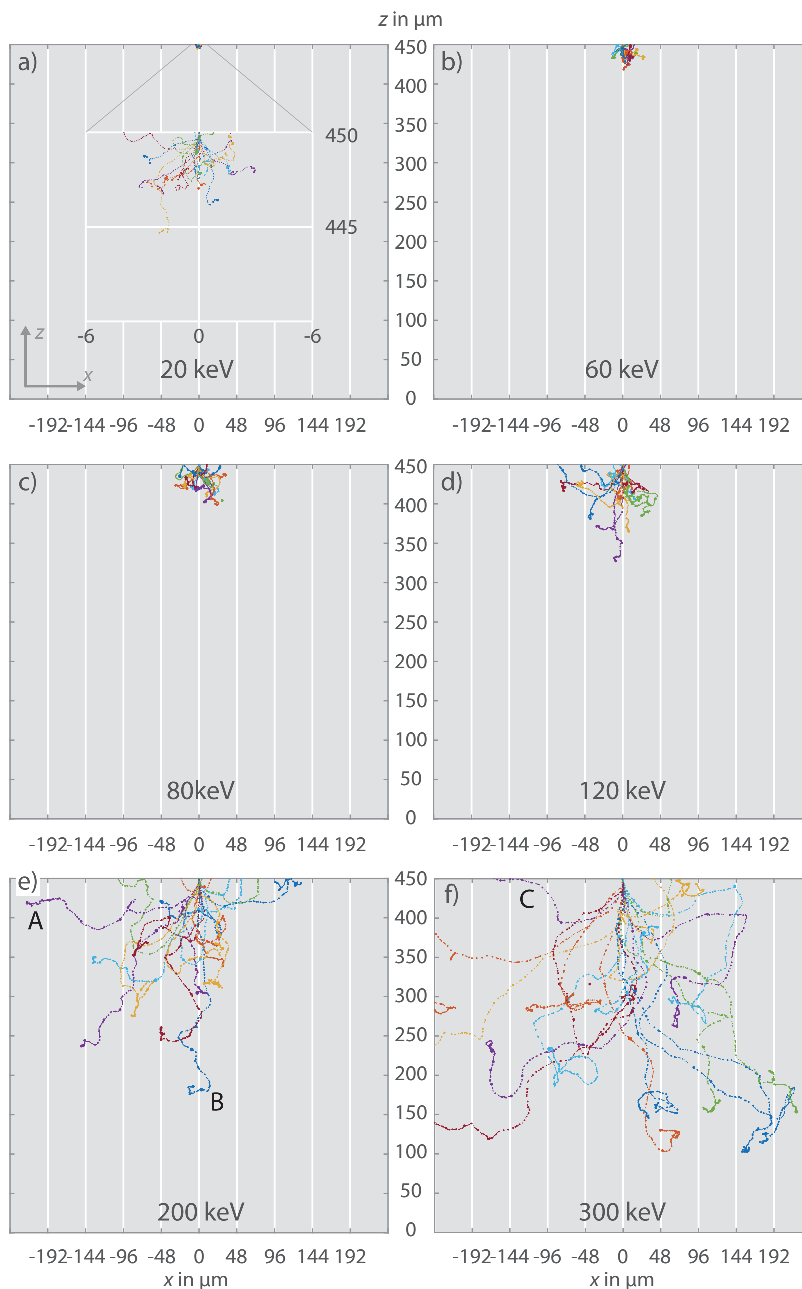

Figure 6.4: 20 Tracks of simulated TEM electrons. A projection in the x-z plane (sideview) is shown with a 1:1 aspect ratio. The grid for the x-coordinate is chosen to represent the pixel size of the used pnCCD. The TEM electrons enter at the top center at (0, 450). The variety of the random tracks is emphasized with two tracks in e) with track A being almost lateral and track B going almost straight in z-direction. There are also primary electrons that scatter out of the detector, for example in f) track C.

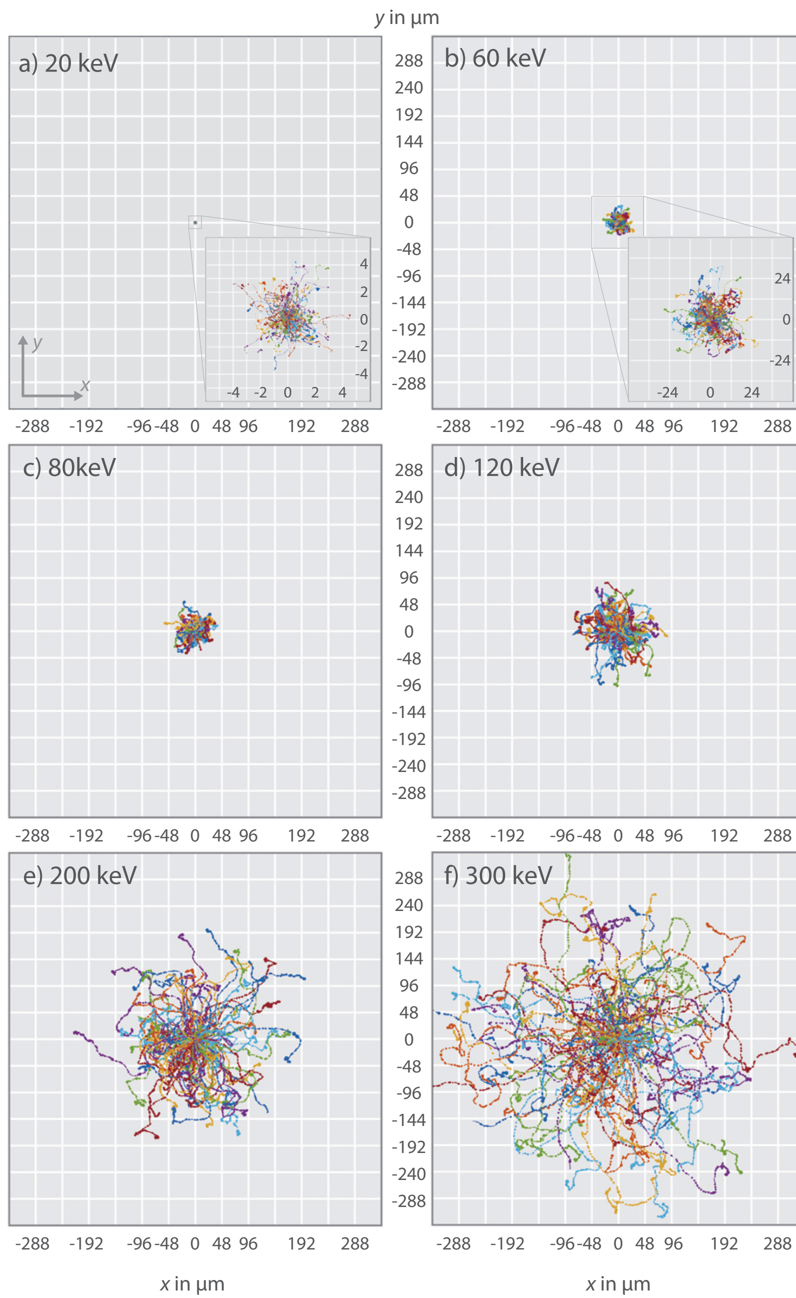

Figure 6.5: 100 tracks of simulated TEM electrons in the x-y plane (top view). The TEM electrons enter at the center at (0, 0). The grid is chosen to represent the pixel size of the used pnCCD.

cover lateral distances (in the x-y-plane) of less than a pixel size of 48 µm. The higher energy electrons cover lateral distances of multiple pixels.

- However, even the 300 keV TEM electrons do not reach the front side of the pnCCD. Thus the structured front side will not be damaged by the TEM electrons leading to a high radiation damage tolerance of the pnCCD.

- Individual primary electrons can scatter very differently from each other. In figure 6.4e), two tracks are marked of which one (A) is almost lateral and the other (B) goes almost straight in the z-direction. Both tracks will lead to different recorded signals in the pixels even though the energy of the TEM electron is the same.

- There are primary electrons that scatter back out of the detector (for example the marked track C in figure 6.4f). The signals generated by such primary electrons lead to a lower deposited energy.

The relative energy deposition distribution (p_D) of many TEM electrons that enter the detector at the same position is shown in figure 6.6 in a projection in x-direction.

$$p_\mathrm{D}(x) = \frac{\mathrm{d}E(x)}{\mathrm{d}x} \cdot \frac{1}{E_\mathrm{total}} \tag{6.1}$$

$$E_\mathrm{total} = \int E(x)\mathrm{d}x \tag{6.2}$$

A similar observation to the previous figures can be made. The energy depositions for the lower TEM electron energies are more concentrated around the position where the TEM electrons enter the detector ($x = 0$ µm). For the higher energies, the depositions are spread out further. In this case, the distribution for many electrons is shown, which is similar to measurements in which not single electrons are imaged but many (using the IIM, see section 5.3).

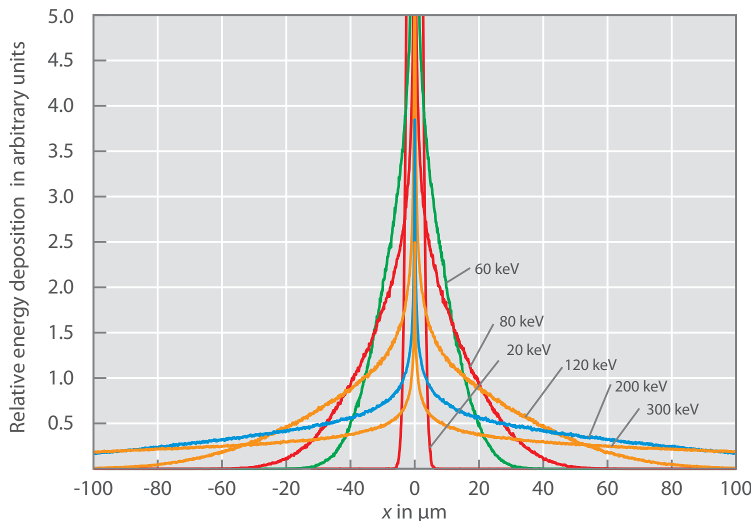

Figure 6.6: Relative distribution of deposited energy in x-direction for many TEM electrons. All TEM electrons entered the detector at the same position ($x = 0$ µm). The distributions are the same in y-direction.

The energy deposition distribution is convolved with a Gaussian function f_G to approximate the charge spreading of the signal electrons in the detector bulk:[9]

$$p_D * f_G = p_D(x) * \exp\left(-\frac{x^2}{2\sigma_{cloud}^2}\right) \tag{6.3}$$

The widths of the Gaussian given by σ_{cloud} is in the range of 5 µm to 20 µm.[10] In figure 6.7 the cumulative distribution function (cdf) of the convolved function is plotted for $\sigma_{cloud} = 10$ µm.

$$\text{cdf}(x) = \int_{-\infty}^{x} p_D(t) * f_G(t) dt \tag{6.4}$$

[9] See section 4.2

[10] Kimmel et al., 2010.

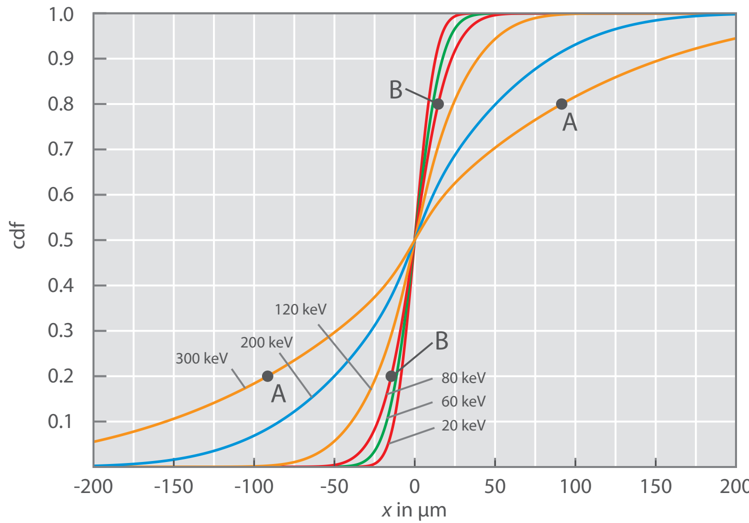

Figure 6.7: Cumulative distribution of energy depositions after convolution with a Gaussian function. The width of the Gaussian is $\sigma_{cloud} = 10$ µm. The spots A and B are referenced in the text. They mark the cdf value at 20 % and 80 % for 300 keV (A) and 80 keV (B). For example, at 300 keV, $\text{cdf}(-91.5\,\mu\text{m}) = 0.20$, which means that 20 % of the collected signal electrons are further away than −91.5 µm to the left of the entry point at $x = 0$ and another 20 % to the right, since the distribution is symmetric around $x = 0$.

For two cdf values of 0.05 and 0.20, the position in x direction is compiled in table 6.1. Again, it can be seen that the energy of the TEM electrons has a great influence on the distribution of the energy deposition. For example, on average, for 300 keV 40 % of the energy

	Position in x-direction in µm					
Energy in keV	20	60	80	120	200	300
$\text{cdf}(x) = 0.05$	16.7	22.6	30.2	52.2	112.4	206.8
$\text{cdf}(x) = 0.20$	8.5	11.4	14.6	23.8	50.1	91.5

Table 6.1: Positions in x-direction at which cdf values of 0.05 and 0.20 are reached.

depositions are further than 91.5 µm away from the point of entry of the TEM electrons (since the cdf is symmetric around $x = 0$ µm). In contrast, for 80 keV 40 % of the energy depositions are further away than 14.6 µm (see marked spots A and B in figure 6.7). From this, it can be deduced that the achievable spatial resolution is better for low energies than for high energies. The spatial resolution is further investigated in chapter 8.

Throughout this thesis, the dependency between the energy of the TEM electron and the spatial distribution of energy deposits plays an important role.

6.3 *Simulation of the Detection Efficiency*

The detection efficiency (DE) is defined as the ratio of the number of detected electrons N_{det} to the number of incoming TEM electrons N_{in}:

$$\mathrm{DE} = \frac{N_{\mathrm{det}}}{N_{\mathrm{in}}} \tag{6.5}$$

The DE can be divided into two parts: A part related to effects of the EW ($\mathrm{DE}_{\mathrm{EW}}$) and a part related to effects in the bulk ($\mathrm{DE}_{\mathrm{bulk}}$). The EW of the pnCCD is nonsensitive, most of the energy that is deposited in the EW does not contribute to the readout signal. Additionally, a small fraction of primary electrons will scatter in the EW and scatter back out again without reaching the sensitive bulk. The probability of such an occurrence depends heavily on the thickness of the EW and the energy of the primary electron. Each of these primary electrons is not detected and not counted, thus decreasing the DE. The part of the DE that describes the effect of the EW is termed $\mathrm{DE}_{\mathrm{EW}}$.

The second part of the DE describes all effects in the sensitive bulk, the signal electron generation, the amplification and readout, and finally post-processing of the data. These effects are included in a threshold parameter E_{T}. For this analysis, a primary electron event is counted if any of its pixels' signal is above the threshold. If the signals of all pixels of the event are below the threshold, it is not counted. The threshold is therefore a kind of noise equivalent. Equation 6.5 can be written as:

$$\mathrm{DE} = \frac{N_{\mathrm{sens}}}{N_{\mathrm{in}}} \cdot \frac{N_{\mathrm{det}}}{N_{\mathrm{sens}}} \tag{6.6}$$

$$= \mathrm{DE}_{\mathrm{EW}} \cdot \mathrm{DE}_{\mathrm{bulk}} \tag{6.7}$$

The number of electrons that reach the sensitive bulk is denoted N_{sens}. The number N_{det} corresponds to the number of detected electrons in the single electron analysis (SEA) after all processing steps, especially after applying the threshold. The N_{det} depends on the threshold energy E_{T} and the energy of the TEM electron E_{tem}.

Simulations provide a good basis for the calculation of DE, since the exact number of incoming electrons is known and the parameters that affect N_{det} are well controlled. The DE was calculated depending on the event threshold. For a given event threshold, all electron events were counted that have at least one pixel above the threshold.

The resulting dependency of the $\mathrm{DE}_{\mathrm{bulk}}$ on the energy threshold is shown in Figure 6.8. As expected, the DE decreases with an increasing threshold for all electron energies.

The entrance window has the greatest influence on the DE, especially for lower electron energies below 80 keV. According to the Bethe-Bloch equation (see equation 3.6), if the EW is thinner, less energy is deposited in the EW (shorter path integral). This effect is stronger for lower electron energies, since the energy loss per distance is greater (see section 3.1).

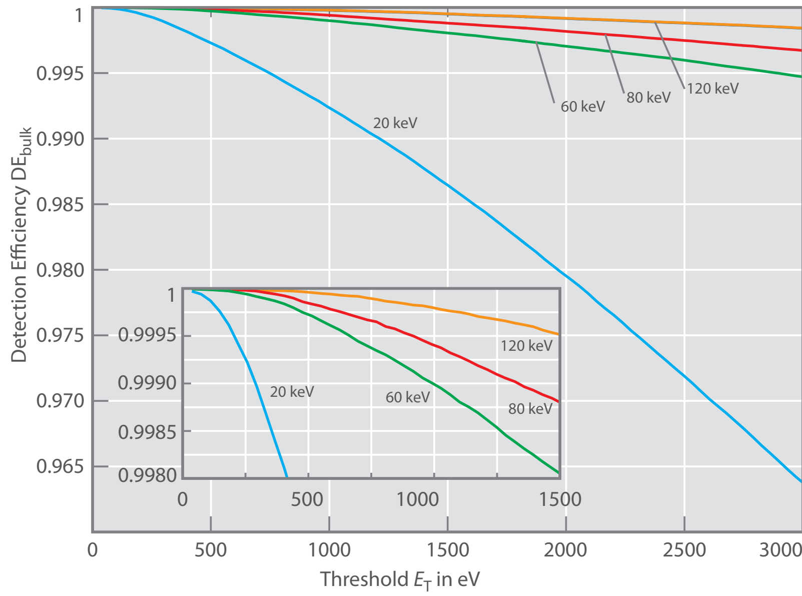

Figure 6.8: The bulk detection efficiency $\mathrm{DE}_{\mathrm{bulk}}$ depending on the detection threshold E_{T} for various TEM electron energies. The inset shows the low energy threshold region.

The DE for specific thresholds that are typically used in the SEA are compiled in Table 6.2 (for more thresholds, see appendix table A.7). Even for a threshold of 0.5 keV the DE is above 99.95 % at an electron energy of 80 keV.

Energy	$1-\mathrm{DE}_{\mathrm{EW}}$		$\mathrm{DE}(E_{\mathrm{T}}=0.5\,\mathrm{keV})$	
	X EW	O EW	X EW	O EW
keV	%	%	%	%
20	0.803	0.151	98.84	99.58
60	0.048	0.005	99.92	99.97
80	0.031	0.003	99.95	99.98
120	-	-	-	99.99
200	-	0.0003	-	100.00
300	-	-	-	100.00

Table 6.2: The detection efficiency (DE) of the detector for both types of entrance windows (EW) (X-ray and optical) for a detection threshold of 0.5 keV and the detection inefficiency ($1-\mathrm{DE}_{\mathrm{EW}}$) of the EW depending on the energy of the primary electron.

6.3.1 *Dependency of the Detection Efficiency on the Number of Discrete Events*

The number of incoming primary electrons has a great influence on the confidence intervals (or percentile distribution). Suppose only ten electrons impinge on the detector. There is a chance that one of them does not enter the sensitive bulk, since $\mathrm{DE}_{\mathrm{EW}} < \mathrm{DE} < 1$ (at least for $E < 120\,\mathrm{keV}$). In this case, the DE drops to 90 %.

This fact must always be considered: The DE and the conversion factor are calculated for a great number of electron events. The values for small numbers of electron events can differ significantly.

For each energy threshold, $\mathrm{DE}_{\mathrm{bulk}}$ was calculated (see table 6.2). With these probabilities $p(E_{\mathrm{T}}) = \mathrm{DE}(E_{\mathrm{T}})$, probabilities $B(k,n,p)$ can be calculated to detect k primary electrons for n incoming electrons. This corresponds to a binomial distribution with n incoming electrons, k detected electrons and the probability $p(E_{\mathrm{tem}}, E_{\mathrm{T}})$ to detect a TEM electron:

$$\mathrm{B}(k,n,p) = \binom{n}{k} p^k (1-p)^{n-k} \tag{6.8}$$

$$p(E_{\mathrm{tem}}, E_{\mathrm{T}}) = \mathrm{DE}_{\mathrm{bulk}}(E_{\mathrm{tem}}, E_{\mathrm{T}}) \tag{6.9}$$

$$\binom{n}{k} = \frac{n!}{k!(n-k)!} \tag{6.10}$$

From Equation 6.8 the probability can be calculated to detect a certain ratio of the incoming electrons for several cases:

- all incoming electrons are detected:
  $\mathrm{B}(k = n, n, p)$
- one incoming electron is not detected:
  $\mathrm{B}(k = n-1, n, p)$
- two incoming electrons are not detected:
  $\mathrm{B}(k = n-2, n, p)$
- generalized, i incoming electrons are not detected:
  $\mathrm{B}(k = n-i, n, p)$

In figure 6.9, the probabilities for 80 keV and the optical EW are shown calculated with a simulation and with equation 6.8.

The practical side of this problem is the inverse problem: If k electrons are detected, what is the probability that there were $n = k$ incoming electrons, $n = k+1$ incoming electrons and so on (in general $n = k+i$ incoming electrons). This problem can be described with the negative binomial distribution:

$$\mathrm{NB}(k,n,p) = \binom{n-1}{k-1} p^k (1-p)^{n-k} \tag{6.11}$$

For two energies (80 keV and 200 keV), the probabilities calculated with the negative binomial distribution are compiled in table 6.3.

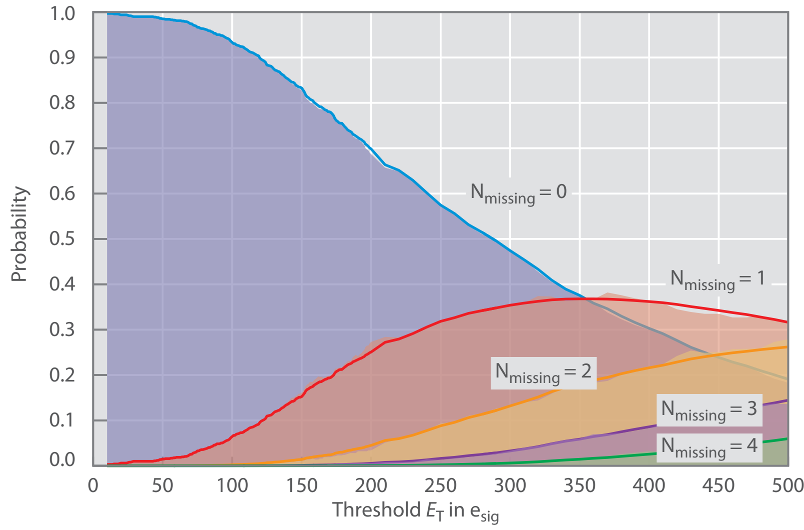

Figure 6.9: Probability distributions of DE_{bulk} for 80 keV and the optical EW. The area curves are calculated from simulations for 1000 groups of 1000 events for the five cases that all incoming electrons are detected ($N_{missing} = 0$) and that $N_{missing} = 1, 2, 3, 4$ incoming electrons are not detected. The line plots are the probabilities calculated from the binomial distribution (Equation 6.8).

	k	$n = k$	$n = k + 1$	$n = k + 2$
	e^-_{tem}	%	%	%
$E = 80$ keV	10	99.9311	0.0689	<0.0001
$DE_{bulk} = 99.9931$ %	100	99.3127	0.6849	0.0024
$E_T = 100\ e^-_{sig}$	1000	93.3356	6.4370	0.2222
	10 000	50.1733	34.6027	11.9333
$E = 200$ keV	10	99.9810	0.0190	<0.0001
$DE_{bulk} = 99.9981$ %	100	99.8105	0.1894	0.0002
$E_T = 100\ e^-_{sig}$	1000	98.1207	1.8615	0.0177
	10 000	82.7196	15.6929	1.4887

Table 6.3: Probabilities calculated from negative binomial distribution to detect all incoming electrons ($i = 0$) and not detect one ($i = 1$) or two ($i = 2$) incoming electrons for 80 keV and 200 keV and the optical EW.

6.4 *Statistical Considerations on the Number of Detectable Electrons*

For applications using the IIM, the quality of the information about a sample depends mainly on the number of detected TEM electrons which are distributed statistically in time. Poisson statistics can be used to describe the number of TEM electrons hitting the detector and to estimate the optimal average rate of incoming electrons. For simplicity, the scattering of the primary electron is not considered in this section. Instead it is assumed that all signal electrons generated by a TEM electron are collected in one pixel.

The maximum number of TEM electrons that can be detected in one pixel is given by the CHC.[11] However, the actual average rate in an experiment should be set to a lower limit, as explained in the following.

[11] See equation 4.2

The probability $P(r,k)$ that k TEM electrons are hitting a unit area (a pixel) depending on the average TEM electron rate r is given by:

$$P(r,k) = \frac{r^k}{k!}e^{-r} \tag{6.12}$$

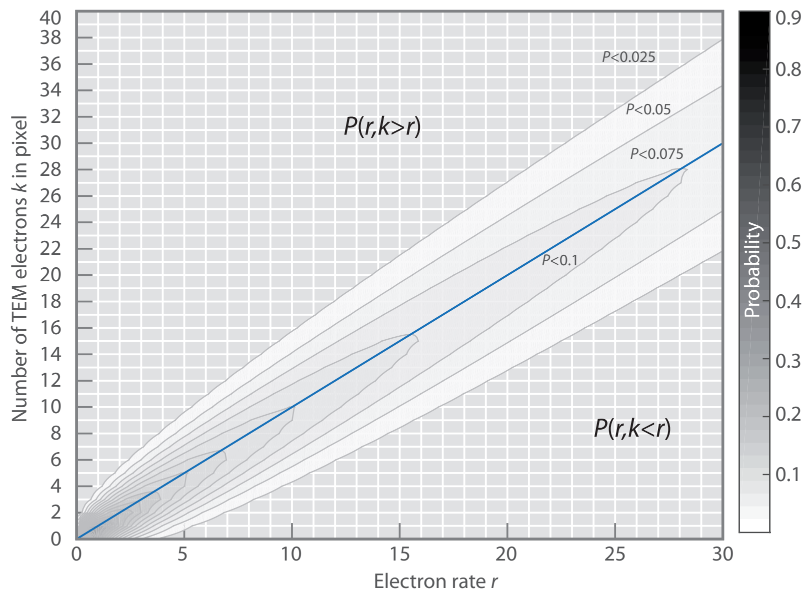

Figure 6.10: Poisson distribution probabilities that k primary electrons hit a unit area depending on the rate r of primary electrons per unit area.

Several aspects can be observed from the probability distributions shown in figure 6.10. The most probable event is always $P(r,k=r)$. The *summed* probabilities of all the events $P_s(r,k<r)$ and $P_s(r,k>r)$ are greater than $P(r,k=r)$. Three major cases and their respective probabilities can be distinguished:

1. $P(r,k=r)$,
   exactly $k=r$ electrons hit the unit area at an electron rate r
   (the diagonal line in figure 6.10)

2. $P_s(r,k<r) = \sum_{k<r} P(r,k)$,
   a number of electrons k hit the unit area that is smaller than the

electron rate r
(each P(r,k) below the diagonal in figure 6.10)

3. $P_s(r, k > r) = \sum_{k>r} P(r, k)$,
a number of electrons k hit the unit area that is greater than the electron rate r
(each P(r,k) above the diagonal in figure 6.10)

Examplary values for electron rates that correspond to the CHC and $k(N_{CHC}, E_{tem})$ of a pixel are compiled in table 6.4.

Electron rate r	$P(r, k = r)$	$P_s(r, k < r)$	$P_s(r, k > r)$
e^-_{tem}/area	%	%	%
3	22.4	42.3	35.3
5	17.6	45.0	38.4
7	14.9	44.1	40.1
12	11.4	46.2	42.4
18	9.4	46.7	43.8

Table 6.4: Probabilities for the three cases of $P(r, k = r)$, $P_s(r, k < r)$ and $P_s(r, k > r)$.

The relationship between the three cases for $k = 18$ is shown in figure 6.11. In addition the SNR for a single pixel is plotted as a quality measure:

$$\mathrm{SNR_{pix}}(n) = \frac{n}{\sigma_n} = \sqrt{n} \tag{6.13}$$

The case #3 that there are more than k electrons hitting a pixel is almost as probable as the case #2 that there are fewer electrons than k. The probability for case #3 ($P_s(r, k > r)$) decreases stronger than the SNR with decreasing r around $r = k$.

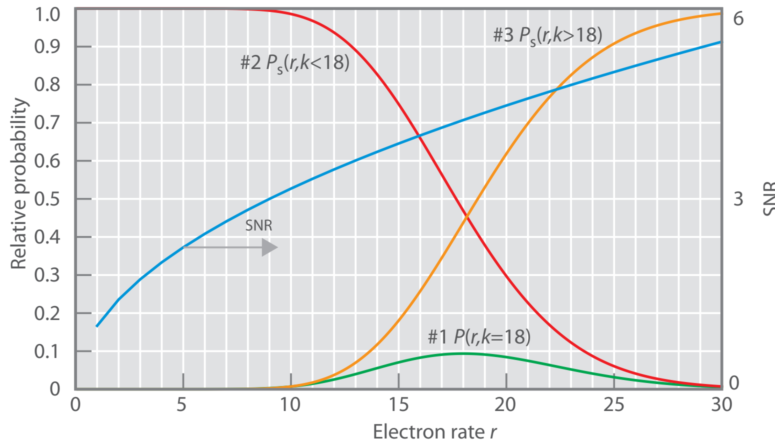

Figure 6.11: Probability distributions for the three cases of $P(r, k = r)$, $P_s(r, k < r)$ and $P_s(r, k > r)$ and the SNR(r). As an example, for an electron rate of $r = 18$, $P_s(r, k < r)$ and $P_s(r, k > r)$ are almost equal. At a lower electron rate of $r = 15$, the probability for overflow is much lower with $P_s(r, k > r) \approx 0.2$. The SNR only decreases slightly from $\mathrm{SNR}(18) = 4.2$ to $\mathrm{SNR}(15) = 3.9$.

A guideline for the optimum electron rate can be derived from the Poisson statistics. The mean number of electrons hitting a pixel should be as high as possible and as close as possible to the limit set by the CHC (k_{CHC}). At the same time, the possibility of overflowing pixels should be as low as possible, since this can deteriorate image quality. A possible criterion is that the number of pixels with more than k_{CHC} electrons should be below a certain percentage, e.g. 10 %. Figure 6.12

shows the relationship between k_{CHC} and the electron rate r_{set} that should be set for different criteria. The values are compiled in table 6.5 for several k_{CHC} corresponding to several energies. Additionally the relative differences are given:

$$\Delta_{kr} = \frac{k_{\mathrm{CHC}} - r_{\mathrm{set}}}{k_{\mathrm{CHC}}} \tag{6.14}$$

$$\Delta_{\mathrm{SNR}} = \frac{\mathrm{SNR}(k_{\mathrm{CHC}}) - \mathrm{SNR}(r_{\mathrm{set}})}{\mathrm{SNR}(k_{\mathrm{CHC}})} \tag{6.15}$$

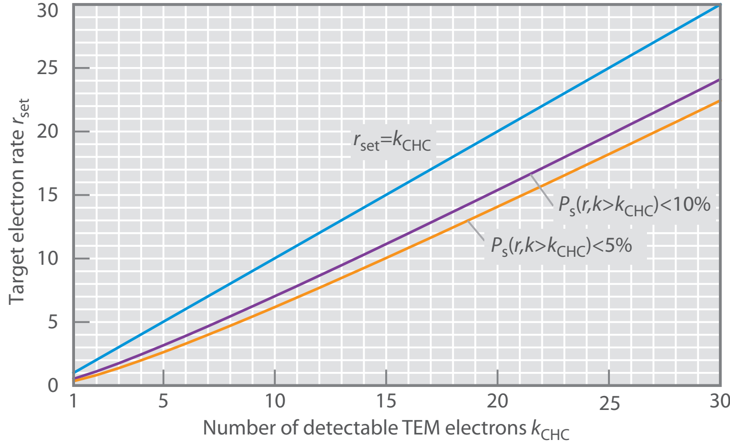

Figure 6.12: The target electron rate r_{set} depending on k_{CHC} for two limit criteria. The limit is that no more than 5 % and 10 % of the pixels should be hit with more than k_{CHC} TEM electrons.

For an experiment with an electron energy of 80 keV operated in the HCHC mode with a CHC of 400,000 signal electrons, corresponding to $k_{\mathrm{CHC}} = 18$ TEM electrons, and a limit that no more than 10 % of the pixels are hit by more than 18 TEM electrons, the electron rate should be adjusted to be $r = 13.67$ TEM electrons per pixel per readout.

Type	CHC N_{CHC}	Energy E_{tem}	CHC limit k_{CHC}	Target r_{set}	Δ_{kr}	SNR $\sqrt{k_{\mathrm{CHC}}}$	SNR $\sqrt{r_{\mathrm{set}}}$	Δ_{SNR}
	$\times 10^6\ \mathrm{e}^-_{\mathrm{sig}}/\mathrm{pix}$	keV	$\mathrm{e}^-_{\mathrm{tem}}/\mathrm{pix}$	$\mathrm{e}^-_{\mathrm{tem}}/\mathrm{pix}$	%			%
C16 48 µm	0.4		3	1.7	42	1.7	1.3	23.8
C16 48 µm	0.4	300	5	3.2	37	2.2	1.8	20.6
C16 48 µm	0.4	200	7	4.7	34	2.6	2.2	18.5
C16 48 µm	0.4	120	12	8.6	28	3.5	2.9	15.2
C16 48 µm	0.4	80	18	13.7	24	4.2	3.7	12.9
C16 75 µm	1.8	80	82	71	13	9.1	8.4	7.0
C14 75 µm	2.8	80	128	114	11	11.3	10.7	5.6
Depfet 90 µm	5.0	80	228	209	8	15.1	14.5	4.3
Depfet 90 µm	10.0	80	456	429	6	21.4	20.7	3.0

Table 6.5: Target electron rates for a limit criterion that no more than 10 % of pixels are hit by more than k_{CHC} electrons.

Three principle conclusions can be drawn from these calculations. First, to achieve the best performance in terms of single pixel SNR, the energy of the primary electrons should be as low as possible. The lower the electron energy, the more primary electrons can be collected in one pixel increasing the SNR.

Second, overflowing pixels are prevented by setting the electron rate just below the limit set by the CHC. Consequently, the nominal maximum number of primary electrons detected in one pixel is not achieved on average.

Third, increasing the CHC has great potential in increasing single pixel SNR. Table 6.5 includes values for other types of pnCCDs with a larger pixel size of 75 µm and different readout anode (C16 75 µm and C14 75 µm). Included is also a new type of detector called DEPFET that is currently being developed.[12] The DEPFET exhibits a CHC in the range of 5 to $10 \times 10^6\,e^-_{sig}$ depending on the pixel design. The single pixel SNR of these types of detectors is potentially greatly increased compared to the C16 48 µm type pnCCD.

[12] Lutz et al., 2008.

In a real experiment, the situation is more complex since the primary electrons are not confined to a single pixel volume but scatter in the detector volume over the range of several pixels. Additionally, the intensity distribution and thus the electron rate is not distributed homogeneously.

The consequences of overflow effects are difficult to assess or predict. The applications presented in chapter 9 do not determine the information of interest directly from the individual pixel intensity values. Rather, the images are further processed and analyzed in highly non-linear ways. The maximum number of overflowing pixels that can be tolerated without degrading the information content of the images must be determined for each specific application or even sample. The electron rates calculated in this section with the help of Poisson statistics provide a reference point from which to further tune the illumination if necessary.

7 *Signal Response to Electron Illumination*

The signals that are read out with the pnCCD under electron illumination are explained and characterized in this chapter. The resulting energy spectrum of the detection of single TEM electrons provides a wealth of information that is used to investigate the signals (see figure 7.1 for images of single electrons at energies between 20 keV to 300 keV). The characteristic features of the energy spectrum are described in detail including contributions from events originating from a single TEM electron and from multiple TEM electrons with overlapping tracks (sections 7.1 and 7.2). The probabilities for overlapping primary electron tracks are determined from simulations and experiments. The dependencies of these probabilities on the energy of the TEM electrons, the electron rate and the detector parameters are presented. The number of pixels per event are linked to these probabilities (section 7.3). The energy spectrum provides the data for

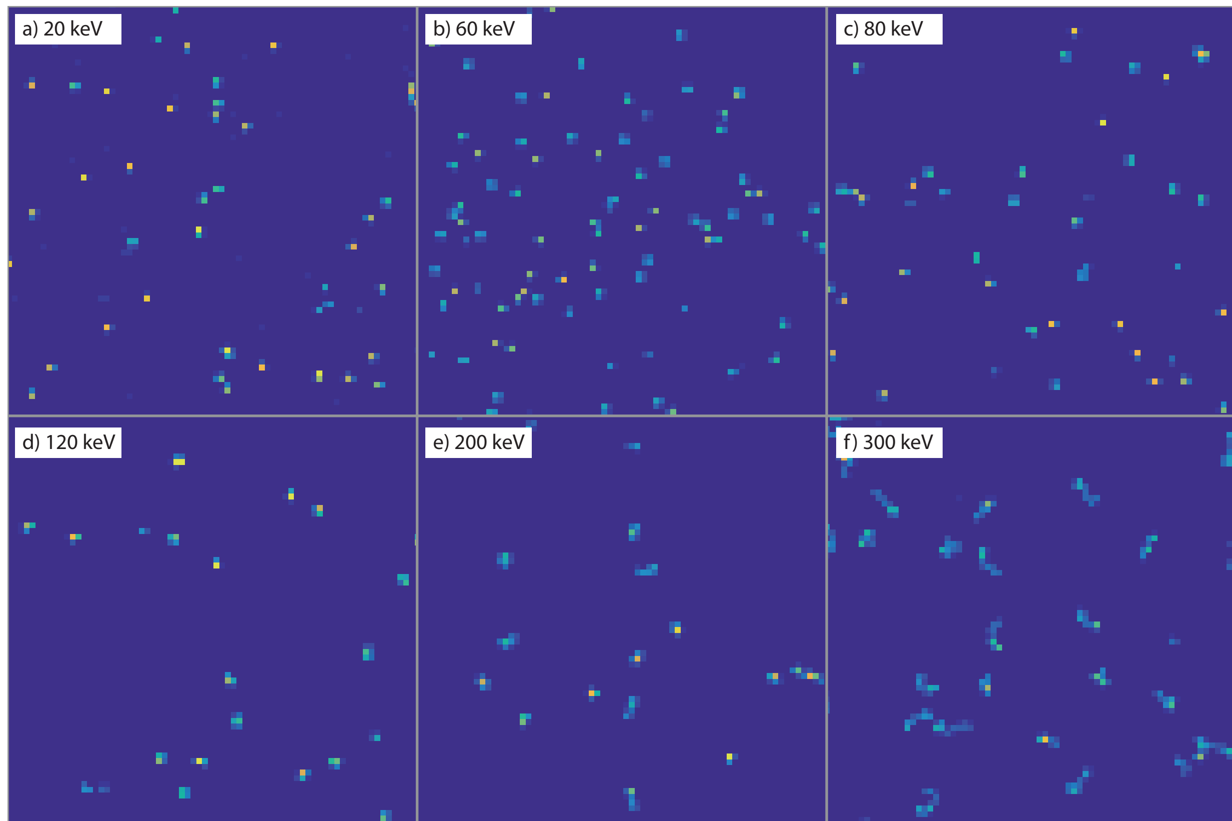

Figure 7.1: Crop of single frames recorded with the pnCCD showing single electrons. The contrast in each image is adjusted individually for visibility but the pixel sizes are equal.

the determination of two factors: The calibration factor (section 7.4), which converts the readout signal in units of adu into units of energy (eV), and the conversion factor (section 7.5), which converts the readout signal in units of adu into an average number of TEM electrons. Additionally, the signal efficiency per TEM electron is calculated and expressed as the detective quantum efficiency (DQE) (section 7.6). The energy resolution is also discussed in this chapter (section 7.7). Data from both experiments and simulations are combined throughout the following sections.

7.1 *Energy Spectrum of the pnCCD under Electron Illumination*

The energy spectra of detected single electrons were determined with the single electron analysis (SEA) as described in section 5.4 from similar images as shown in figure 7.1.

A typical example of an experimental energy spectrum of TEM electrons ($E = 200\,\text{keV}$) is shown in figure 7.2. For the following graphs, the unit that is used for energy is adu.[1] Several characteristic features can be seen in the energy spectrum:

[1] See section 5.1.

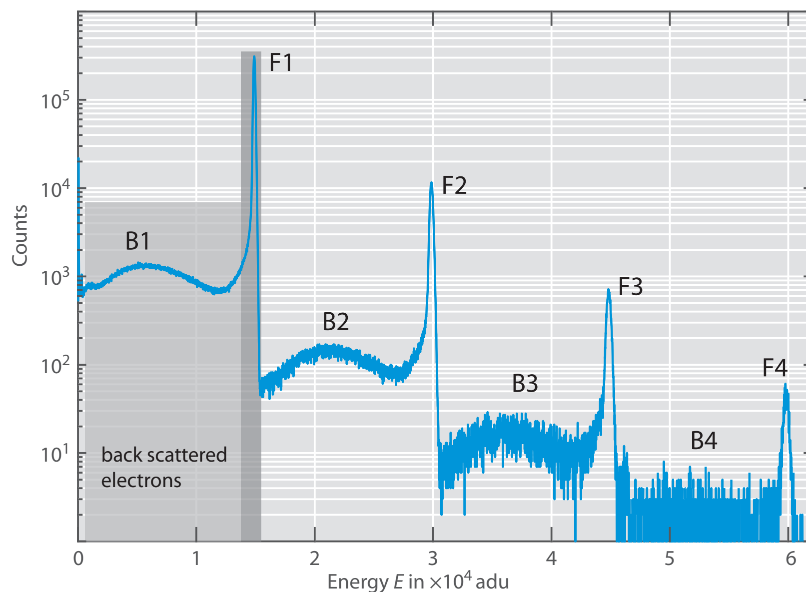

Figure 7.2: A typical experimental energy spectrum of electrons with an energy of 200 keV recorded with the pnCCD. Note the semi logarithmic scale. The peak F1 originates from events in which a single TEM electron deposits its whole energy in the detector. The peaks F2-F4 originate from events in which multiple TEM electrons deposit their whole energy in the detector and in which their tracks in the bulk overlap. The broad distributions B1-B4 to lower energies before the peaks F1-F4 originate from events in which the TEM electron(s) do not deposit their whole energy in the detector, but scatter out of the sensitive volume.

- F1: The peak with the highest number of counts originates from events in which a single TEM electron deposits its whole energy in the detector. For low electron rates, this is the most probable event. The mean signal E_{F1} corresponds to the energy of the TEM electron:
  $E_{\text{F1}} = E_{\text{tem}}$
- F2-F4: The peaks F2, F3 and F4 originate from pile-up events in which multiple (two, three and four) TEM electrons deposit their whole energy in the detector and in which their tracks in

the silicon bulk overlap.[2] The pixels that show signal due to the TEM electrons, are not separated from each other, so that the SEA detects this as one event (see figure 7.3). The mean sum signal $E_{\mathrm{F}n}$ equals the mean signal of a single TEM electron times the number of TEM electrons n that contribute to this event:
$E_{\mathrm{F}n} = n \cdot E_{\mathrm{F1}}$

- B1: The broad distribution with a lower energy E_{B1} than the peak F1 originates from events in which a single TEM electron scatters out of the sensitive volume. Only part of its energy is deposited in the detector:
  $E_{\mathrm{B1}} < E_{\mathrm{F1}}$
- B2-B4: These broad distributions originate mostly[3] from events in which one ore more TEM electrons deposit their whole energy in the detector and one TEM electron deposits only part of its energy. The sum signal $E_{\mathrm{B}n}$ is:
  $E_{\mathrm{B}n} = (n-1) \cdot E_{\mathrm{F1}} + E_{\mathrm{B1}} < n \cdot E_{\mathrm{F1}}$

[2] See also section 7.2 about pile-up probabilities.

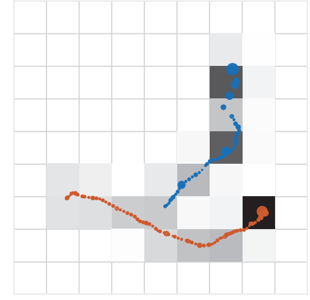

Figure 7.3: Two simulated electron tracks ($E = 300\,\mathrm{keV}$) that result in signal distributions with connected pixels. In the SEA, this distribution is detected as one F2 event.

[3] See section 7.2.1 and table 7.2 for more details.

The following nomenclature is used here: If an event is identified to originate from a single primary electron, the type of event is called a *single* or S1. If an event is identified to originate from two (*double*), three (*triple*) or more primary electrons, the shorthand notation Sn is used, where the n stands for the number of primary electrons. With this nomenclature, the counts N for each type are denoted:

$$N_{\mathrm{S}n}(E) = N_{\mathrm{B}n}(E) + N_{\mathrm{F}n}(E) \tag{7.1}$$

and the total energy spectrum is given by:

$$N(E) = \sum_n N_{\mathrm{S}n}(E) \tag{7.2}$$

The energy spectrum can also be expressed as a probability distribution p by dividing by the total number of events:

$$p(E) = \frac{N(E)}{\sum N(E)} \tag{7.3}$$

In figure 7.4, the previously shown energy spectrum is overlaid with the function $M(E)$ (see equation 5.12) that counts the number of TEM electrons contributing to an event. The energy limits for this function can be determined from such an energy spectrum.

There is a small chance, that an Sn type event actually originates from a number of TEM electrons that is greater than n. As an example, two TEM electrons with overlapping tracks could deposit an energy that is lower than the full energy of a single TEM electron:

$$0 < E_{\mathrm{B1,1}} + E_{\mathrm{B1,2}} < E_{\mathrm{F1}} \tag{7.4}$$

These cases are further explained in section 7.2 about pile-up events.

The general shape of the energy spectra for each energy of the TEM electrons is the same. The energy spectrum is characterized in detail in the next sections, while the ratios of the probabilities of the different types of events is investigated in section 7.2.

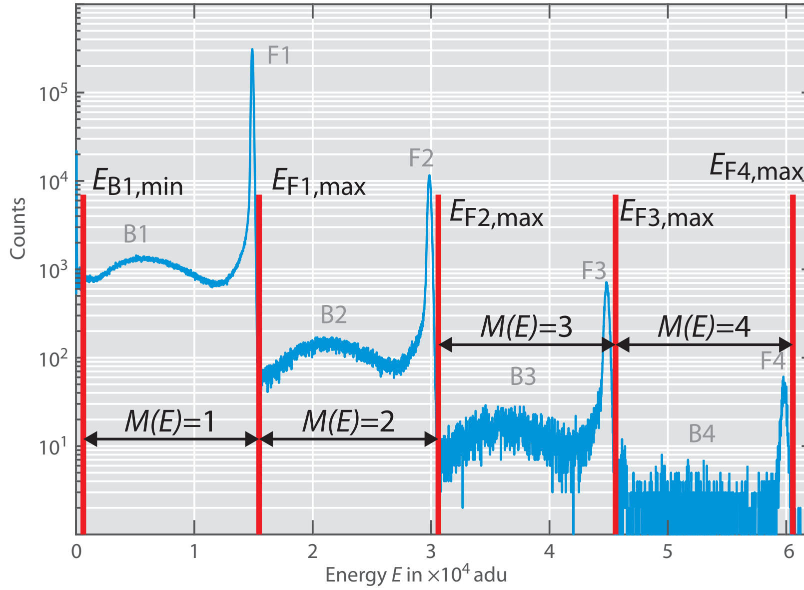

Figure 7.4: Evaluation of the multiplicity function $M(E)$ of equation 5.12. The limits for the function are determined from the energy spectrum as indicated by the vertical red lines.

7.1.1 *Full Energy Deposition*

In figure 7.5 the energy spectrum is shown of a simulation ($E = 80\,\mathrm{keV}$) in which the TEM electrons deposited their whole energy in the detector (type F1 event) before conversion of the data into pnCCD format files. To be precise, these are events in which the TEM electrons did not escape the detector after entering.[4] The TEM electrons do deposit a small amount of energy in the entrance window (EW) (the red distribution in figure 7.5). As a TEM electron scatters through

[4] Remember figure 6.3.

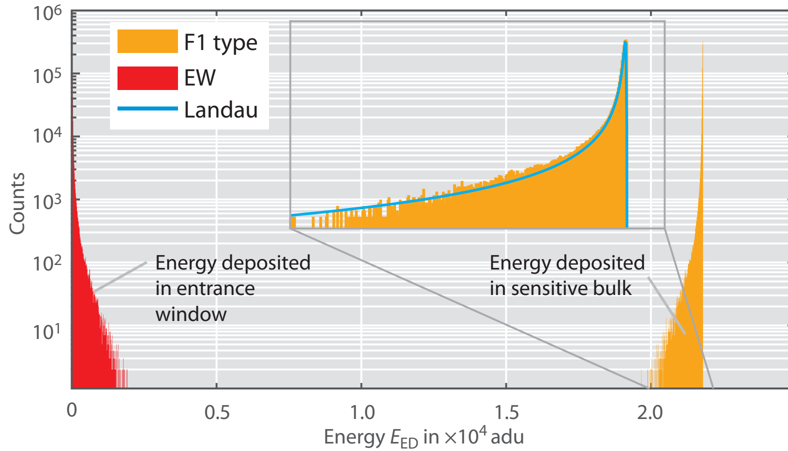

Figure 7.5: Energy spectrum of simulated electrons with an energy of 80 keV and a gain of 1 adu/e^-_{sig}. Only events are shown in which the electron deposits all of its energy in the detector including the EW. The sum of the energy that is deposited in the non-sensitive EW (red distribution) and the energy that is deposited in the sensitive bulk (yellow distribution) equals the energy of the TEM electron. The inset shows that the energy distribution follows a Landau distribution.

the EW, it will loose part of its energy. The EW can be considered as thin ($d < 250\,\mathrm{nm}$). As described in section 7.5, the total energy loss of electrons in thin absorbers can be described with Landau distributions of type:[5]

[5] Landau, 1944.

$$N_L(E) = A\frac{1}{\pi}\int_0^\infty e^{-t\ln t - b\cdot t}\sin(\pi t)\mathrm{d}t \tag{7.5}$$

The parameters A and b are functions of the energy of the TEM electron, the deposited energy, the absorber's thickness and material

properties.[6] As can be seen in the inset of figure 7.5, a fitted Landau distribution matches the simulated distribution well.

The two distributions of the energy that is deposited in the EW and in the sensitive silicon bulk are opposite. The sum of two entries in the two distributions of a single simulated F1 event equals the energy of the TEM electron. The energy difference that is missing in the deposited energy compared to the TEM electron's energy is deposited in the EW:

$$E_{\text{tem}} - E_{\text{EW}} = E_{\text{F1}} \tag{7.6}$$

In this text, the TEM electrons of F1 events are said to have their full energy deposited in the detector, even though a small fraction is deposited in the non-sensitive EW.

For the simulation and the energy distribution of the deposited energy of F1 events, a Landau distribution is assumed that is mirrored with respect to the energy of the TEM electron:

$$N_{\text{F1}}(E) = N(E_{\text{tem}} - E_{\text{EW}}) \tag{7.7}$$

After conversion of the energy deposit data into pnCCD format files (including the Fano statistics explained in section 3.6 and collection of the signal electrons in the pixels) the energy peak is widened. In figure 7.6, the energy spectrum of the events after the SEA is compared to the energy spectrum of the energy depositions in the sensitive silicon bulk. The F1 peak of the events after the SEA is broader than the peak

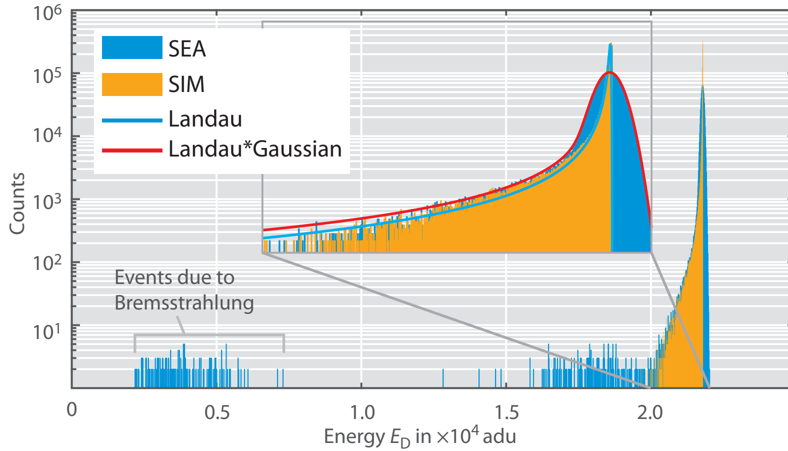

Figure 7.6: Energy spectrum of simulated electrons with an energy of 80 keV and a gain of 1 adu/e^-_{sig}. Only events are shown in which the electron deposits all of its energy in the detector including the EW. The yellow, sharp distribution represents the energy deposition only. The blue, broadened peak is the energy distribution of the events after the conversion into pnCCD files and the SEA. The yellow curve is convolved with a Gaussian function due to the Fano statistics. The events due to Bremsstahlung are explained in the text (see section 7.1.4).

of the Landau distribution of the pure simulation data. This is the result of the variance in the energy that is required in the involved processes generating one electron-hole pair as described in section 3.2 (Fano statistics). Basically, the Landau distribution is convolved with a Gaussian function. The width of the Gaussian function σ_G is also energy dependent.

$$N_{\text{F1}}(E) = N_L(E) * N_G(E, \sigma_G) \tag{7.8}$$

[6] See appendix A.6 for more details.

7.1.2 *Backscattered Electrons*

In figure 7.7, the energy spectrum is shown of events of simulated electrons ($E = 80\,\text{keV}$) that scatter back out of the detector without depositing their whole energy in the sensitive bulk (type B1 events).

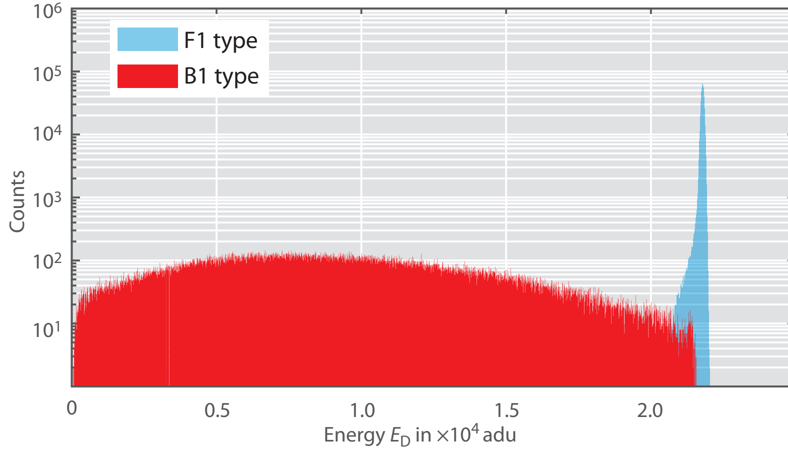

Figure 7.7: Energy spectrum of simulated electrons with an energy of 80 keV and a gain of $1\,\text{adu}/e^-_{\text{sig}}$. Events of backscattered electrons are shown in which the electron does not deposit all of its energy in the detector (B1 type). For comparison, the F1 events are included.

The shape of the spectrum can be explained with figure 7.8 in which three simulated tracks of backscattered electrons are compared, one with a low, a medium and a high amount of deposited energy relative to the TEM electron energy. The amount of energy E_D that is

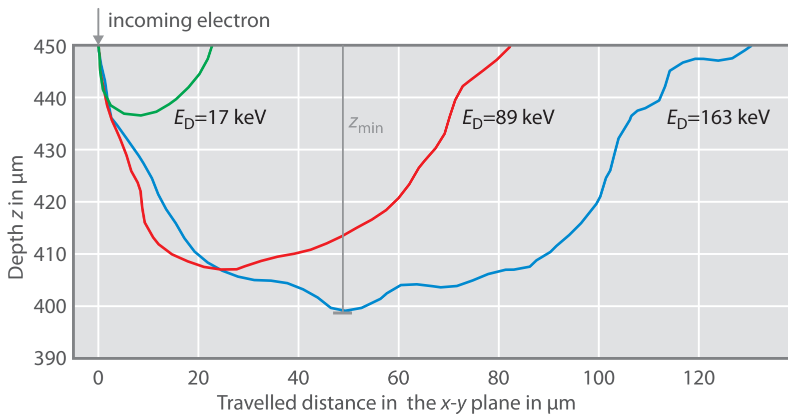

Figure 7.8: Tracks of three simulated electrons that are backscattered ($E = 200\,\text{keV}$). The electrons deposit an increasing amount of energy E_D in the sensitive volume of the detector with increasing path length. The path length is correlated to the minimum depth z_{min}.

deposited by the primary electron before it scatters out of the sensitive bulk depends on the path length of its track. A longer track results in a greater amount of deposited energy, and is more probable when the primary electron scatters deeper into the detector.

In figure 7.9, many tracks are shown divided into three categories based on the deposited energy, with $E_D < 60\,\text{keV}$ (green), $100\,\text{keV} < E_D < 120\,\text{keV}$ (red) and $E_D > 180\,\text{keV}$ (blue). Again it can be seen that in general the probability for a higher energy deposition is higher, when the primary electrons scatter deeper.

Looking at the energy spectrum, starting from zero to increasing energies (energy of zero up to around 6000 adu), the probability that the primary electron scatters out of the sensitive bulk increases (see marker A in figure 7.10).

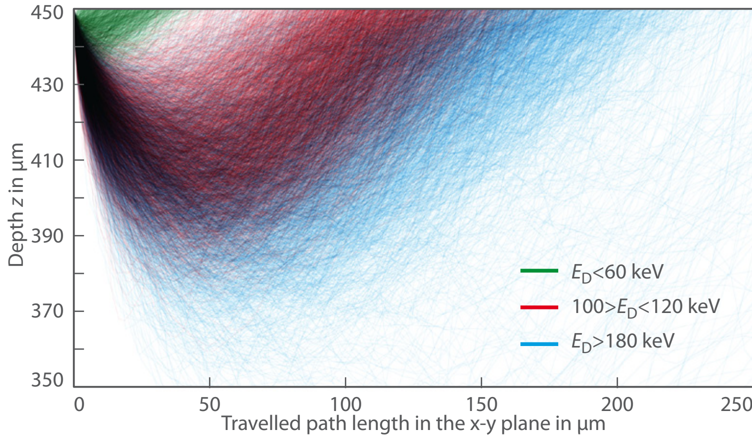

Figure 7.9: Dependency of the reached depth z and traveled distance on the deposited energy. Three categories of backscattered tracks are shown depending on the deposited energy.

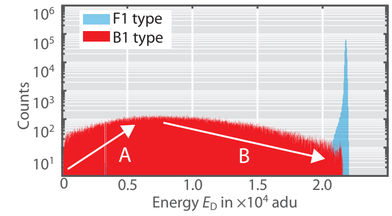

Figure 7.10: Details of the energy spectrum for backscattered TEM electrons. See text for marker A and B.

The probability, that the primary electron deviates from its original trajectory increases as it scatters deeper into the bulk. The probability for forward scattering is higher (see section 3.8). Therefore, the probability that the primary electron will scatter out of the sensitive bulk shortly after entering the sensitive bulk is low. This probability increases as the primary electron scatters more deeply into the bulk, which is seen as an increase in counts in the energy spectrum.

The probability then decreases with increasing energy (see marker B in figure 7.10). This is due to the fact, that the probability that the primary electron scatters out of the sensitive bulk decreases with the increasing depth that the electron reaches. The further the primary electrons scatters away from the EW, the lower its chance to escape the sensitive bulk through the EW.

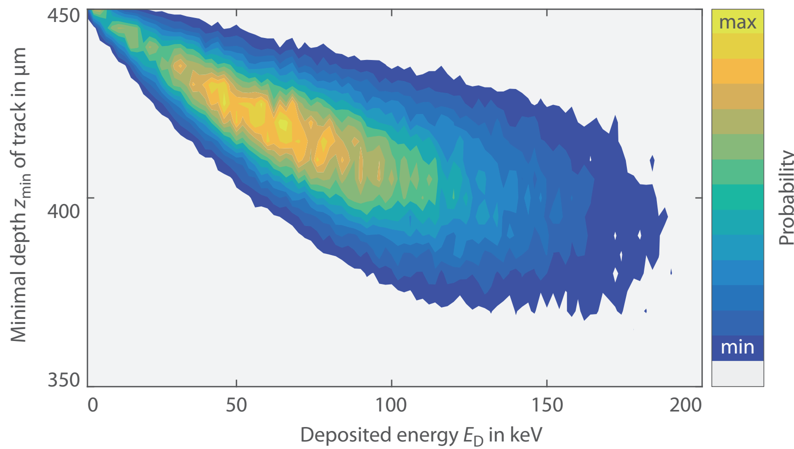

Figure 7.11: Relation between the probability that a primary electron (E = 200 keV) scatters back out of the detector depending on the deposited energy E_D to the minimal depth z_{min} that the the primary electron reaches. Shown are isolines of the probability. The further the primary electron scatters into the bulk, the more energy is deposited in the bulk. Summation of the probabilities in the z-direction leads to the spectrum of the backscattered electrons.

These trends in the probabilities are summarized in figure 7.11. The probability that the primary electron escapes depends on the minimum depth z_{min} and the deposited energy E_D. A summation of the probabilities in z-direction produces the shape of the energy spectrum for the back-scattered electrons:

$$p_{B1}(E) = \int p(z, E_D) dz \tag{7.9}$$

These principles and thus the shape of the energy spectrum of the back-scattered primary electrons apply for all energies. This can also be seen in figure 7.12, in which the energy spectra for multiple electron energies are compared.

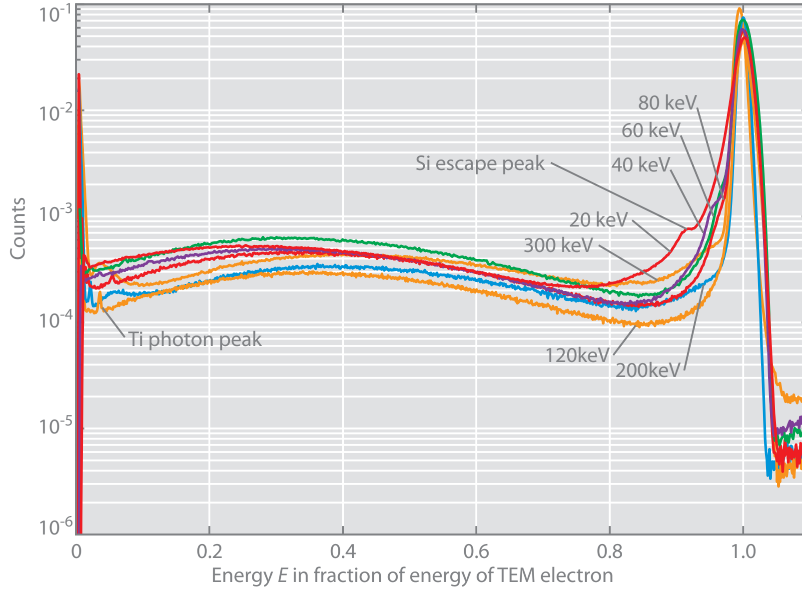

Figure 7.12: Energy spectra of one measurement series with the same settings from 20 keV to 300 keV. The counts for all spectra are normalized to one from 0.1 to 1.0 TEM electrons. All measurements were recorded with slightly different electron rates. The marked features (Ti photon peak, Si escape peak) are explained in section 7.1.4. See appendix A.10 for measurement details using the processing identifiers (PIDs): PID300_001, PID200_002, PID120_001, PID80_002, PID60_003, PID40_001, PID20_002.

7.1.3 *The Backscattering Coefficient*

The backscattering coefficient η is given by the ratio of number of TEM electrons that deposit only part of their energy in the detector to the number of incoming electrons.

$$\eta = \frac{N_{B1}}{N_{B1} + N_{F1}} \tag{7.10}$$

The calculation of the backscattering coefficient from experimental pnCCD data is sensitive to the energy limit E_{BF1} that differentiates an event of a backscattered TEM electron (B1) from an event with full energy deposition (F1). Additionally, the lower limit for the B1 events also influences the calculated backscattering factor. For a precise determination, these limits have to be chosen carefully. The backscattering coefficient depending on the energy limit is given in figure 7.13 for various energies of the TEM electron and one set of limits of $E_{B1,min} = 0.03$ and $E_{F1,max} = 1.05$. Depending on the choices of the energy limits, the monotonic decrease in the backscattering factor with increasing energy can be interrupted (e.g. for 200 keV and 300 keV). Nevertheless, the calculated values are in the order of the literature values[7] (see table 7.1), especially considering that the values in the literature are measured by detecting the backscattered electrons outside of the scattering material.

[7] Ito, Andreo, and Tabata, 1992; Reimer, 1998.

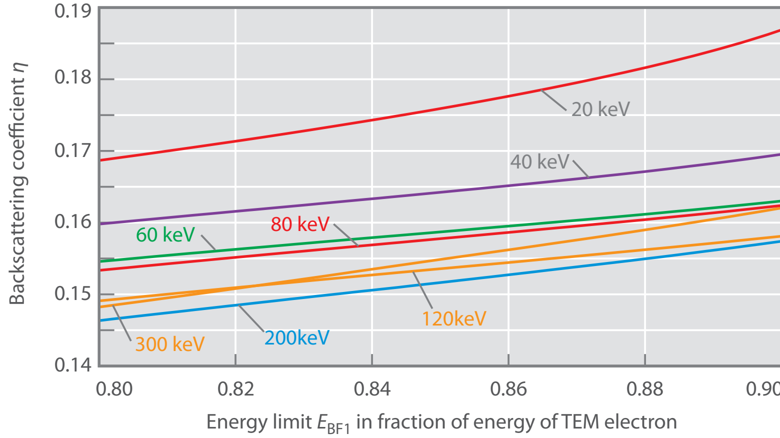

Figure 7.13: Backscattering coefficient η depending on choice of limit E_{BF1} that differentiates between B1 and F1 type of events. The lower limit for B1 events is $E_{\mathrm{B1,min}} = 0.03$ and the maximum limit for F1 events is $E_{\mathrm{F1,max}} = 1.05$ in fraction of the energy of the TEM electron. See table 7.1 for PIDs.

E keV	η_{exp} %	η_{Ito} %	processing identifier (PID)
20	17.1	16.7	PID20_003
40	16.2	15.7	PID40_001
60	15.6	15.2	PID60_003
80	15.5	14.8	PID80_002
120	15.1	14.2	PID120_001
200	14.9	13.4	PID200_002
300	15.1	12.7	PID300_001

Table 7.1: The backscattering coefficient η determined for the pnCCD for $E_{\mathrm{BF1}} = 0.82$. The literature values η_{Ito} were calculated with the empirical formula taken from Ito, Andreo, and Tabata, 1992.

7.1.4 *Photon Events*

The primary electron can generate photons while scattering in the silicon bulk as described in chapter 3.

The energy of photons that are created in silicon through atomic relaxation (see section 3.5) is below 1.9 keV. Photons with such low energies are absorbed in close proximity to the primary electron.[8] If the scattering of the TEM electrons occurs mostly near the front side, the characteristic X-ray photon of the silicon K transition ($E_{\mathrm{Si\,K}\alpha} = 1.73$ keV) can also escape the detector. The energy of the photon is then missing and a shifted energy peak is visible in the energy spectrum.

$$E_{\mathrm{Si}} = E_{\mathrm{F1}} - E_{\mathrm{Si\,K}} \tag{7.11}$$

This is the case for 20 keV TEM electrons, as can be seen in the energy spectrum shown in figure 7.14. For higher energies ($E > 60$ keV), the silicon escape peak is not separable from the F1 peak.

[8] The mass attenuation coefficient for silicon and a photon energy of 1.84 keV is 3192 cm²/g, resulting in 99.999 % absorption in a distance of 15 µm.

Photons generated through the Bremsstrahlung effect can have such a high energy that the probability is high enough that the photon is not absorbed in the silicon bulk in close proximity to the primary electron, but in some distance away. The events in figure 7.6, with an energy E_{D} below 2×10^4 adu, are events in which the primary electrons loose part of their energy through the creation of a photon with considerate energy through the Bremsstrahlung effect. For these events shown

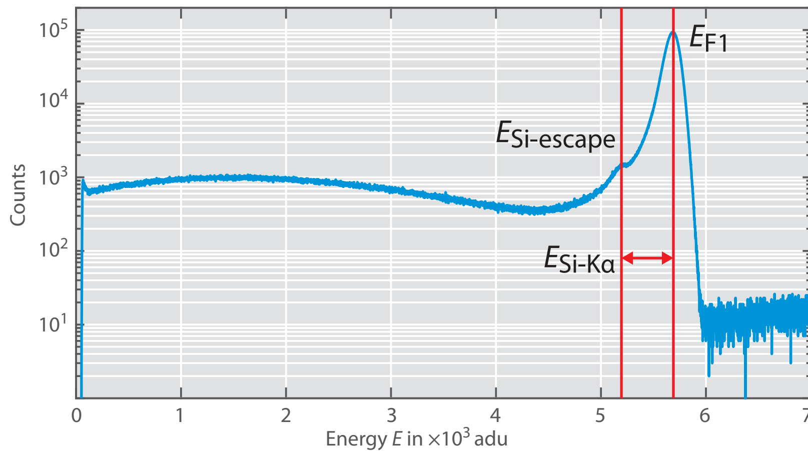

Figure 7.14: Silicon escape peak in a 20 keV measurement. The position of the F1 peak is at $E_{F1} = 5690$ adu and the silicon escape peak at $E_{Si} = (20\,\text{keV} - 1.73\,\text{keV}) \cdot (5690\,\text{adu}/20\,\text{keV}) = 5195$ adu. Measurement: PID20_002

in the spectrum, the created photon is not absorbed in the silicon in close proximity to the primary electron (see figure 7.15). The photon is absorbed in some distance and the pixels with signal due to the photon are not connected to the pixels with signal due to the primary electron. During the SEA, these two signal distributions are detected as two separate events (two B1 events). The sum of the energy of these two events equals the energy of the TEM electron.

Figure 7.15: One simulated electron event ($E = 80$ keV) in which a Bremsstrahlung photon is created. The photon is absorbed in the silicon bulk several pixel lengths away from the electron. The resulting signal distribution is recognized during the SEA as two B1 events.

$$E_{\text{tem}} = E_{\text{prim}} + E_{\text{photon}} \tag{7.12}$$

This can also be seen in figure 7.6 in the two separate clusters of counts around $E \approx 0.4 \times 10^4$ adu and $E \approx 1.8 \times 10^4$ adu with $E_{F1} \approx 2.2 \times 10^4$ adu. Events are also possible in which multiple photons are created and detected in separate events.

The probability for such photon events is low due to the low total cross section for Bremsstrahlung interaction at energies investigated here (see section 3.1 and figure 3.1). For a simulation with $E = 80$ keV without noise, 854 256 S1 events were generated and in only 0.0588 % of these events, one or more photons were created and detected as separate events.

Another X-ray peak can be seen at very low energies in the experimental energy spectra of TEM electrons with energies in the range of 80 keV to 300 keV (see figure 7.12 and for a detailed view at 120 keV in figure 7.16). The X-ray photons are generated by stray electrons that hit the material near the pnCCD. Directly near the entrance window is the cooling mask made up of titanium. The energy of the events contributing to this peak is approximately 4.5 keV which is the titanium K_α transition ($E_{K_\alpha} = 4.5$ keV).

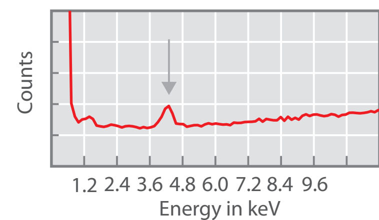

Figure 7.16: Titanium photon peak.

7.2 Pile-Up Events

When two TEM electrons enter the pnCCD in close proximity, they can scatter in such a way that the pixels with signal are connected or that the signal in pixels originates from both primary electrons (as illustrated in figure 7.17). In such a case, the electron tracks cannot be

separated and the primary electrons cannot be identified individually. The measured energy E_{pu} for such a pile-up event is the sum of both electrons' deposited energy. Generalized for k multiple primary electrons:

$$E_{\mathrm{pu}} = \sum_{i=1}^{k} E_{\mathrm{D}}(i) \tag{7.13}$$

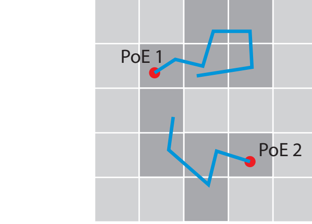

Figure 7.17: Two primary electrons create a signal which overlaps resulting in a pile up-event.

The energy spectrum for events originating from more than one TEM electron is explained based on the energy spectrum of the type S1 events. In the next section, a model of the energy spectrum for pile-up events is developed on the basis of simulation data. In the second section, experimental data is used for the verification of the model of pile-up energy spectra. In the third section, the influence of the electron rate and the energy of the TEM electrons on the probabilities of the occurrence for pile-up events is investigated.

7.2.1 *Energy Spectrum of Pile-Up Events*

The probability distributions $p_{\mathrm{S}n}(E_{\mathrm{tem}}, E)$[9] for pile-up events are a $(n-1)$-multiple convolution of the distribution of the single TEM electron event:

$$p_{\mathrm{S2}} = p_{\mathrm{S1}} * p_{\mathrm{S1}} \tag{7.14}$$

$$p_{\mathrm{S}n} = p_{\mathrm{S1}} * p_{\mathrm{S}n-1} \tag{7.15}$$

[9] For readability, the explicit dependence on E_{tem} is dropped in further uses of p_n

The distributions for the first four event types are shown in figure 7.18 in which the data for p_{S1} is calculated with a simulation ($E = 80\,\mathrm{keV}$).

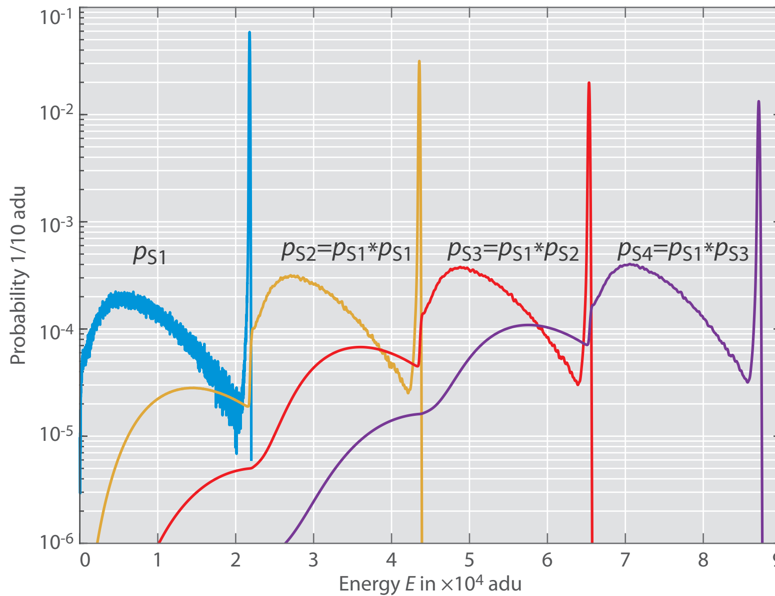

Figure 7.18: Energy spectrum for events of type S1 to S4. The probabilities for the events consisting of n multiple TEM electrons are calculated by a $(n-1)$-multiple convolution with p_{S1}. Simulation, $E = 80\,\mathrm{keV}$, no noise.

The different event types Sn do not occur with the same probability. The chance that the tracks of for instance four TEM electrons overlap is lower than the chance that the tracks of three TEM electrons overlap at low electron rates at which individual primary electrons can be distinguished.[10]The distributions are weighted with the probability $w_{\mathrm{S}n}$

[10] At higher electron rates, the SEA cannot be applied and hence there is no conventional energy spectrum of single TEM electrons.

that such an event occurs which depends on the electron rate r and the energy of the TEM electrons E_{tem}:

$$D_{Sn}(E_{\text{tem}}, r, E) = p_{Sn}(E_{\text{tem}}, E) \cdot w_{Sn}(E_{\text{tem}}, r) \tag{7.16}$$

The weighted distributions for an electron rate of $r = 0.004\,97\,\text{e}^-_{\text{tem}}/(\text{pix fr})$ and an energy of 80 keV are shown in figure 7.19.

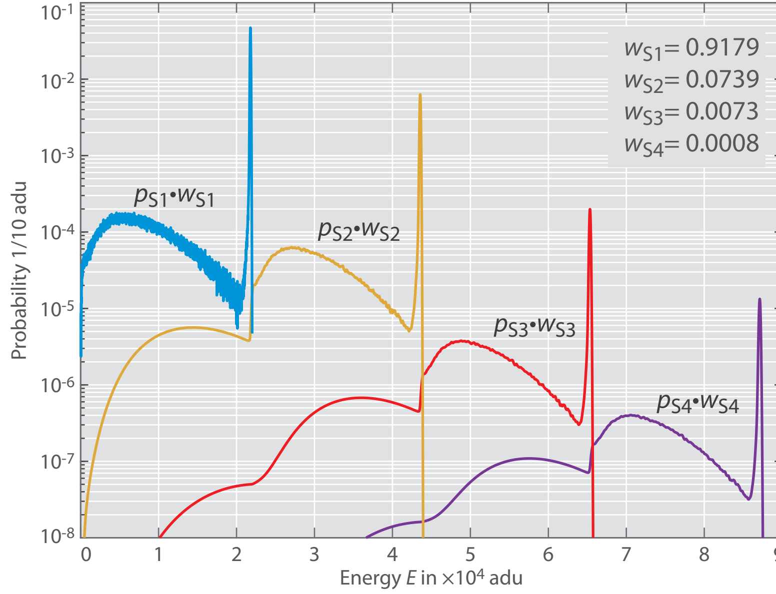

Figure 7.19: Weighted probabilities for the first four event types. The electron rate is $0.004\,97\,\text{e}^-_{\text{tem}}/(\text{pix fr})$. Simulation, $E = 80\,\text{keV}$, no noise.

The weighting factor depends on the energy of the TEM electron and the electron rate r. With a low electron rate, the chance is low that two or more electron tracks overlap. If the electron rate is held constant, a higher energy of the TEM electron results in a longer track length and thus a higher chance for multiple tracks to overlap. These dependencies are further investigated in section 7.2.3.

The full energy spectrum D_{total} is given by the sum of the probabilities over all event types.

$$D_{\text{total}}(E_{\text{tem}}, r, E) = \sum_n D_{Sn}(E_{\text{tem}}, r, E) \tag{7.17}$$

There is an non vanishing probability that an event resulting from multiple TEM electrons is not registered correctly with respect to the number of contributing TEM electrons. For example, two incoming primary electrons with overlapping tracks scatter out of the detector and deposit a sum energy that is lower than the energy of one TEM electron that deposits its whole energy:

$$E_D = E_{B1,1} + E_{B1,2} < E_{F1} \tag{7.18}$$

However, the overall contribution of such events to the sum energy spectrum is negligible. In figure 7.20, the cumulative probabilities ($\text{cdf}(p_n)$) of the first four events are shown.

$$\text{cdf}(f(x), x_i) = \sum_{x=x_0}^{x_i} f(x) \tag{7.19}$$

As can be seen by the indicated values, the cumulative probability for the case of counting two B1 type of events as one S1 is below 4 %. After weighting with the probability that two tracks overlap at an electron rate of $0.004\,97\,\mathrm{e}^-_{\mathrm{tem}}/(\mathrm{pix\,fr})$, the summed probability is below 0.3 %. The summed probabilities for the other event types before and after weighting are compiled in table 7.2 for an energy of 80 keV.

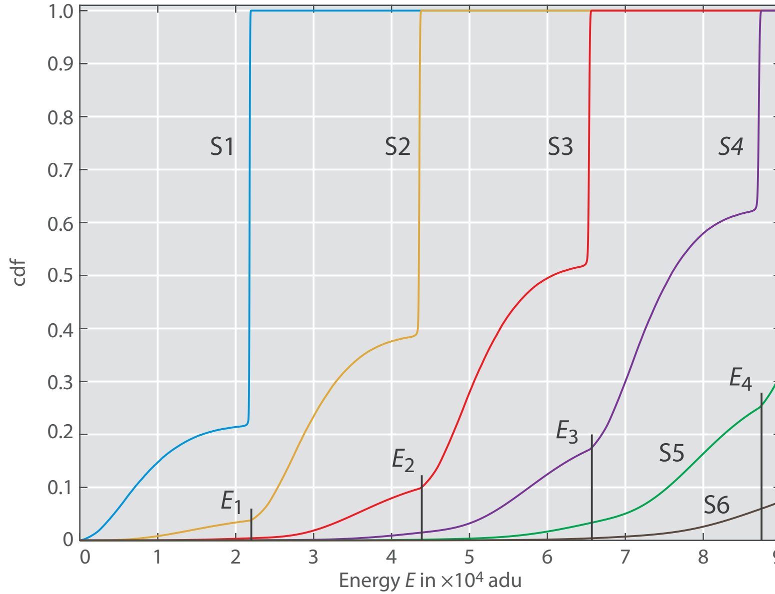

Figure 7.20: Cumulative non-weighted probabilities for the first six event types S1-S6. The indicated energies $E1$-$E6$ show the cdf value up to which the events are correlated with an incorrect number of TEM electrons. For example, for the S3 type of event (three TEM electrons), 10 % of the events have a deposited energy below the energy of the F2 type of event with two TEM electrons depositing their full energy. The cdf for each type must be weighted according to the electron rate to obtain the spectrum that is measured. Simulation: $E = 80\,\mathrm{keV}$, no noise and a gain of $1\,\mathrm{adu}/\mathrm{e}^-_{\mathrm{sig}}$.

n	E	$\mathrm{cdf}\,(p_{\mathrm{S}n}, E)$	$w_{\mathrm{S}n}(r_1)$	$\mathrm{cdf}\,(r_1)$	$w_{\mathrm{S}n}(r_2)$	$\mathrm{cdf}\,(r_2)$
	adu	%	%	%	%	%
2	22 005	3.84	7.39	0.283	18.63	0.715
3	22 005	0.41	0.73	0.003	6.08	0.025
3	44 005	10.22	0.73	0.075	6.08	0.622
4	44 005	1.50	0.08	0.001	2.13	0.032
4	66 005	18.02	0.08	0.014	2.13	0.384
5	66 005	3.44	0.01	0.000	0.83	0.029
6	66 005	0.42	<0.01	<0.001	0.32	0.001
5	88 005	26.49	0.01	0.003	0.83	0.026
6	88 005	6.26	<0.01	<0.001	0.32	0.020
electron rate $\mathrm{e}^-_{\mathrm{tem}}/(\mathrm{pix\,fr})$:			$r_1 = 0.004\,97$		$r_2 = 0.019\,87$	

Table 7.2: Cumulative probabilities without and with weighting for two electron rates extracted from simulated data of figure 7.20. The highlighted values correspond to the ones indicated in figure 7.20. For both electron rates, the weighted, summed probability that n multiple TEM electrons deposit less energy than $E_{\mathrm{F}n-1}$ is below 0.1 %.

For a confirmation of this model, the weighting factors are determined with the SEA from a simulation with an electron rate of $r = 0.004\,97\,\mathrm{e}^-_{\mathrm{tem}}/(\mathrm{pix\,fr})$. The probabilities for the single events (p_{S1}), the energy spectrum, are determined from a simulation with an electron rate of *one* TEM electron per frame, thus excluding any pile-up. The energy spectrum is then calculated via the steps described above, by convoluting the probabilities of the single event multiple times and weighting the results depending on the occurrences of multiple events.

The calculated energy spectrum reproduces the energy spectrum of the other simulation with the higher electron rate as shown in figure 7.21. Thus the model is shown to be valid. In the next section, the model is also applied to experimental data.

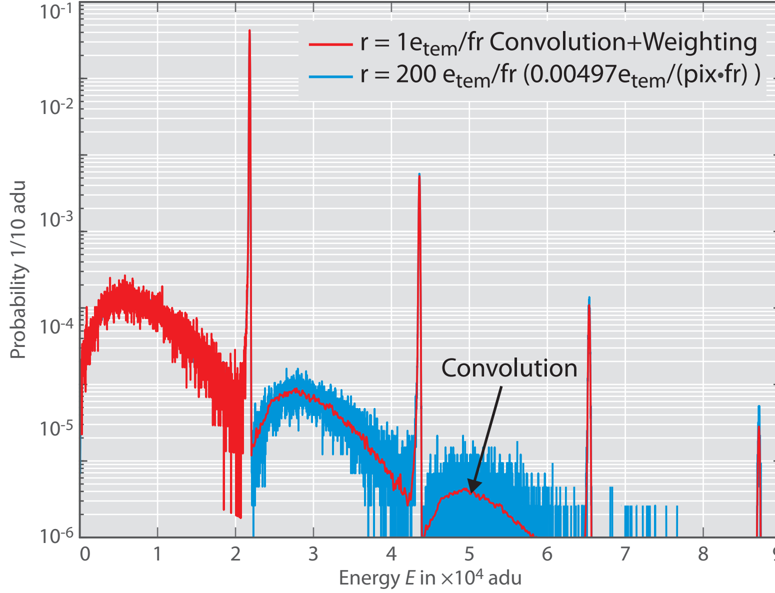

Figure 7.21: Comparison of convolution model with simulation of higher electron rate. The model is determined from a simulation with an electron rate of one TEM electron per frame. The weighting factors are determined from the simulation with the higher electron rate in which pile up occurs.

7.2.2 *Experimental Energy Spectrum of Pile-Up Events*

In this section, experimental data from two measurements at two different electron rates are used to demonstrate the validity of the signal response model. The energy of the TEM electrons is 80 keV. Pile-up events with up to ten TEM electrons can be seen in the energy spectrum of the measurement with the higher electron rate (see figure 7.22).

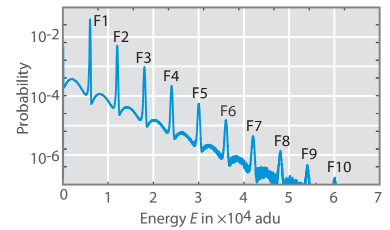

Figure 7.22: Energy spectrum of single TEM electrons at a high electron rate showing pile-up.

Compared to the simulation data without noise effects, a further analysis step is necessary. As will be shown in the following, the energy spectrum must be shifted by a small offset determined from the experimental data.

After the SEA, the first step is to determine the positions of the Fn type events. That is important, because these are the event types in which the TEM electrons deposit their full energy which can be used as a reference[11]. To each Fn peak, a single Gaussian function was fitted of type:

$$f_G(E, n) = A_{Fn} \cdot \exp\left(-\frac{(E_{Fn} - E)^2}{2\sigma_{Fn}^2}\right) \tag{7.20}$$

Each Fn peak in the energy spectrum is described by the fitting parameters: A_{Fn} is the amplitude, E_{Fn} is the position (the energy) and σ_{Fn} is the width.

In figure 7.23, the positions of the peaks are plotted as a function of the number of TEM electrons that contribute to an event. As expected,

[11] See also the next section 7.4.

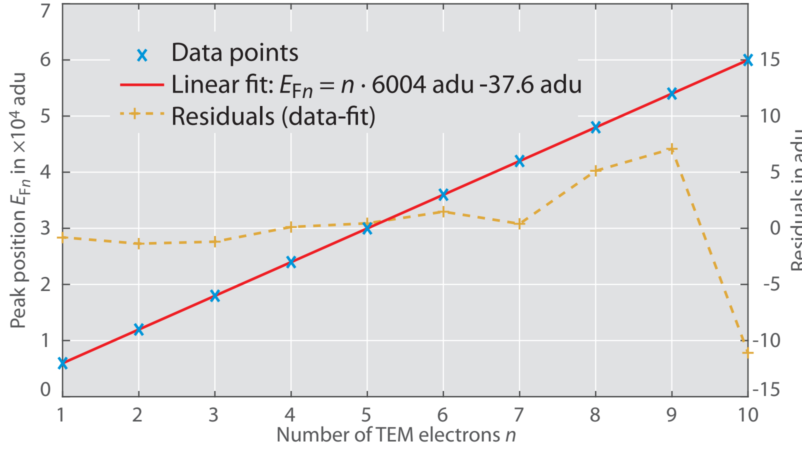

Figure 7.23: Fit of peak positions. Measurement: PID80_003

there is a linear dependency, shown by the good agreement of the linear function that is fitted to the data points:

$$E_{\mathrm{F}n} = n \cdot E_1 + E_{\mathrm{off}} \tag{7.21}$$

The fitting parameter E_{off} can be interpreted as an offset of the energy spectrum. The negative value means that the measured spectrum is shifted to lower energies. This offset originates from the fact that during the SEA, a threshold is applied to discriminate between noise and signal in the pixels. If there are signal electrons in the pixels that cause a readout signal below the threshold, such signal electrons do not contribute to the overall signal of the event. This lost part of the signal is part of the offset of the energy spectrum.

The peak positions in the energy spectra of both measurements were analyzed and then shifted with the method described above. From the measurement with the low electron rate, the part of the energy spectrum was used that contributes to the S1 type of events, providing the single TEM electron probability distribution $p_{\mathrm{S}1}$. This spectrum was then convoluted with itself 9 times, resulting in the distributions $p_{\mathrm{S}2}$-$p_{\mathrm{S}10}$. From the measurement with the high electron rate, the weighting factors $w_{\mathrm{S}n}$ for each event type Sn were determined. These weighting factors were then multiplied to each $p_{\mathrm{S}n}$ according to equation 7.16. Finally, the sum over all probability distributions results in the total energy spectrum. Both energy spectra, the one calculated from the measurement with the low electron rate and the one measured with the high electron rate are compared in figure 7.24. Again, both energy spectra match well confirming the model.

There are small deviations, especially at slightly higher energies after each of the Fn peaks. The deviations can probably be attributed to the fact that the energy spectrum used for the convolution is not from a measurement without pile-up events. Another factor might be different noise contributions in both measurements. The principle behind the generation of energy spectra with pile-up, however, is shown to be valid with a very good agreement between the model and the experimental data.

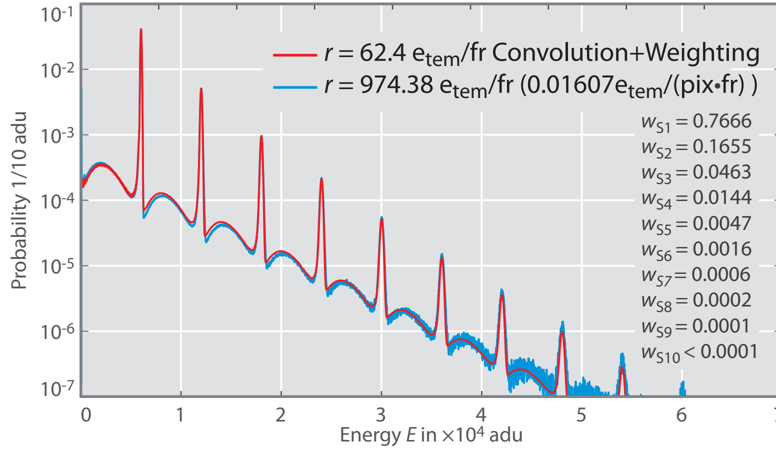

Figure 7.24: Comparison of convolution model with experimental data of low and high electron rate. Measurements: PID80_002 (low electron rate) and PID80_003 (high electron rate)

7.2.3 *Pile-Up Probability Dependencies*

In this section, the probabilities for the occurrence of the different event types are investigated. The pile-up rates depend on several parameters of the microscope and the detector: The electron rate r, the TEM electron energy E_{tem}, the readout frame rate f_{ro}, the readout noise n_{ro}, the back contact voltage of the pnCCD U_{bc} and the pixel size w_{pix}. The one parameter that is usually adjustable is the electron rate, since for a given experiment, the energy of the TEM electron is fixed. Several simulations were run in which these parameters were varied.

Considering the characteristics of electron scattering, the dependency on the relative probability p_{S1} for the S1 event is found to be:

$$\text{Readout rate:} \quad f_{\mathrm{ro}} \nearrow \Rightarrow p_{\mathrm{S1}} \nearrow \tag{7.22}$$

$$\text{Electron rate:} \quad r \nearrow \Rightarrow p_{\mathrm{S1}} \searrow \tag{7.23}$$

$$\text{Energy:} \quad E_{\mathrm{tem}} \nearrow \Rightarrow p_{\mathrm{S1}} \searrow \tag{7.24}$$

$$\text{Back contact voltage:} \quad U_{\mathrm{bc}} \nearrow \Rightarrow p_{\mathrm{S1}} \nearrow \tag{7.25}$$

$$\text{Readout noise:} \quad n_{\mathrm{ro}} \nearrow \Rightarrow p_{\mathrm{S1}} \nearrow \tag{7.26}$$

$$\text{Pixel size:} \quad w_{\mathrm{pix}} \nearrow \Rightarrow p_{\mathrm{S1}} \searrow \quad \text{with} \quad r = \text{const} \tag{7.27}$$

$$\text{Pixel size:} \quad w_{\mathrm{pix}} \nearrow \Rightarrow p_{\mathrm{S1}} \nearrow \quad \text{with} \quad r \cdot w_{\mathrm{pix}} = \text{const} \tag{7.28}$$

An increase in the readout frame rate f_{ro} effectively reduces the electron rate r, so the dependency on the readout frame rate is not explained separately but included implicitly in the electron rate. The second and third dependencies (7.23, 7.24) on electron rate and TEM electron energy are shown in figure 7.25. For a given energy E_{tem}, the probability p_{S1} decreases with increasing electron rate r, owing to the fact that the probability for overlapping tracks increases and events Sn with $n > 1$ become increasingly probable. The probability for doubles p_{S2} increases with increasing electron rate r up to around $p_{\mathrm{S2}} = 0.2$ and then decreases again. The decrease is due to the fact that there are so many TEM electrons per frame with overlapping

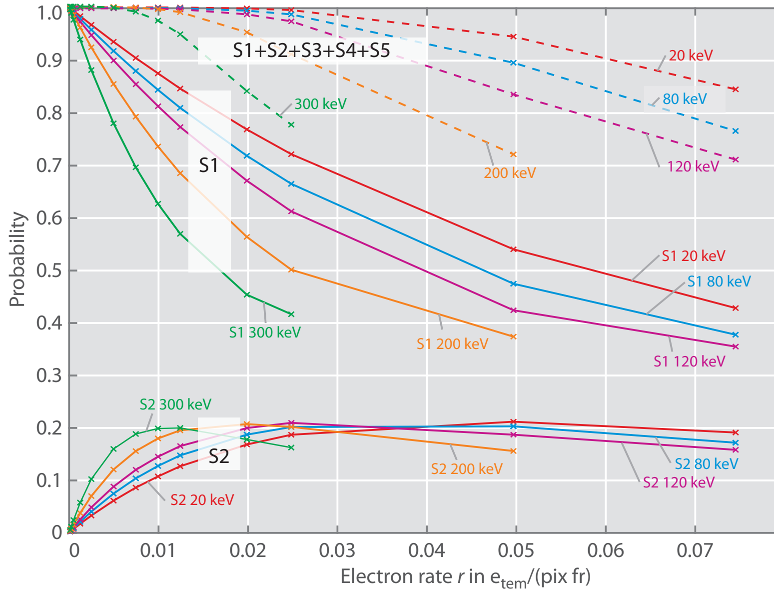

Figure 7.25: Dependency of pile-up probability on TEM electron rate for various energies. For each energy the probabilities are shown for the single event S1, the double event S2 and the sum of the events with one to five TEM electrons (S1-5) (dashed lines). The simulation was calculated with a pixel size of 48 µm, $U_{bc} = -240$ V and no noise.

tracks that the overall probability for singles, doubles and so on shifts to events with multiple TEM electrons in excess of five TEM electrons. This can be seen in the decrease of the *summed* probability $p_{S1\text{-}5} = p_{S1} + p_{S2} + p_{S3} + p_{S4} + p_{S5}$ for the first five Sn events.

Looking at the energy of the TEM electron, p_{S1} decreases with increasing energy for a given electron rate. A higher energy leads to a longer electron track which results in a higher probability that the tracks overlap (see also section 7.3). For example, at an electron rate of $r = 0.02\,\mathrm{e}^-_{\mathrm{tem}}/(\mathrm{pix\,fr})$, for $E_{\mathrm{tem}} = 300$ keV the probability for an event originating from a single TEM electron is below 50 %. At the same electron rate but at an energy of $E_{\mathrm{tem}} = 80$ keV, the probability is around 70 %. For a visual impression, a single frame for each energy is shown in figure 7.26.

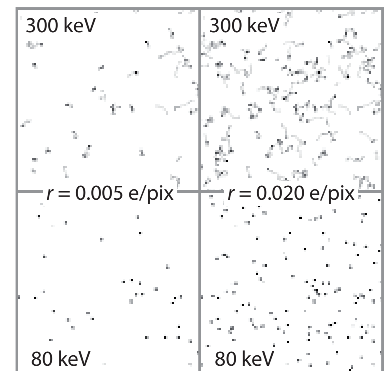

Figure 7.26: Comparison of single frames at two electron rates.

The consequence is that for measurements in which single electrons should be imaged, the electron rate must be much lower for electrons with a higher energy than for TEM electrons with a lower energy. For the comparison between 300 keV and 20 keV, to reach about the same occurrence of S1 events, the electron rate for 300 keV must be four times lower than the electron rate for 20 keV. To reach the same signal in the image with regard to the number of TEM electrons, a four times longer exposure is needed. This drawback can be compensated by increasing the readout rate, if possible.

The dependency on the back contact voltage and the readout noise are shown in figure 7.27. Both parameters influence the number of pixels with signal that belong to an event. If the back contact voltage is lowered, the drift time of the signal electrons from the point of their generation until they are collected in the pixel wells increases (see section 4.2). The longer drift time leads to a larger lateral diffusion of the signal electrons and thus leads to a greater number of pixels that belong to an event (see also section 7.3). Since there are more pixels with signal, the probability increases that these pixels connect

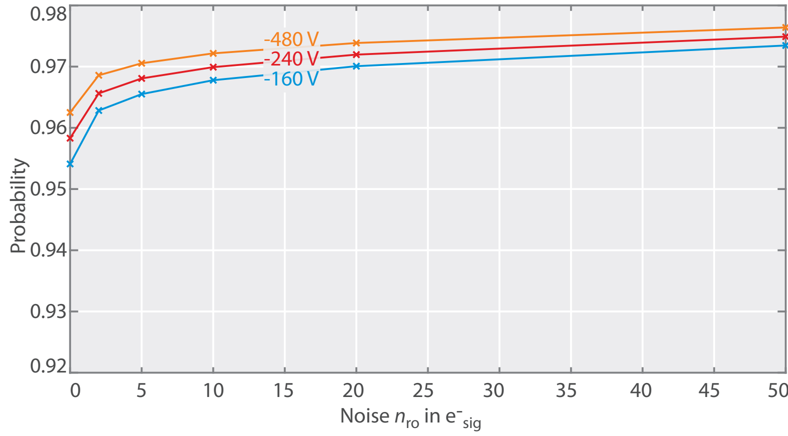

Figure 7.27: Probability for p_{S1} depending on readout noise n_{ro} and back contact voltage U_{bc} at an electron rate of $r = 0.002\,48\,e^{-}_{tem}/(\text{pix fr})$. Simulation at 80 keV.

or overlap with pixels from other events. Thus, the probability for S1 events decreases with a more positive back contact.

The readout noise has a similar effect on the number of pixels of an event. During the SEA, pixels with a signal below a certain threshold are considered to be pixels with only noise. This threshold is usually set to a multiple of the noise floor. Therefore, if the readout noise increases, more pixels are considered to just contain noise and are not associated to the pixels of an event, even though such pixels might contain signal from signal electrons. Thus the number of pixels of an event decreases with increasing noise.

The dependency of noise on the number of pixels of an event is also seen in the distributions of the number of pixels. For several noise values, the distributions of simulated data for $E_{tem} = 80$ keV are shown in figure 7.28. In the extreme case of no noise, the average

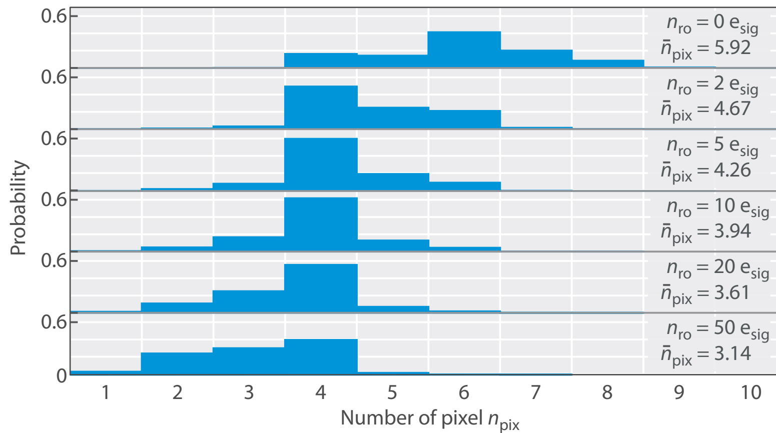

Figure 7.28: Distribution of number of pixels in the S1 event depending on noise. Simulation with 80 keV, $U_{bc} = -240$ V and a noise threshold multiplier of $\sigma = 6$. The average value $\bar{n}_{pix}$ decreases with increasing noise due to the increasing threshold that is on average $\sigma \cdot n_{ro}$.

value is $\bar{n}_{pix} = 5.9$ pix. With increasing noise, the average value decreases. At a typical value of $n_{ro} = 10\,e^{-}_{sig}$, $\bar{n}_{pix} = 3.9$ pix.

When varying the pixel size, there are two cases to distinguish. The electron rate is kept constant (equation 7.27) or the illuminated area A_{ill} is kept constant (equation 7.28). The illuminated area can be calculated with the pixel size w_{pix} and the number of pixel $n_{ill,pix}$ in

the illuminated area:

$$A_{\mathrm{ill}} = A_{\mathrm{pix}} \cdot n_{\mathrm{ill,pix}} \tag{7.29}$$

$$A_{\mathrm{pix}} = w_{\mathrm{pix}}^2 \tag{7.30}$$

The electron rate is usually given in units of $\mathrm{e}^-_{\mathrm{tem}}/(\mathrm{pix\,fr})$. Thus, if the number of TEM electrons per frame is kept fixed and the illuminated area is kept fixed, increasing the pixel size actually increases the electron rate because there are fewer pixels $n_{\mathrm{ill,pix}}$ in the illuminated area. The dependency on pixel size is shown in figure 7.29 for two TEM electron energies of 80 keV and 300 keV. At a constant number

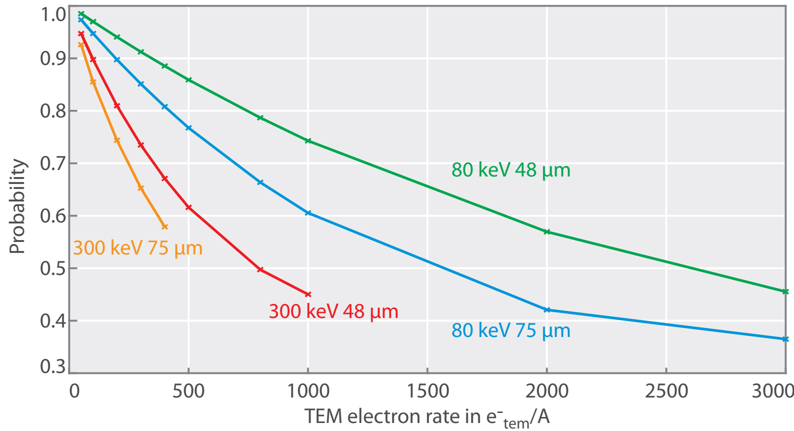

Figure 7.29: Dependency of pile-up on pixel size calculated from a simulation. The probability for the S1 event is shown. The illuminated area A_{ill} was kept constant ($n_{\mathrm{ill,pix}}(48\,\mu\mathrm{m}) = 40\,260\,\mathrm{pix}$, $n_{\mathrm{ill,pix}}(75\,\mu\mathrm{m}) = 16\,490\,\mathrm{pix}$). A noise of 10 adu was used, $U_{\mathrm{bc}} = -240\,\mathrm{V}$.

of electrons per illuminated area, the larger pixel size leads to a higher probability for pixels with signal to connect. Thus the probability for the S1 event decreases with increasing pixel size.

7.3 *Probability Distributions on Number of Pixels per Event*

Recalling the images of the single electrons at the beginning of this chapter (figure 7.1), it can be seen that the number of pixels in an event depends on the energy of the TEM electron. As the energy increases, the average track length increases and the signal is spread over more pixels. In figure 7.30 the distributions for the number of pixel per event for energies from 20 keV to 300 keV are shown for one series of measurements. The distributions for the S1 type (a single TEM electron) are shown as well as the contribution of the F1 type event (a single TEM electron that deposits its whole energy). At 20 keV, most events have signal in two to four pixels. As the energy increases, the maximum of the distribution shifts to more pixels (around 11 pixel at 300 keV) and the width of the distribution increases. The biggest contribution always comes from the F1 type events, since the F1 type events make up around 85 % of the S1 events (see section 7.1.2). The difference between the S1 and F1 distribution at the lower number of pixels is made up by the B1 events. The B1 events scatter in the detector over a shorter distance and hence spread their signal over fewer pixels than the primary electrons of the F1 events.

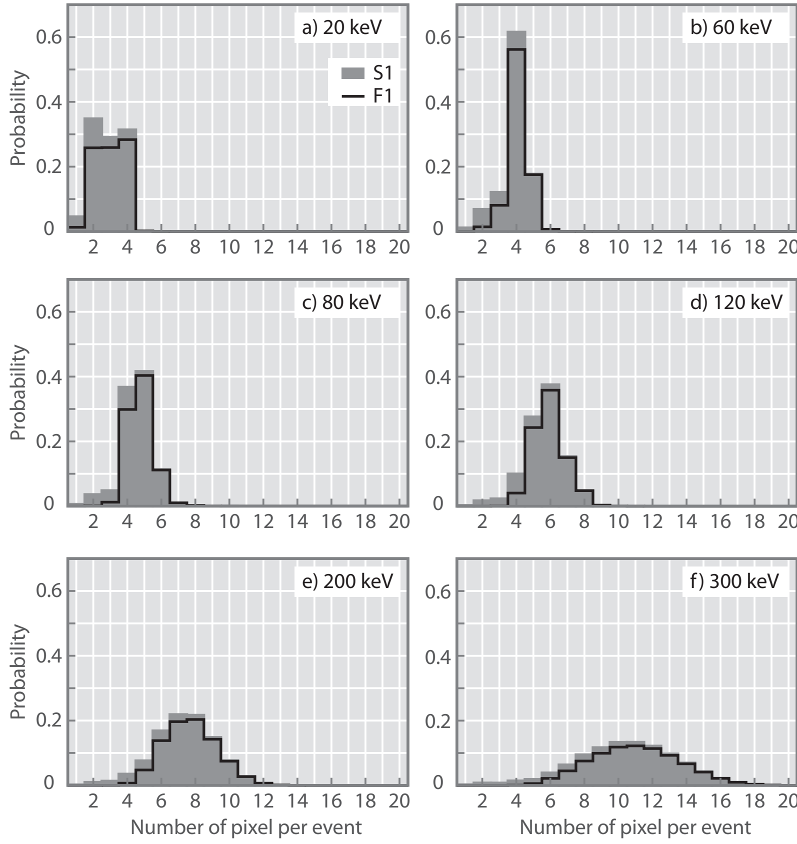

Figure 7.30: Number of pixel per event distributions. The average number of pixels per S1 event $\bar{n}_{pix}$ decreases with decreasing energy of the TEM electron. The black line shows the contribution of the F1 type event. All measurements were recorded with the same back contact voltage $U_{bc} = 420\,V$.

The average number of pixel $\bar{n}_{pix}$ in an event is calculated for each event type by:

$$\bar{n}_{pix} = \sum p_{pix}(i) \cdot i \tag{7.31}$$

The results are summarized in table 7.3 including the electron rate for each measurement. The distribution for all events Sn depends also on the pile-up probability. An increasing probability that the signal distributions of multiple TEM electrons overlap results in an increase of the probability for a larger average number of pixels per event.

Energy	$\bar{n}_{pix}$			r	PID
	S1	F1	Sn		
keV	pix	pix	pix	$e^-_{tem}/(\text{pix fr})$	
20	2.9	3.0	2.9	0.001 00	PID20_001
40	3.5	3.7	3.6	0.002 04	PID40_001
60	3.9	4.1	4.0	0.001 31	PID60_003
80	4.5	4.8	4.6	0.001 17	PID80_001
120	5.6	5.9	5.8	0.001 32	PID120_001
200	7.4	7.7	7.5	0.001 16	PID200_001
300	10.4	11.0	10.8	0.000 92	PID300_001

Table 7.3: The average number of pixels in an event for various electron energies. In each analysis, the limits for for the event types are 0.05, 0.9 and 1.05 in fraction of the TEM electrons' energy.

For the data series in figure 7.30, the back contact voltage U_{bc} has been kept fixed at $-420\,V$. The back contact voltage influences the

signal spread and hence the number of pixels per event as explained in section 7.2.3. The number of pixel distributions for two voltages (-240 V and -420 V) are compared in figure 7.31 and in table 7.4 for a TEM electron energy of 60 keV. The average number of pixels

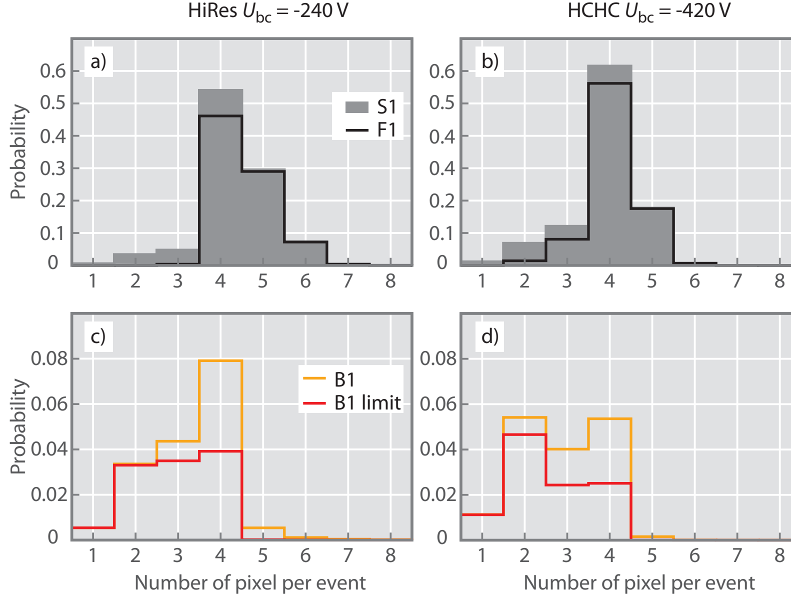

Figure 7.31: Comparison of distributions of the number of pixel per event for the HiRes and HCHC mode ($E = 60$ keV). In c) and d) the contributions from the B1 events are shown as well as the lower energy part of B1 (B1 limit; The limit in fraction of the energy of one TEM electron is 0.05 to 0.50).

per S1 event decreases from 4.3 pixel at $U_{bc} = -240$ V to 3.9 pixel at $U_{bc} = -420$ V. The difference in the average number of pixel might

Op-mode	U_{bc}	$\bar{n}_{pix}$				Noise	PID
		S1	F1	B1	B1 limit		
	V	pix	pix	pix	pix	e^-_{sig}	
HiRes	-240	4.3	4.5	3.3	3.0	14.99	PID60_001
HCHC	-420	3.9	4.1	2.9	2.6	15.68	PID60_003

Table 7.4: Comparison on the average number of pixels in an event between the HiRes and HCHC operation mode ($E = 60$ keV). In each analysis, the limits for for the event types are 0.05, 0.9 and 1.05 in fraction of the TEM electrons' energy.

not look significant. But an important difference can be seen in the distributions of the B1 event and especially the lower energy half of the B1 event (B1 limit: Events of backscattering TEM electrons that deposit an energy in the range of 0.05 to 0.50 of the energy of the TEM electron). At $U_{bc} = -420$ V (figure 7.31d) the probability for two pixels is the highest one. At $U_{bc} = -240$ V (figure 7.31c) the probabilities for two, three and four pixels is approximately the same for the B1 limit events. The number of pixels per event is important for the calculation of the PoE of individual TEM electrons. If there are only two pixels in one event, one coordinate direction is only one pixel wide (see figure 7.32).

The maximum spatial precision in that direction is then limited to an area where the TEM electron might have entered and oppositely, where it could *not* have entered. This area depends mainly on the energy of the TEM electron and the back contact voltage. For X-ray

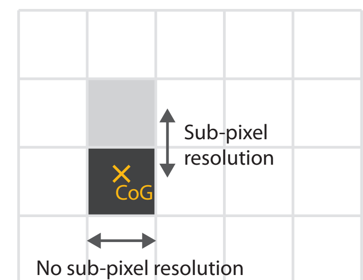

Figure 7.32: An event with two pixels has a sub-pixel resolution in only one direction.

photons, this case has been investigated in detail.[12] For practical purposes, in this work, the PoE is put at the center. As will be shown in the next chapter 8, the number of pixels per event should be maximized for a good sub-pixel spatial resolution. This is why the back contact voltage is set to $-240\,\mathrm{V}$ in the HiRes operation mode (see section 4.5.1).

[12] Ihle et al., 2017.

7.4 *The Calibration Factor*

The digital readout signal can be calibrated with the energy spectra and the known energy of the TEM electrons. The calibration factor C_{eV} converts the intensity values in units of adu into energy units eV. The calibration factor is calculated by fitting a Gaussian function to each peak of the events with full energy depositions (Fn), as described in section 7.2.2. The position of the peaks in terms of energy is fitted with a linear function. For convenience, both functions are repeated here:

$$f_{\mathrm{G}}(E,n) = A_{\mathrm{F}n} \cdot \exp\left(-\frac{(E_{\mathrm{F}n} - E)^2}{2\sigma_{\mathrm{F}n}^2}\right) \tag{7.32}$$

$$E_{\mathrm{F}n} = n \cdot E_1 + E_{\mathrm{off}} \tag{7.33}$$

The fit parameter E_1 represents the signal in adu that is readout for a deposited energy equal to the energy of one TEM electron. The calibration of the intensity in units of eV is then given by:

$$C_{\mathrm{eV}} = \frac{E_1}{E_{\mathrm{tem}}} \tag{7.34}$$

$$[C_{\mathrm{eV}}] = \frac{\mathrm{adu}}{\mathrm{eV}} \tag{7.35}$$

7.5 *The Conversion Factor*

It is of interest to know the number of TEM electrons that contribute to the intensity that is measured in single or multiple frames that were recorded with a high electron rate. For such images, a SEA is not possible and the TEM electrons cannot be *counted* individually. The number of detected TEM electrons is given by the conversion factor C_{tem} that converts the intensity in an image into a number of TEM electrons. A simple division of the sum intensity by the energy E_1 underestimates the number of TEM electrons, since there is also a considerate number of back scattered electrons that only deposit part of their energy. The correct value is provided by the *average* response to a single TEM electron that is calculated by the expectation value of the probability distribution for the S1 event:

$$C_{\mathrm{tem}} =< p_{\mathrm{S1}} > \tag{7.36}$$

$$= \sum_{E_{\mathrm{B1,min}}}^{E_{\mathrm{F1,max}}} p(E) \cdot E \tag{7.37}$$

$$p(E) = \frac{1}{\sum N(E)} N(E) \tag{7.38}$$

Alternatively, the average over all Sn type of events can be used:

$$C_{\text{tem}} = \sum p(E) \cdot E \cdot \frac{1}{M(E)} \tag{7.39}$$

The conversion factor C_{tem} is the average signal in units of adu that is generated by one TEM electron.

$$[C_{\text{tem}}] = \frac{\text{adu}}{\text{e}^-_{\text{tem}}} \tag{7.40}$$

7.6 *The Detective Quantum Efficiency*

A figure of merit characterizing the transfer of an input signal to an output signal of a detector is the detective quantum efficiency (DQE). The DQE describes how much a noisy input signal has deteriorated at the output of a detector. It is given by the square of the ratio of the signal to noise ratio (SNR) of the output (SNR_{out}) to the SNR of the input (SNR_{in}):[13]

[13] Reimer and Kohl, 2008, p. 132.

$$\text{DQE} = \frac{\text{SNR}^2_{\text{out}}}{\text{SNR}^2_{\text{in}}} \tag{7.41}$$

A perfect detector would have a DQE of 1, thus not impairing the input signal. For the pnCCD, the main effect to the DQE is the variance in the deposited energy for each TEM electron caused by the possibility of back-scattered electrons.

The input signal can be assumed to be Poisson distributed. In this case the DQE can be calculated from the energy spectra:[14,15]

[14] McMullan et al., 2009.

[15] See appendix A.2 for the derivation.

$$\text{DQE} = \frac{(\sum E \cdot p(E))^2}{\sum E^2 \cdot p(E)} = \frac{< p_{\text{S1}} >^2}{\sum_{E_{\text{B1,min}}}^{E_{\text{F1,max}}} E^2 \cdot p(E)} \tag{7.42}$$

The DQE was determined from various experimental measurements at energies from 20 keV to 300 keV. The values are compiled in table 7.5. For all energies the DQE is above 0.93. Thus the input SNR is

Energy keV	DQE	PID
20	0.93	PID20_001
60	0.93	PID60_001
80	0.94	PID80_001
120	0.94	PID120_001
200	0.94	PID200_001
300	0.94	PID300_001

Table 7.5: The DQE for various electron energies.

transferred well without significant deterioration to the output of the detector.

As a remark, the DQE values presented here apply to images recorded in the intensity imaging mode in which a distinction between single TEM electrons is not possible. If the electron rate is low enough,

however, the SEA will detect each single TEM electron that deposits enough energy above a certain threshold removing the variability in the signal response caused by back-scattered electrons. In that case the DQE is limited by the readout noise with values > 0.99. This case is investigated in section 6.3 with the help of simulations.

The DQE calculated in this section refers to the spatial frequency independent DQE(0). In future work, the DQE calculation can be extended to include the dependence on the size of the features imaged, called DQE(w).[16,17]

[16] McMullan et al., 2009.

[17] See section 8.1 for more on spatial frequencies.

7.7 *Energy Resolution of the pnCCD under Electron Illumination*

With the SEA, an energy spectrum is created of the energy that is deposited by the TEM electrons in the detector. Due to the possibility of backscattering electrons, not only a peak at the energy of the TEM electron is recorded but also a broad continuous distribution with lower energies, though at a lower probability. However, a meaningful energy resolution can be derived for the F1 peak by calculating its full width at half maximum (FWHM).

The width of the F1 peak depends mainly on the energy of the TEM electrons and on the correction of the raw frames data. A good correction of gain and common mode (see section 5.2) result in better energy resolutions.

FWHMs of the F1 type event are compiled in table 7.6 for various TEM electron energies and measurements. For comparison, the width σ_{Fano} due to pure Fano statistics[18] as a lower limit is also included:

[18] See section 3.6

$$\text{FWHM}_{\text{Fano}} = 2.35 \cdot w \cdot \sigma_{\text{Fano}} \tag{7.43}$$

$$= 2.35 \cdot \sqrt{0.115 \cdot w \cdot E_{\text{tem}}} \tag{7.44}$$

$$\text{with} \quad w = 3.67\,\text{eV}$$

Energy	FWHM	$2.35 \cdot \sigma_{\text{Fano}}$	FWHM/E	PID
keV	eV	eV	%	
20	538	216	2.7	PID20_003
40	874	305	2.2	PID40_001
60	975	374	1.6	PID60_005
80	1819	432	2.3	PID80_002
120	2281	529	1.9	PID120_001
200	2657	683	1.3	PID200_002
300	4278	836	1.4	PID300_002

Table 7.6: Energy resolution given by the FWHM of the F1 energy peak. For comparison, the FWHM due to pure Fano statistics calculated with equation 7.44 is given.

The widths of the F1 peak increases with increasing energy of the TEM electron as expected from equation 7.44. The experimentally measured widths are higher than the ones due to pure Fano statistics. A larger FWHM than theoretically possible is caused by the scattering of the primary electrons including the backscattered

ones, the contributions of the readout noise sources and the non perfect corrections. Nevertheless, the achievable energy resolution provides enough precision to determine the characteristic response of the pnCCD for TEM electrons as shown in this chapter. Even more important, as opposed to detectors that only count TEM electrons, the pnCCD provides spatial data with a sufficient energy resolution that is essential to reconstruct the point of entry of single TEM electrons (see next chapter 8).

For spectroscopy on the TEM electrons that leave the sample, the energy differences that are of interest in EM and that must be detected are in the range of a few eV to a few keV. Even a perfect detector cannot achieve this energy resolution by directly measuring the energy as shown by the Fano statistics. For these kinds of measurements, energy dispersive methods must be applied (see section 3.9.4).

For future experiments that require the precise determination of the energy of the TEM electrons, the calculation method and experimental verification of the gain map should be a topic to look into for further improvements.

7.8 *Summary on the Signal Response*

The signal response of the pnCCD to electron illumination has been explained in this chapter. It was shown that the energy spectrum is comprised of a part that originates from TEM electrons that deposit their whole energy in the detector and of a part that originates from TEM electrons that deposit only a portion of their energy. The whole spectrum can be described with a model, in which the probability distribution for single TEM electrons is convoluted with itself multiple times and the different events with multiple TEM electrons are weighted according to the probability of their occurrence. The weighting factors mainly depend on the energy of the TEM electrons, the electron rate, the pixel size and the back contact voltage. The measurement of the energy spectrum for only single events with a very low electron rate thus provides all the data necessary to describe signal responses at different electron rates.

The calibration factor and the conversion factor can be calculated with the energy spectra data. The calibration factor relates the digital readout units adu to energy units of eV, thus calibrating the energy spectra. The conversion factor provides the average response in units of adu to a single TEM electron, providing a measure to determine the number of TEM electrons in intensity images.

8 Spatial Resolution in Single Electron Imaging

Each electron that enters the pnCCD scatters in the sensitive volume. The resulting signal distribution over several pixels can be used to determine the point of entry (PoE) of single electrons with a higher precision than given by the physical pixel size.

Four models for the calculation of the PoE are investigated in this chapter. The applicability of each model depends on the energy of the TEM electrons. The first one is applicable to all energies (Center of Gravity (CoG) model, section 8.3.1). The second and third model (Gauss and Eta model, section 8.3.2 and 8.3.3) are applicable for lower energies, especially for $E \leq 80\,\mathrm{keV}$. These two models assume a Gaussian like distribution of signal electrons in the pixels which is often not the case for long electron tracks of energies above 120 keV. Complementary, the fourth model (long track furthest pixel away (LTFPA) model, section 8.3.4) improves the PoE determination for higher energies, especially 300 keV. With the Gauss and Eta model, sub-pixel spatial resolutions can be achieved. For the moment, with the LTFPA model, no sub-pixel resolution is achieved, however, the image contrast is increased. To determine the PoE for the higher electron energies better than the physical pixel size a more detailed analysis is required.

The chapter starts with a description on how the spatial resolution is measured in experiments and how it is expressed with the modulation transfer function (MTF) (section 8.1). As a reference, the MTF is calculated for intensity images without sub-pixel resolution created in the IIM (section 8.2). Further descriptive measures for the PoE models are introduced (section 8.3) before each model is explained and applied to experimental data. Finally, the results of the models and their applicability are discussed (section 8.4).

8.1 Quantification of Spatial Resolution

The spatial resolution of a pnCCD under electron illumination is quantified with the MTF, which describes how much contrast from an object is transferred by an imaging system to a final image. Each imaging system introduces a decrease in contrast, which depends on the projecting optics and the detector characteristics. Additionally, the transferred contrast depends on the object's structures sizes. Usually less contrast is transferred with decreasing structure size. Therefore,

the MTF is given in dependence of spatial frequencies ω.[1] The unit for spatial frequency is given in fraction of the Nyquist frequency ($1\,\mathrm{Ny} = 1/(2\,\mathrm{pix})$).[2]

[1] See appendix A.1 for further graphical explanations of the MTF.

[2] Shannon, 1949.

Other widely used measures for spatial resolution are the point spread function (PSF), the line spread function (LSF) and the the edge spread function (ESF). Assuming a Gaussian function for the PSF, all four functions can be expressed as:[3]

[3] McMullan et al., 2009.

$$\mathrm{PSF_G}(r) = \frac{1}{\pi\lambda^2}\exp(-r^2/\lambda^2) \tag{8.1}$$

$$\mathrm{LSF_G}(x) = \frac{1}{\pi\lambda}\exp(-x^2/\lambda^2) \tag{8.2}$$

$$\mathrm{ESF_G}(x) = \frac{1}{2}\mathrm{erfc}(-x/\lambda) \tag{8.3}$$

$$\mathrm{MTF_G}(\omega) = \exp(-\pi^2\lambda^2\omega^2/4) \tag{8.4}$$

$$= \mathcal{F}\left(\mathrm{LSF_G}(x)\right) \tag{8.5}$$

The PSF is rotational symmetric with $r^2 = x^2 + y^2$ and the length parameter λ given by $\mathrm{PSF_G}(r = \lambda) = 1/e\mathrm{PSF_G}(0)$. Visually speaking, the parameter λ defines how sharp or pointlike the PSF appears.

The MTF is the Fourier transform of the LSF. The LSF is the extension of the PSF in one direction. The ESF is an extension of the LSF in orthogonal direction. The relationships between the PSF, LSF and ESF are shown visually in figure 8.1. The MTF is chosen for the quantification of spatial resolution because imaging a sharp edge representing the ESF is experimentally viable. On the other hand, generating a stable spot illumination smaller than a pixel with such a low electron rate that single electrons are imaged has shown experimentally very difficult.

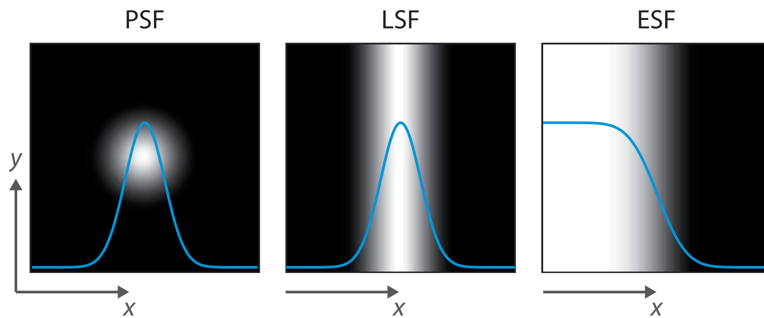

Figure 8.1: Relationship between the PSF, LSF and ESF. The overlaid curves are the intensity profile in left-right direction. The LSF is the derivative of the ESF. The LSF is an extension of the PSF in one direction. The parameter λ in equations 8.1 to 8.4 determines the sharpness of the ESF and the width of the PSF.

For the experimental data of this thesis, a region in the image is chosen that is blocked from electron illumination by the cooling mask (see figure 8.2). The edge is slightly slanted with respect to the pixel geometry resulting in a sampling of the edge at all positions inside a pixel dimension. The ESF is fitted to the edge.[4] The fitting parameter λ_{fit} determines the MTF. A larger λ translates to a less sharp edge and poorer spatial resolution. All data is in reference to the physical pixel size, so that different sub-pixel resolutions s can be compared.

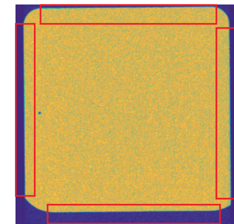

Figure 8.2: The sharp edges used in the determination of the MTF.

[4] The detailed MTF calculation procedure is given in appendix A.1.

$$\lambda = \frac{\lambda_{\mathrm{fit}}}{s} \tag{8.6}$$

Measuring the spatial resolution for single TEM electrons is more complex as two cases have to be discriminated: 1) For events originating from a single TEM electron (S1) or 2) for events originating from single *and* multiple TEM electrons (S1,S2,...). The PoE of S1 events can be determined with a higher precision. The PoE for Sn with $n > 1$ is the average of two or more TEM electrons. Ideally to measure the spatial resolution of the S1 events, the electron rate would be so low that the chance of events originating from multiple TEM electrons is negligible. However, in real applications, the electron rate is usually higher, so that there are always events originating from multiple TEM electrons. As a compromise, in this thesis, the MTF is calculated from all events and the electron rate is stated (see the data reference in appendix A.10).

Using only the S1 events from data with Sn events does not provide the same data as images with very low electron rate with only S1 events. The reason is that the average electron rate at the edge is lower and therefore the probability for S1 events is higher at the edge, which might influence the calculation of the MTF. As a consequence, all event types are used to create the image from which the MTF is determined.

8.2 *Spatial Resolution in Intensity Imaging Mode*

As a reference, the MTF is determined from intensity images without using further processing. In figure 8.3 a detail of the intensity images is shown for each energy. In figure 8.4 a comparison of the MTF at

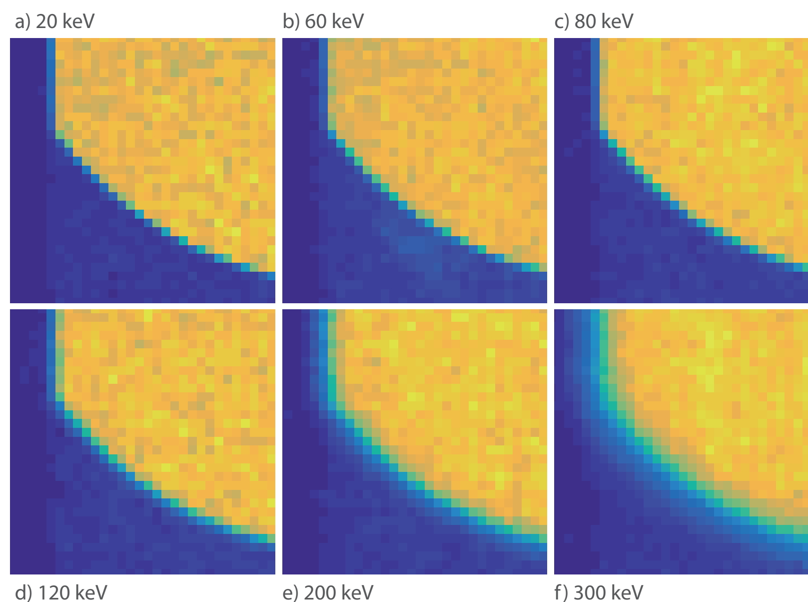

Figure 8.3: Detail of intensity images at energies from 20 keV to 300 keV. With increasing energy of the TEM electrons the edge appears increasingly diffuse.

various TEM electron energies is shown (for the fitting parameter λ_{fit} see table 8.1). The contrast of the edge increases with decreasing energy of the TEM electrons. This is a direct consequence of the

shorter track length of the lower energy electrons. At high TEM electron energies, the primary electrons scatter in the detector volume covered by the cooling mask. Hence, the edge appears blurry by a few pixels. The range of the scattering is a few pixels, which results in a diffuse edge. This effect is visually seen in figure 8.3d-f). The

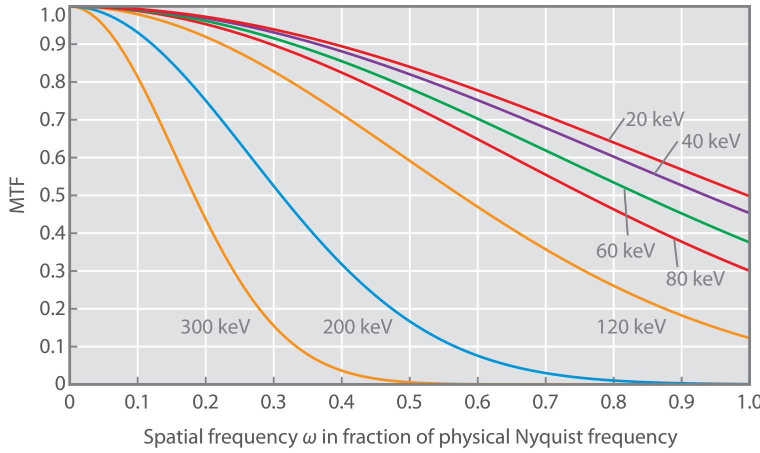

Figure 8.4: Comparison of the MTF at various energies in intensity imaging mode.

MTF shows a corresponding sharp drop, especially at 300 keV and 200 keV.

Visually, there is not much difference in the images in figure 8.3 for 20 keV, 60 keV and 80 keV. However, the MTF does show a greater contrast.

8.3 *Point of Entry Models*

Apart of the MTF, another key figure for the performance of each model is the distribution of the decimal part of x and y coordinates of PoEs over the dimensions of the physical pixel. Under homogenous illumination, each pixel area should be hit with an equal probability. Theses probabilities are expressed as the probability density function (pdf) and the cumulative distribution function (cdf):

$$\mathrm{pdf}(x) = P(a \leq X \leq b) = \int_a^b f_X(x)\mathrm{d}x \quad (8.7)$$

$$\mathrm{cdf}(c) = P(-\infty < X \leq c) = \int_{-\infty}^c f_X(x)\mathrm{d}x \quad (8.8)$$

$$a = x - \mathrm{d}x, b = x + \mathrm{d}x$$

$$x \in [0, 1]$$

The pdf describes the probability that the position of an event is in an interval $[a, b]$. The cdf describes the integrated probabilities up to a limit c.

In figure 8.5, the ideal pdf and the cdf are shown under homogeneous illumination. Each pixel area is hit with the same probability. After the SEA, the distributions of the calculated PoEs should be equal to the ideal ones. However, the measured (experimental) data deviates from the ideal curve in a systematic way for the models for each of the PoE models. Note that the models introduced in this

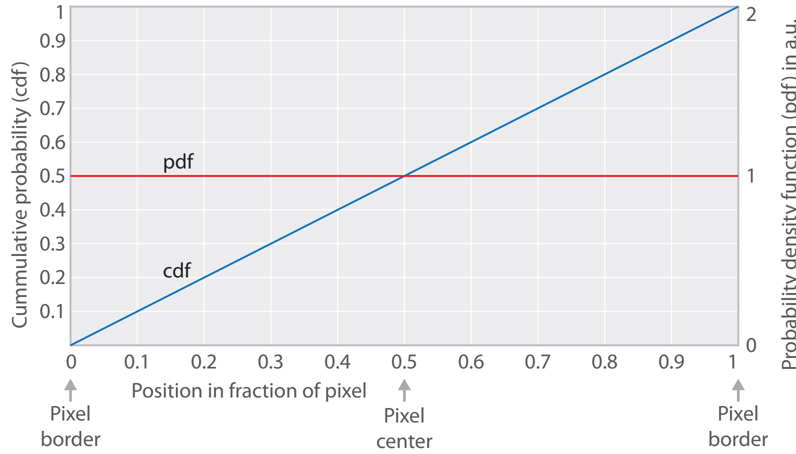

Figure 8.5: Ideal cdf and pdf of PoE positions under homogenous illumination. The convention is chosen such that the center of a pixel is at $x = 0.5$ and the borders are at $x = 0$ and $x = 1$.

chapter apply only to S1 events improving only the spatial resolution of the S1 events. Since S1 events are the most probable ones ($> 80\,\%$), the influence of S1 events is dominant to the overall spatial resolution in images using all events.

8.3.1 *Center of Gravity Method*

The standard method to determine the PoE coordinate $R_{\text{CoG}}\,(x, y)$ of an event is to calculate the weighted centroid of the pixels of the event that contain signal. This method is called Center of Gravity (CoG) method.

$$x = \frac{1}{T} \sum_{k=1}^{n} S_k \cdot x_k \tag{8.9}$$

$$T = \sum_{k=1}^{n} S_k \tag{8.10}$$

with S_k the signal in pixel k, x_k the x-coordinate of the pixel k (likewise for the y-coordinate) and T is the total signal of the event.

The calculated distribution of the position of the CoG inside a pixel is not homogeneous under homogeneous illumination (see figure 8.6).

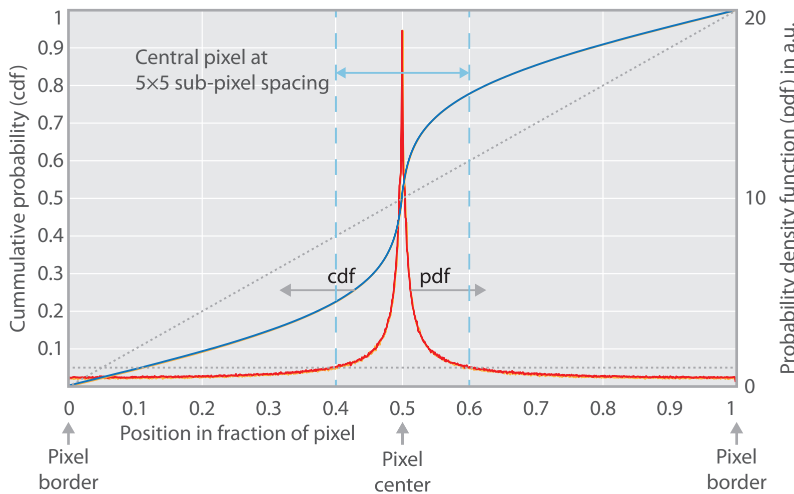

Figure 8.6: Distribution of the position of the CoG over the pixel geometry calculated according to equations 8.7 and 8.9 from simulated electrons ($E = 20\,\text{keV}$) without any noise. Both x and y directions show the same distribution. The cdf exhibits a S-shape, corresponding to the peak in the pdf at $x = 0.5$. The dotted lines show the ideal cdf and pdf under homogenous illumination where each position has the same probability to be hit.

A straightforward calculation yields a systematic error that needs

to be corrected.As an example under optimal conditions without noise, figure 8.6 shows the cdf and pdf for simulated data at 20 keV. With the CoG method, the calculated PoEs are shifted towards the centers of the physical pixels compared to the actual PoE. The same characteristic is seen in experimental data, for example at 20 keV and 60 keV (see figure 8.7).

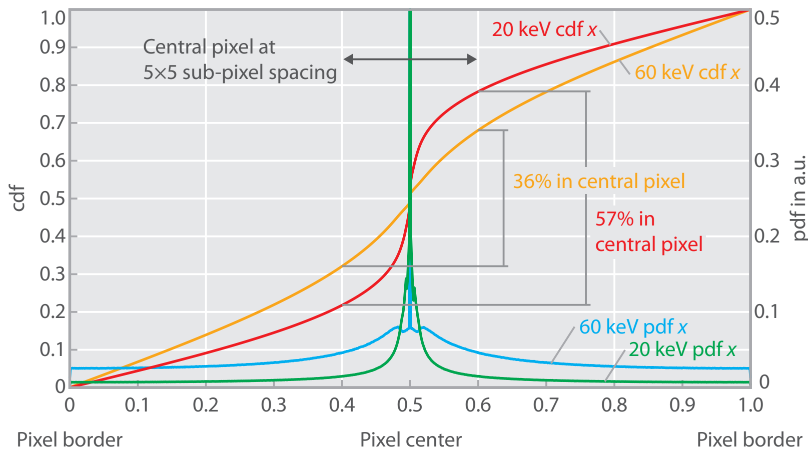

Figure 8.7: Distributions (cdf and pdf) of the position of the CoG over the pixel geometry for experimental data for 20 keV and 60 keV. Only S1 events are used. The x-coordinate is shown. The distributions for the y-coordinate is almost identical. The central pixel for a 5×5 sub-pixel spacing is indicated. 36 % of all S1 events are counted in the central pixel for 60 keV. For 20 keV, 57 % are counted in the central pixel. See figure 8.8 for the resulting images. Measurements: PID20_002 and PID60_001

An image created with a 5×5 sub-pixel resolution for 20 keV and 60 keV is shown in figure 8.8. The effect of the systematic deviation is apparent in the regular pattern of pixels with high counts. Most events are counted at the (sub-) pixels that are at the centers of the physical pixels (corresponding to the indicated region in figure 8.7).

The CoG method is a first approximation to the actual PoE of the incoming TEM electron. The point of entry models of the next two sections try to correct the effect of uneven distributions.

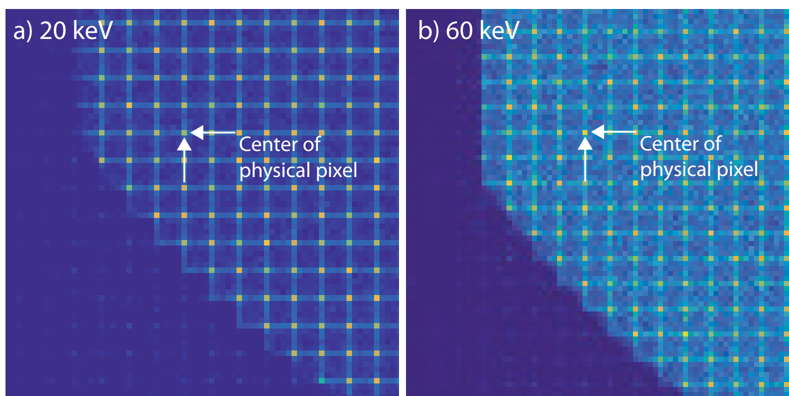

Figure 8.8: Detail of images with 5×5 sub-pixel resolution and the CoG method at 20 keV and 60 keV. The sub-pixels at the center of the physical pixels appear with increased intensity due to the systematic errors of the PoE calculation. Same measurements as in figure 8.7.

8.3.2 *Gauss Correction Method*

The Gaussian correction model assumes a Gaussian shaped charge cloud at the collection depth of the detector volume. The Gaussian distribution is integrated over the pixel borders, discretizing a continuous function. The center of the distribution and the center of gravity of the discrete signal are not at the same position. However,

the difference between both positions is systematic. The position of the center of the Gaussian distribution R_{Gauss} can thus be determined from the calculated CoG position R_{CoG}.

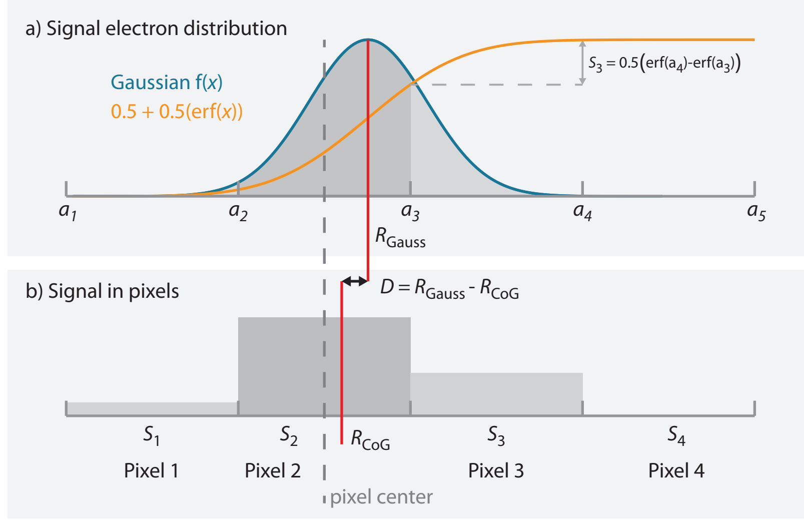

Figure 8.9: A Gaussian distribution that is integrated over pixel boundaries a_i. The position of the center of the Gaussian distribution R_{Gauss} differs from the position of the CoG R_{CoG} calculated over the integrated signal in the pixel boundaries. The position of the CoG is always shifted towards the center of the pixel compared to the actual center of the Gaussian distribution.

As shown in figure 8.9, a continuous Gaussian distribution $f(x)$ of signal electrons is assumed over a discrete region representing pixels. The function $f(x)$ is integrated over each pixel yielding the signal $S(i)$ in pixel i. The integral of a Gaussian distribution with mean μ and width σ is described with the error function $\text{erf}(x)$:

$$f(x) = e^{-\frac{1}{2}\left(\frac{\mu-x}{\sigma}\right)^2} \tag{8.11}$$

$$S_i = \int_{a_i}^{a_{i+1}} f(x)\mathrm{d}x \tag{8.12}$$

$$\text{erf}(a_i) = \int_0^{a_i} e^{-\frac{1}{2}\left(\frac{\mu-x}{\sigma}\right)^2}\mathrm{d}x \tag{8.13}$$

$$S_i = \frac{1}{2}(1+\text{erf}(a_{i+1})) - \frac{1}{2}(1+\text{erf}(a_i)) \tag{8.14}$$

$$= \frac{1}{2}(\text{erf}(a_{i+1}) - \text{erf}(a_i)) \tag{8.15}$$

In this context, the mean μ represents the position of the incoming TEM electron, so that $R_{\text{Gauss}} = \mu$.

The CoG is calculated from the signal collected in the pixels with equation 8.9. The difference D_g to the center of the Gaussian distribution is calculated which is then used to produce the corrected coordinates $R_{\text{G-Exp}}$.

$$D_g(x,\sigma) = R_{\text{Gauss}}(\mu,\sigma) - R_{\text{CoG-Sim}}(x) \tag{8.16}$$

$$R_{\text{G-Exp}} = R_{\text{CoG-Exp}} + D_g \tag{8.17}$$

The difference is calculated for each position of the Gaussian distribution inside the pixel geometry and for several values of the charge cloud size expressed by the parameter σ_{cloud}. A correction look-up table can thus be calculated. The CoG position for both x and y

directions are independent and can be calculated separately, even with different values for σ_{cloud}.

Correction functions for various σ_{cloud} are shown in figure 8.10.[5]

[5] For the code, see appendix A.8.

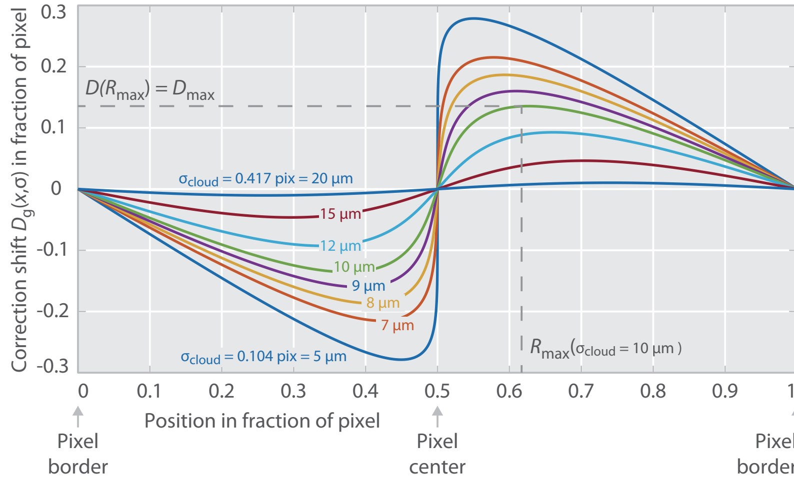

Figure 8.10: Correction shift D_g for an assumed Gaussian distribution and a pixel size of 48 µm. The correction depends on the width σ_{cloud} of the charge cloud. The PoE is always shifted away from the pixel center towards the pixel border. The correction is very sensitive around the center of the pixel as seen by the high gradient at $x = 0.5$, especially at small values of $\sigma_{cloud} < 0.21$ pix $\equiv$ 10 µm. For $\sigma_{cloud} = 0.21$ pix, the position R_{max} and value of the maximum correction shift D_{max} are indicated.

The sensitivity of the correction to the CoG is very high around the center position ($x = 0.5$) for values of $\sigma_{cloud} < 10$ µm. A small variation in the position of the CoG results in a large variation in the applied correction shift. Therefore, factors that influence the CoG, especially noise, become more significant (also choice of threshold σ_{sea} for the SEA, operation mode of the pnCCD).

A reasonable Gaussian correction requires signal in at least two or three pixels in each direction per event. Therefore the size of the charge cloud is tuned using the back contact voltage to achieve a better resolution. A lower back contact voltage results in longer drift times of the charge cloud moving from the back to the front side. Accordingly, the charge cloud has more time to spread due to diffusion and repulsion over a greater area.[6] A low back contact voltage is used in the HiRes operation mode of the pnCCD (see section 4.5.1).

[6] See section 7.3

To achieve the best possible correction of the PoE, the choice of the σ_{cloud} and hence the correction function is crucial. The value for σ_{cloud} can be determined from 1) dedicated experiments,[7] 2) model calculations[8] or 3) with a fit to the distribution of the CoG positions calculated from the experimental data.

[7] Kimmel et al., 2010.

[8] Ihle et al., 2017.

The determination of the charge cloud size with a dedicated experiment is in itself a complex experiment and might give varying results for different pnCCDs (varying wafer processing, spread of processing parameters) and under different operation conditions (timings, voltages, electron mobility depending on operation temperature). Model calculations of the pnCCD (including simulations) might not include all effects that affect the charge cloud size.

In the third method, the experimental data itself determines the suitable value of σ_{cloud}. The experimental cdf of the positions of the CoG is fitted with the cdf of a pure Gaussian signal distribution. Here, the maximum correction shift (D_{max}) and the position

$D(R_{max}) = D_{max}$ are determined for $0.1\,\text{pix} < \sigma_{cloud} < 0.5\,\text{pix}$ from a model calculation. The experimental and the theoretical values (either D_{max} or R_{max}) are compared and the value of σ_{cloud} is chosen that has the lowest difference.

Figure 8.11 shows the cdf and pdf before and after Gauss correction. The pdf after Gauss correction is almost flat like the ideal pdf

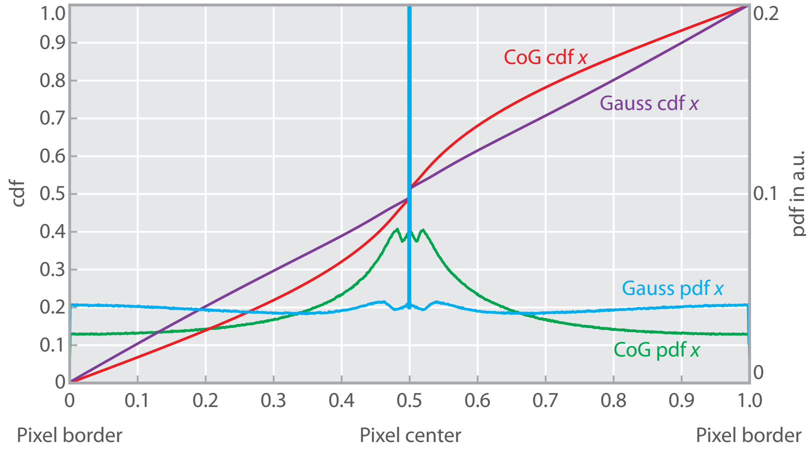

Figure 8.11: Comparison of cdf and pdf before (CoG) and after Gauss correction ($E = 60\,\text{keV}$). Here, $\sigma_{cloud} = 0.237\,\text{pix}$. (HiRes mode, measurement: PID60_001).

implying a good correction. There is a small difference of the cdf to the ideal cdf indicating that the distribution is not pure Gaussian.

The cdf distribution of the CoG positions that is calculated directly from the experimental data can also be used for the correction of the PoE, which is explained in the next section 8.3.3.

8.3.3 Eta Correction Method

All effects leading to a deviation from a pure Gaussian distribution can be accounted for in a correction function that is derived from the measured data itself (either experimental or simulated data). The difference of the *actual* cdf to the *ideal* cdf provides the correction function called $\eta(x)$:[9]

$$\eta(x) = \text{cdf}(x) - x \tag{8.18}$$

$$x_{eta}(i) = x_{cog}(i) + \eta(x_{cog}(i)) \tag{8.19}$$

[9] The correction function is named η in reference to a publication in which this idea was used for the correction of PoEs of photons detected with a silicon strip detector. Belau et al., 1983

The cdf is calculated from all S1 events. The $x_{cog}(i)$ and $y_{cog}(i)$ coordinate of each event i calculated with the CoG method is corrected with the η function (figure 8.12). Visually speaking, the PoEs are shifted away from the center of the pixel towards the border of the pixel reversing the effect of the pure CoG method.

Figure 8.13 shows the cdf and the pdf after the Eta correction in comparison to the CoG method ($E = 60\,\text{keV}$). The pdf of the Eta corrected data is homogeneous indicating a good correction. The discontinuity at $x = 0.5$ is due to the events with only one or two pixel (one pixel in one direction). The improvement in the MTF is discussed in section 8.4.

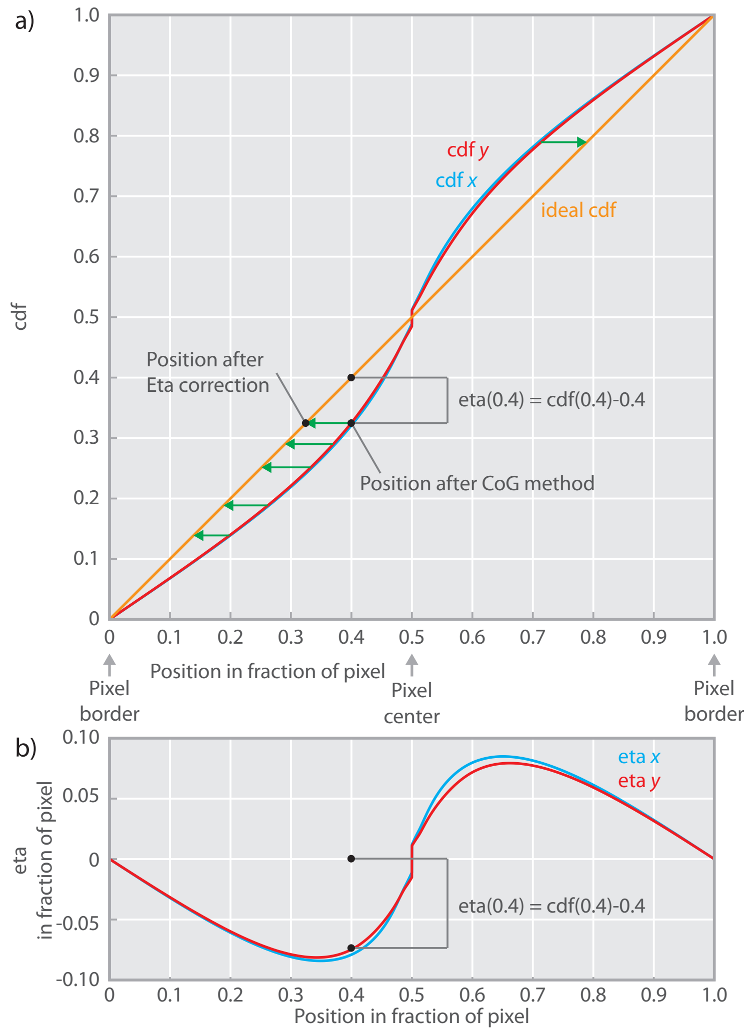

Figure 8.12: a) Cdf and b) Eta correction function ($E = 60\,\text{keV}$). The Eta function is the difference of the actual cdf to the ideal cdf. As an example, the Eta function is calculated for one position at $x = 0.4$ as indicated with the black dots. The PoE determined with the CoG is shifted away from the center of the pixel towards the border (green arrows).

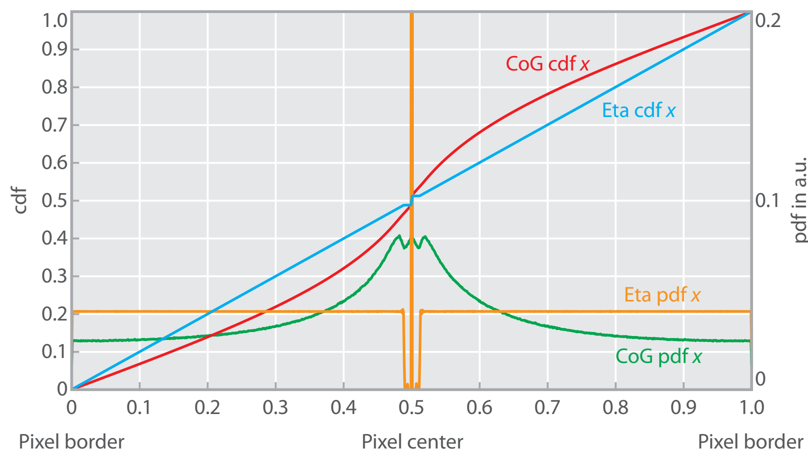

Figure 8.13: Comparison of cdf and pdf before (CoG) and after Eta correction ($E = 60\,\text{keV}$). (HiRes mode, measurement: PID60_001).

8.3.4 *Long Track Furthest Pixel Away Method*

For TEM electrons with energies of 200 keV and 300 keV a method can be applied that uses the long track nature of the scattered primary electron. The fact that more energy is deposited at the end of the track leads to higher signal at the end of the track. Therefore, it is more probable that the PoE of the electron is located at the opposite end of the track (see figure 8.14). For TEM electron energies above 200 keV scattered primary electrons produce long tracks at which they deposit a large part of their energy at the end of the track.

Therefore, the LTFPA model assumes that the PoE lies in the pixel in largest distance to the pixel with the highest intensity. For each event, the algorithm finds the pixel with the highest signal and sets the pixel that is furthest away from this pixel as the PoE. Only the S1 events are corrected that have at least six pixels in one dimension. Events with less pixels do not show a strong directional track and are not corrected.

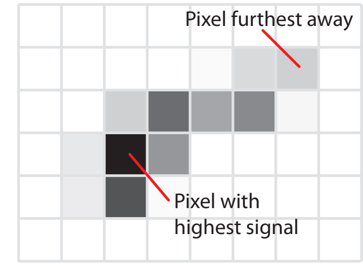

Figure 8.14: Example of a long electron track ($E = 300$ keV). The PoE is probably not near the pixel with the highest signal, but closer to the pixel that is furthest away from the pixel with the highest signal.

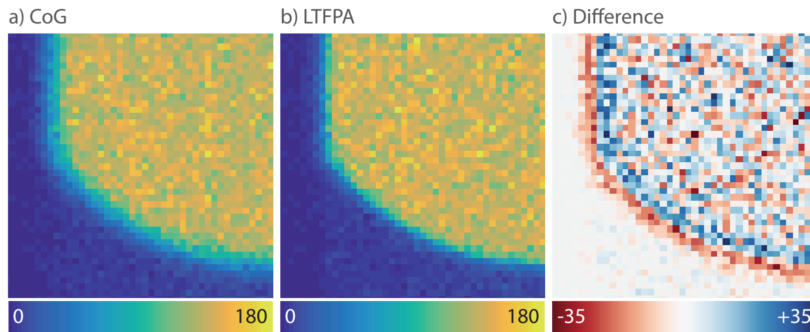

Figure 8.15: Comparison of images created with the CoG model and the LTFPA model (300 keV). For these images, only the corrected S1 events are used. c) The difference between both images (LTFPA-CoG) shows that fewer events are positioned in the masked area (the red edge).

Figure 8.15 shows a comparison of images created with the CoG method and the LTFPA method using S1 events. The contrast of the edge is higher in the LTFPA model corrected image as compared to the CoG model corrected image. In addition, the difference map clearly shows fewer events in the masked area of the LTFPA image compared to the CoG image. Correspondingly, for 300 keV the MTF fitting parameter decreases from $\lambda_{\text{fit}} = 2.778$ (CoG method) to $\lambda_{\text{fit}} = 1.732$ (LTFPA method). For 200 keV at which the tracks are shorter and less directional in comparison, the fitting parameter decreases from $\lambda_{\text{fit}} = 1.563$ (CoG method) to $\lambda_{\text{fit}} = 1.387$ (LTFPA method).

8.4 *Discussion of Models*

The MTF functions for all measured energies are shown in figure 8.16 determined in the IIM and EIM at various sub-pixel resolutions. The determined fitting parameter and MTF values for TEM electron energies from 20 keV to 300 keV are compiled in table 8.1. The spatial resolution increases with decreasing energy of the TEM electrons.
Concerning the Gauss and Eta model, the corrections depend mainly on three parameters: 1) The back contact voltage U_{bc} that mainly determines the signal cloud size σ_{cloud}. 2) The combination of the

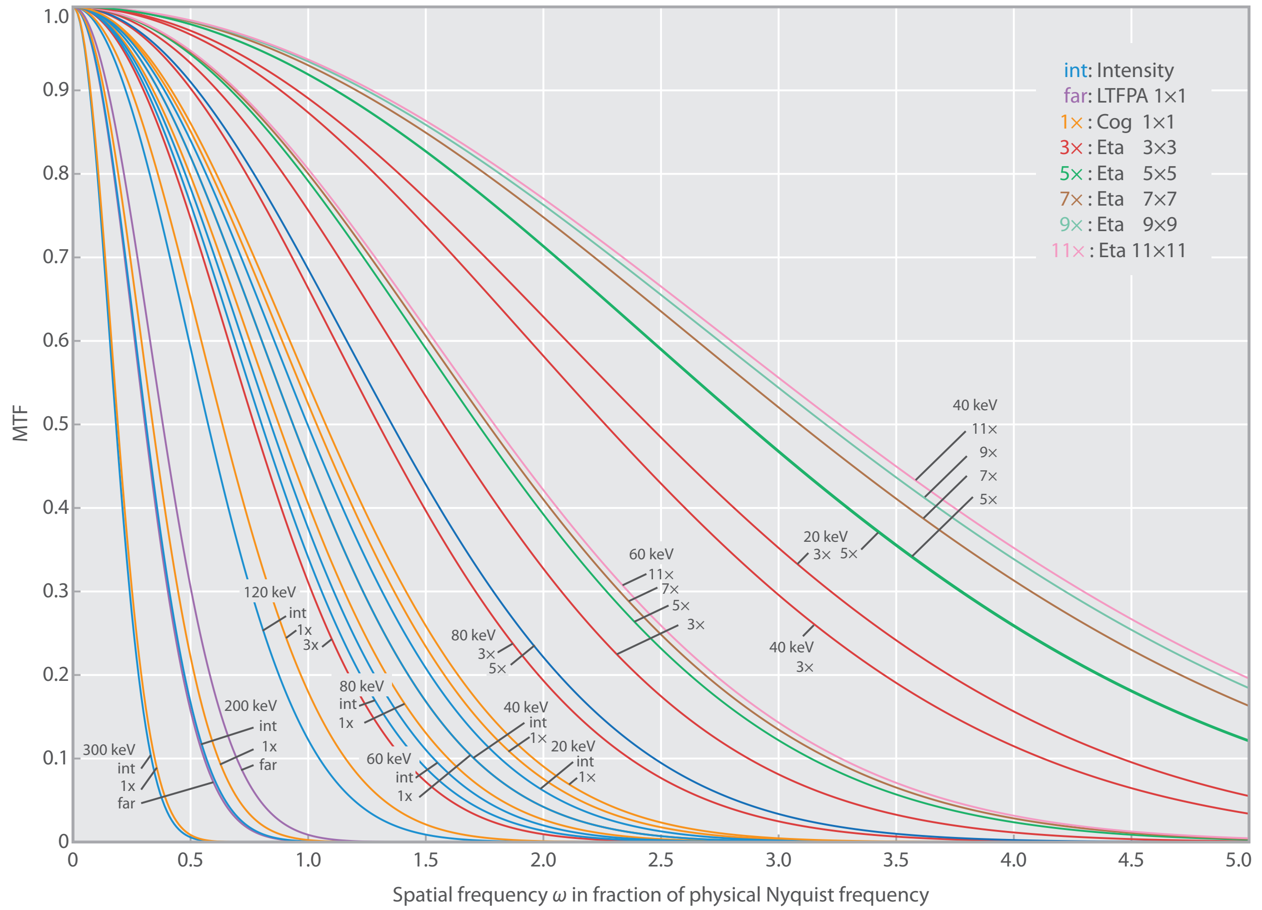

Figure 8.16: Comparison of the MTF for all energies. Four MTF functions overlap (60 keV 1× and 40 keV int, 20 keV 5× and 40 keV 5×).

Energy	λ_{fit}/s				PID
	int	CoG	Eta	Eta	
keV	-	$s = 1$	$s = 3$	$s = 5$	
20	0.532	0.493	0.217	0.185	PID20_004
40	0.567	0.511	0.234	0.185	PID40_002
60	0.630	0.566	0.336	0.308	PID60_001
80	0.661	0.605	0.408	0.391	PID80_004
120	0.922	0.834	0.688	0.680	PID120_001
200	1.703	1.563	-	-	PID200_002
300	2.896	2.778	-	-	PID300_002

Table 8.1: MTF values determined from intensity images (int) and images created with the CoG model and the Eta model. The CoG and Eta mode provide the same result at no sub-pixel resolution ($s = 1$). Results of the Gauss model are not shown since the Eta model results in better images (see text and figure 8.18). For energies of 200 keV and 300 keV, the Eta correction was not applied since the signal distribution of their tracks is not similar to a Gaussian distribution. All values are derived from experimental data.

noise level and the threshold σ_{sea} that is used in the SEA. 3) The energy of the primary electron. In combination, these three parameters determine the pdf and cdf distributions of the positions of the CoG in the pixel. A better reconstruction of the PoE is achieved, if the gradient of the cdf around the center of the pixel ($x \approx 0.5$) is minimized. This means that these two correction methods do not depend strongly on slight variations in the initial position calculated with the CoG.

Following the cdf from the border to the center of the pixel, the distance between the point at which the cdf does not increase to the pixel's center should be minimized (see figure 8.17). Practically, this means that there are fewer events that have only one pixel with signal or that have only one pixel spread in one direction. This can be achieved by tuning the above mentioned three parameters. Generally, the pnCCD should be operated in the HiRes mode if images are created from single electrons.

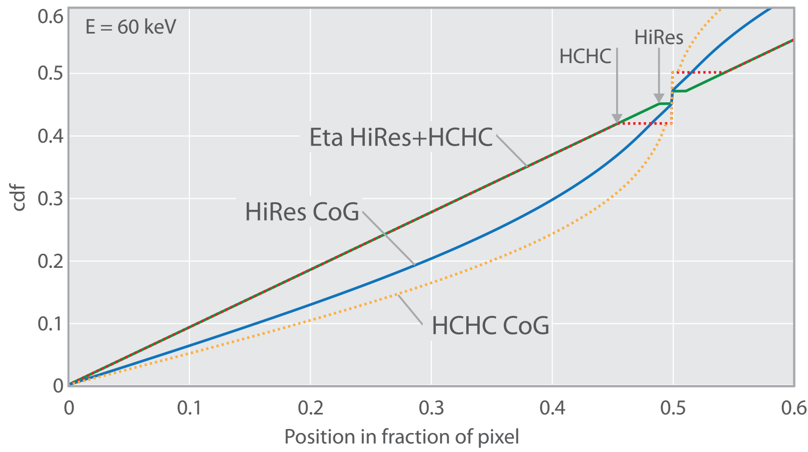

Figure 8.17: Comparison of cdfs between HiRes and HCHC mode ($E = 60\,\text{keV}$). The gradient of the CoG cdf near the pixel center ($y = 0.5$) is greater in the HCHC mode than in the HiRes mode. After the Eta correction, the position from which the cdf does not increase (indicated by the two arrows) to the pixel center is further away in the HCHC mode than in the HiRes mode, which can lead to a less than optimal correction (see also figure 8.21). Experimental data.

In figure 8.18, 5×5 sub-pixel images calculated with the CoG, Gaussian and Eta method for 60 keV are compared. All images show a

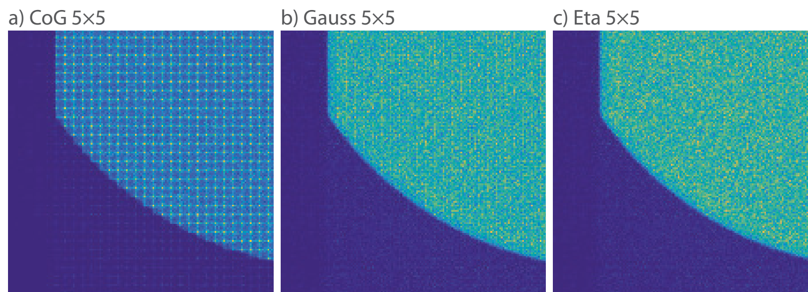

Figure 8.18: Comparison of 5×5 sub-pixel images ($E = 60\,\text{keV}$).

sharp edge. The image created with only the CoG method shows the systematic errors explained before (see section 8.3.1). The image created with the Gauss model shows slightly inhomogeneous intensity with partially highlighted columns. The Eta model provides better results compared to the Gauss model (see figure 8.19) which relies on the assumption of a pure Gaussian distribution of signal electrons.

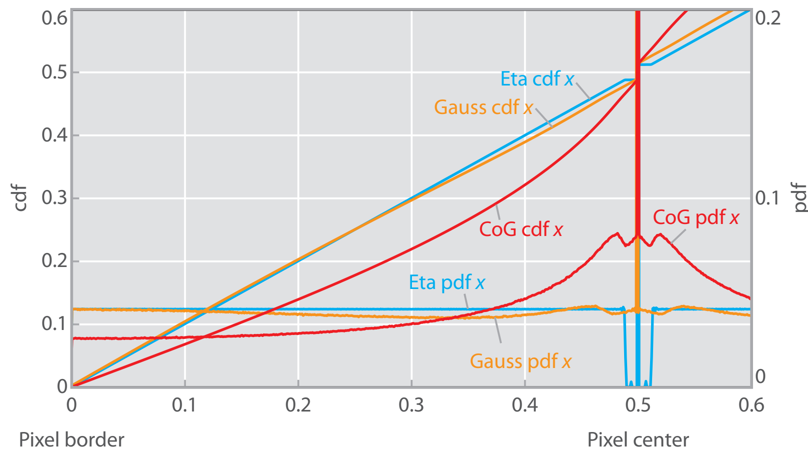

Figure 8.19: Comparison of CoG, Gauss and Eta methods. Both the Gauss and Eta method show an improvement compared to the CoG method. The Gauss cdf shows a slight deviation from the ideal cdf, along with a non-flat pdf. The Eta method provides the best correction.

An increase in sub-pixel resolution results in a decrease in the number of TEM electrons N_{im} per sub-pixel in the image. The total number of TEM electrons N_{tem} that hit a physical pixel is divided by the number of sub-pixel per physical pixel:

$$N_{\mathrm{im}} = \frac{N_{\mathrm{tem}}}{s^2} \tag{8.20}$$

with the sub-pixel factor s (see equation 5.14). For example, assuming that $N_{\mathrm{tem}} = 100$ TEM electrons hit a physical pixel, the average number of TEM electrons that are counted in a sub-pixel with a 5×5 sub-pixel resolution is $N_{\mathrm{im}} = 4$. To compensate and to reach the same statistics, a 25 times longer measurement would be needed. Therefore there is tradeoff between sub-pixel resolution and the number of counts in a sub-pixel. In figure 8.20, a series of images with increasing sub-pixel resolution are shown along with the MTF fitting parameter in table 8.2. The contrast in the MTF does not increase significantly

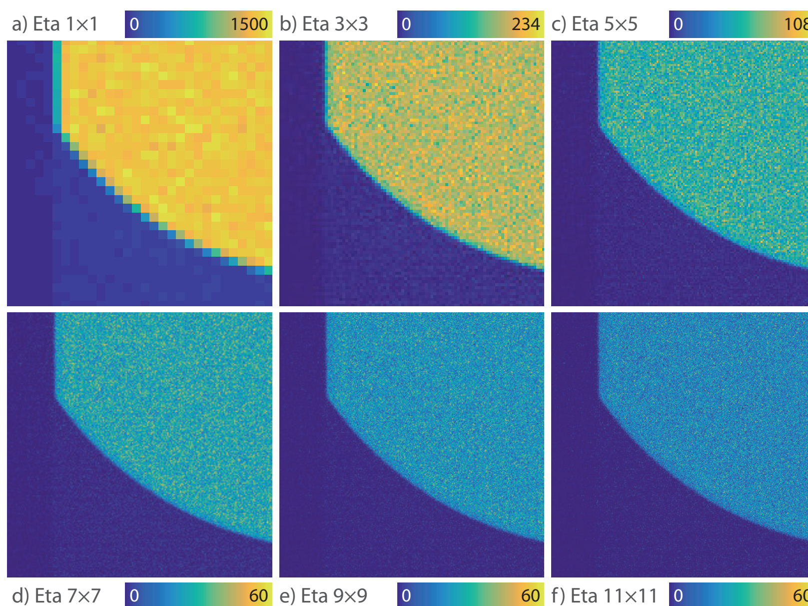

Figure 8.20: Comparison of images with increasing sub-pixel resolution (E = 60 keV). With increasing sub-pixel factor, the average number of TEM electrons $\bar{N}_{\mathrm{im}}$ per image pixel decreases (see also table 8.2).

beyond a 5×5 sub-pixel resolution. However, the average number of TEM electrons in a sub-pixel decreases significantly proportionally with s^2 along with a relative increase in the variance σ^2_{im}. These findings are compiled in table 8.2.

s	λ/s	MTF		$\bar{N}_{\mathrm{im}}$	σ_{im}	$\bar{N}_{\mathrm{im}}/\sigma_{\mathrm{im}}$
		0.5 Ny	1.0 Ny	e^-_{tem}	e^-_{tem}	
1	0.567	0.820	0.453	1311.5	46.3	28.3
3	0.336	0.933	0.756	145.7	15.2	9.6
5	0.308	0.943	0.791	52.5	9.0	5.8
7	0.301	0.946	0.800	26.8	6.4	4.2
9	0.297	0.947	0.804	16.2	4.9	3.3
11	0.296	0.947	0.806	10.8	4.0	2.7

Table 8.2: MTF values and statistics on number of TEM electrons depending on sub-pixel resolution. $E = 60\,\mathrm{keV}$, measurement: PID60_001

There is potential for very high spatial resolution at low TEM electron energies, especially at 20 keV. The TEM electrons do not scatter over a long distance and their energy deposition is localized to a few micrometers. The initial charge cloud is similar to the one generated by X-ray photons. For X-rays, it has been shown that a spatial resolution down to a few micrometers can be achieved.[10]

[10] Ihle et al., 2017.

Due to limited operation time at a TEM capable of energies down to 20 keV, only measurements in the HCHC mode ($U_{\mathrm{bc}} = -420\,\mathrm{V}$) were recorded at 20 keV and 40 keV during this thesis. The high back contact voltage leads to a small spread of the signal electrons (see section 7.3). In the case of TEM electrons with an energy of 20 keV, there are many events that only have one or two pixels. The effect of the high back contact voltage can be countered to some degree with a lower threshold used in the SEA. With a lower threshold, more pixels are assumed to have real signal and the chance for events with more than two pixels increases (see figure 7.28). In figure 8.21 the cdf and pdf distributions are shown of the positions after the Eta correction calculated with a threshold of $\sigma_{\mathrm{thresh}} = 3$. Several observations can be made:

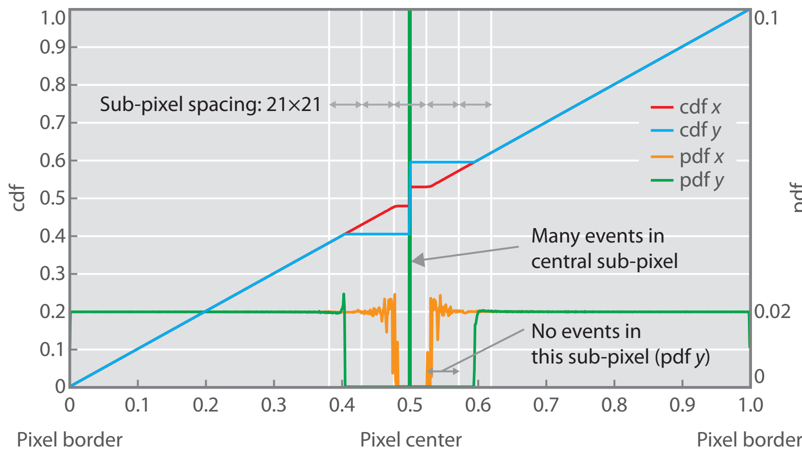

Figure 8.21: Distribution of positions in HCHC mode at 20 keV. For a 21×21 sub-pixel spacing, the central 5 pixels are indicated. There are no events positioned in the row before and after the central pixels, corresponding to pdf(y) values of zero. See also figure 8.22. PID20_004

- The positions in x and y direction are distributed homogeneously from 0.0 to 0.4 and from 0.6 to 1.0.
- This shows, that the Eta correction works well in these intervals.
- There is a difference in the distribution for the x and y direction.
- There are more events with only one pixel in y direction (rows), about 20 %, seen in the cdf values from 0.4 to 0.6.
- As a consequence, there is an inhomogeneous distribution of counts in sub-pixel images. For example, at a 21×21 sub-pixel resolution, the central pixel in y direction has 20 % of the events. The neighboring pixels have no counts leading to empty rows in the image (see figure 8.22).

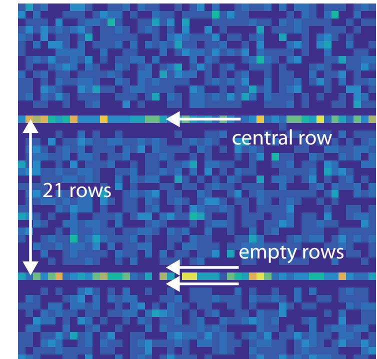

Figure 8.22: Detail of 21×21 sub-pixel image. The average number of counts in the central pixel is approximately three times higher than in the other pixels excluding the ones in the empty row.

The main reason for the disparity between the distributions in x and y direction is presumably the asymmetric potential of the pixel well inside the detector.[11]

[11] Schmidt, 2017.

However, the homogeneous distribution outside the few central pixels indicates a good correction and a good spatial resolution. In figure 8.23 images with high sub-pixel resolutions up to 25×25 are shown. At high sub-pixel resolutions, the artifact of one bright row

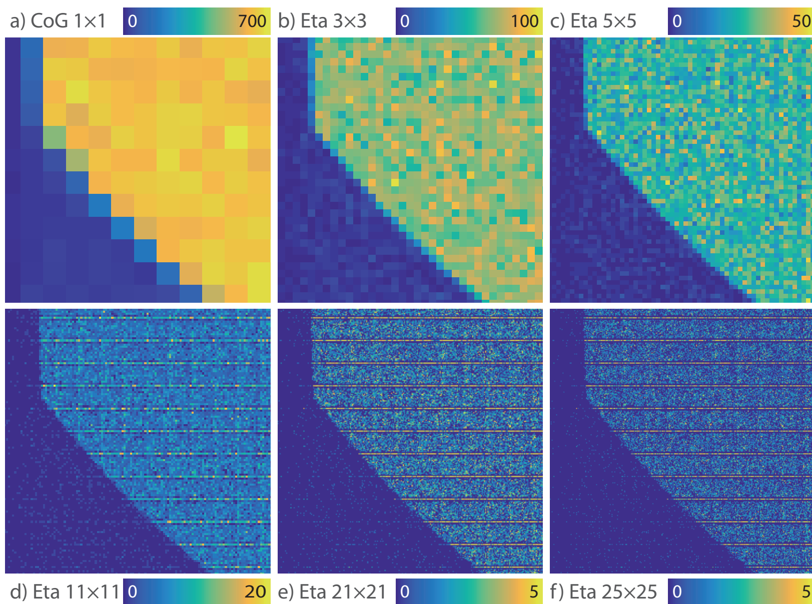

Figure 8.23: Comparison of sub-pixel images at 20 keV. With increasing sub-pixel resolution rows can be seen that are brighter than the average. This artifact was caused by the back contact voltage that was not set optimally, being too high. See also figure 8.21. Disregarding the bright row, the edge remains sharp even at sub-pixel resolution beyond 11×11. PID20_004

between two or more empty rows can be seen. Nevertheless, disregarding this artifact, the imaged edge appears to stay sharp. The conclusions of section 7.3 provide strong evidence that with an appropriate back contact voltage the artifact will be removed. A true high spatial sub-pixel resolution can be achieved for 20 keV in the range of a few micrometers. Due to the artifact, for 20 keV the MTF could only be reasonably determined up to a 5×5 sub-pixel resolution (see table 8.1).

As a remark, the particular TEM that was used to record the low energy electrons was not optimized for such low energies ($< 80\,\text{keV}$). As a result, the illumination was not homogenous but showed a low variation across the image (see figure 8.24). The effect on the calculated MTF is probably marginal, however, the calculated MTF should be confirmed under homogenous illumination, if possible.

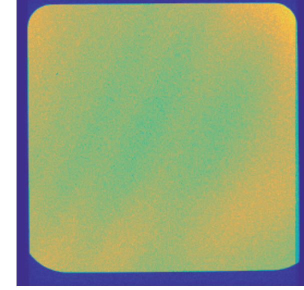

Figure 8.24: Uneven illumination for measurements recorded at 20 keV.

For 40 keV, the primary electrons scatter far enough that the high back contact voltage does not have such an adverse effect as for 20 keV. In combination with a low threshold used in the SEA ($\sigma_{\text{thresh}} = 3$), the bright rows can be avoided. An improvement in spatial resolution is seen up to around $s = 9$ (see table 8.3). The improvement in the

s	1	3	5	7	9	11
λ_{fit}/s	0.512	0.234	0.185	0.172	0.166	0.163

Table 8.3: MTF fitting parameter for 40 keV for increasing sub-pixel resolutions after Eta correction. Measurement: PID40_002

MTF fitting parameter can also be seen in the images (see figure 8.25). The rounded corner is sharp and not blurry even at 11×11 sub-pixel resolution and fine details of a rough edge become apparent. As mentioned before in this section, the number of counts is greatly reduced at high sub-pixel resolutions, which reduces the contrast.

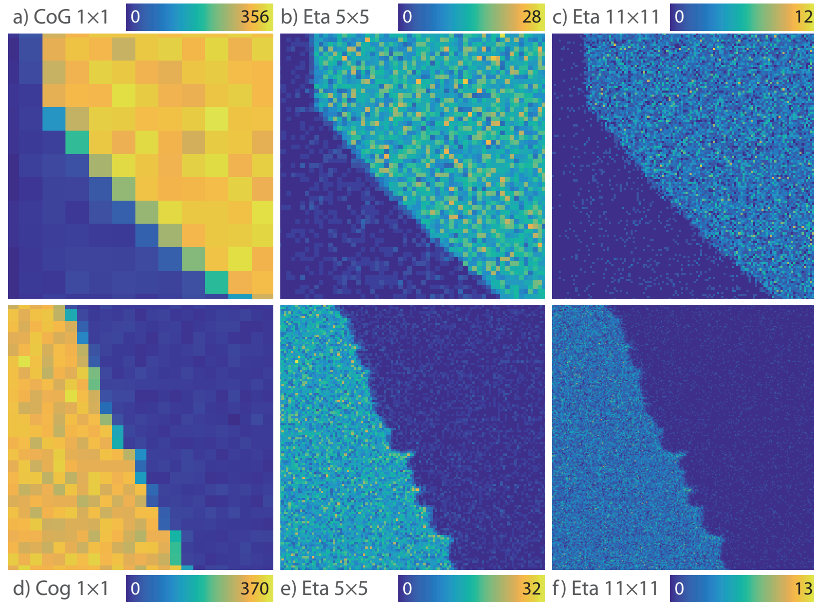

Figure 8.25: Details of images for $E = 40\,\text{keV}$. Much smaller details are resolved with 5×5 sub-pixel resolution compared to no sub-pixel resolution. Visually, the improvement beyond 5×5 sub-pixel resolution is minor. Measurement: PID40_002

There is potential for further models to be investigated, especially for high energy electrons. Spatial resolution could be improved for example by using the shape of the track, weighting the far away pixels, clustering the tracks depending on their properties (number of pixel, bounding box dimensions, ratio of bounding box dimensions, signal distribution) and correcting each class of track with a specific model. Machine learning methods could be used to effectively automate the task of finding the most precise PoE of the TEM electron.

9 Application of the pnCCD in Transmission Electron Microscopy

The pnCCD has been used as a spatially resolving imager in several applications and experiments of which five are presented in this chapter. The first experiment is the demonstration of the wave-particle duality of electrons (section 9.1). Similar to Young's double slit experiment the wave nature of the electron was shown by recording an interference pattern. At the same time, individual single electrons could be seen, due to the capability of the pnCCD to record single TEM electrons. With sub-pixel resolution, the contrast in the interference pattern could be increased.

In the second application, the pnCCD was used to record the three dimensional structure of a nanotube (section 9.2). The sample was imaged from many angles and in post-processing the structure was reconstructed with the tomography method. Tomography relies on many images that need to be recorded and typical measurement times are longer than 10 min. With the pnCCD, the measurement took only a few seconds.

The third, fourth and fifth application are measurements done in the scanning mode of the TEM. These measurements can be grouped into a method called 4D-STEM because a four dimensional data set is recorded (section 9.3). During the measurement, for each probe position of the electron beam (two dimensions), one image is recorded (two dimensions). Conventional STEM detectors only record one measurement from a single spatial element or a few elements.[1] Since many probe positions are required, a fast imager is needed for 4D-STEM, like the pnCCD.

[1] Remember the groups of detectors depending on number of detection elements in section 2.3.

In the third experiment, magnetic domains of a sample are imaged (section 9.4). Due to the magnetic field in the sample, the electron beam is deflected. The deflection is recorded in two dimensions with the pnCCD and the magnetic field can be reconstructed. This measurement demonstrates nicely the 4D-STEM method.

In the fourth application, the lattice strain of two samples is determined. With the pnCCD, measurement times could be reduced by a factor of 200 compared to previously used detectors.

In the fifth application, the pnCCD is used in ptychography with electrons. Ptychography is a method to retrieve the phase of the electron wave that was modified by the sample. It is shown that

samples that are otherwise difficult to image can now be characterized with Ptychography and the pnCCD.

9.1 *Demonstration of the Wave-Particle Duality of Electrons*

The wave-particle duality of electrons was demonstrated with the pnCCD in a quasi double-slit experiment.[2] During the measurement, due to a low electron rate, individual electrons could be seen in the images, showing the particle character of the electron. The integration of many frames resulted in an image in which an interference pattern was visible, showing the wave character of the electron.

[2] Ryll et al., 2015.

The setup of the experiment included an electron biprism[3] which was put into the trajectory of the TEM electrons. An electron biprism consists of a thin wire between two parallel plates. The wire has a diameter of several hundred nanometer and is made of gold coated glass. The wire is at a positive potential that is externally adjustable in the range of 0 V to +200 V. The plates are at ground potential. Due to the electrostatic field around the wire, the TEM electrons will be deflected.

[3] Möllenstedt and Düker, 1956.

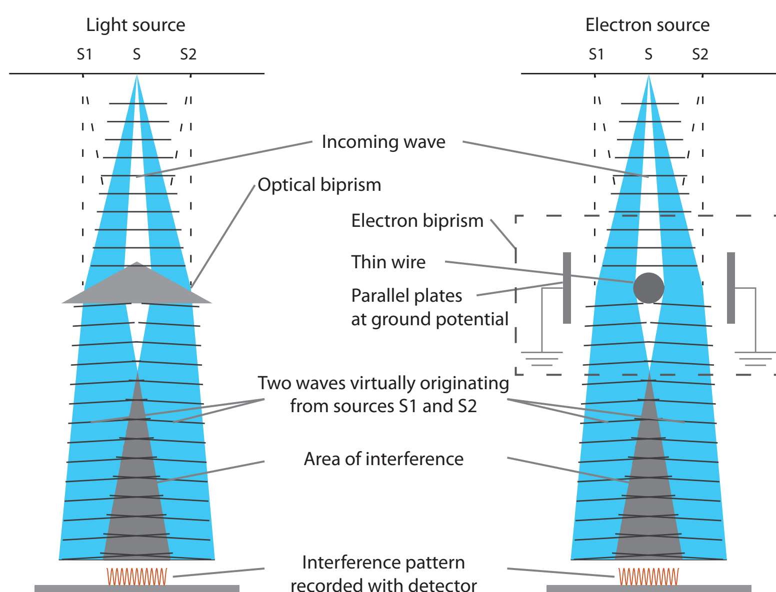

Figure 9.1: Principle of an optical and electron biprism.

The functional principle of the electron biprism is comparable to the optical biprism (see figure 9.1). In a setup with an optical biprism, an incoming light wave is refracted such that, that after the biprism, there are two waves that are inclined so that they seem to originate from two virtual sources (S1 and S2). These virtual sources are comparable to the two slits of a double slit interference experiment. In the area where the two waves overlap, they will interfere. The detection of the intensity distribution in the overlapping area shows the typical interference pattern. The principle is the same for electron waves. In this case, the electrons are detected with the pnCCD.

Note, that in the actual TEM setup, there are several electron lenses

that project and magnify the interference pattern on to the detector with a magnification on the order of 100 000 to 750 000. Otherwise the fringe spacing which can be below 1 nm could not be resolved.

The recorded intensity $I(\alpha)$ varies periodically depending on the angle α:

$$I(\alpha) = I_0 \cdot \underbrace{\mathrm{sinc}^2\,\gamma}_{\text{diffraction}} \cdot \underbrace{\cos^2\delta}_{\text{interference}} \tag{9.1}$$

$$\gamma = b \cdot \frac{k_z}{2} \cdot \sin\alpha \tag{9.2}$$

$$\delta = d \cdot \frac{k_z}{2} \cdot \sin\alpha \tag{9.3}$$

$$k = \frac{2\pi}{\lambda} \tag{9.4}$$

$$w = \lambda \frac{z}{d} \tag{9.5}$$

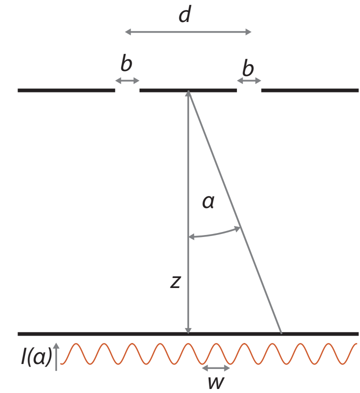

Figure 9.2: Geometry of the double slit and the used figures.

With b the slit width, d the distance between the slits, α the angle, z the distance from the slit plane to the detection plane and w the fringe spacing (see figure 9.2).

Since the slit width is small compared to the distance between the slits ($d/b > 10^5$) the diffraction term has a negligible effect on the intensity of the maxima in the observed area (see Appendix A.3 for more details).

In figure 9.3, a sequence of images is shown in which an increasing number of frames are integrated ($E = 60\,\mathrm{keV}$). In the first images, single electrons can be seen, which seem to be randomly distributed over the area. At around 100 integrated frames, a striped pattern starts to emerge, the interference pattern. Increasing the number of integrated frames shows the interference pattern with an increased contrast. The orientation of the fringes is optically parallel to the wire of the biprism.

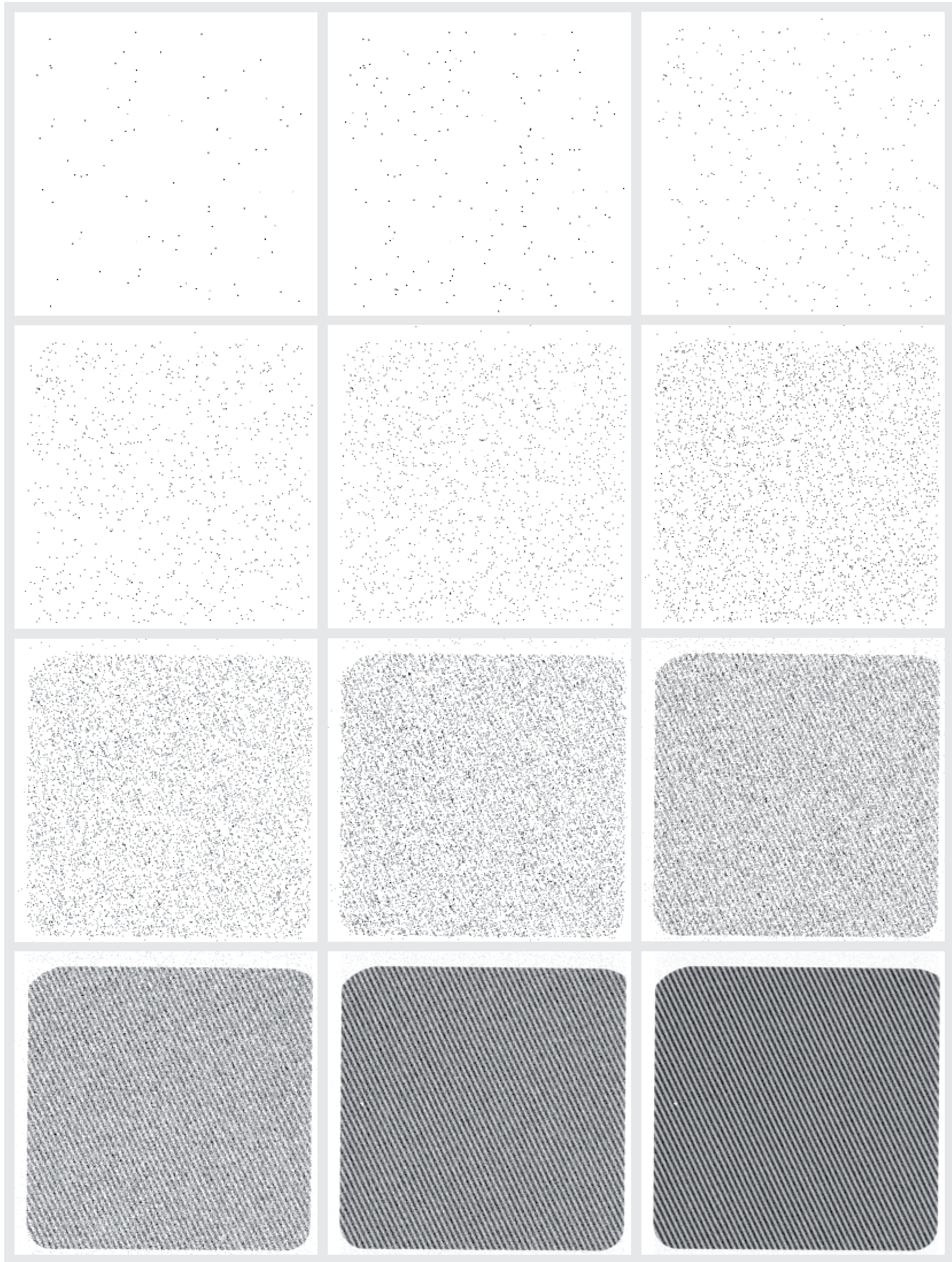

Figure 9.3: Montage of intensity images ($E = 60\,\mathrm{keV}$) with increasing number of frames that are integrated to create the image, from left to right, top to bottom: 1, 2, 4, 10, 20, 40, 100, 200, 700, 2200, 12 200 and 62 200.

9.1.1 *Single Electron Imaging in Holography*

The contrast in the interference pattern can be quantified with the interferometric visibility. In this section, it is shown that the interferometric visibility can be increased by using sub-pixel resolution. The models developed in section 8.3 have been applied in holography measurements. The electron rate was reduced so that single electrons could be distinguished in the single frames and the SEA could be applied. Two measurements are presented here, one with an electron energy of 60 keV and one with 300 keV.

The interferometric visibility is defined as:

$$V = \frac{I_{\text{max}} - I_{\text{min}}}{I_{\text{max}} + I_{\text{min}}} = \frac{A}{d} \in [0, 1] \tag{9.6}$$

with the maximum intensity I_{max} and minimum intensity I_{min} (see also figure 9.4).

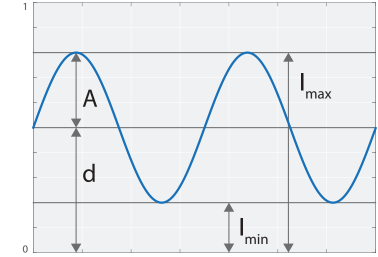

Figure 9.4: Interferometric visibility.

Figure 9.5 shows a comparison of an interference pattern without sub-pixel resolution created by integrating many frames (an intensity image) and an interference pattern with 5×5 sub-pixel resolution at $E = 60$ kev. For the calculation of the visibility, the intensity was averaged in the direction of the fringes (as indicated by the arrow in figure 9.5). The averages are shown in figure 9.6. The interferometric visibility was calculated from the average for both images. The interferometric visibility increased from $V_{\text{int}} = 0.49$ for the intensity image to $V_{5\times5} = 0.58$ for the sub-pixel resolution image.

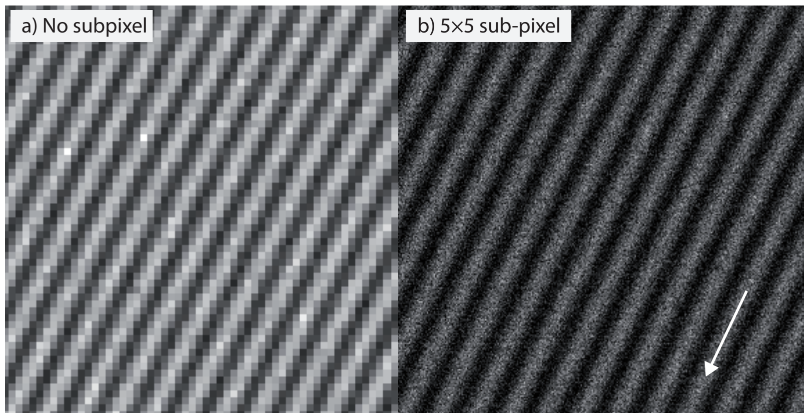

Figure 9.5: Comparison of images with and without sub-pixel in a holography experiment ($E = 60$ keV). a) No sub-pixel are used. b) The image is formed with 5×5 sub-pixels and the Eta-method, showing the finer resolved interference fringes. The arrow indicates the direction in which the intensity of the fringes is averaged.

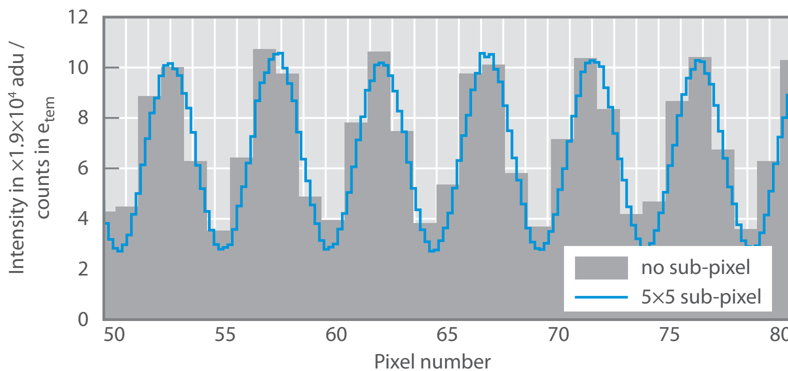

Figure 9.6: Averaged intensity of interference fringes. The solid area is without sub-pixel resolution, the line steps is with 5×5 sub-pixel resolution. For this comparison, the maximum of the intensity was normalized to the maximum count of the sub-pixel image.

9.2 *Electron Tomography with the pnCCD*

Electron tomography (ET) is an essential method in electron microscopy to study the three-dimensional structure of samples. For example, biological samples like cells and proteins can be better understood in their function if the structure is resolved in 3D at the nanometer scale.[4]

[4] Baumeister, 2002; Midgley et al., 2007.

In ET, the problem of acquiring a three dimensional image with a two dimensional detector is solved by illuminating the sample from many angles. The sample is tilted and for each tilt angle in a series, a two dimensional projection is recorded (see figure 9.7). The rotation can be around one or two tilt axes. Afterward, in post-processing, the images of the projections are used to reconstruct the 3D structure of the sample, called the tomogram (see figure 9.8).

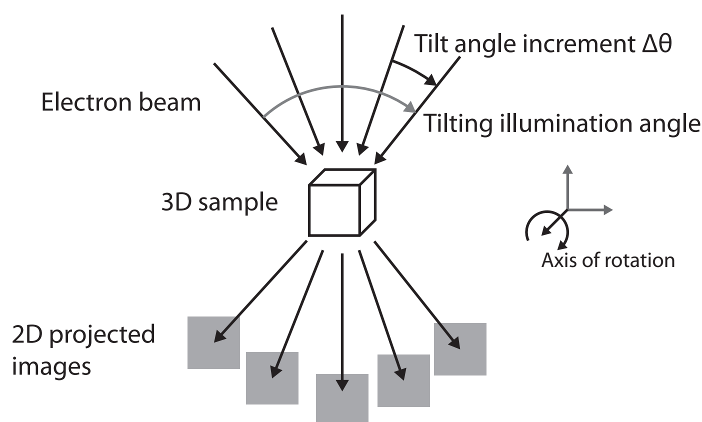

Figure 9.7: Principle of tomography. For each illumination angle, a two dimensional projection is recorded. In the actual TEM, the sample is tilted rather than changing the angle of the incident beam.

The tilt range and the number of projections influence the quality of the reconstructed image:[5] 1) The tilt range should be as large as possible. Ideally, the sample would be tilted the full $\pm 90°$ range, but there are practical limits since the sample appears thicker the more it is tilted and because of mechanical restrictions inside the TEM. In practice, tilt ranges around $\pm 70°$ are possible. The missing angle range is called *missing wedge* and the missing information can cause artifacts in the reconstructed tomogram. 2) The number of projections should be as high as possible, equivalent to small tilt angle increments. For samples that are sensitive to beam damage (biological ones, soft matter polymers), the electron dose for each projection must be minimized. This results in noisy images or in a small number of projections equivalent to large tilt angle increments.

[5] Crowther, DeRosier, and Klug, 1970; Midgley et al., 2007.

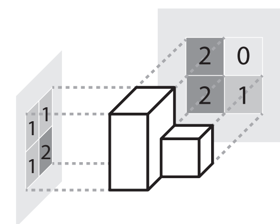

Figure 9.8: Principle of back projection in tomography. In this simple example, the two, two dimensional images provide unambiguous information to reconstruct the three dimensional sample.

Measurement times for full tilt series can be 20 minutes or even hours when recorded with cameras that are readout around the 20 fps frame rate.[6] The microscope and the sample must be stable during the whole time, otherwise the sample drifts or the imaging conditions change and the reconstructed structure will lose resolution. With high frame rates, more data can be collected in a shorter time. Shorter measurement times, in turn, relax the stability requirements on the microscope.

[6] Migunov et al., 2015, supplement.

The pnCCD has potential as a detector for ET because of the high readout rates and the high sensitivity. With a frame rate of 1150 fps, a whole tilt series can be recorded in a few seconds.

To test this, the pnCCD was installed on an FEI Titan 60-300 TEM. The TEM energy was set to 60 keV. The pnCDD was operated in the HCHC mode and read out at 1150 fps. There was no synchronization between the camera and the TEM. The sample holder was set to start tilting continuously and the readout was started shortly before. The goniometer of the microscope was tilted from −70° to +70°. The sample was a lanthanide-based nanotube[7] placed on a lacey carbon support.

[7] Panchakarla et al., 2014; Migunov et al., 2015.

Single frames of a tomographic tilt series are shown in figure 9.9 for various tilt angles. The shown rotational symmetric nanotube features a irregular three dimensional structure at one end to better provide an impression of the rotation. Due to the rotation of the sample holder and non-perfect eucentric focus of the sample position, the field of view on the sample moved. This was a limitation of the available sample holder.

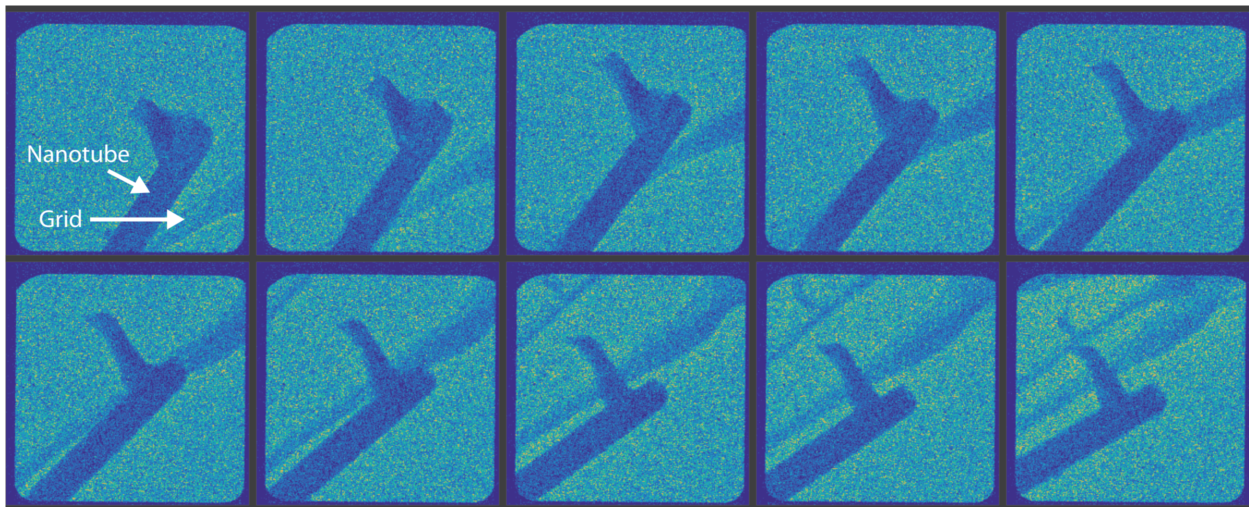

Figure 9.9: Single frames of a tomography tilt series. The sample is a lanthanide-based nanotube supported on a grid. The field of view changes because of the non-perfect eucentric focus.

Single frames of the measurement that was used to reconstruct the nanotube are shown in figure 9.10. At the end of the tilt range, the nanotube moved outside the field of view. In the end, there were 3500 frames that were used for the reconstruction, equivalent to a tilt range of −70° to +30°. The number of frames that were used for the reconstruction correspond to a measurement time of 3.0 s. The resulting tilt increment is 0.029° per projection, which is more than an order of magnitude smaller compared to tilt increments of 1° to 2° used in conventional ET.

The nanotube could be reconstructed[8] from this data set. Several views of the nanotube under three different angles are shown in figure 9.11, as well as one cut view through the nanotube. The morphology of a nanotube is clearly seen.

[8] For the reconstruction process see Migunov, . . . , Ryll, . . . , et al., 2015.

The total dose integrated over all images is lower by an order of magnitude compared to conventional tilt series.[9]Radiation sensitive

[9] Migunov, . . . , Ryll, . . . , et al., 2015.

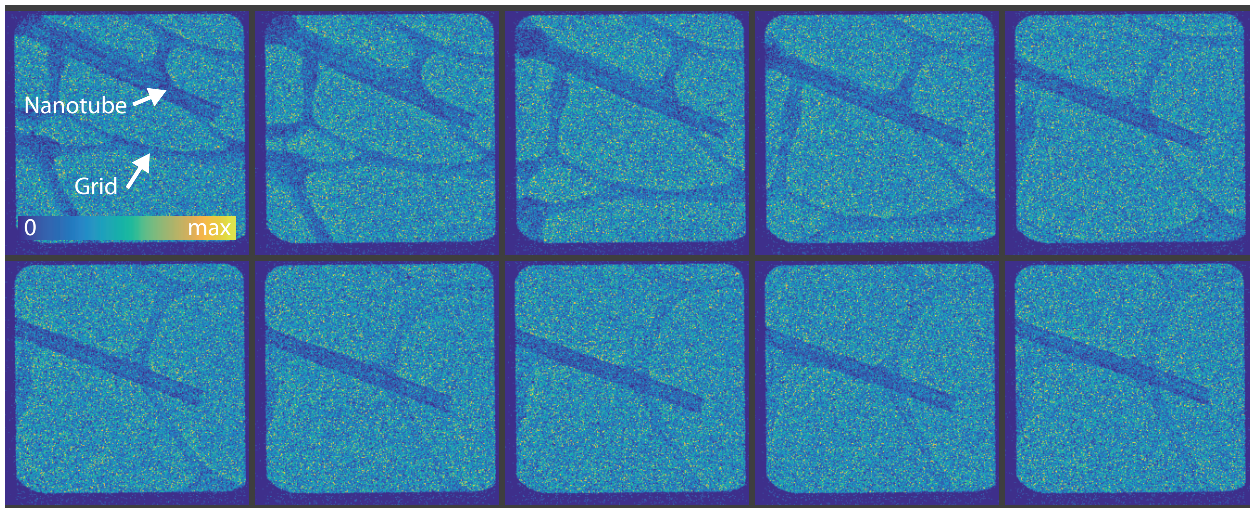

Figure 9.10: Single frames of a tomography tilt series. The sample is a lanthanide-based nanotube supported on a grid.

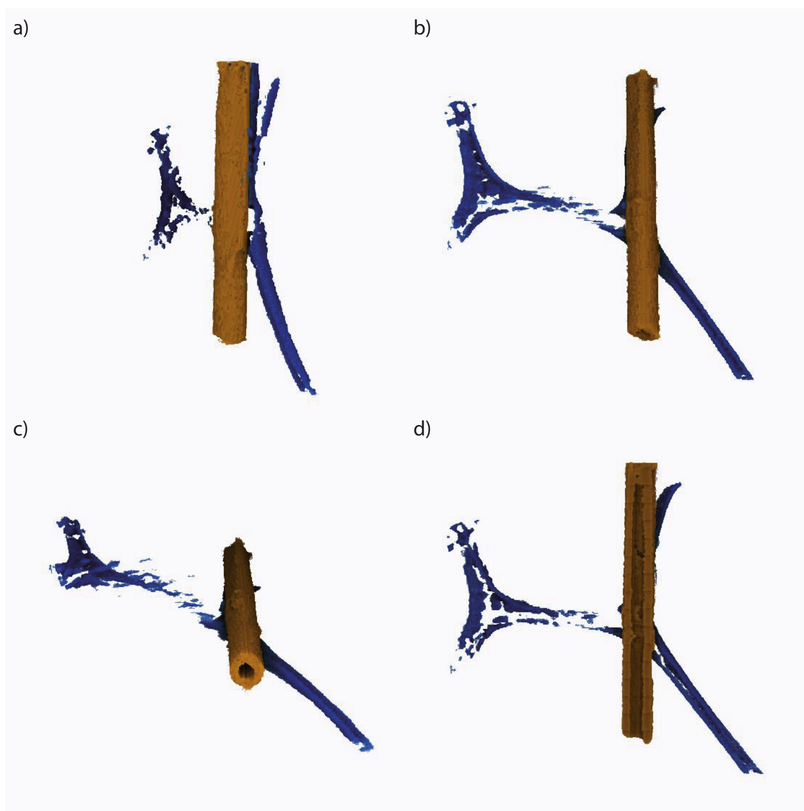

Figure 9.11: Various views on the reconstructed nanotube (orange) on a support grid (blue). A cut through the nanotube is shown in d). Images from Migunov, . . . , Ryll, . . . , et al., 2015

samples can therefore be imaged with a high number of projections without damaging the sample.

The reconstruction algorithm took in the order of 20 s on a current desktop computer. The image acquisition took about the same time. Overall, including some overhead, with the pnCCD it is technically feasible to record and reconstruct a three dimensional sample in under 40 s. A workflow in which the three dimensional structure of a sample is accessible in a few minutes instead of half an hour or more changes the way samples can be investigated tremendously. Additionally, the throughput of samples is greatly increased.

9.3 4D-STEM Imaging

4D-STEM imaging describes an imaging technique in the scanning mode of the microscope. As is normal in STEM mode, the electron beam is focused on the sample down to a small spot size in the order of 0.5 Å. The electron beam is then scanned over the sample over an area of interest.[10] Typical numbers of probe positions range between 256×256 or 2048×2048 probe positions. For each probe position $\vec{p}$, a two dimensional image is recorded (see figure 9.13a). The intensity distribution that is imaged on the detector originates from various signals of the transmitted electron beam depending on the settings of the microscope. These signals include the bright field disc (figure 9.12a), diffraction patterns (figure 9.12b) or a single selected diffraction peak (or disc).

[10] Most microscopes do a continuous scan, some move and wait.

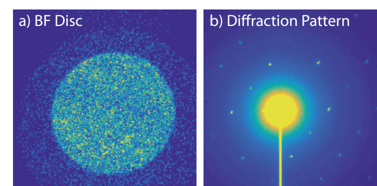

Figure 9.12: Examples of recorded signals in 4D-STEM.

Since a two dimensional image is recorded for a two dimensional scanning raster, in total a 4D data set is recorded. Specific information can be extracted from each 2D image of each probe position that correlate to the properties of the sample at the probe position.

An example application is the imaging of magnetic domains in a sample. In a simple interpretation, the magnetic field of the sample deflects the electron beam as it passes the thin sample (see figure 9.13b and c). As part of the transmitted electron beam, the imaged BF disc moves accordingly. The position of the disc in the detector image at each STEM probe position is convertible into the strength and direction of the magnetic field in the sample.

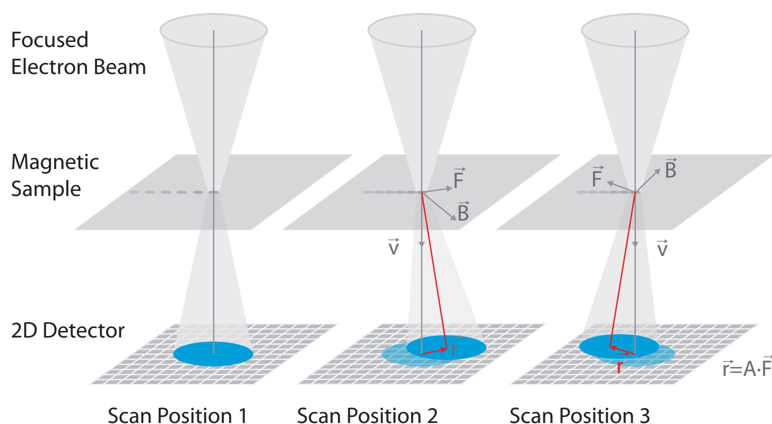

Figure 9.13: Principle of 4D-STEM imaging with a magnetic sample. The electron beam is focused to a spot on the sample and scanned over the sample. For each probe position $\vec{p}$ a two-dimensional image is recorded. The transmitted electron beam is deflected depending on the sample's magnetic field at the probe position. The shift $\vec{r}$ of the imaged disc is proportional to the Lorentz force $\vec{F}$ and hence the magnetic field $\vec{B}$.

The major requirement for a detector to be suited for 4D-STEM is a fast readout. In table 9.1, various STEM image sizes and readout rates are compiled to demonstrate that the detector readout rate has a great impact on the measurement time.

For a STEM image of 256×256 probe positions, a total number of 65 536 2D images need to be recorded. The pnCCD can record this number of probe positions in less than 70 s in full frame mode with 264×264 pixels in the detector images and a dwell time of 1 ms.

4D-STEM applications are not feasible with slow readouts as keeping a sample stable for over an hour is impossible if high spatial

Readout time	Frame rate	Number of probe positions		
		265 × 265	512 × 512	1024 × 1024
ms	fps			
500	2	9.8 h	36.4 h	145.6 h
200	5	3.9 h	14.6 h	58.3 h
50	20	1.0 h	3.6 h	14.6 h
20	50	0.4 h	1.5 h	5.8 h
5	200	5.9 min	21.8 min	87.4 min
1	1000	70 s	262 s	17.5 min
0.5	2000	35 s	131 s	8.7 min
0.25	4000	18 s	66 s	4.4 min

Table 9.1: Overview of measurement times depending on number of probe positions for various frame rates.

resolution is required.

By recording the full two dimensional intensity distribution, signals of standard and non-standard STEM detectors can be synthesized in post-acquisition. For a given detector geometry, the intensity is integrated over user defined areas. Examples of such synthetic detector areas resembling existing devices are shown in figure 9.14. In addition to these, any arbitrary area can be defined. Thus, a comparison between signals is possible, signals depending on scattering angles can be analyzed[11]and selected areas in diffraction patterns can be chosen for image formation[12].

[11] Jones, . . . , Ryll, . . . , et al., 2015.

[12] Kotula, . . . , Ryll, . . . , et al., 2016.

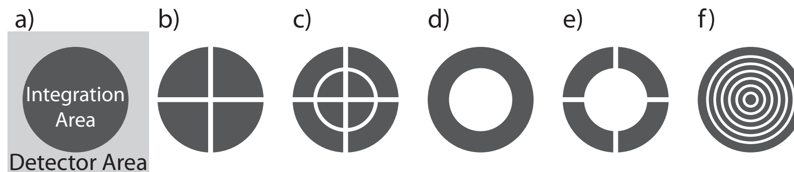

Figure 9.14: Patterns of synthetic detectors in 4D-STEM that are formed by integrating the intensity in the shown area. a) BF signal. b) 4 and c) 8 segmented BF signal for DPC analysis. d) ADF signal. e) and f) Segmented ADF signal. In principle, any synthetic detector can be created in post acquisition from the pnCCD data.

In the following sections, three applications in 4D-STEM are shown that benefit particularly from the pnCCD's high frame rates. The applications include imaging of magnetic domains, measurement of lattice strain in semiconductors and ptychography of carbon nanotubes. The first application demonstrates the principle of 4D-STEM nicely. The intensity distribution that is recorded is basically a disc that moves depending on the probe position. This movement is the source of information about the sample and needs to be determined. In the second application, a moving disc is recorded that exhibits strongly varying intensity distributions. Theses distributions are not the source for the information of interest, but must be considered in the data analysis determining the movement of the disc. This is an example where it is mandatory to record the intensity distribution with a two dimensional imager. In the third application, the intensity distributions inside the disc are the source of information about the sample. This also necessitates a fast two dimensional imager.

9.4 Imaging Magnetic Domains

The magnetic field vectors of magnetic domains in a nickel sample were imaged with a JEOL JEM-2800 microscope and the pnCCD at an electron energy of 100 keV.[13]

[13] Ryll et al., 2016.

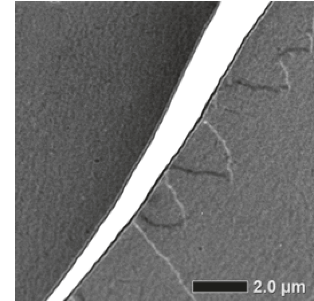

Figure 9.15: Image of the magnetic sample. The white area is a crack in the sample effectively being a vacuum region.

The TEM was operated with a switched off objective lens so that no external magnetic field was present at the sample position. The varying magnetic field in the sample causes a deflection $\mathbf{R}(x, y)$ of the electron beam corresponding to the strength and direction of the magnetic field $\mathbf{B}(x, y)$ at each sample position (x, y).

$$\mathbf{R}(x, y) \propto \mathbf{B}(x, y) \tag{9.7}$$

The BF disc at the detector plane of each STEM probe position moves in a correlative, two-dimensional way (see figure 9.13c). For two probe positions, the recorded images are shown in figure 9.16. The intensity distribution inside the disc is homogenous. The pnCCD was operated in the XPlus mode. Therefore, the TEM could be configured to deliver a high intensity in the BF disc with homogenous intensity distribution. The goal was to create a clear image of the BF disc that is well separated from the noise. A good separation makes the algorithm for finding the correct disc position easier and less error prone.

The pnCCD was operated in a windowing mode (264×132 pixels) at a readout rate of 2000 fps. A STEM image with 256×256 probe positions and a dwell time of 0.5 ms was acquired in 37 s.

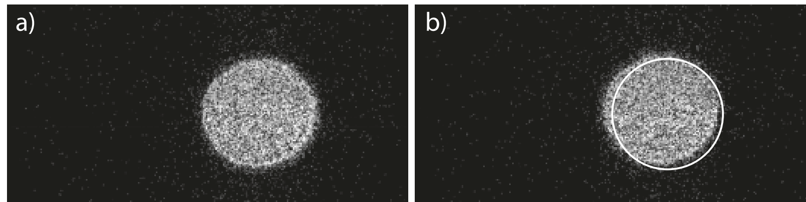

Figure 9.16: Example images of the BF disc in STEM at two different probe positions. The corresponding circle of the position of the disc in a) is overlayed in b) for comparison.

In principle the deflection $\mathbf{R}_{\text{sample}}(x, y)$ of the disc gives the magnetic field. The descanning[14] of the electron beam below the sample contributed partially to the movement of the BF disc. To account for this additional shift, a scan was recorded with the electron probe positioned in vacuum so that only the descanning caused a shift $\mathbf{R}(x, y)_{\text{vacuum}}$ in the position of the imaged BF disc. For both scans, the positions of the BF disc in each image were determined by calculating the center of gravity of the intensity distribution above an intensity threshold. The disc positions of the vacuum scan were then subtracted from the positions of the sample scan.

[14] See figure 2.4

In figure 9.17, a subset of the calculated positions for the x- and y-coordinates for both the scan in the sample and in vacuum are shown. The positions in the vacuum show a repetitive pattern caused by the descanning of the electron beam. Figure 9.17c shows the disc position after correction.

An additional constant offset in the position of the electron beam between the scan with and without the specimen was present. To

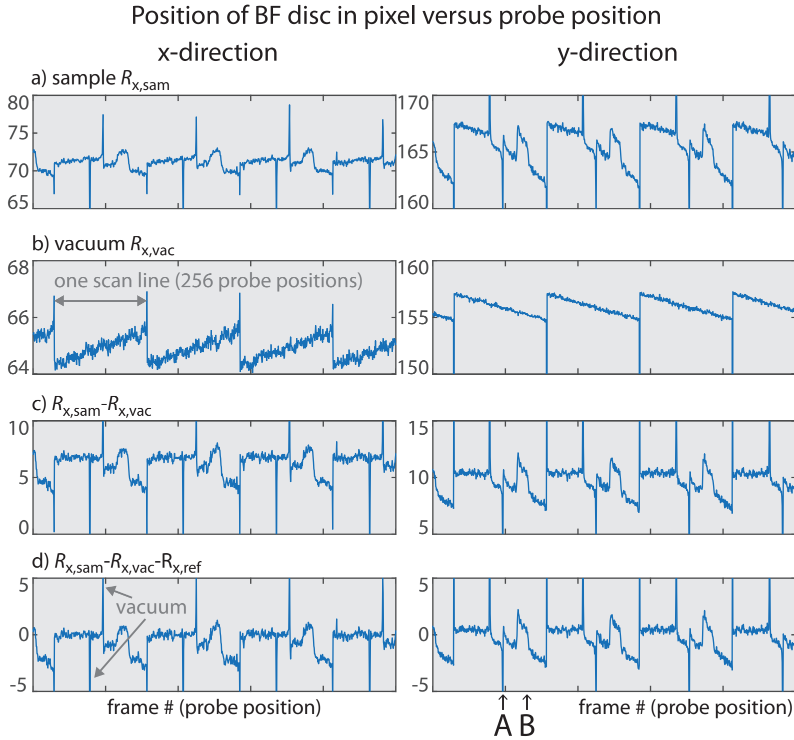

Figure 9.17: Positions of the BF disc depending on the probe positions in x and y direction. All units in pixels. In a) the electron beam is scanned over the sample, while in b) the electron beam is positioned and scanned in vacuum to determine the shift of the BF disc due to the scanning coils seen in the sawtooth pattern. c) Subtracting the contribution of b) from a) results in c), which still has a constant offset, that is removed in d). The features A and B are indicated again in figure 9.18b. The periodic peaks marked 'vacuum' originate from the edges of the crack in the sample. Measurements: PID100_001 and PID100_002

account for this constant offset, one reference position $\mathbf{R}_{\text{reference}}$ in vacuum was chosen (at a crack in the sample). The magnetic vector field was then calculated by subtracting the disc positions of each probe position from this reference position (see figure 9.17d):

$$\mathbf{R}(x,y) = \mathbf{R}(x,y)_{\text{sample}} - \mathbf{R}(x,y)_{\text{vacuum}} - \mathbf{R}_{\text{reference}} \quad (9.8)$$

In figure 9.18, the image acquired in standard Lorentz TEM mode with a conventional camera is compared to the image acquired with the pnCCD. The same features in the sample are visible. But in addition to the information where the magnetic domains and their boundaries are located, the direction of the magnetic field can be determined from the pnCCD images, which is shown in figure 9.18b and c. The magnetic field strength is determined in units of deflection of the BF disc in pixels. The absolute magnitude of the field vector can be determined from a reference measurement with a sample of known magnetic field strength.

Based on the same principle of a deflected electron beam, measurements of electric fields have been done.[15]

[15] Ritz, . . . , Ryll, . . . , et al., 2016.

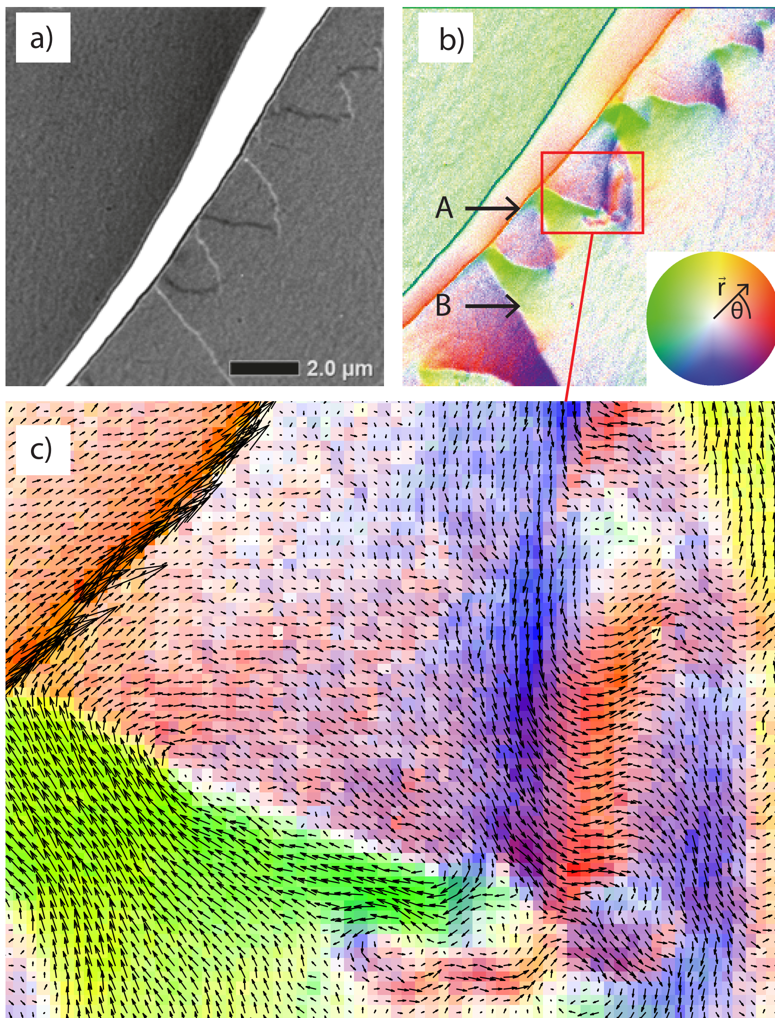

Figure 9.18: a) Standard Lorentz TEM mode image visualizing magnetic domain boundaries inside a magnetic sample. The white diagonal part is caused by a crack in the sample, effectively being a vacuum region. b) The same sample area imaged with the pnCCD using the 4D-STEM imaging method visualizing a proportional amplitude and direction of the magnetic field inside the sample. The magnetic field vector is calculated for each STEM probe position and color encoded as shown in the inset. The color hue represents the angle (red 0°, yellow 90°, green 180°, blue 270°) and the color saturation represents the amplitude of the vector (the saturation increases with increasing amplitude). The marker position A and B correspond the the ones in figure 9.17. c) Enlarged view of the marked region in b) with the magnetic field vectors as overlay revealing a greater detail of information compared to the standard Lorentz TEM imaging mode.

9.5 *Lattice-Strain Measurement*

The lattice strain of semiconductor materials strongly influences the electron mobility. As described in the introduction, smaller semiconductor devices and more efficient LEDs can be manufactured with materials that have a high electron mobility.[16]

[16] The same applies to the mobility of holes.

One possibility to tailor strain and hence electron mobility is to use compound semiconductors for example SiGe or InGaAs layers.[17] The strain that is induced due to lattice mismatches of the different crystal structures must be characterized in order to understand the performance of the final devices and further improve them. A direct method to measure the lattice strain in EM is the technique of convergent beam electron diffraction (CBED).[18]

[17] Sun, S. E. Thompson, and Nishida, 2007.

[18] Müller et al., 2012a.

CBED is a STEM technique in which a convergent electron beam is focused at the sample (see figure 9.19). A small interaction volume per probe position is achieved with a small beam spot diameter of a few nanometers down to 0.5 nm. A two dimensional diffraction pattern is recorded for each probe position. Since the probe is a convergent beam, the diffraction peaks appear as discs.[19] While the probe is scanned over the sample, the electron probe is at positions with varying local strain. The varying strain results in a varying condition for Bragg's law, resulting in a shift of the diffracted discs (see figure 9.19b). The shift of positions of the discs is the actual information that needs to be extracted from the recorded images. The lattice constant and hence strain is then given directly by Bragg's law:[20]

[19] Williams and Carter, 2009, p. 337.

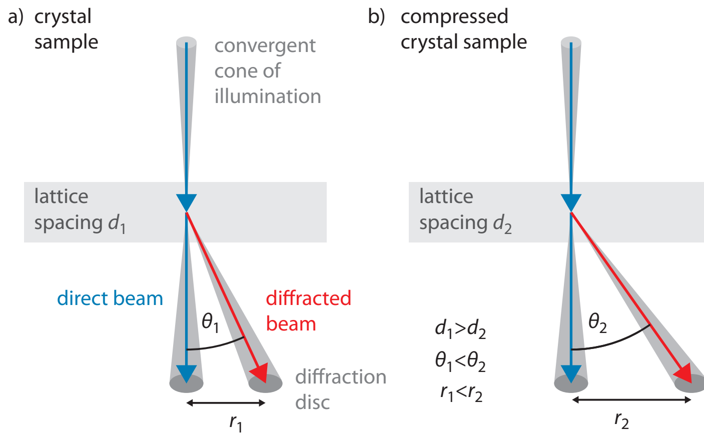

Figure 9.19: Principle of CBED and lattice strain measurement in 4D-STEM. a) A convergent electron beam leads to diffraction discs instead of peaks. The angle or distance between the direct beam and a diffracted beam depends on the spacing between the diffracting lattice planes in the sample. b) A changed lattice constant due to compressive strain results in a greater angle θ_2 that satisfies Bragg's law. The pictured angles and distances are exaggerated.

[20] W. H. Bragg and W. L. Bragg, 1913.

$$\lambda = 2d_{\text{hkl}}(\vec{p}) \cdot \sin\theta^{\text{B}}_{\text{hkl}}(\vec{p}) \tag{9.9}$$

For a given lattice plane denoted by the Miller indices (hkl), the lattice constant d_{hkl} and the scattering Bragg angle $\theta^{\text{B}}_{\text{hkl}}$ are functions of the probe position $\vec{p}$. Scattering into small angles of $\theta_{\text{B}} < 1°$ can be assumed with typical values of the wavelength $\lambda < 10\,\text{pm}$ and lattice constants of $d < 1\,\text{nm}$. Then θ_{B} is approximated by the distance $\vec{r}$ between the direct beam and the diffracted beam.

$$2\sin\theta_{\text{B}} \approx 2\theta_{\text{B}} = \theta \approx \vec{r} \tag{9.10}$$

In practice, not the whole DP must be recorded but it is sufficient to image a single diffraction disc. The strain can be calculated in terms of relative movements of the position of the imaged disc at a strained location compared to an unstrained location.[21]

[21] Müller, ..., Ryll, ..., et al., 2012b.

Similar to the previous application of magnetic domain imaging, the positions of the diffraction discs contain the information about the sample. The difference is that the disc exhibits a strong inhomogeneous intensity distribution. Additionally, the intensity changes strongly in distribution and quantity as the electron beam is scanned over the sample as shown in figure 9.20 for three probe positions.

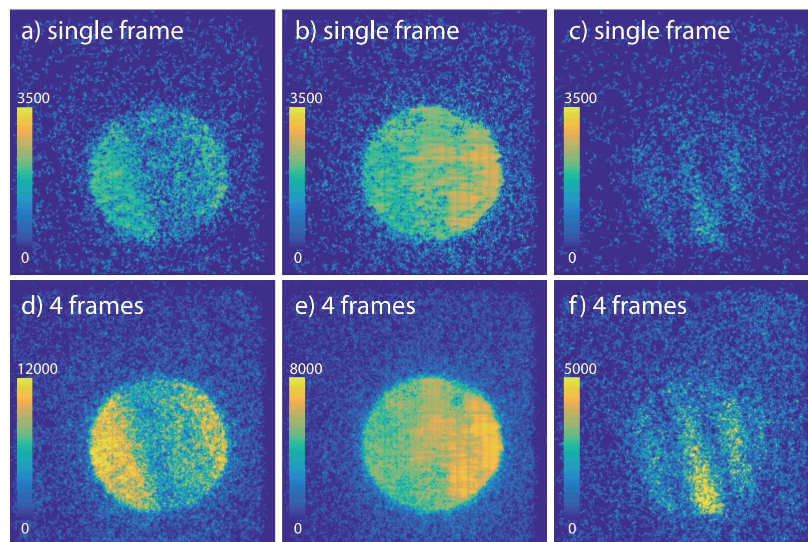

Figure 9.20: Example images of a diffraction disc at three probe positions. The intensity distribution inside the disc is inhomogeneous due to dynamic scattering of the TEM electrons in the sample. The total intensity and its distribution varies at different probe positions a), b) and c). The recorded intensity is very low for c) and the sum of four frames delivers a better signal in f). The positions of the disc change depending on the local strain in the sample. The TEM electrons outside the disc are caused by inelastic scattering.

Dynamic scattering of electrons inside the sample leads to the inhomogeneous and varying intensity distribution.[22] It could be argued, that in the previous case of the magnetic field imaging, the information could be retrieved with a segmented detector (non pixelated, 4-8 detector cells)[23], due to the homogenous intensity inside the BF disc. With intensity distributions shown in figure 9.20, a segmented ring detector would deliver a signal that might be interpreted falsely. Therefore, for CBED, a detector that provides intensity information in a two dimensional image is mandatory.

[22] Williams and Carter, 2009, p. 339.

[23] See section 2.3

Algorithms have been developed that successfully determine the positions of the disc, even from images with low intensity and inhomogeneous intensity distributions such as the one in figure 9.20c.[24]

[24] Müller et al., 2012a.

For this experiment, the camera was installed on an FEI Titan 80/300 microscope. The electron energy was set to 300 keV. Two types of experiments have been performed: 1) a linear scan over a well characterized sample and 2) a two dimensional scan.

In the first experiment, a heterogeneous semiconductor sample was investigated, consisting of alternating layers under compressive and tensile strain buffered in unstrained layers of GaAs with element compositions as shown in figure 9.21.

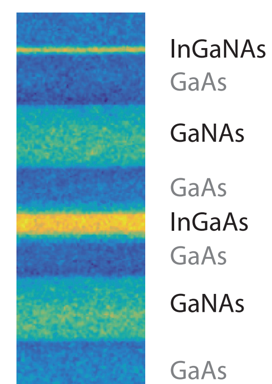

Figure 9.21: STEM-HAADF image of the investigated heterogeneous semiconductor sample.

This sample had been investigated before in a proof of concept measurement with a scintillator based camera that was read out with a frame rate of 2 fps. That previous measurement serves as a reference

to the measurements done with the pnCCD. The pnCCD was operated in the HiRes mode[25] and read out with 1000 fps. The probe position dwell time was set to 200 ms. The temporal oversampling allowed an integration of many frames and a comparison of the results depending on the (virtual) dwell time. In hindsight, this also allows a comparison of the HiRes and HCHC mode and what kind of improvement the higher CHC delivers for this kind of experiment.[26]

[25] At the time of the experiment, the HCHC mode was not yet available.

[26] Schmidt, 2017.

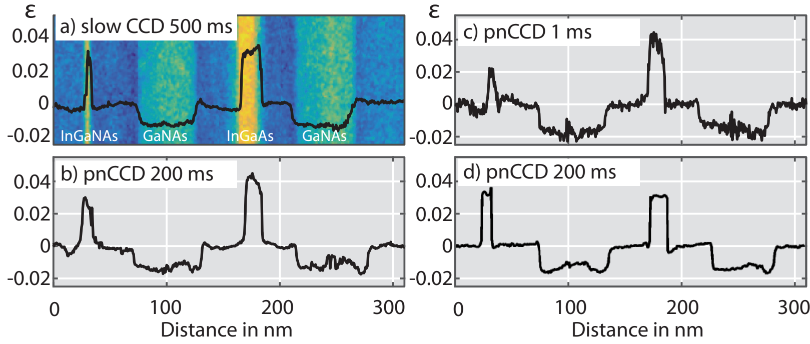

Figure 9.22: Strain profile of the strained semiconductor sample. a) The background image shows a DF image of the sample. The strain profile was acquired with a previously used camera. b)-d) Strain profiles acquired with the pnCCD that reproduce the reference measurement of a). The effective dwell time are given at the top. b) and c) The 004 disc was recorded. d) The 008 disc was recorded. Adapted from Müller, . . . , Ryll, . . . , et al., 2012b; Müller, . . . , Ryll, . . . , et al., 2014

A comparison of lattice strain profiles determined in the reference measurement and from data recorded with the pnCCD is shown in figure 9.22. The relative strain ϵ compared to an unstrained region is given (GaAs region on the very right in figure 9.22a). In all measurements the same compressive and tensile features can be seen. For the measurement of the 004 disc with the pnCCD, the strain profile was calculated from single frames per probe position equal to a dwell time of 1 ms (figure 9.22c) and by integrating 200 frames equal to a virtual dwell time of 200 ms (figure 9.22b).

The precision in the determination of strain was calculated by taking the standard deviation of values from an unstrained region in GaAs (on the right end in the strain profiles). The precision depends on the dwell time and which diffraction disc is used (see figure table 9.2). The precision for the reference measurement and the pnCCD

	Slow camera	pnCCD		
Diffraction disc	004	004	004	008
Dwell time in ms	500	200	1	200
Precision $\times 10^{-4}$	7.3	7.0	13.0	4.0

Table 9.2: Comparison of precision in lattice strain measurements. Data from Müller, . . . , Ryll, . . . , et al., 2014.

measurement using 200 frames is comparable. However, the dwell time for the pnCCD measurement is 2.5$\times$ shorter. If single frames are used (dwell time of 1 ms), the precision is reduced by a factor of two, but the measurement time is also reduced by a factor of 200 (500$\times$ compared to the reference measurement). The precision is still high enough for most applications.[27]The precision measured with the 008 disc at a virtual dwell time of 200 ms is higher than for the 004 disc. The 008 diffraction disc is more sensitive to strain (a change of the lattice constant d) due to the larger scattering angle θ_B. The intensity in the disc is usually also lower. Since the pnCCD yields a large signal

[27] Müller, . . . , Ryll, . . . , et al., 2012b.

for each TEM electron, the reduction in intensity is not a drawback.

In the second experiment, a MOSFET sample was investigated. Strain was induced due to the inclusion of Ge_xSi_{1-x}/Si. The probe position was moved in a two dimensional area. A similar, reference measurement had been done before with a scintillator based camera. Due to the low readout rate, the strain map of the reference measurement was recorded at a coarse spatial sampling with 45×60 probe positions in approximately 10 min (≈ 5 fps), though at a large field of view. The strain map recorded with the pnCCD was recorded with 256×256 probe positions and an oversampling of four frames per probe position (dwell time of 4 ms) resulting in an acquisition time of 4.3 min.

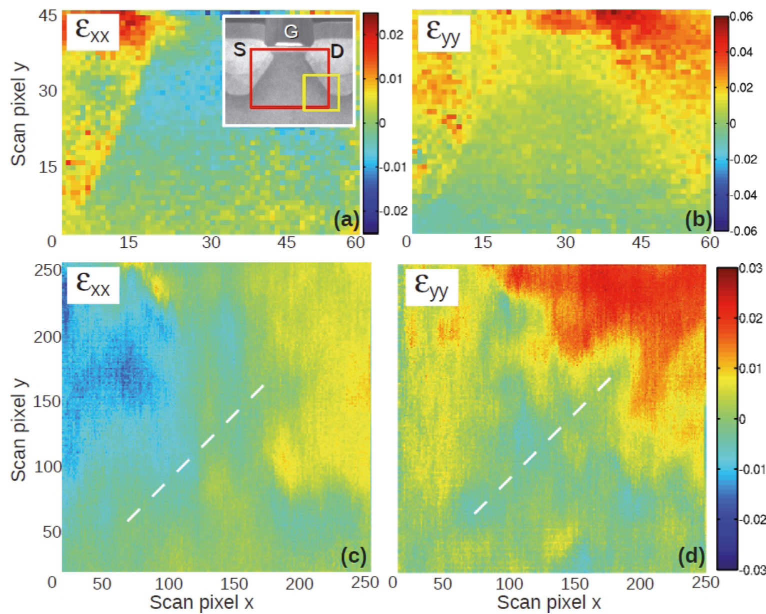

Figure 9.23: Lattice strain maps of a MOSFET sample with induced strain due to the use of Ge_xSi_{1-x}/Si. The relative strain ϵ compared to an unstrained region is shown in x and y direction. Strain maps in a) and b) are acquired with a low readout rate camera, with a coarse sampling and 45×60 probe positions. Strain maps c) and d) are acquired with the pnCCD with a finer sampling and 256×256 probe positions. The inset in a) shows a DF image of the sample and the scanned areas (the red rectangle for a) and b), the yellow square for c) and d)). Images taken from Müller, . . . , Ryll, . . . , et al., 2014.

In figure 9.23, the two dimensional strain maps of both measurements are shown. The reference measurement shows the strain below the gate region in a wide field of view. The measurement with the pnCCD shows the strain in a smaller region than in the other field of view. The strain acquired with the pnCCD map is much finer sampled and yet recorded in less time. Due to the fine sampling, a stacking fault can be seen as indicated in figure 9.23d.

Both measurements of lattice strain show that the pnCCD is an improvement in terms of readout speed over the slower detectors that had been used in previous measurements. The improvement means that a measurement of 256×256 probe positions can be recorded in less than 70 s. Compared to the previously used camera, this is a factor of 200 increase. The pnCCD is fast enough to enable the measurement of lattice strain in semiconductors in practicable time frames and at high spatial sampling.

9.6 *Ptychography with the pnCCD*

Ptychography is a method to retrieve the phase of the electron wave exiting the sample. When the electron wave passes through the sample, the phase of the electron wave is modified by the atomic potentials inside the sample. Thus the phase reveals information about the imaged structure.

The possibility to retrieve the phase is especially important for samples that mainly affect the phase of the electron wave but not the amplitude. An amplitude change can be interpreted as scattering which gives rise to Z-contrast. Light elements generate little or no Z-contrast. However, biological samples, for example, consist mostly of carbon, oxygen or nitrogen.

A direct measurement of the electron wave's amplitude and phase is not possible but only of its intensity ($I = |\Psi|^2$). Therefore the phase must be retrieved from intensity images. In TEM imaging, holographic methods use interference to encode the phase in recorded intensity. Another method is the acquisition of a through focal series, in which the focus of the electron beam is varied in depth in the sample.[28] Ptychography is a 4D-STEM method to retrieve the phase of the exit wave function. The electron beam conditions are chosen such that parts of the direct beam and diffracted beams overlap (see figure 9.24a). The electron waves of the different beams interfere in the overlapping regions. The phase information is encoded in these areas where the direct and diffracted beam interfere. During the measurement, the convergent electron beam is scanned over the sample. For each probe position $\mathbf{R}_\mathrm{p}$, the diffraction pattern is recorded in a two dimensional image $\mathbf{K}_\mathrm{f}$ (see figure 9.24b), resulting in a four dimensional data set (two dimensions in the sample and two dimensions in the recorded image).

[28] An overview is given for example in Yang, . . . , Ryll, . . . , et al., 2016

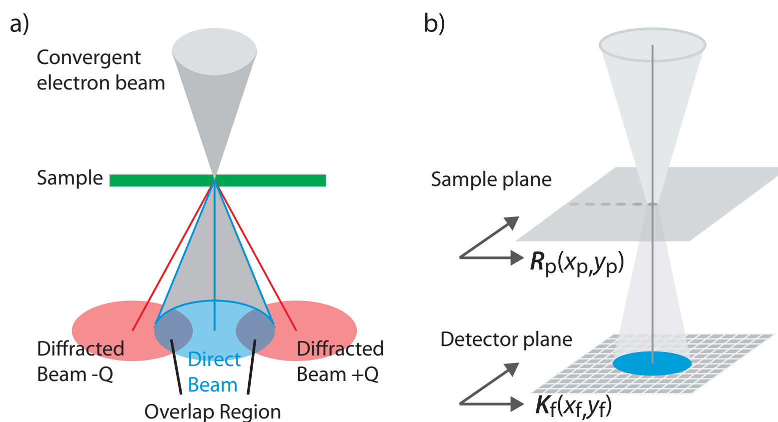

Figure 9.24: Beam configuration for 4D-STEM ptychography. a) Due to the convergent electron beam, the diffraction spots widen to diffraction discs, which are imaged. Depending on the TEM settings, diffracted beams can overlap with the direct beam resulting in interference. b) The electron beam is scanned over the sample at positions $\mathbf{R}_\mathrm{p}$. The diffraction pattern is recorded at the detector plane with intensity values at the pixel coordinates $\mathbf{K}_\mathrm{f}$. In practice only an area a little bit larger than the BF disc is imaged.

Ptychography with regard to EM has been described by Rodenburg et al. in 1992.[29] Experimental measurements proved that the ptychographic method works.[30] However, only small images with 32×32 probe positions could be recorded due to a low frame rate and significant drift of the sample. In a more recent experiment,

[29] Rodenburg and Bates, 1992.

[30] Rodenburg, McCallum, and Nellist, 1993.

64×64 probe positions were recorded in approximately three minutes.[31] The missing component for a feasible experimental realization had been a fast spatially resolving detector. The pnCCD fulfills the requirements of a detector suited for ptychography[32].

[31] Pennycook et al., 2015.

[32] Yang, ..., Ryll, ..., et al., 2015b; Yang, ..., Ryll, ..., et al., 2016.

The principal steps involved in ptychography imaging are shown in figure 9.25. First a 4D data set of the the sample is recorded (denoted $|M(\mathbf{K}_f, \mathbf{R}_p)|^2$). A two dimensional Fourier transform with respect to probe position $\mathbf{R}_p$ results in a 4D data set $G(\mathbf{K_f}, \mathbf{Q_p})$ with complex entries. From this complex data set, the amplitude and phase can be reconstructed to create a phase image of the sample.

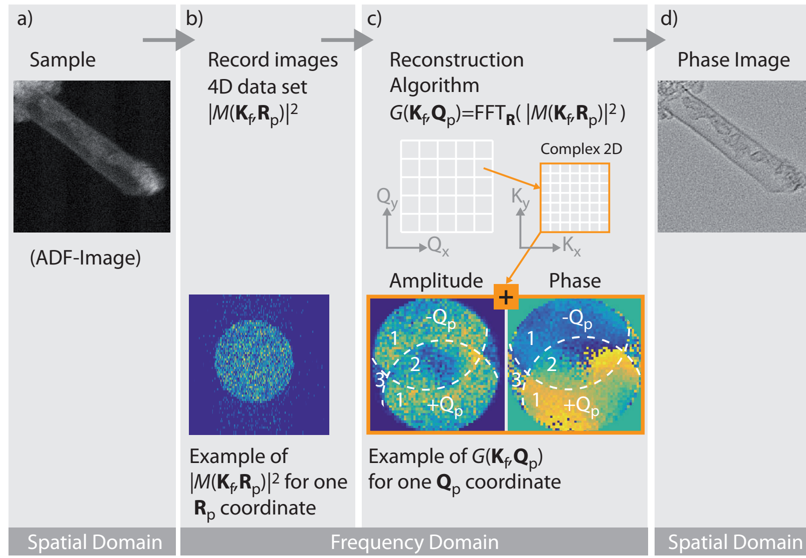

Figure 9.25: Principal steps of ptychography in 4D-STEM. a) An ADF image of the investigated nanotube containing fullerenes. b) For each probe position p, the BF disc of the diffraction pattern is recorded in a two dimensional image. For one probe position, an example image is shown. c) The amplitude and phase is reconstructed from the whole 4D data set. For each frequency component Q_p, a two dimensional complex image is obtained, from which the phase and amplitude is determined. The amplitude and phase for one Q_p is shown. d) A phase image of the sample is obtained via an inverse Fourier transform. Images in a) and d) adapted from Yang et al., 2016.

Following the notation in[33], the diffraction pattern can be described as:

[33] Yang, ..., Ryll, ..., et al., 2016.

$$M(\mathbf{K}_f, \mathbf{R}_p) = \int P(\mathbf{R} - \mathbf{R}_p)\psi(\mathbf{R}) \exp(2i\pi \mathbf{K}_f \cdot \mathbf{R}) d\mathbf{R} \quad (9.11)$$

with the probe function $P(\mathbf{R} - \mathbf{R}_p)$ and the specimen transmission function $\psi(\mathbf{R})$. Note that $\mathbf{K}_f = (K_x, K_y)$ and $\mathbf{R}_p = (R_x, R_y)$ are two dimensional vectors at the detector plane ($\mathbf{K}_f$) and the sample plane ($\mathbf{R}_p$). M is not recorded directly, but the intensity $|M|^2$. A Fourier Transform of $|M(\mathbf{K}_f, \mathbf{R}_p)|^2$ with respect to the probe positions $\mathbf{R}_p$ gives:

$$G(\mathbf{K_f}, \mathbf{Q_p}) = \mathcal{F}_{\mathbf{R}_p}\left(\left|M(\mathbf{K}_f, \mathbf{R}_p)\right|^2\right) \quad (9.12)$$

$$= A(\mathbf{K}_f)A^*(\mathbf{K}_f + \mathbf{Q}_p) \otimes_{\mathbf{K}_f} \Psi(\mathbf{K}_f)\Psi^*(\mathbf{K}_f - \mathbf{Q}_p) \quad (9.13)$$

The convolution $\otimes_{\mathbf{K}_f}$ is carried out with respect to $\mathbf{K}_f$. The first and second term depend on the probe forming aperture function $A(\mathbf{K}_f)$ and the Fourier transform of the specimen transmission function $\Psi(\mathbf{K}_f)$.

From equation 9.13, the phase can be calculated. For the kind of data recorded with the pnCCD, two methods have been used successfully as a reconstruction method:[34]The single-side band (SSB)

[34] Yang, ..., Ryll, ..., et al., 2016; Yang, ..., Ryll, ..., et al., 2017.

method[35] and the Wigner distribution deconvolution (WDD) method.[36]

Experiments with several samples have been conducted to investigate the suitability of the pnCCD in ptychography methods. For these experiments, the pnCCD camera was installed at a JEOL ARM200-CF microscope operated at 80 keV and 200 keV. The HCHC mode was used with various readout modes. The full frame readout with 1150 fps and binning up to 4× with 4000 fps was used. With the 4× binning mode, a whole 4D data set consisting of 256×265 probe positions could be recorded in ≈16 s. As explained in section 9.3, a short measurement time is important, reducing effects of instability in the microscope and increasing the imaged field of view. The ADF signal was recorded with a DF detector simultaneously with the pnCCD images. Complementary information is obtained in this way, with contrast due to strong scattering (Z-dependent, heavy elements) and contrast due to weak sample interaction (the phase contrast, light elements). Exemplary single frames in a ptychography measurement are shown in figure 9.26. In each of these two images, approximately 11 600 TEM electrons impinged on the detector in the BF disc area, which averages to about 0.44 TEM electrons per pixel.

[35] Pennycook et al., 2015.

[36] Rodenburg and Bates, 1992.

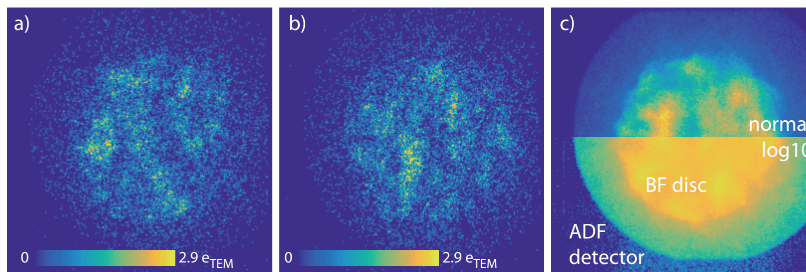

Figure 9.26: Exemplary single frames in a ptychography measurement. a) and b) Single frames showing the inhomogeneous intensity distribution inside the BF disc. c) 100 frames are integrated to better show the position of the BF disc. The lower half shows the logarithm of the intensity, showing more clearly that the ADF detector blocks part of the beam.

In a first experiment[37], GaN was imaged along the $[2\bar{1}\bar{1}0]$ orientation. For the following images, the number of probe positions was 256×256, the pnCCD was read out at 4000 fps in a 4× binning mode. In addition to the ADF image, a synthetic ABF image[38] was formed by integrating the intensity in a ring with a collection angle of 7.2 mrad to 14.4 mrad.

[37] Yang, . . . , Ryll, . . . , et al., 2015a.

[38] See figure 9.14d for the geometry.

In figure 9.27, the ADF image, a synthetic ABF image and the amplitude and phase image obtained through the ptychography reconstruction are shown. The GaN sample is clearly reproduced in all images. The higher intensity peaks in the ADF image match the inverted contrast in the ABF, amplitude and phase image. The TEM electrons are mostly scattered from the heavier Ga atom columns which leads to a higher signal in the ADF image and an inverted signal in the ABF image. This corresponds to absorption in the amplitude and phase image. The advantage of ptychography compared to standard DF imaging, however, is seen in the phase image. The phase image of GaN reveals the position of the lighter N columns which are not visible in the ADF or ABF image. As a primary result, the method of the ptychography in conjunction with the pnCCD works, including the retrieval of the phase shift induced by a weakly scattering sample.

In a further experiment[39], a complex sample was investigated

[39] Yang, . . . , Ryll, . . . , et al., 2016.

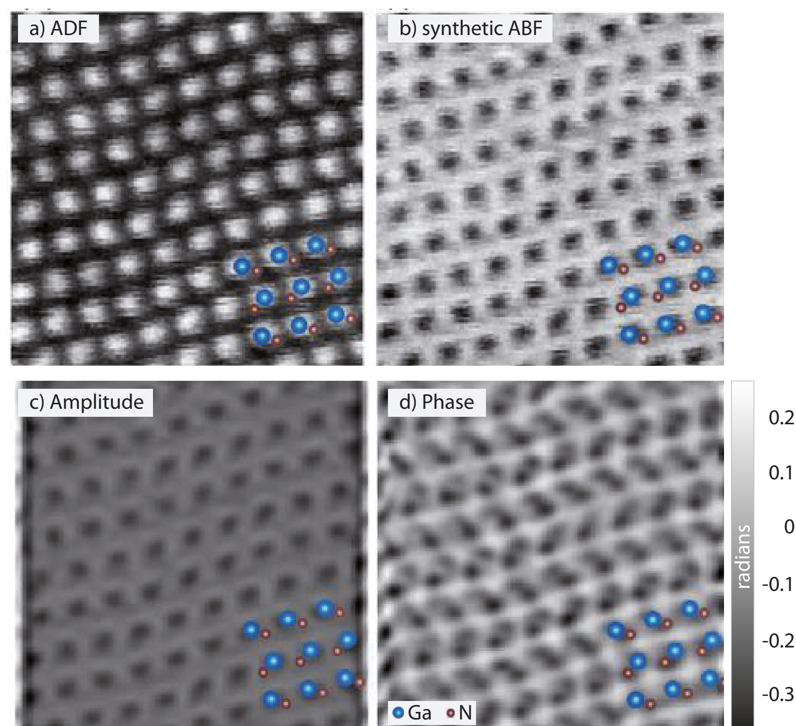

Figure 9.27: Comparison of images of a GaN sample recorded with a ADF detector and the pnCCD. a) The ADF signal was recorded simultaneously and clearly shows the Ga columns. b) A synthetic ABF image shows similar inverted contrast to the ADF image. c) The amplitude image and d) the phase image of the ptychographic reconstruction. In the phase image, the columns of the lighter N can be seen, which is not the case for the ADF image a). Images adapted from Yang, . . . , Ryll, . . . , et al., 2015a.

that was mentioned in the introduction as a drug delivery system. The sample consists of a carbon nanotube (CNT) to which a C_{60} carbon fullerene is attached with a functionalized tether (see figure 9.28a).[40] In principle, the active medicine should be contained in the

[40] For a detailed description of the sample, see supplementary information in Yang, . . . , Ryll, . . . , et al., 2016

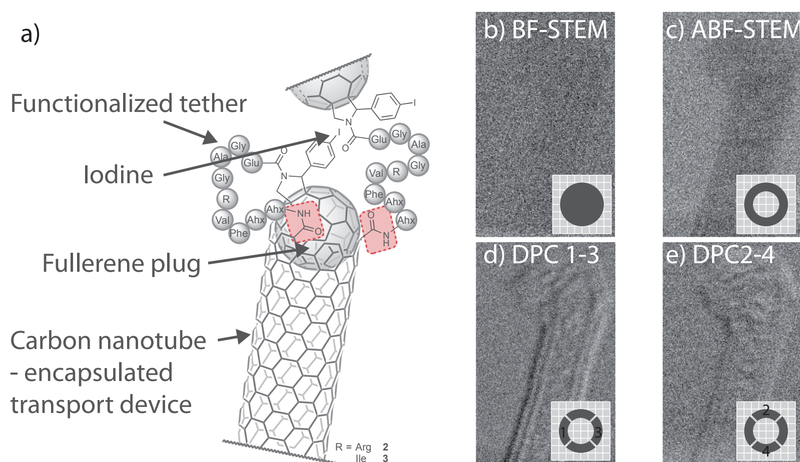

Figure 9.28: a) Intended design of a functionalized carbon nanotube proposed for drug delivery. b-e) Comparison of images created from synthesized detectors shown as insets. For such a sample, there is almost no contrast in the BF signal b). Images taken from Yang, . . . , Ryll, . . . , et al., 2016.

CNT. Inside the body of the patient, the tether should dock only to an intended recipient (cell, protein or other structure) upon which the tether pulls the fullerene plug and the drug is released. The synthesis of such a sample is a complex procedure, therefore the characterization of such a system is of great importance to ensure a successful synthesis.

The characterization is difficult because the sample consists mostly of weakly scattering elements (i.e. carbon). Additionally there are some heavy iodine atoms acting as markers. With conventional

imaging methods, only images with no contrast or little contrast can be recorded. As an example, in figure 9.28b)-e) images are shown that are created from detectors that are synthesized from pnCCD data. With conventional BF- and ABF-STEM imaging only a slight shadow of the CNT is seen. With DPC imaging the outlines of the CNT can be seen but it is not clear what is inside of the CNT. However the phase of the passing electron wave is modified which should provide contrast in ptychographic imaging.

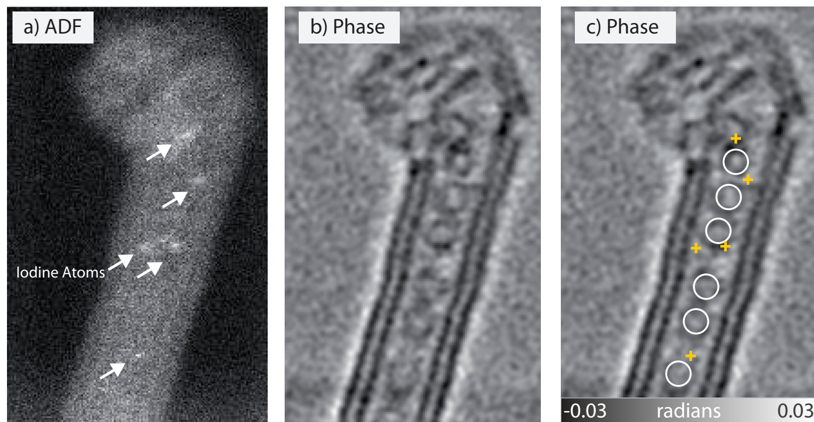

Figure 9.29: ADF and phase contrast image of carbon nanotube system. Images adapted from Yang, . . . , Ryll, . . . , et al., 2016.

Figure 9.29 shows the ADF image and the reconstructed phase image of such a CNT system. The ADF image clearly shows the iodine atoms, due to strong scattering. Only a shadow of the CNT is seen in the ADF image. In the phase image, the double walled CNT is clearly seen. In addition fullerenes can be identified (white circles in figure 9.29c) that have entered the CNT which was not intended. By comparing both images, the iodine atoms can be located outside the fullerenes. Such an image provides scientists researching CNT systems with valuable feedback, in this case that the intended synthesis did not fully work out. Such characterization helps to better synthesize such CNT systems, different fabrication schemes can be tested and their rate of successful fabrication can be determined. This shows that ptychography with the pnCCD is a valuable tool for material characterization.

The inherent aberrations of the electron lenses which are included in the aperture function $A(\mathbf{K}_f)$ of equation 9.13 can be determined in post-processing with the WDD method.[41]The phase change caused by the sample and the phase change introduced by the aberrations of the lenses can be deconvolved and images with increased contrast can thus be created. A further opportunity lies in optical sectioning. With the phase data, the focus of the electron beam can be shifted in z direction, giving rise to contrast of features in different depths in the sample.[42]

[41] Yang, . . . , Ryll, . . . , et al., 2016.

[42] Ibid.

9.7 Summary of Applications

In this chapter, it is shown that the pnCCD can be used in electron microscopy applications successfully. The key features of the pnCCD,

its fast readout and high sensitivity, improve existing methods. In electron tomography, it was shown that a whole tilt series can be recorded in a few seconds. This opens up high speed, high throughput tomography. With three further experiments, it was shown that the pnCCD is a fast, spatially resolving detector that renders 4D-STEM methods feasible. In a first experiment, the magnetic field of magnetic domains in a sample was determined. Second, the lattice strain in semiconductor samples was determined with the pnCCD. Compared to previous proof of principle measurements with slow readout cameras, the pnCCD speeds up the acquisition by a factor of 200. In the third experiment it was shown that the pnCCD unlocks the potential of the emerging field of ptychography. The phase of the electron wave was determined from samples that are otherwise difficult to characterize.

10 Conclusions

The present work explains the signal response of the pnCCD under electron illumination. The detailed analysis of readout data provides an unprecedented understanding on the interdependence of the pnCCD's parameters, the energy of the impinging electrons and the recorded signals. Furthermore, the conducted experiments prove that the pnCCD is a step forward for electron imaging applications in transmission electron microscopy.

A camera with the pnCCD was developed that was mounted at TEMs at numerous research institutes. With the recorded data, the response of the pnCCD to electron illumination was determined. Single electrons were imaged and an analysis on single electrons yielded energy spectra. Based on the data of the energy spectra, the signal response could be explained. A TEM electron entering the pnCCD scatters inside the sensitive bulk, generating signal electrons along its track. Most TEM electrons deposit their whole energy in the pnCCD which can be identified as a peak in the energy spectrum. A fraction of the TEM electrons do not deposit their whole energy in the detector, but scatter outside the pnCCD, creating a broad distribution in the energy spectrum. Both parts of the energy spectrum could be explained based on the theory of scattering of electrons, also supported with additional simulations. With the established model, the correct number of TEM electrons can be determined in intensity images with backscattered electrons correctly taken into account. The energy of the TEM electrons is the main parameter influencing the signals recorded with the pnCCD including the spatial resolution.

The spatial resolution of the pnCCD under electron illumination was determined for electron energies of 20 keV to 300 keV. Several models were developed to improve the spatial resolution when imaging single TEM electrons. For low energy electrons between 20 keV and 80 keV the point of entry of the TEM electrons could be determined with a sub-pixel resolution. For 40 keV, images with an 11×11 sub-pixel resolution, corresponding to 2904×2904 pixels, show fine details smaller than the physical pixel size. For higher energies of 200 keV and 300 keV, a model based on the directional scattering track of the electrons increases the spatial resolution and the contrast.

With several TEM applications, it was shown that the pnCCD is an excellent imager for electrons. The high readout rates proved particularly beneficial. For electron tomography, the pnCCD opens

the door to fast and high throughput 3D imaging of samples at the nanometer scale. The data for a three-dimensional reconstruction of a nanotube could be recorded in under 3.5 s.

For applications in the scanning mode of the TEM, it was shown that the pnCCD is a capable spatially resolving detector. The pnCCD enables the determination of lattice strain in semiconductor samples on the nanometer scale with short measurement times. A speed-up by a factor of 200 to 500 is achieved with the pnCCD compared to previous measurements with slow cameras. With further STEM experiments it was shown that the pnCCD enables ptychography with electrons. The ptychographic method allowed the retrieval of the phase information of the electron wave after passing a complex nanotube system consisting of weakly scattering elements. The data recorded with the pnCCD provided conclusions about the sample that were not accessible before. Previously, applications that required spatial information at each scanning point were hindered by slow cameras. Now, with the pnCCD, fast and efficient imaging is enabled for STEM applications.

10.1 Future Devices

The models and methods developed in this thesis and the acquired understanding provide input for the development of future electron imaging devices. One important parameter worth improving is the charge handling capacity (CHC). The investigated pnCCD is limited at 200 keV to about 5.5 TEM electrons per pixel. If this value can be increased, the signal in images is increased. One possibility is to use larger pixels with an increased CHC. For example, the type of pnCCD with 75 µm pixel size has a CHC of about $1.8 \times 10^6\, e^-_{sig}$ (equivalent to 33 TEM electrons at 200 keV).[1]

[1] Schmidt, 2017.

A different type of detector currently being developed based on the depleted p-channel field-effect transistor (DEPFET) shows promising capabilities.[2] The DEPFET exhibits a CHC of up to $5 \times 10^6\, e^-_{sig}$. In addition, readout rates of up to 4.5×10^6 fps are possible in a burst operation mode. Considering electronic constraints and data stream rates, in a continuous operation mode the readout rate is in the order of 10^5 fps. As is shown in this thesis, a further improvement in readout rates by a factor of 100 enables new methods in TEM.

[2] Kemmer and Lutz, 1987; Porro et al., 2012.

The DEPFET, but also other types of future detectors, will be characterized and optimized with the developed methods of this work. The scattering of electrons in the detector and the resulting signals in the pixels depend on the specific detector geometry, technology and operation parameters and their relationships can be explained based on physical principles as shown in the previous chapters. For these reasons, this dissertation will provide a comprehensive foundation for the development of next generation electron imagers.

A Appendix

A.1 Modulation Transfer Function

The modulation transfer function (MTF) describes how much contrast of the object function is transferred by the imaging process depending on the spatial frequency. This is shown visually in figure A.1.

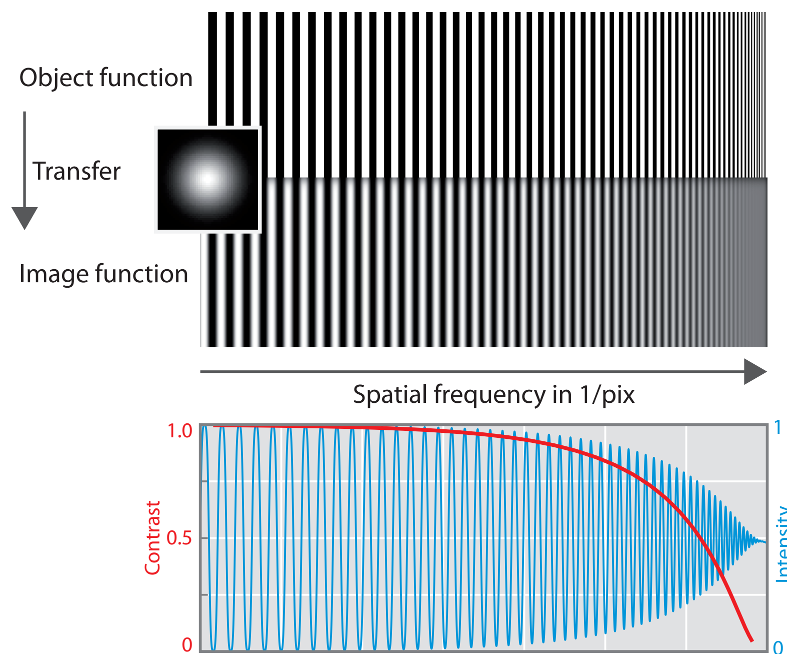

Figure A.1: Visual concept of the MTF. An object containing components with increasing spatial frequencies is imaged. The imaging process can be described as a convolution of the object function with a Gaussian PSF. The resulting image shows decreased contrast with increasing spatial frequencies.

The procedure to determine the MTF consists of the following steps:

- acquire image with a slanted edge, A_{edge}
- define region in image that contains the edge
- for each row in the ROI of the image, find the edge
- fit ESF for each line, use center position b as edge position
  $f(x) = a * \text{erf}((b - x)/c) + d$
- fit line through edge positions, $f(x) = m * x + \text{const}$
- create oversampled ESF,
  shift each line, so that edge position is at the same coordinate for each line

- fit ESF to oversampled edge
- use analytic relationship between ESF and MTF, fit parameter c

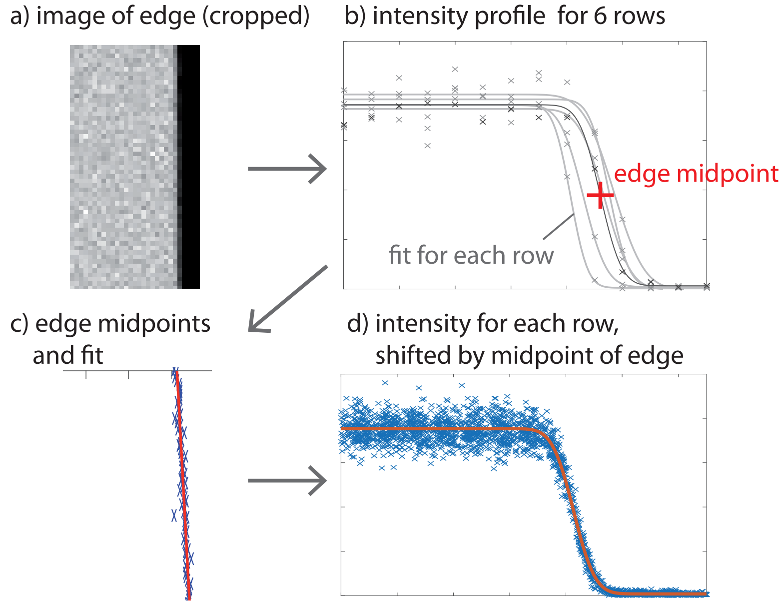

Figure A.2: Procedure for the calculation of the MTF. a) An image region is chosen with homogeneous illumination on the bright side and in which the slanted edge covers all pixel positions. b) For each row, an ESF is fitted to the data and the edge midpoint is determined (parameter b in equation A.5). For clarity, only six rows are shown here. c) A linear function is fitted through the edge positions for each row. From this fit, the (sub-pixel) shift of each row is determined so that the edge position is at the same position for each row. d) The over sampled ESF is fitted resulting in the parameter λ.

According to:[1]

$$\mathrm{PSF_G}(r) = \frac{1}{\pi\lambda^2}\exp(-r^2/\lambda^2) \tag{A.1}$$

$$\mathrm{LSF_G}(x) = \frac{1}{\pi\lambda}\exp(-x^2/\lambda^2) \tag{A.2}$$

$$\mathrm{ESF_G}(x) = \frac{1}{2}\mathrm{erfc}(-x/\lambda) \tag{A.3}$$

$$\mathrm{MTF_G}(\omega) = \exp(-\pi^2\lambda^2\omega^2/4) \tag{A.4}$$

The LSF is basically the PSF extended in one dimension (or a cut through its middle). The Fourier transform of the LSF is the MTF. The LSF can be obtained by differentiating the ESF (very noisy) or by fitting the analytic expression A.3 and using the fitting parameter λ.

The ESF that is shifted by b (edge position at b) is:

$$\mathrm{ESF}(x) = \frac{1}{2}\mathrm{erfc}\left(-\frac{(x-b)}{\lambda}\right) \tag{A.5}$$

$$\mathrm{LSF}(x) = \frac{1}{dx}\mathrm{ESF}(x) \tag{A.6}$$

$$\mathrm{MTF}(\omega) = \mathcal{F}(\mathrm{LSF}(x)) \tag{A.7}$$

[1] McMullan et al., 2009.

A.2 *Detective Quantum Efficiency*

The detective quantum efficiency DQE,[2] with the average gain $\bar{g}$, gain variance σ_g^2 and Poisson distributed input signal S_{in}:

[2] McMullan et al., 2007; McMullan et al., 2009; Zweig, 1965.

$$\text{DQE} = \frac{\text{SNR}_{\text{out}}^2}{\text{SNR}_{\text{in}}^2} \tag{A.8}$$

$$\text{SNR} = \frac{S}{N} = \frac{\mu}{\sigma} = \frac{\mu}{\sqrt{\text{var}}} \tag{A.9}$$

$$S_{\text{out}} = \bar{g} S_{\text{in}} \tag{A.10}$$

$$N_{\text{out}}^2 = \bar{g}^2 N_{\text{in}}^2 + \sigma_g^2 S_{\text{in}} \tag{A.11}$$

$$N_{\text{in}}^2 = S_{\text{in}} \tag{A.12}$$

$$\text{SNR}_{\text{out}} = \frac{\bar{g} S_{\text{in}}}{\sqrt{\bar{g}^2 N_{\text{in}}^2 + \sigma_g^2 S_{\text{in}}}} \tag{A.13}$$

$$\text{DQE} = \frac{\frac{(\bar{g} S_{\text{in}})^2}{\bar{g}^2 N_{\text{in}}^2 + \sigma_g^2 S_{\text{in}}}}{\frac{S_{\text{in}}^2}{N_{\text{in}}^2}} \tag{A.14}$$

$$= \frac{\frac{\bar{g}^2 S_{\text{in}}^2}{\bar{g}^2 S_{\text{in}} + \sigma_g^2 S_{\text{in}}}}{S_{\text{in}}} \tag{A.15}$$

$$= \frac{\bar{g}^2}{\bar{g}^2 + \sigma_g^2} \tag{A.16}$$

$$\bar{g} = \sum E \rho(E) \tag{A.17}$$

$$\sigma_g^2 = \sum E^2 \rho(E) - \bar{g}^2 \tag{A.18}$$

$$\text{DQE} = \frac{\left(\sum E \rho(E)\right)^2}{\sum E^2 \rho(E)} \tag{A.19}$$

A.3 Intensity Distribution of Interference Pattern

The intensity distribution of the interference pattern caused by an electron biprism depends on several parameters. The biprism voltage U_{bp} determines the distance of the virtual slits (also the angle α in Figure REF). The magnification M effectively determines the distance z from the slit plane to the detector.

$$I(\alpha) = I_0 \cdot \underbrace{\operatorname{sinc}^2 \gamma}_{\text{diffraction}} \cdot \underbrace{\cos^2 \delta}_{\text{interference}} \tag{A.20}$$

$$\gamma = \frac{k_z}{2} \cdot b \cdot \sin \alpha \tag{A.21}$$

$$\delta = \frac{k_z}{2} \cdot d \cdot \sin \alpha \tag{A.22}$$

$$k = \frac{2\pi}{\lambda} \tag{A.23}$$

$$w = \lambda \frac{z}{d} \tag{A.24}$$

With b the slit width (electron beam spot size determined by convergence angle and aperture size), d the distance between the slits, α the angle, z the distance from the slit plane to the detection plane and w the fringe spacing.

In Figure A.3 the dependency is shown of the ratio of the slit distance to the slit width (d/b) on the resulting intensity distribution.

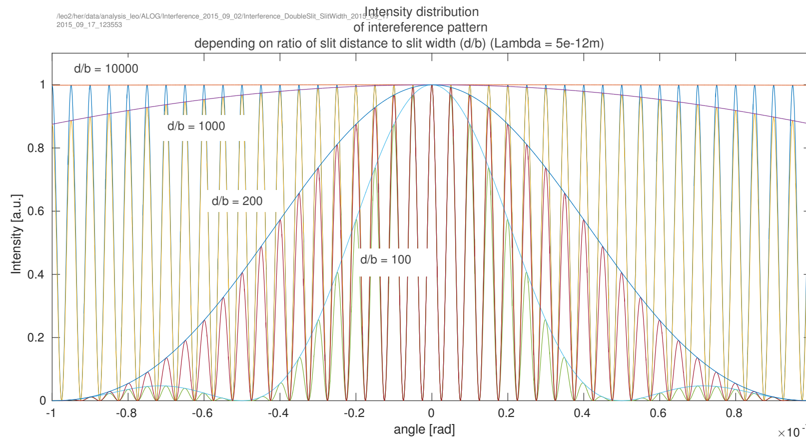

Figure A.3: Intensity distribution of the interference pattern and its dependency on the ratio of slit distance d to slit width b. The blue enveloping curves are given by the diffraction term of Equation A.21. For a given wavelength and angle (or number of maxima), the influence of the diffraction on the intensity maxima decreases with increasing ratio d/b.

A ratio d/b of greater than 10 000 can be assumed with typical dimensions of $d = 10\,\text{mm}$ and $b \approx 100\,\text{nm}$. For a given wavelength of $\lambda = 5\,\text{pm}$ and the requirement, that the intensity in the maxima does not drop below 99.9 % of the maximum intensity I_{max} (due to diffraction), and a ratio of $d/b = 10\,000$, more than 340 maxima fulfill this condition. For this reason, the intensity in the maxima does not decrease for the recorded fringes shown in this thesis. This is in contrast to the typical, students table-top two-slit interference experiments with lasers, where the influence of diffraction is easily seen (typical dimensions: $d = 5\,\text{mm}, b = 25\,\mu\text{m}, d/b = 200$).

A.4 Calculation of Stopping Power

Care must be taken in using the right units when calculating the stopping power according to equation 3.6 and 3.8. In order to mitigate this potential problem when trying to reproduce values, the derivation of the units is given here:

$$-\frac{\mathrm{d}E}{\mathrm{d}x} = \frac{e^4 N_\mathrm{A} \rho Z}{4\pi\epsilon_0^2 A m_\mathrm{e} c^2 \beta^2} \ln\left(1.166 \frac{E_\mathrm{kin} + kI}{I}\right) \tag{A.25}$$

$$\left[-\frac{\mathrm{d}E}{\mathrm{d}x}\right] = \frac{\mathrm{e}^4 \cdot 1/\mathrm{mol} \cdot \mathrm{g}/\mathrm{cm}^3 \cdot 1}{\mathrm{F}^2/\mathrm{m}^2 \cdot \mathrm{g}/\mathrm{mol} \cdot \mathrm{kg} \cdot \mathrm{m}^2/\mathrm{s}^2} \tag{A.26}$$

$$= \mathrm{e} \cdot \left(1.602 \times 10^{-19}\,\mathrm{C}\right)^3 \cdot 10^3 \frac{1}{\mathrm{kg}} \cdot 10^3 \frac{\mathrm{kg}}{\mathrm{m}^3} \cdot \left(\frac{\mathrm{V} \cdot \mathrm{m}}{\mathrm{C}}\right)^2 \cdot \frac{\mathrm{s}^2}{\mathrm{kg} \cdot \mathrm{m}^2} \tag{A.27}$$

$$= \left(1.602 \times 10^{-19}\right)^3 \cdot 10^6 \cdot \frac{\mathrm{eV}}{\mathrm{m}} \cdot \mathrm{V} \cdot \mathrm{C} \cdot \frac{\mathrm{s}^2}{\mathrm{kg} \cdot \mathrm{m}^2} \tag{A.28}$$

$$= \left(1.602 \times 10^{-19}\right)^3 \cdot 10^6 \cdot \frac{\mathrm{eV}}{\mathrm{m}} \tag{A.29}$$

$$= \left(1.602 \times 10^{-19}\right)^3 \cdot \frac{\mathrm{eV}}{\mu\mathrm{m}} \tag{A.30}$$

$$\text{with} \tag{A.31}$$

$$\mathrm{V} = \frac{\mathrm{kg} \cdot \mathrm{m}^2}{\mathrm{A} \cdot \mathrm{s}^3}, \quad \mathrm{C} = \mathrm{A} \cdot \mathrm{s}, \quad \mathrm{F} = \frac{\mathrm{C}}{\mathrm{V}} \tag{A.32}$$

A.5 Stopping Power and Electron Path Length

Collected values of the stopping power of electrons in Si calculated with the Bethe formula 3.8. The path length is calculated from Equation 3.9 with a lower integration energy of $E_{min} = 150$ eV.

Table A.1: Stopping power of electrons in silicon. The path length is integrated from $E_{min} = 150$ eV.

Energy	dE/dx		Path Length
	$k = 0$	$k = 0.822$	$k = 0.822$
keV	eV/µm	eV/µm	µm
1	17 432	18 647	0.03
2	11 917	12 232	0.10
3	9210	9352	0.20
4	7591	7671	0.32
5	6503	6555	0.46
6	5716	5753	0.62
7	5119	5145	0.80
8	4647	4668	1.01
9	4265	4282	1.23
10	3949	3962	1.48
20	2366	2369	4.87
40	1426	1427	16.20
60	1075	1075	32.58
80	889	889	53.18
100	773	773	77.41
120	694	694	104.80
140	636	636	134.95
160	593	593	167.56
180	559	559	202.34
200	531	531	239.07
250	482	482	338.13
300	450	450	445.65
350	427	427	559.79
400	411	411	679.19
450	399	399	802.81
500	389	389	929.86

A.6 The Landau Distribution Function

The energy loss distribution f_L of electrons passing a thin absorber as derived by Lev D. Landau is given by:[3,4]

$$f_L(x, \Delta) = \frac{\theta(\lambda)}{\xi} \tag{A.33}$$

$$\theta(\lambda) = \frac{1}{\pi} \int_0^\infty e^{-t \ln t - \lambda \cdot t} \sin(\pi t) \mathrm{d}t \tag{A.34}$$

$$\lambda(x, \Delta) = \frac{\Delta - \langle \Delta \rangle}{\xi} - \beta^2 - \ln(k) - 1 + C_E \tag{A.35}$$

$$\xi(x) = 0.1535 \frac{e^2 Z}{A \beta^2} \rho \cdot x \tag{A.36}$$

$$k = \frac{\langle \Delta \rangle}{E_{\max}} \tag{A.37}$$

$$\beta = \frac{v}{c} \tag{A.38}$$

Δ: energy loss, $\langle \Delta \rangle$: mean energy loss, x: thickness of absorber, $E_{\max}$: maximum transferable energy in one collision, Z: atomic number, A atomic weight, ρ: density of absorber, C_E: Euler constant (0.5772)

[3] Landau, 1944; Meroli, Passeri, and Servoli, 2011.

[4] Here, the original nomenclature is used. Note that in equations A.33-A.35 the $\lambda(x, \Delta)$ is not the the wavelength.

A.7 *Detection Efficiency Data*

Extended version of Table 6.2, listing the DE values for primary electron energies ranging from 20 keV to 300 keV calculated from simulations using Equation 6.7.

Threshold	Detection Efficiency							
	20 keV		60 keV		80 keV		120 keV	300 keV
eV	X EW %	O EW %	X EW %	O EW %	X EW %	O EW %	O EW %	O EW %
50	99.19	99.85	99.95	99.99	99.97	100.00	100.00	100.00
100	99.18	99.84	99.95	99.99	99.97	100.00	100.00	100.00
200	99.12	99.80	99.95	99.99	99.97	100.00	100.00	100.00
300	99.03	99.74	99.94	99.99	99.96	99.99	100.00	100.00
400	98.94	99.66	99.93	99.98	99.96	99.99	100.00	100.00
500	98.84	99.58	99.92	99.97	99.95	99.98	99.99	100.00
600	98.73	99.49	99.91	99.95	99.95	99.97	99.99	100.00
700	98.62	99.39	99.89	99.94	99.94	99.97	99.99	100.00
800	98.51	99.29	99.88	99.93	99.93	99.96	99.99	99.99
900	98.38	99.19	99.86	99.91	99.92	99.95	99.98	99.99
1000	98.26	99.08	99.84	99.89	99.91	99.94	99.98	99.99
1100	98.13	98.97	99.83	99.88	99.90	99.93	99.97	99.99
1200	97.99	98.86	99.81	99.86	99.89	99.91	99.97	99.99
1300	97.85	98.75	99.79	99.84	99.88	99.90	99.96	99.99
1400	97.71	98.62	99.77	99.82	99.86	99.89	99.96	99.99
1500	97.57	98.50	99.75	99.80	99.85	99.88	99.95	99.99
1600	97.42	98.36	99.73	99.78	99.84	99.87	99.94	99.99
1700	97.27	98.23	99.71	99.76	99.83	99.85	99.94	99.99
1800	97.11	98.09	99.69	99.74	99.81	99.84	99.93	99.99
1900	96.95	97.95	99.67	99.72	99.80	99.83	99.92	99.99
2000	96.78	97.80	99.65	99.70	99.78	99.81	99.92	99.99

Table A.2: DE for various primary electron energies depending on the detection threshold.

A.8 Gauss Correction Code

For convenience, the MATLAB code that calculates the data for the Gauss correction that is described in section 8.3.2 is shown here. This code is a condensed version, optimized for page space.

```
%% MATLAB code to calculate the data for the Gauss correction
dSigma = 0.1;
vPix = -3:1:3;
vPixBorder = -3.5:1:3.5;
nPix = numel(vPixBorder)-1;

vMu = -0.5:0.0001:0.5; % also used for pixel geometry
nMu = numel(vMu);

aPixSignal = zeros(nMu,3);
aPixSignal(:,1) = vMu;

for iMu=1:nMu
    b1 = (vPixBorder-vMu(iMu) ) / (sqrt(2)*dSigma);
    vTmp1 = erf(b1);
    vTmp2 = 0.5*diff(vTmp1);

    dCog = sum(vPix.*vTmp2) /1; % should be normed -> /1
    aPixSignal(:,2) = dCog;
end

%% Transpose
% from Cog(Mu) to Mu(Cog)
aPixSignal(:,3) = interp1( aPixSignal(:,2), vMu, vMu, 'linear');

%% Calc correction data
aPixSignal(:,3) = aPixSignal(:,3)-vMu';
```

A.9 Gauss Correction Comparison

In order to provide an impression on the relative widths of the charge clouds σ_{cloud} in comparison with the pixels, different Gaussian distributions corresponding to different σ_{cloud} are shown in figure A.4. For each σ_{cloud}, the curve is shown with the maximum difference between the center of the distribution and the resulting calculated CoG. It can be seen that the position of the maximum difference shifts towards $x = 0.25\,\text{pix}$. If the Gaussian distribution is sampled with approximately three pixels in one direction, almost no difference between the center position of the distribution and the calculated CoG exists.

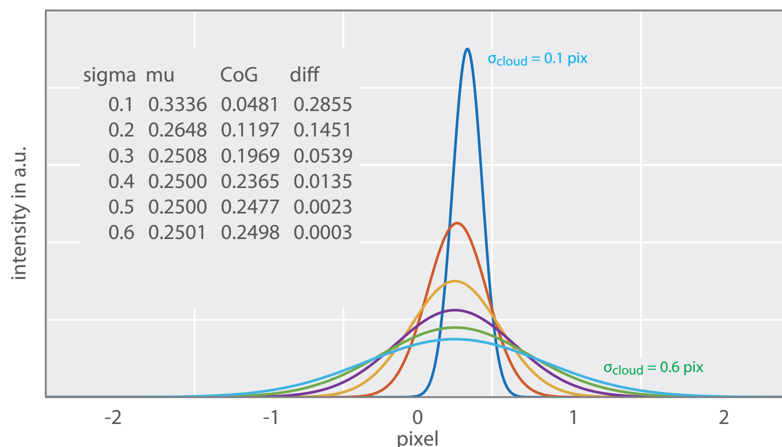

Figure A.4: Comparison of Gaussian distributions. The center μ of the distribution is chosen, so that the difference to the calculated CoG is largest, to show where the greatest correction would be applied. All distributions are normalized to unity.

A.10 Data Reference

The experimental data that is presented in this thesis was processed with the parameters given in table A.3. In the text, the processed data is referenced as given by the processing identifier (PID) in the first column. The same original data referenced by the measurement identifier (MID) can be processed with different parameters, which results in multiple PIDs for a single MID. For the description of the processing and the parameters, see the data analysis chapter 5.

PID	MID	Energy	σ_{sea}	Noise	rate
		keV		adu	$\times 10^{-3} e^-_{tem}/\mathrm{pix}$
PID20_003	C16_15_24_140212_39	20	6	6.3	0.84
PID20_002	C16_15_24_140212_40	20	6	9.9	1.01
PID20_004	C16_15_24_140212_40	20	3	9.9	1.01
PID40_001	C16_15_24_140212_34	40	6	6.3	2.05
PID40_002	C16_15_24_140212_34	40	3	6.3	2.05
PID60_001	C16_15_24_140415_098	60	6	8.0	13.09
PID60_003	C16_15_24_140212_30	60	6	4.3	1.33
PID60_005	C16_15_24_140415_100	60	6	8.0	6.81
PID80_001	C16_15_24_140212_27	80	6	4.3	2.47
PID80_002	C16_15_24_140212_26	80	6	4.3	1.18
PID80_003	C16_15_24_140212_29	80	6	4.3	18.48
PID80_004	C16_15_24_150523_050	80	6	4.3	8.73
PID100_001	C16_15_24_140313_20	100	-	-	-
PID100_002	C16_15_24_140313_22	100	-	-	-
PID120_001	C16_15_24_140212_23	120	6	4.3	1.32
PID200_001	C16_15_24_140212_19	200	6	4.1	2.77
PID200_002	C16_15_24_140212_18	200	6	4.1	1.16
PID300_001	C16_15_24_140212_14	300	6	3.5	2.44
PID300_002	C16_15_24_140212_13	300	6	3.5	0.92

Table A.3: Reference of the PIDs of experimental data and their SEA processing parameters.

All listed measurements were analyzed with the SEA and the given threshold σ_{sea} (except PID100_001 and PID100_002, which were only used in the IIM). A linewise correction of common mode was applied. A gainmap was applied, with one gain value per octant of the image area. The parameters that were used to record the experimental data are listed in table A.4.

MID	Energy keV	Mode	U_{bc} V	V	CDS	G	F_{bin}	F_{win}	N_{rows}
C16_15_24_140212_39	20	HCHC	−420	32	1	16	1	1	132
C16_15_24_140212_40	20	HCHC	−420	32	2	32	1	1	132
C16_15_24_140212_34	40	HCHC	−420	32	1	16	1	1	132
C16_15_24_140415_098	60	HiRes	−240	16	2	16	1	1	132
C16_15_24_140415_100	60	HiRes	−240	16	2	16	1	1	132
C16_15_24_140212_30	60	HCHC	−420	16	1	8	1	1	132
C16_15_24_140212_26	80	HCHC	−420	16	1	8	1	1	132
C16_15_24_140212_27	80	HCHC	−420	16	1	8	1	1	132
C16_15_24_140212_29	80	HCHC	−420	16	1	8	1	1	132
C16_15_24_150523_050	80	HCHC	−440	8	1	4	1	1	132
C16_15_24_140313_20	100	XPlus	−480	2	1	1	1	2	66
C16_15_24_140313_22	100	XPlus	−480	2	1	1	1	2	66
C16_15_24_140212_23	120	HCHC	−420	16	1	8	1	1	132
C16_15_24_140212_18	200	HCHC	−420	8	1	4	1	1	132
C16_15_24_140212_19	200	HCHC	−420	8	1	4	1	1	132
C16_15_24_140212_13	300	HCHC	−420	4	1	2	1	1	132
C16_15_24_140212_14	300	HCHC	−420	4	1	2	1	1	132

Table A.4: Reference of the MIDs of experimental data and their parameters. $G = V \cdot CDS/2$

Bibliography

[1] E. K. Abbe. 'Beiträge zur Theorie des Mikroskops und der mikroskopischen Wahrnehmung'. *Archiv für mikroskopische Anatomie* 9.1 (1873), 456–468 (see p. 22)

[2] S. Agostinelli et al. 'Geant4-a simulation toolkit'. *Nuclear Instruments and Methods in Physics Research Section A: Accelerators, Spectrometers, Detectors and Associated Equipment* 506.3 (2003), 250–303 (see p. 63)

[3] R. C. Alig, S. Bloom, and C. W. Struck. 'Scattering by ionization and phonon emission in semiconductors'. *Phys. Rev. B* 22 (12 1980), 5565–5582 (see p. 38)

[4] J. Allison, K. Amako, J. Apostolakis, H. Araujo, P. A. Dubois, M. Asai, G. Barrand, R. Capra, S. Chauvie, R. Chytracek, G. A. P. Cirrone, G. Cooperman, G. Cosmo, G. Cuttone, G. G. Daquino, M. Donszelmann, M. Dressel, G. Folger, F. Foppiano, J. Generowicz, V. Grichine, S. Guatelli, P. Gumplinger, A. Heikkinen, I. Hrivnacova, A. Howard, S. Incerti, V. Ivanchenko, T. Johnson, F. Jones, T. Koi, R. Kokoulin, M. Kossov, H. Kurashige, V. Lara, S. Larsson, F. Lei, O. Link, F. Longo, M. Maire, A. Mantero, B. Mascialino, I. McLaren, P. M. Lorenzo, K. Minamimoto, K. Murakami, P. Nieminen, L. Pandola, S. Parlati, L. Peralta, J. Perl, A. Pfeiffer, M. G. Pia, A. Ribon, P. Rodrigues, G. Russo, S. Sadilov, G. Santin, T. Sasaki, D. Smith, N. Starkov, S. Tanaka, E. Tcherniaev, B. Tome, A. Trindade, P. Truscott, L. Urban, M. Verderi, A. Walkden, J. P. Wellisch, D. C. Williams, D. Wright, and H. Yoshida. 'Geant4 developments and applications'. *IEEE Transactions on Nuclear Science* 53.1 (2006), 270–278 (see p. 63)

[5] *AMD 14 nm*. 2016. URL: `amd.com/en-us/press-releases/Pages/amd-demonstrates-2016jan04.aspx` (visited on 2017-01-11) (see p. 18)

[6] R. Ballabriga, M. Campbell, E. Heijne, X. Llopart, L. Tlustos, and W. Wong. 'Medipix3: A 64 k pixel detector readout chip working in single photon counting mode with improved spectrometric performance'. *Nuclear Instruments and Methods in Physics Research Section A: Accelerators, Spectrometers, Detectors and Associated Equipment* 633, Supplement 1 (2011), S15–S18 (see p. 29)

[7] J. Barthel, L. Houben, and K. Tillmann. 'FEI Titan G3 50-300 PICO'. *Journal of large-scale research facilities* 1.A34 (2015) (see p. 40)

[8] W. Baumeister. 'Electron tomography: towards visualizing the molecular organization of the cytoplasm'. *Current Opinion in Structural Biology* 12.5 (2002), 679–684 (see p. 128)

[9] S. Bedell, A. Khakifirooz, and D. Sadana. 'Strain scaling for CMOS'. *MRS Bulletin* 39.2 (2014), 131–137 (see p. 18)

[10] E. Belau, R. Klanner, G. Lutz, E. Neugebauer, H. Seebrunner, A. Wylie, T. Bähringer, L. Hubbeling, P. Weilhammer, J. Kemmer, U. Kätz, and M. Riebesell. 'Charge collection in silicon strip detectors'. *Nuclear Instruments and Methods in Physics Research* 214 (1983), 253–260 (see p. 113)

[11] B. R. Bennett, T. F. Chick, J. B. Boos, J. G. Champlain, and A. A. Podpirka. 'Strained InGaAs/InAlAs quantum wells for complementary III-V transistors'. *Journal of Crystal Growth* 388 (2014), 92–97 (see p. 18)

[12] M. J. Berger and S. M. Seltzer. 'Tables of Energy Losses and Ranges of Electrons and Positrons. NASA SP-3012'. *NASA Special Publication* 3012 (1964) (see p. 35)

[13] M. Berger, J. S. Coursey, M. A. Zucker, and J. Chang. *ESTAR, PSTAR, and ASTAR: Computer Programs for Calculating Stopping-Power and Range Tables for Electrons, Protons, and Helium Ions (version 1.2.3)*. 2005 (see p. 34)

[14] H. Bethe. „Bremsformel für Elektronen relativistischer Geschwindigkeit". *Zeitschrift für Physik* 76.5 (1932), 293–299 (siehe S. 34)

[15] H. Bethe. „Zur Theorie des Durchgangs schneller Korpuskularstrahlen durch Materie". *Annalen der Physik* 397.3 (1930), 325–400 (siehe S. 34)

[16] H. Bichsel. 'Straggling in thin silicon detectors'. *Rev. Mod. Phys.* 60 (3 1988), 663–699 (see p. 35)

[17] J. Bihr, G. Benner, D. Krahl, A. Rilk, and E. Weimer. 'Design of an analytical TEM with integrated imaging Ω-spectrometer'. *Proc. 49th Ann. Meet. Electron Microsc. Soc. Am., ed. GW Bailey, San Francisco Press, San Francisco, CA* (1991), 354–355 (see p. 42)

[18] O. Blunck and S. Leisegang. 'Zum Energieverlust schneller Elektronen in dünnen Schichten'. *Zeitschrift für Physik* 128.4 (1950), 500–505 (see p. 35)

[19] W. H. Bragg and W. L. Bragg. 'The Reflection of X-rays by Crystals'. *Proceedings of the Royal Society of London A: Mathematical, Physical and Engineering Sciences* 88.605 (1913), 428–438 (see pp. 44, 137)

[20] J. Brew. *TEM image under Creative Commons 3.0*. URL: https://commons.wikimedia.org/w/index.php?curid=5309032 (visited on 2017-01-11) (see p. 21)

[21] L. V. P. R. de Broglie. 'Recherches sur la théorie des quanta, 1924' (1924) (see p. 22)

[22] M. Brusa, F. Civano, A. Comastri, T. Miyaji, M. Salvato, G. Zamorani, N. Cappelluti, F. Fiore, G. Hasinger, V. Mainieri, A. Merloni, A. Bongiorno, P. Capak, M. Elvis, R. Gilli, H. Hao, K. Jahnke, A. M. Koekemoer, O. Ilbert, E. L. Floc'h, E. Lusso, M. Mignoli, E. Schinnerer, J. D. Silverman, E. Treister, J. D. Trump, C. Vignali, M. Zamojski, T. Aldcroft, H. Aussel, S. Bardelli, M. Bolzonella, A. Cappi, K. Caputi, T. Contini, A. Finoguenov, A. Fruscione, B. Garilli, C. D. Impey, A. Iovino, K. Iwasawa, P. Kampczyk, J. Kartaltepe, J. P. Kneib, C. Knobel, K. Kovac, F. Lamareille, J.-F. Leborgne, V. L. Brun, O. L. Fevre, S. J. Lilly, C. Maier, H. J. McCracken, R. Pello, Y.-J. Peng, E. Perez-Montero, L. de Ravel, D. Sanders, M. Scodeggio, N. Z. Scoville, M. Tanaka, Y. Taniguchi, L. Tasca, S. de la Torre, L. Tresse, D. Vergani, and E. 'The XMM-Newton Wide-field Survey in the Cosmos Field (XMM-COSMOS): Demography and Multiwavelength Properties of Obscured and Unobscured Luminous Active Galactic Nuclei'. *The Astrophysical Journal* 716.1 (2010), 348– (see p. 17)

[23] R. A. Crowther, D. J. DeRosier, and A. Klug. 'The Reconstruction of a Three-Dimensional Structure from Projections and its Application to Electron Microscopy'. *Proceedings of the Royal Society of London A: Mathematical, Physical and Engineering Sciences* 317.1530 (1970), 319–340 (see p. 128)

[24] C. Davisson and L. H. Germer. 'Diffraction of Electrons by a Crystal of Nickel'. *Phys. Rev.* 30 (6 1927), 705–740 (see p. 22)

[25] *DDD DE-16 Datasheet*. URL: `www.directelectron.com/documents/Specs-DE16.pdf` (visited on 2017-01-10) (see p. 29)

[26] R. Egerton. *Electron Energy-Loss Spectroscopy in the Electron Microscope*. 3rd ed. Springer, 2011 (see p. 40)

[27] U. Fano. 'Ionization Yield of Radiations. II. The Fluctuations of the Number of Ions'. *Phys. Rev.* 72 (1 1947), 26–29 (see p. 38)

[28] A. Faruqi and R. Henderson. 'Electronic detectors for electron microscopy'. *Current Opinion in Structural Biology* 17.5 (2007), 549–555 (see p. 29)

[29] K. R. Ferguson, M. Bucher, J. D. Bozek, S. Carron, J.-C. Castagna, R. Coffee, G. I. Curiel, M. Holmes, J. Krzywinski, M. Messerschmidt, M. Minitti, A. Mitra, S. Moeller, P. Noonan, T. Osipov, S. Schorb, M. Swiggers, A. Wallace, J. Yin, and C. Bostedt. 'The Atomic, Molecular and Optical Science instrument at the Linac Coherent Light Source'. *Journal of Synchrotron Radiation* 22.3 (2015), 492–497 (see p. 17)

[30] R. P. Feynman. *There's Plenty of Room at the Bottom*. 1959 (see p. 17)

[31] G. Fraser, A. Abbey, A. Holland, K. McCarthy, A. Owens, and A. Wells. 'The X-ray energy response of silicon Part A. Theory'. *Nuclear Instruments and Methods in Physics Research Section A: Accelerators, Spectrometers, Detectors and Associated Equipment* 350.1-2 (1994), 368–378 (see p. 33)

[32] E. Gatti and P. Rehak. 'Semiconductor drift chamber - An application of a novel charge transport scheme'. *Nuclear Instruments and Methods in Physics Research* 225.3 (1984), 608–614 (see p. 45)

[33] *Geant4*. URL: `geant4.web.cern.ch/geant4/` (visited on 2016-04-01) (see p. 63)

[34] *Geant4: Physics Reference Manual*. 2016 (see p. 65)

[35] A. Gubbens, M. Barfels, C. Trevor, R. Twesten, P. Mooney, P. Thomas, N. Menon, B. Kraus, C. Mao, and B. McGinn. 'The {GIF} Quantum, a next generation post-column imaging energy filter'. *Ultramicroscopy* 110.8 (2010), 962–970 (see p. 27)

[36] M. Haider, H. Rose, S. Uhlemann, B. Kabius, and K. Urban. 'Towards 0.1 nm resolution with the first spherically corrected transmission electron microscope'. *Journal of Electron Microscopy* 47.5 (1998), 395–405 (see p. 26)

[37] S. Herrmann, W. Buttler, R. Hartmann, N. Meidinger, M. Porro, and L. Strueder. 'CAMEX readout ASICs for pnCCDs'. *2008 IEEE Nuclear Science Symposium Conference Record*. 2008, 2952–2957 (see p. 48)

[38] *IBM 7 nm*. 2015. URL: `nytimes.com/2015/07/09/technology/ibm-announces-computer-chips-more-powerful-than-any-in-existence.html` (visited on 2017-01-11) (see p. 18)

[39] S. Ihle, P. Holl, D. Kalok, R. Hartmann, **H. Ryll**, and L. Strüder. 'Direct measurement of the position accuracy for low energy X-ray photons with a pnCCD'. *JINST* (2017) (see pp. 100, 112, 119)

[40] J. A. Irwin, W. P. Maksym, G. R. Sivakoff, A. J. Romanowsky, D. Lin, T. Speegle, I. Prado, D. Mildebrath, J. Strader, J. Liu, and J. M. Miller. 'Ultraluminous X-ray bursts in two ultracompact companions to nearby elliptical galaxies'. *Nature* 538.7625 (2016), 356–358 (see p. 17)

[41] R. Ito, P. Andreo, and T. Tabata. 'Reflection ratios of electrons and photons from solids'. *Bull. Univ. Osaka Pref. A* 41.2 (1992), 69–76 (see pp. 86, 87)

[42] L. Jones, H. Yang, K. E. MacArthur, **H. Ryll**, M. Simson, H. Soltau, Y. Kondo, R. Sagawa, H. Banba, and P. D. Nellist. 'Opportunities in Angularly Resolved Dark-field STEM using Pixelated Detectors'. *Microscopy and Microanalysis* 21.S3 (2015), 2411–2412 (see p. 133)

[43] D. C. Joy and S. Luo. 'An empirical stopping power relationship for low-energy electrons'. *Scanning* 11.4 (1989), 176–180 (see p. 34)

[44] J. Kemmer and G. Lutz. 'New detector concepts'. *Nuclear Instruments and Methods in Physics Research Section A: Accelerators, Spectrometers, Detectors and Associated Equipment* 253.3 (1987), 365–377 (see p. 148)

[45] N. Kimmel, R. Andritschke, R. Hartmann, P. Holl, N. Meidinger, R. Richter, and L. Strüder. 'Experimental and theoretical study of the signal electron motion in fully depleted silicon'. *Nuclear Instruments and Methods in Physics Research Section A: Accelerators, Spectrometers, Detectors and Associated Equipment* 624.2 (2010), 334–339 (see pp. 46, 69, 112)

[46] N. Kimmel. 'Analysis of the charge collection process in solid state X-ray detectors'. PhD thesis. University of Siegen, 2009 (see p. 46)

[47] C. T. Koch, W. Sigle, R. Höschen, M. RÃ¼hle, E. Essers, G. Benner, and M. Matijevic. 'SESAM: Exploring the Frontiers of Electron Microscopy'. *Microscopy and Microanalysis* 12.6 (2006), 506–514 (see p. 42)

[48] P. Kotula, M. V. Benthem, **H. Ryll**, M. Simson, and H. Soltau. 'Multivariate Statistical Analysis of Series of Diffraction Patterns'. *Microscopy and Microanalysis* 22.S3 (2016), 482–483 (see p. 133)

[49] M. Krajnak, D. McGrouther, D. Maneuski, V. O. Shea, and S. McVitie. 'Pixelated detectors and improved efficiency for magnetic imaging in STEM differential phase contrast'. *Ultramicroscopy* 165 (2016), 42–50 (see p. 29)

[50] B. Krieger, D. Contarato, P. Denes, D. Doering, D. Gnani, J. Joseph, and S. Schindler. 'Fast, radiation hard, direct detection CMOS imagers for high resolution Transmission Electron Microscopy'. *Nuclear Science Symposium and Medical Imaging Conference (NSS/MIC), 2011 IEEE*. 2011, 1946–1949 (see p. 29)

[51] O. Krivanek and P. Mooney. 'Applications of slow-scan CCD cameras in transmission electron microscopy'. *Ultramicroscopy* 49.1-4 (1993), 95–108 (see p. 29)

[52] O. L. Krivanek, A. J. Gubbens, and N. Dellby. 'Developments in EELS instrumentation for spectroscopy and imaging'. *Microsc. Microanal. Microstruct.* 2.2-3 (1991), 315–332 (see p. 42)

[53] M. Kuijper, G. van Hoften, B. Janssen, R. Geurink, S. D. Carlo, M. Vos, G. van Duinen, B. van Haeringen, and M. Storms. 'FEI's direct electron detector developments: Embarking on a revolution in cryo-TEM'. *Journal of Structural Biology* 192.2 (2015), 179–187 (see pp. 29, 30)

[54] L. Landau. 'On the energy loss of fast particles by ionization'. *J. Phys.(USSR)* 8 (1944), 201–205 (see pp. 35, 82, 157)

[55] P. Lechner. 'Zur Ionisationsstatistik in Silicium'. PhD thesis. Technical University of Munich, 1998 (see pp. 32, 38)

[56] P. Lechner and L. Strüder. 'Ionization statistics in silicon X-ray detectors - new experimental results'. *Nuclear Instruments and Methods in Physics Research Section A: Accelerators, Spectrometers, Detectors and Associated Equipment* 354.2 (1995), 464–474 (see p. 38)

[57] X. Li, P. Mooney, S. Zheng, C. R. Booth, M. B. Braunfeld, S. Gubbens, D. A. Agard, and Y. Cheng. 'Electron counting and beam-induced motion correction enable near-atomic-resolution single-particle cryo-EM'. *Nat Meth* 10.6 (2013), 584–590 (see p. 58)

[58] S. Luo, X. Zhang, and D. C. Joy. 'Experimental determinations of electron stopping power at low energies'. *Radiation Effects and Defects in Solids* 117.1-3 (1991), 235–242 (see p. 35)

[59] G. Lutz, S. Herrmann, P. Lechner, M. Porro, R. H. Richter, L. Strüder, and J. Treis. *New DEPFET structures: concepts, simulations and experimental results*. 2008 (see p. 77)

[60] G. Lutz. *Semiconductor Radiation Detectors*. 1st. Springer Berlin Heidelberg, 2007 (see p. 45)

[61] G. McMullan, D. M. Cattermole, S. Chen, R. Henderson, X. Llopart, C. Summerfield, L. Tlustos, and A. R. Faruqi. 'Electron imaging with Medipix2 hybrid pixel detector'. *Ultramicroscopy* 107.4 (2007), 401–413 (see p. 153)

[62] G. McMullan, S. Chen, R. Henderson, and A. Faruqi. 'Detective quantum efficiency of electron area detectors in electron microscopy'. *Ultramicroscopy* 109.9 (2009), 1126–1143 (see pp. 29, 101, 102, 106, 152, 153)

[63] G. McMullan, A. Faruqi, D. Clare, and R. Henderson. 'Comparison of optimal performance at 300 keV of three direct electron detectors for use in low dose electron microscopy'. *Ultramicroscopy* 147.0 (2014), 156–163 (see p. 29)

[64] G. McMullan, A. Faruqi, and R. Henderson. 'Chapter One - Direct Electron Detectors'. *The Resolution Revolution: Recent Advances In cryoEM*. Ed. by R. Crowther. Vol. 579. Methods in Enzymology. Academic Press, 2016, 1–17 (see p. 30)

[65] *Medipix Collaboration*. 2017. URL: `medipix.web.cern.ch/MEDIPIX/` (visited on 2017-01-10) (see p. 29)

[66] N. Meidinger, R. Andritschke, S. Ebermayer, J. Elbs, O. Hälker, R. Hartmann, S. Herrmann, N. Kimmel, G. Schächner, F. Schopper, H. Soltau, L. Strüder, and G. Weidenspointner. 'Development of the focal plane PNCCD camera system for the X-ray space telescope eROSITA'. *Nuclear Instruments and Methods in Physics Research Section A: Accelerators, Spectrometers, Detectors and Associated Equipment* 624.2 (2010), 321–329 (see p. 17)

[67] S. Meroli, D. Passeri, and L. Servoli. 'Energy loss measurement for charged particles in very thin silicon layers'. *Journal of Instrumentation* 6.06 (2011), P06013 (see p. 157)

[68] P. A. Midgley, E. P. W. Ward, A. B. Hungria, and J. M. Thomas. 'Nanotomography in the chemical, biological and materials sciences'. *Chem. Soc. Rev.* 36 (9 2007), 1477–1494 (see p. 128)

[69] V. Migunov, **H. Ryll**, X. Zhuge, M. Simson, L. Strüder, K. J. Batenburg, L. Houben, and R. E. Dunin-Borkowski. 'Rapid low dose electron tomography using a direct electron detection camera'. *Scientific Reports* 5 (2015), 14516 (see pp. 128–130)

[70] A.-C. Milazzo, A. Cheng, A. Moeller, D. Lyumkis, E. Jacovetty, J. Polukas, M. H. Ellisman, N.-H. Xuong, B. Carragher, and C. S. Potter. 'Initial evaluation of a direct detection device detector for single particle cryo-electron microscopy'. *J. Struct. Biol.* 176.3 (2011), 404–408 (see p. 29)

[71] G. Möllenstedt und H. Düker. „Beobachtungen und Messungen an Biprisma-Interferenzen mit Elektronenwellen“. *Zeitschrift für Physik* 145.3 (1956), 377–397 (siehe S. 124)

[72] M. Mukai, E. Okunishi, M. Ashino, K. Omoto, T. Fukuda, A. Ikeda, K. Somehara, T. Kaneyama, T. Saitoh, T. Hirayama, and Y. Ikuhara. 'Development of a monochromator for aberration-corrected scanning transmission electron microscopy'. *Microscopy* 64.3 (2015), 151–158 (see p. 27)

[73] K. Müller, A. Rosenauer, M. Schowalter, J. Zweck, R. Fritz, and K. Volz. 'Strain Measurement in Semiconductor Heterostructures by Scanning Transmission Electron Microscopy'. *Microscopy and Microanalysis* 18.05 (2012), 995–1009 (see pp. 18, 40, 137, 138)

[74] K. Müller, **H. Ryll**, I. Ordavo, S. Ihle, M. Huth, M. Simson, J. Zweck, K. Volz, H. Soltau, P. Potapov, L. Strüder, M. Schowalter, C. Mahr, D. Erben, and A. Rosenauer. 'Strain Analyisis by Nano-Beam Electron Diffraction using millisecond frames of a direct electron pnCCD detector'. *18th International Microscopy Congress (IMC)*. 2014 (see pp. 139, 140)

[75] K. Müller, **H. Ryll**, I. Ordavo, S. Ihle, L. Strüder, K. Volz, J. Zweck, H. Soltau, and A. Rosenauer. 'Scanning transmission electron microscopy strain measurement from millisecond frames of a direct electron charge coupled device'. *Applied Physics Letters* 101.21, 212110 (2012), 212110 (see pp. 18, 138, 139)

[76] H. T. Nguyen-Truong. 'Determination of the maximum energy loss for electron stopping power calculations and its effect on backscattering electron yield in Monte-Carlo simulations applying continuous slowing-down approximation'. *Journal of Applied Physics* 114.16, 163513 (2013) (see p. 34)

[77] H. T. Nguyen-Truong. 'Modified Bethe formula for low-energy electron stopping power without fitting parameters'. *Ultramicroscopy* 149 (2015), 26–33 (see p. 34)

[78] F. Nicastro, F. Senatore, Y. Krongold, S. Mathur, and M. Elvis. 'A Distant Echo of Milky Way Central Activity Closes the Galaxy's Baryon Census'. *The Astrophysical Journal Letters* 828.1 (2016), L12 (see p. 17)

[79] E. Nogales. 'The development of cryo-EM into a mainstream structural biology technique'. *Nat Meth* 13.1 (2016), 24–27 (see p. 30)

[80] I. Ordavo, S. Ihle, V. Arkadiev, O. Scharf, H. Soltau, A. Bjeoumikhov, S. Bjeoumikhova, G. Buzanich, R. Gubzhokov, A. Günther, et al. 'A new pnCCD-based color X-ray camera for fast spatial and energy-resolved measurements'. *Nuclear Instruments and Methods in Physics Research Section A: Accelerators, Spectrometers, Detectors and Associated Equipment* 654.1 (2011), 250–257 (see pp. 17, 43)

[81] L. S. Panchakarla, R. Popovitz-Biro, L. Houben, R. E. Dunin-Borkowski, and R. Tenne. 'Lanthanide-Based Functional Misfit-Layered Nanotubes'. *Angewandte Chemie* 126.27 (2014), 7040–7044 (see p. 129)

[82] T. J. Pennycook, A. R. Lupini, H. Yang, M. F. Murfitt, L. Jones, and P. D. Nellist. 'Efficient phase contrast imaging in STEM using a pixelated detector. Part 1: Experimental demonstration at atomic resolution'. *Ultramicroscopy* 151.0 (2015), 160–167 (see pp. 18, 142, 143)

[83] S. Perkins, D. Cullen, and S. Seltzer. *Tables and graphs of electron-interaction cross sections from 10 eV to 100 GeV derived from the LLNL Evaluated Electron Data Library (EEDL), Z = 1–100*. 1991 (see p. 32)

[84] P. M. Petroff, R. A. Logan, and A. Savage. 'Nonradiative recombination at dislocations in III-V compound semiconductors'. *Journal of Microscopy* 118.3 (1980), 255–261 (see p. 42)

[85] M. Porro, L. Andricek, S. Aschauer, M. Bayer, J. Becker, L. Bombelli, A. Castoldi, G. De Vita, I. Diehl, F. Erdinger, et al. 'Development of the depfet sensor with signal compression: A large format x-ray imager with mega-frame readout capability for the European XFEL'. *IEEE Transactions on Nuclear Science* 59.6 (2012), 3339–3351 (see p. 148)

[86] C. Presler. *Squirrel image under Creative Commons 3.0*. URL: `thenounproject.com/term/squirrel/27309/` (visited on 2017-05-05)

[87] L. Reimer. *Scanning Electron Microscopy*. 2nd ed. Vol. 45. Springer-Verlag Berlin Heidelberg, 1998 (see p. 86)

[88] L. Reimer and H. Kohl. *Transmission Electron Microscopy*. 5th. Springer-Verlag New York, 2008 (see pp. 23, 39, 101)

[89] R. Ritz, M. Huth, S. Ihle, M. Simson, H. Soltau, V. Migunov, M. Duchamp, R. E. Dunin-Borkowski, **H. Ryll**, and L. Strüder. 'Imaging of Electric Fields with the pnCCD (S)TEM Camera'. 2016 (see p. 135)

[90] J. M. Rodenburg and R. H. T. Bates. 'The Theory of Super-Resolution Electron Microscopy Via Wigner-Distribution Deconvolution'. *Philosophical Transactions of the Royal Society of London A: Mathematical, Physical and Engineering Sciences* 339.1655 (1992), 521–553 (see pp. 141, 143)

[91] J. M. Rodenburg, B. C. McCallum, and P. D. Nellist. 'Experimental tests on double-resolution coherent imaging via STEM'. *Ultramicroscopy* 48.3 (1993), 304–314 (see pp. 18, 141)

[92] H. Rose and E. Plies. 'Design of a magnetic energy analyzer with small aberrations'. *Optik* 40.3 (1974), 336–341 (see p. 42)

[93] H. H. Rose. 'Historical aspects of aberration correction'. *Journal of Electron Microscopy* 58.3 (2009), 77–85 (see p. 26)

[94] W. D. Ruijter. 'Imaging properties and applications of slow-scan charge-coupled device cameras suitable for electron microscopy'. *Micron* 26.3 (1995), 247–275 (see p. 29)

[95] E. Ruska. *Ernst Ruska - Nobel Lecture: The Development of the Electron Microscope and of Electron Microscopy*. 1986 (see p. 22)

[96] E. Ruska. 'Über Fortschritte im Bau und in der Leistung des magnetischen Elektronenmikroskops'. *Zeitschrift für Physik A Hadrons and Nuclei* 87.9 (1934), 580–602 (see p. 22)

[97] **H. Ryll**, M. Simson, C. B. Boothroyd, R. Dunin-Borkowski, C. Dwyer, R. Hartmann, M. Huth, S. Ihle, V. Migunov, K. Müller-Caspary, A. Rosenauer, J. Schmidt, H. Soltau, and L. Strüder. 'The wave-particle duality of electrons demonstrated with sub-pixel resolution by recording off-axis electron holograms on a pnCCD direct detector'. *Microscopy Conference MC 2015*. 2015 (see p. 124)

[98] **H. Ryll**, M. Simson, R. Hartmann, P. Holl, M. Huth, S. Ihle, Y. Kondo, P. Kotula, A. Liebel, K. Müller-Caspary, A. Rosenauer, R. Sagawa, J. Schmidt, H. Soltau, and L. Strüder. 'A pnCCD-based, fast direct single electron imaging camera for TEM and STEM'. *Journal of Instrumentation* 11.04 (2016), P04006 (see pp. 51, 134)

[99] *Samsung 10 nm*. 2016. URL: `news.samsung.com/global/samsung-starts-industrys-first-mass-production-of-system-on-chip-with-10-nanometer-finfet-technology` (visited on 2017-01-11) (see p. 18)

[100] J. Schmidt, R. Hartmann, P. Holl, M. Huth, G. Lutz, U. Pietsch, **H. Ryll**, S. Send, M. Simson, H. Soltau, J. Soltau, D. Steigenhöfer, and L. Strüder. 'Controlled charge extraction - antiblooming capabilities in pnCCD imaging sensors'. *Journal of Instrumentation* 11.01 (2016), P01012 (see p. 51)

[101] J. Schmidt, R. Hartmann, P. Holl, M. Huth, G. Lutz, **H. Ryll**, S. Send, M. Simson, D. Steigenhöfer, J. Soltau, H. Soltau, and L. Strüder. 'Extending the dynamic range of fully depleted pnCCDs'. *Journal of Instrumentation* 9.10 (2014), P10008 (see p. 50)

[102] J. Schmidt. 'A study of the charge collection, storage and processing in pixelated semiconductor detectors'. PhD thesis. University of Siegen, 2017 (see pp. 45, 46, 49, 120, 139, 148)

[103] F. Scholze, H. Henneken, P. Kuschnerus, H. Rabus, M. Richter, and G. Ulm. 'Determination of the electron-hole pair creation energy for semiconductors from the spectral responsivity of photodiodes'. *Nuclear Instruments and Methods in Physics Research Section A: Accelerators, Spectrometers, Detectors and Associated Equipment* 439.2-3 (2000), 208–215 (see p. 33)

[104] G. van der Schot, M. Svenda, F. R. N. C. Maia, M. Hantke, D. P. DePonte, M. M. Seibert, A. Aquila, J. Schulz, R. Kirian, M. Liang, F. Stellato, B. Iwan, J. Andreasson, N. Timneanu, D. Westphal, F. N. Almeida, D. Odic, D. Hasse, G. H. Carlsson, D. S. D. Larsson, A. Barty, A. V. Martin, S. Schorb, C. Bostedt, J. D. Bozek, D. Rolles, A. Rudenko, S. Epp, L. Foucar, B. Rudek, R. Hartmann, N. Kimmel, P. Holl, L. Englert, N.-T. Duane Loh, H. N. Chapman, I. Andersson, J. Hajdu, and T. Ekeberg. 'Imaging single cells in a beam of live cyanobacteria with an X-ray laser'. *Nature Communications* 6 (2015), 5704– (see p. 17)

[105] S. Send, A. Abboud, N. Wiesner, M. Shokr, M. Klaus, C. Genzel, T. Conka-Nurdan, D. Schlosser, M. Huth, R. Hartmann, L. Strüder, and U. Pietsch. 'Application of a pnCCD for energy-dispersive Laue diffraction with ultra-hard X-rays'. *Journal of Applied Crystallography* 49.1 (2016), 222–233 (see p. 17)

[106] C. E. Shannon. 'Communication in the presence of noise'. *Proceedings of the IRE* 37.1 (1949), 10–21 (see p. 106)

[107] H. Shinotsuka, S. Tanuma, C. Powell, and D. Penn. 'Calculations of electron stopping powers for 41 elemental solids over the 50 eV to 30 keV range with the full Penn algorithm'. *Nuclear Instruments and Methods in Physics Research Section B: Beam Interactions with Materials and Atoms* 270 (2012), 75–92 (see p. 34)

[108] C. S. Smith. 'Piezoresistance Effect in Germanium and Silicon'. *Phys. Rev.* 94 (1 1954), 42–49 (see p. 18)

[109] J. C. H. Spence and J. M. Zuo. 'Large dynamic range, parallel detection system for electron diffraction and imaging'. *Review of Scientific Instruments* 59.9 (1988), 2102–2105 (see p. 29)

[110] L. Strüder, H. Bräuninger, U. Briel, R. Hartmann, G. Hartner, D. Hauff, N. Krause, B. Maier, N. Meidinger, E. Pfeffermann, M. Popp, C. Reppin, R. Richter, D. Stötter, J. Trümper, U. Weber, P. Holl, J. Kemmer, H. Soltau, A. Viehl, and C. Zanthier. 'A 36 cm2 large monolythic pn-charge coupled device x-ray

detector for the European XMM satellite mission'. *Review of Scientific Instruments* 68.11 (1997), 4271–4274 (see p. 17)

[111] L. Strüder, U. Briel, K. Dennerl, R. Hartmann, E. Kendziorra, N. Meidinger, E. Pfeffermann, C. Reppin, B. Aschenbach, W. Bornemann, H. Bräuninger, W. Burkert, M. Elender, M. Freyberg, F. Haberl, G. Hartner, F. Heuschmann, H. Hippmann, E. Kastelic, S. Kemmer, G. Kettenring, W. Kink, N. Krause, S. Müller H, A. Oppitz, W. Pietsch, M. Popp, P. Predehl, A. Read, K. H. Stephan, D. Stötter, J. Trümper, P. Holl, J. Kemmer, H. Soltau, R. Stötter, U. Weber, U. Weichert, C. von Zanthier, D. Carathanassis, G. Lutz, R. H. Richter, P. Solc, H. Böttcher, M. Kuster, R. Staubert, A. Abbey, A. Holland, M. Turner, M. Balasini, G. F. Bignami, N. L. Palombara, G. Villa, W. Buttler, F. Gianini, R. Lainé, D. Lumb, and P. Dhez. 'The European Photon Imaging Camera on XMM-Newton: The pn-CCD camera'. *Astronomy & Astrophysics* 365.1 (2001), L18–L26 (see pp. 17, 45)

[112] L. Strüder, J. Englhauser, R. Hartmann, P. Holl, N. Meidinger, H. Soltau, U. Briel, K. Dennerl, M. Freyberg, F. Haberl, G. Hartner, E. Pfeffermann, T. Stadlbauer, and E. Kendziorra. 'pnCCDs on XMM-Newton—42 months in orbit'. *Nuclear Instruments and Methods in Physics Research Section A: Accelerators, Spectrometers, Detectors and Associated Equipment* 512.1–2 (2003), 386–400 (see p. 17)

[113] L. Strüder, S. Epp, D. Rolles, R. Hartmann, P. Holl, G. Lutz, H. Soltau, R. Eckart, C. Reich, K. Heinzinger, C. Thamm, A. Rudenko, F. Krasniqi, K.-U. Kühnel, C. Bauer, C.-D. Schröter, R. Moshammer, S. Techert, D. Miessner, M. Porro, O. Hälker, N. Meidinger, N. Kimmel, R. Andritschke, F. Schopper, G. Weidenspointner, A. Ziegler, D. Pietschner, S. Herrmann, U. Pietsch, A. Walenta, W. Leitenberger, C. Bostedt, T. Müller, D. Rupp, M. Adolph, H. Graafsma, H. Hirsemann, K. Gärtner, R. Richter, L. Foucar, R. L. Shoeman, I. Schlichting, and J. Ullrich. 'Large-format, high-speed, X-ray pnCCDs combined with electron and ion imaging spectrometers in a multipurpose chamber for experiments at 4th generation light sources'. *Nuclear Instruments and Methods in Physics Research Section A: Accelerators, Spectrometers, Detectors and Associated Equipment* 614.3 (2010), 483–496 (see p. 17)

[114] Y. Sun, S. E. Thompson, and T. Nishida. 'Physics of strain effects in semiconductors and metal-oxide-semiconductor field-effect transistors'. *Journal of Applied Physics* 101.10, 104503 (2007) (see p. 137)

[115] H. Tan, S. Turner, E. Yücelen, J. Verbeeck, and G. Van Tendeloo. '2D Atomic Mapping of Oxidation States in Transition Metal Oxides by Scanning Transmission Electron Microscopy and Electron Energy-Loss Spectroscopy'. *Phys. Rev. Lett.* 107 (10 2011), 107602 (see p. 42)

[116] M. W. Tate, P. Purohit, D. Chamberlain, K. X. Nguyen, R. Hovden, C. S. Chang, P. Deb, E. Turgut, J. T. Heron, D. G. Schlom, D. C. Ralph, G. D. Fuchs, K. S. Shanks, H. T. Philipp, D. A. Muller, and S. M. Gruner. 'High Dynamic Range Pixel Array Detector for Scanning Transmission Electron Microscopy'. *Microscopy and Microanalysis* 22.1 (2016), 237–249 (see p. 29)

[117] A. C. Thompson, J. Kirz, and D. T. Attwood, eds. *X-ray Data Booklet*. 3rd. 2009 (see p. 38)

[118] S. E. Thompson, M. Armstrong, C. Auth, M. Alavi, M. Buehler, R. Chau, S. Cea, T. Ghani, G. Glass, T. Hoffman, C. H. Jan, C. Kenyon, J. Klaus, K. Kuhn, Z. Ma, B. Mcintyre, K. Mistry, A. Murthy, B. Obradovic, R. Nagisetty, P. Nguyen, S. Sivakumar, R. Shaheed, L. Shifren, B. Tufts, S. Tyagi, M. Bohr, and Y. El-Mansy. 'A 90-nm logic technology featuring strained-silicon'. *IEEE Transactions on Electron Devices* 51.11 (2004), 1790–1797 (see p. 18)

[119] TU Dresden. *Versuchsanleitung TEM*. URL: `tu-dresden.de/mn/physik/isp/tbg/ressourcen/dateien/lehre/TEM.pdf` (visited on 2017-01-09) (see p. 23)

[120] P. Vavilov. 'Ionization Losses Of High-energy Heavy Particles'. *Soviet Phys. JETP* 5 (1957) (see p. 35)

[121] G. Weidenspointer. *Conversion Module* (see p. 64)

[122] J. Welser, J. L. Hoyt, and J. F. Gibbons. 'NMOS and PMOS transistors fabricated in strained silicon/relaxed silicon-germanium structures'. *1992 International Technical Digest on Electron Devices Meeting*. 1992, 1000–1002 (see p. 18)

[123] D. B. Williams and C. B. Carter. *Transmission Electron Microscopy*. 2nd ed. New York, USA: Springer, 2009 (see pp. 25, 37, 42, 137, 138)

[124] G. O. de Xivry and S. Rabien. 'A test bench for ARGOS: integration of sub-systems and validation of the wavefront sensing'. *SPIE Astronomical Telescopes+ Instrumentation*. International Society for Optics and Photonics. 2012, 844751–844751 (see p. 17)

[125] N. Yamamoto, J. C. H. Spence, and D. Fathy. 'Cathodoluminescence and polarization studies from individual dislocations in diamond'. *Philosophical Magazine Part B* 49.6 (1984), 609–629 (see p. 42)

[126] H. Yang, L. Jones, **H. Ryll**, M. Simson, H. Soltau, Y. Kondo, R. Sagawa, H. Banba, I. MacLaren, and P. D. Nellist. '4D STEM: High efficiency phase contrast imaging using a fast pixelated detector'. *Journal of Physics: Conference Series* 644.1 (2015), 012032 (see pp. 143, 144)

[127] H. Yang, R. N. Rutte, L. Jones, M. Simson, R. Sagawa, **H. Ryll**, M. Huth, T. J. Pennycook, M. Green, H. Soltau, Y. Kondo, B. G. Davis, and P. D. Nellist. 'Simultaneous atomic-resolution electron ptychography and Z-contrast imaging of light and heavy elements in complex nanostructures'. *Nature Communications* 7 (2016), 12532– (see pp. 18, 141–145)

[128] H. Yang, L. Jones, **H. Ryll**, M. Simson, H. Soltau, Y. Kondo, R. Sagawa, H. Banba, T. J. Pennycook, and P. D. Nellist. 'High Efficiency Phase Contrast Imaging In STEM Using Fast Direct Electron Pixelated Detectors'. *Microscopy and Microanalysis* 21 (Supplement S3 2015), 2303–2304 (see p. 142)

[129] H. Yang, I. MacLaren, L. Jones, G. T. Martinez, M. Simson, M. Huth, **H. Ryll**, H. Soltau, R. Sagawa, Y. Kondo, C. Ophus, P. Ercius, L. Jin, A. Kovács, and P. D. Nellist. 'Electron ptychographic phase imaging of light elements in crystalline materials using Wigner distribution deconvolution'. *Ultramicroscopy* 180 (2017), 173–179 (see p. 142)

[130] A. Zoglauer, R. Andritschke, and F. Schopper. 'MEGAlib The Medium Energy Gamma-ray Astronomy Library'. *New Astronomy Reviews* 50.7-8 (2006), 629–632 (see p. 63)

[131] H. J. Zweig. 'Detective Quantum Efficiency of Photodetectors with Some Amplification Mechanisms'. *J. Opt. Soc. Am.* 55.5 (1965), 525–528 (see p. 153)

List of Figures

2.1 Image of a replica of an electron microscope from 1933 21
2.2 Three types of electrons 21
2.3 Schematic side view cut illustration and a front view image of a TEM 23
2.4 TEM and STEM illumination 24
2.5 Ray path diagram in a TEM after the sample 25
2.6 Schematic cut view of a basic magnetic lens 25
2.7 The most used detectors in STEM and electron scattering angles in transmission direction 26
2.8 Segmented ADF and BF detector 27

3.1 Total cross sections in silicon 32
3.2 Schematic of an electron track in a solid 33
3.3 Energy loss per unit path length $\mathrm{d}E/\mathrm{d}x$ for electrons in Si 35
3.4 Simulated electron tracks with an energy of 300 keV 36
3.5 Path length of electrons in Si 36
3.6 Example track of a 300 keV electron 37
3.7 Characteristic X-ray emission and Auger electron transition 37
3.8 Cross sections for elastic and inelastic scattering 39
3.9 Overview of signals from sample 41
3.10 Example of images with back scattered electrons and X-ray photons 41
3.11 Schematic of the cathodoluminescence process 41
3.12 Schematic of electron energy loss spectroscopy (EELS) 42
3.13 Schematic of electron energy loss spectroscopy (EELS) in STEM 43
3.14 Schematic of the energy filtered TEM (EFTEM) 43
3.15 Example STEM images of the BF and DF 43
3.16 Constructive interference of electron waves under Bragg conditions 44
3.17 Diffraction pattern recorded with the pnCCD 44

4.1 Principle of sideward depletion 45
4.2 Generation of electron-hole pairs and charge separation 46
4.3 Charge spreading of signal electrons in the pnCCD 47
4.4 Side view of the pnCCD 47
4.5 Readout scheme of the pnCCD 48
4.6 Principle of windowing 48
4.7 Comparison of operation modes 51

4.8 Cross section and image of the pnCCD camera system for TEM applications 52

5.1 Example of a raw dark frame 54
5.2 Example of an offset corrected dark frame 54
5.3 Example of a noise map 54
5.4 Example of a CM corrected dark frame 54
5.5 Data analysis steps for pnCCD frame data 55
5.6 Orientation of the four readout quadrants 57
5.7 Thresholding in single electron analysis 58
5.8 Example of an event and its properties 58
5.9 Example of an energy spectrum recorded under electron illumination 59
5.10 The rectangular (rect) function 59
5.11 Center of gravity (CoG) for a single event 59

6.1 Overview of the simulation process 64
6.2 Schematic of condensed algorithm in Geant4 64
6.3 Schematic setup for the Geant4 simulations 65
6.4 Tracks of simulated TEM electrons 66
6.5 Tracks of simulated TEM electrons in the x-y plane 67
6.6 Relative distribution of deposited energy 68
6.7 Cumulative distribution of energy depositions after convolution with a Gaussian function 69
6.8 Detection efficiency depending on detection threshold 71
6.9 Probability distributions of DE_{bulk} for 80 keV 73
6.10 Poisson distribution probabilities for various electron rates 74
6.11 Probability distribution 75
6.12 Target electron rate 76

7.1 Crop of single frames recorded with the pnCCD showing single electrons 79
7.2 Typical energy spectrum of electrons after SEA 80
7.3 Example of F2 event 81
7.4 Evaluation of the multiplicity function $M(E)$ 82
7.5 Energy spectrum of events with full energy deposition 82
7.6 Energy spectrum of events with full energy deposition 83
7.7 Energy spectrum of events with partial energy deposition 84
7.8 Tracks of simulated electrons that are backscattered 84
7.9 Dependency of the reached depth z and traveled distance on the deposited energy 85
7.10 Details of the energy spectrum for backscattered TEM electrons 85
7.11 Dependence of deposited energy on minimal depth of electron tracks 85
7.12 Energy spectra for energies ranging from 20 keV to 300 keV 86
7.13 Backscattering coefficient η 87
7.14 Silicon escape peak in a 20 keV measurement 88
7.15 Example of Bremsstrahlung event 88
7.16 Titanium photon peak 88

7.17 Two electron pile up-event 89
7.18 Energy spectrum for events of type S1 to S4 89
7.19 Weighted probabilities for the first four event types 90
7.20 Cumulative non-weighted probabilities for the first six event types S1-S6 91
7.21 Comparison of convolution model with simulation of higher electron rate 92
7.22 Energy spectrum of single TEM electrons at a high electron rate showing pile-up 92
7.23 Positions of energy peaks depending on number of contributing TEM electrons 93
7.24 Comparison of convolution model with simulation of higher electron rate 94
7.25 Dependency of pile-up probability on TEM electron rate and energy 95
7.26 Comparison of single frames at two electron rates 95
7.27 Probability for p_{S1} depending on readout noise n_{ro} and back contact voltage U_{bc} 96
7.28 Distribution of number of pixels in the S1 event 96
7.29 Dependency of pile-up on pixel size 97
7.30 Number of pixel per event distributions depending on energy 98
7.31 Comparison of distributions of the number of pixel per event for the HCHC and HiRes mode ($E = 60$ keV) 99
7.32 Sub-pixel resolution in one direction 99

8.1 Relationship between the PSF, LSF and ESF 106
8.2 The sharp edges used in the determination of the MTF 106
8.3 Comparison of intensity images at verious energies 107
8.4 Comparison of the MTF in intensity imaging mode 108
8.5 Ideal cdf and pdf of PoE positions under homogenous illumination 109
8.6 Distribution of the position of the CoG over the pixel geometry calculated from simulated electrons ($E = 20$ keV) without any noise 109
8.7 Distributions of the position of the CoG over the pixel geometry for experimental data for 20 keV and 60 keV 110
8.8 Detail of images with 5×5 sub-pixel resolution and the CoG method 110
8.9 Gaussian distribution that is integrated over pixel boundaries 111
8.10 Correction shift D_g that is applied to the calculated CoG position to determine the correct PoE for an assumed Gaussian distribution 112
8.11 Comparison of cdf and pdf before (CoG) and after Gauss correction ($E = 60$ keV) 113
8.12 Graphical representation of Eta correction 114
8.13 Comparison of cdf and pdf before (CoG) and after Eta correction ($E = 60$ keV) 114
8.14 Example of a long electron track 115

8.15 Comparison of images created with the CoG model and the LTFPA model 115
8.16 Comparison of the MTF for all energies 116
8.17 Comparison of cdfs between HiRes and HCHC mode 117
8.18 Comparison of 5×5 sub-pixel images 117
8.19 Comparison of Gauss and Eta methods 118
8.20 Comparison of images with increasing sub-pixel resolution 118
8.21 Distribution of positions in HCHC mode at 20 keV 119
8.22 Detail of 21×21 sub-pixel image 120
8.23 Comparison of sub-pixel images at 20 keV 120
8.24 Image showing uneven illumination for measurements recorded at 20 keV 121
8.25 Comparison of images for 40 keV up to a 11×11 sub-pixel resolution 121

9.1 Principle of an optical and electron biprism 124
9.2 Geometry of the Double Slit 125
9.3 Montage of intensity images ($E = 60$ keV) with increasing number of frames that are integrated to create the image 126
9.4 Interferometric visibility 127
9.5 Sub-pixel image in holography 127
9.6 Averaged intensity of interference fringes with and without sub-pixel resolution 127
9.7 Principle of tomography 128
9.8 Principle of back projection 128
9.9 Single frames of a tomography tilt series 129
9.10 Single frames of a tomography tilt series 130
9.11 Reconstructed Nanotube 130
9.12 Examples of recorded signals in 4D-STEM 132
9.13 Principle of 4D-STEM Imaging 132
9.14 Patterns of synthetic detectors in 4D-STEM 133
9.15 Image of a magnetic sample 134
9.16 Example frames of the BF disc in STEM 134
9.17 Positions of the BF disc 135
9.18 Comparison of standard Lorentz image and 4D-STEM image 136
9.19 Principle of CBED and lattice strain measurement in 4D-STEM 137
9.20 Example images of a diffraction disc 138
9.21 STEM-HAADF image of the investigated heterogeneous semiconductor sample 138
9.22 Strain profiles of heterogeneous semiconductor sample 139
9.23 Lattice strain maps of a MOSFET sample 140
9.24 Beam configuration for 4D-STEM ptychography 141
9.25 Principal steps of ptychography in 4D-STEM 142
9.26 Single frames of a ptychography measurement 143
9.27 Comparison of images of GaN 144
9.28 Images of a complex nanotube sample 144
9.29 ADF and phase contrast image of carbon nanotube system 145

A.1 Visual concept of the MTF 151

A.2 Procedure for the calculation of the MTF 152
A.3 Intensity distribution and its dependency on the ratio of slit distance to slit width 154
A.4 Comparison of Gaussian distributions 160

List of Tables

2.1 Overview of electron energies and their corresponding de Broglie wavelengths 23
2.2 Specifications of further direct detectors 29

3.1 Path length of electrons in Si 36
3.2 Achievable spatial resolution for various EM techniques 40

4.1 Frame rates depending on windowing and binning 49
4.2 Charge Handling Capacity 50

5.1 Pixel sizes for sub-pixel resolution 60

6.1 Cumulative values for energy distribution 69
6.2 Detection Efficiency 71
6.3 Negative binomial distribution probabilities for 80 keV and 200 keV 73
6.4 Poisson Distribution 75
6.5 Target electron rates 76

7.1 Backscattering coefficient determined from experimental data 87
7.2 Cumulative probabilities 91
7.3 The average number of pixels in an event for various electron energies 98
7.4 Comparison of number of pixels for HCHC and HiRes mode 99
7.5 DQE for various electron energies 101
7.6 Energy resolution of the pnCCD under electron illumination 102

8.1 Overview of MTF 116
8.2 Statistics for sub-pixel resolutions 119
8.3 Sub-pixel resolutions for 40 keV 121

9.1 Overview of measurement times depending on number of probe positions 133
9.2 Comparison of precision in lattice strain measurements 139

A.1 Stopping power of electrons in silicon 156
A.2 Extended Table of Detection Efficiency Values 158
A.3 Reference of PIDs 161
A.4 Reference of MIDs 162

List of Symbols

A atomic weight 34

β ratio v/c 22

c speed of light 22
C_{eV} calibration factor 100
C_{tem} conversion factor 100

d distance, length 44
$\mathrm{d}\sigma/\mathrm{d}\Omega$ differential cross section 39

E energy 32
E_{dep} deposited energy 34
E_{kin} kinetic energy 34
E_{tem} energy of TEM electron 34
e elementary charge 22
ϵ_0 vacuum permitivity 34
η backscattering coefficient 86
$\eta(x)$ eta correction function 113

F Fano factor 38

h Planck constant 22

I mean excitation energy 34

γ Lorentz factor 22
λ length parameter 106
λ wavelength 22

m_0 electron rest mass 22

N_{A} Avogadro constant 34
N_{CHC} charge handling capacity 49
N_{sig} number of signal electrons 34
N_{tem} number of TEM electrons 49

p momentum 22
p probability (distribution) 81

r electron rate 74
ρ density 34

S stopping power 32
s path length 35
s sub-pixel factor 60

θ angle 39

U potential, voltage 22

v velocity 22

w mean electron-hole pair generation energy 33
w_{physical} physical pixel size 59
w_{pix} image pixel size 59
$w_{\text{S}n}$ probability weighting factor 89
ω spatial frequency 106

Z atomic number 34

Acknowledgments

This work was built with the support of many people to whom I am deeply grateful:

I thank Prof. Dr. Lothar Strüder for his supervision and the enlightening discussions. His humor and guidance supported this work in essential ways.

I thank Prof. Dr. Ulrich Pietsch for being my second advisor.

I thank Dr. Heike Soltau for initially giving me the opportunity to work on this dissertation and for the encouragement to keep pushing forward through many discussions.

I am grateful to the people I met and worked together with during the research projects for their great teamwork and the diverse experiences.

I thank my colleagues whom I had the pleasure to work with during this time, share the offices, experiment in dark labs and meet at the coffee machines, namely Sebastian, Ivan, Andreas, Dieter, Stefan, Robert, Alois, Peter, Martin, Daniel, Martin, Julia, Petra, Jeff and Robert. I thank all the other colleagues for their various support and the production of the detectors.

I thank my family for their support and for being a place to recharge.

A big thanks to my friends for always keeping the spirit high even during though times, especially S.M.C..

Eidesstattliche Erklärung

Ich erkläre hiermit an Eides statt, dass ich die vorliegende Arbeit ohne unzulässige Hilfe Dritter und ohne Benutzung anderer, nicht angegebener Hilfsmittel angefertigt habe. Die aus anderen Quellen direkt oder indirekt übernommenen Daten und Konzepte sind unter Angabe der Quelle gekennzeichnet.
Die Arbeit wurde bisher weder im In- noch im Ausland in gleicher oder ähnlicher Form einer anderen Prüfungsbehörde vorgelegt.
Es wurden keine Dienste eines Promotionsvermittlungsinstituts oder einer ähnlichen Organisation in Anspruch genommen.